Semiconductor Nanoplatelets for Imaging and Energy Transfer

Dissertation

Zur Erlangung des Grades

„Doktor rerum naturalium" (Dr. rer. nat.)

dem Fachbereich 09 - Chemie, Pharmazie und Geowissenschaften

Der Johannes Gutenberg-Universität Mainz

Henry Halim

(geb. in Jakarta, Indonesien)

Mainz, den 06.01.2021

Max Planck **Graduate Center**
mit der Johannes Gutenberg-Universität

MAX-PLANCK-INSTITUT
FÜR POLYMERFORSCHUNG
MAX PLANCK INSTITUTE
FOR POLYMER RESEARCH

JOHANNES GUTENBERG
UNIVERSITÄT MAINZ

JG|U

Author's note

This thesis was carried out from August 2017 to January 2021 at the Max Planck Institute for Polymer Research, within the framework of Max Planck Graduate Center with the Johannes Gutenberg University of Mainz.

Supervisor: Prof. Dr. Katharina Landfester

Co-Supervisor: Prof. Dr. Thomas Basché

Mentors: Dr. Andreas Riedinger, Dr. Stanislav Balouchev

Daily Supervisor: Dr. Andreas Riedinger

Date of oral examination:

Declaration

I hereby declare that I wrote the dissertation submitted without any unauthorized external assistance and used only sources acknowledged in the work. All textual passages which are appropriated verbatim or paraphrased from published and unpublished texts as well as all information obtained from oral sources are duly indicated and listed in accordance with bibliographical rules. In carrying out this research, I complied with the rules of standard scientific practice as formulated in the statutes of Johannes Gutenberg-University Mainz to insure standard scientific practice.

Henry Halim

Acknowledgements

List of Abbreviations

9-anthracene carboxylic acid	9-ACA
correlative light and electron microscopy	cLEM
confocal laser scanning microscopy	cLSM
4,7-di(thiophen-2-yl)benzo[c][1,2,5]thiadiazole	DBT
5-(7-(thiophen-2-yl)benzo[c][1,2,5]thiadiazol-4-yl)thiophene-2-carboxylic acid	DBTCA
Dulbecco Modified Eagle Medium	DMEM
9,10-diphenylanthracene	DPA
fetal bovine serum	FBS
fluorescence correlation spectroscopy	FCS
Förster resonance energy transfer	FRET
human serum	HS
inductively coupled plasma-optical emission spectrometry	ICP-OES
isothermal titration calorimetry	ITC
monolayer	ML
nanoplatelets	NPLs
1-octadecene	ODE
Dulbecco's Phosphate Buffered Saline	PBS
photoluminescence	PL
quantum dots	QDs
quantum yield	QY or Φ
transient absorption	TA
time-correlated single photon counting	TCSPC
transmission electron microscopy	TEM
time resolved photoluminescence	TRPL
triplet-triplet annihilation	TTA
upconversion	UC

Table of contents

Contents

Abstract

This work deals with the application of CdSe nanoplatelets (NPLs) for imaging and energy transfer. NPLs are semiconductor nanocrystals which experience 1D quantum confinement due to their geometry, thus behaving as colloidal quantum wells. The 1D quantum confinement enables new possibilities relative to the well-studied 3D confined quantum dot counterpart. In the framework of imaging and energy transfer, this includes the possibility of overcoming the problem of inhomogeneous broadening, arising from colloidal synthesis of nanocrystals and the possibility of increasing the absorption cross section of the particle without changing its band gap i.e. its spectral properties. To utilize the excited state of NPLs to do useful work is a matter of controlling how they are quenched. In essence, this is done by controlling the distance between the NPL and their potential quenchers. In this work, triplet energy transfer was achieved by close attachment of 9-anthracene carboxylic acid ligands on NPLs to allow Dexter-like energy transfer. Förster Resonance Energy Transfer was achieved through similar means by using an organic fluorophore, which absorbs in the region of the NPLs' photoluminescence. The photoexcited NPLs were also used to catalyze the transformation of nitrobenzene to azoxybenzene, without overreduction to aniline. When fluorescence is desired for application in imaging, the quenchers are put aside by introducing a shell of CdZnS and organic polymer, isolating the surface of the NPL electronically and chemically. This work also shows the benefit of the polymer coating, allowing the NPLs to be colloidally stable in biological medium and withstanding the conditions for encapsulation, allowing them to be used as imaging markers to visualize nanocarriers. In short, this work demonstrates the viability of NPLs for imaging and energy transfer applications and revealed key parameters relevant to develop the NPLs better for such applications.

Zusammenfassung

Diese Arbeit befasst sich mit CdSe-Nanoplättchen (NPLs) für Bildgebung und Energieübertragung. NPLs sind Halbleiter-Nanokristalle, die aufgrund ihrer Geometrie eine 1D-Größenquantisierung erfahren und sich somit wie kolloidale Quanten-Wells verhalten. Die 1D-Größenquantisierung ermöglichte neue Möglichkeiten im Vergleich zur gut untersuchten 3D-Größenquantisierung im Quantenpunkt-Pendant. Für die Bildgebung und den Energietransfer schließt dies die Möglichkeit ein, das Problem der inhomogenen Verbreiterung zu überwinden, das sich aus der kolloidalen Synthese von Nanokristallen ergibt, sowie die Möglichkeit, den Absorptionsquerschnitt des Teilchens zu erhöhen, ohne seine Bandlücke, d.h. seine spektralen Eigenschaften, zu verändern. Um den angeregten Zustand von NPLs zu nutzen, muss man kontrollieren, wie die angeregten Zustände „gequencht" werden. Im Wesentlichen geschieht dies durch die Steuerung des Abstands zwischen den NPLs und ihren potenziellen Quenchern. In dieser Arbeit wurde die Triplett-Energieübertragung durch enge Bindung von 9-Anthracen-Carbonsäureliganden an NPLs erreicht, um eine Dexter-ähnliche Energieübertragung zu ermöglichen. Der Förster-Resonanzenergietransfer wurde auf ähnliche Weise durch die Verwendung eines organischen Fluorophors erreicht, das im Bereich der Photolumineszenz der NPLs absorbiert. Die photoangeregten NPLs wurden auch verwendet, um die Umwandlung von Nitrobenzol in Azoxybenzol ohne eine Überreduktion zu Anilin zu katalysieren. Da Photolumineszenz für die Anwendung in der Bildgebung erwünscht ist, wurden die Quencher „ausgeschlossen", indem eine Hülle aus CdZnS und organischem Polymer eingeführt wurde, wodurch die Oberfläche des NPLs elektronisch und chemisch isoliert wurde. Diese Arbeit zeigt auch den Vorteil der Polymerbeschichtung, die es ermöglicht, dass die NPLs im biologischen Medium kolloidal stabil sind und den Bedingungen für die Verkapselung standhalten, so dass sie als bildgebende Marker zur Visualisierung von Nanocarriern verwendet werden können. Kurz gesagt, diese Arbeit demonstriert, wie die speziellen Eigenschaften von NPLs für Bildgebungs- und Energieübertragungsanwendungen optimal genutzt werden können und offenbart Schlüsselparameter, die für eine weitere Entwicklung der NPLs für solche Anwendungen relevant sind.

Context

In the field of materials science, we always strive to develop newer and better materials. More precisely, we aim to achieve greater tunability of properties, create robust systems and challenge what we believe to be the fundamental limits. The field of nanomaterials is one of the greatest examples of this, as it has changed the way we thought of materials completely. By adjusting the structure in nanoscale, it is possible to obtain new properties that are completely different from the material's usual bulk property. This change can arise from several reasons. One is grounded in the fact that the surface of a material behaves differently to its bulk due to the presence of dangling bonds. Since the surface area per unit mass of nanomaterials are so large, their behavior is much more affected by the nature of these surfaces compared to the materials usual bulk form. The other reason for the change in property arises due to the increasing role of quantum effects, namely quantum confinement. Quantum confinement gave birth to a whole new field of fluorescent materials based on semiconductors.

Years of development lead to optimized samples of semiconductor quantum dots, made of variety of different materials, giving a vast range of different properties for almost every application imaginable. However, the property control of quantum dots suffers from a fundamental issue. The quantum confinement in the quantum dots is controlled by the length of the quantum confinement, in other words the particle size. Due to the colloidal synthesis of quantum dots, particles will always have a size distribution, so it is impossible to precisely control the size of quantum dots. Therefore, the resulting material will always have some inhomogeneous broadening. This will alter processes which demand precise control of energies like energy transfer since every particle will transfer energies slightly differently. So even for acceptors with a good match to the quantum dots emission wavelength will have some energy losses from the sub optimally aligned sub population in the quantum dot sample.

As of now, the best way to prepare semiconductor nanocrystals is through colloidal synthesis since alternative methods tend to create undesirable defect states. In order to obtain high quality semiconductor nanocrystals and avoid inhomogeneous broadening, a new approach should be taken. To do this, quantum confinement in the nanocrystal must be changed from 3D quantum

confinement inside a quasi-sphere to a 1D quantum confinement inside a quasi 2D nanocrystal. These quasi 2D nanocrystals, known as nanoplatelets (NPLs) or colloidal quantum wells have thicknesses of few nanometers and lateral sizes of tens of nanometers. As a result of this anisotropic geometry, the quantum confinement highly depends on the thickness, which can be controlled in an atomically precise fashion. This leads to the possibility of avoiding inhomogeneous broadening since every NPL with the same thickness have the same bandgap so they can emit exactly the same way, without being much affected by the colloidal distribution in their lateral size.

Consequently, it is possible to increase the absorption cross-section of NPLs by extending their lateral size. This feature is known as absorption cross-section scaling and allows NPLs to reach higher absorption cross sections than quantum dots. Therefore, by using NPLs, we are able to study a system possessing precisely defined emission while having the high and broad absorption profile of nanocrystals. This also enables us to understand how nanocrystals transfer their energy without disturbance from inhomogeneous broadening. In addition, the number of binding sites on the surface of NPLs can be increased without affecting the energy levels. These parameters give room to a larger space of possibility to optimize energy transfer systems and opportunity to design platforms previously not achievable by quantum dots e.g. blue emitting nanocrystal with a very large particle size.

The main project of this work is precisely to look at how the energy transfer of NPLs works and if we can benefit from larger absorption cross-sections, in Dexter-like transfer, FRET and photocatalyst systems. We also look at the photoluminescence of NPLs framework of imaging, taking advantage of their high absorption cross sections to develop bright markers. The results from these studies highlights the benefits of using NPLs but also the complications coming from their quasi 2D geometry (e.g. interaction with ligands) which could be used as a guide to design improved NPL based systems in the future.

Chapter 1: Introduction - Theories and State of The Art

1.1 Properties of CdSe NPLs

This section will expand on the topics discussed in *context* and discuss the basic properties of NPLs relevant to the studies conducted in this work.

Quantum Confinement in Nanocrystals

Bulk semiconductors, consisting of many atoms, form valence bands and conduction bands[1] (Figure 1.1). These bands are separated by an energy gap. If we provide more energy than the gap, we can promote an electron from the valence band to the conduction band. The formation of bands in bulk material from energy levels in atoms is due to the immense number of atoms interacting with one another by overlapping orbitals.[1] The result of the combination of those orbitals is many energy levels, so close to one another that they are almost indistinguishable. Hence, they can be grouped together into what is called a band.

If we try to decrease the size of the bulk material, the number of atoms decreases. In other words, when the particle size is small, the number of atoms that contribute orbitals also decreases.[1] Eventually the gaps between the combination of orbitals become distinguishable again, closer to an atom or molecule. This transition from bulk to molecular characteristic is what is observed in nanomaterials and is a result of quantum confinement.[2]
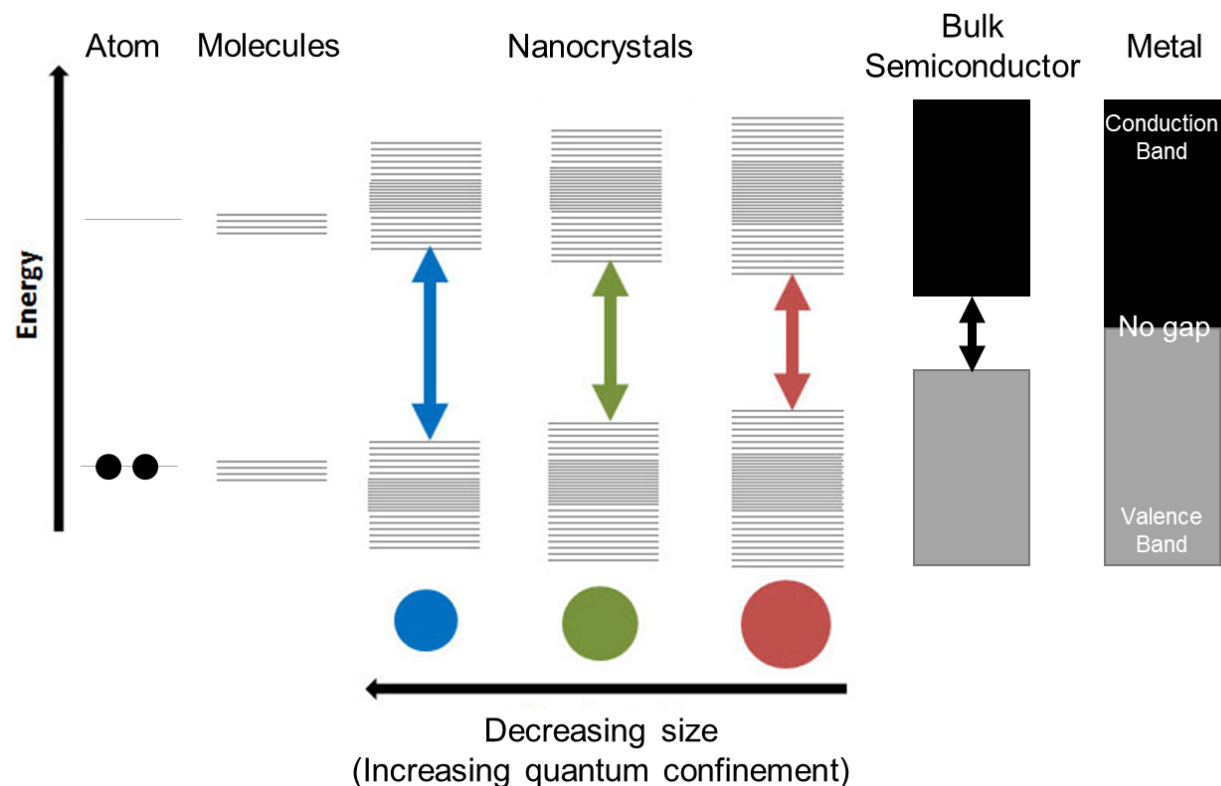
Figure 1.1. Electronic states of different materials. Lines represent the energy level of orbitals. As orbitals interact with one another, the energy gap becomes so close that they resemble more of a band. Figure is adapted and modified from Sigma Aldrich.[3]

The transition from bulk to nanocrystal can be determined more concretely from the dimensions of the material, when its size goes below the calculated Bohr radius e.g. CdSe < 4 nm, InAs < 29 nm.[4] The Bohr radius can be thought of as how much space the delocalized electron needs to feel "free". When the materials' dimensions go under the Bohr radius, the electron is affected and starts to be confined. This confinement effect can be modelled by the particle in a box model, where the box size will determine the energy levels the electron can be allowed in. For quantum dots this model portrays the confinement in three dimensions due to the material being smaller than the Bohr radius in x, y and z direction.

This changes for NPLs since their lateral dimensions are larger than the Bohr radius, while their thicknesses are below. This means that their electrons are only weakly confined in their lateral dimensions but are strongly confined in their thickness. Therefore, the quantum confinement

mainly happens in one dimension. As a result, the NPLs are no longer like particle in a box but rather a quantum well. Extension of the lateral sizes will have minor effects on the quantum confinement (Figure 1.2) in NPLs, therefore their energy levels are effectively independent of the lateral size (unless it too goes under the Bohr radius). This has a profound implication to the properties of NPLs discussed in the next sections.
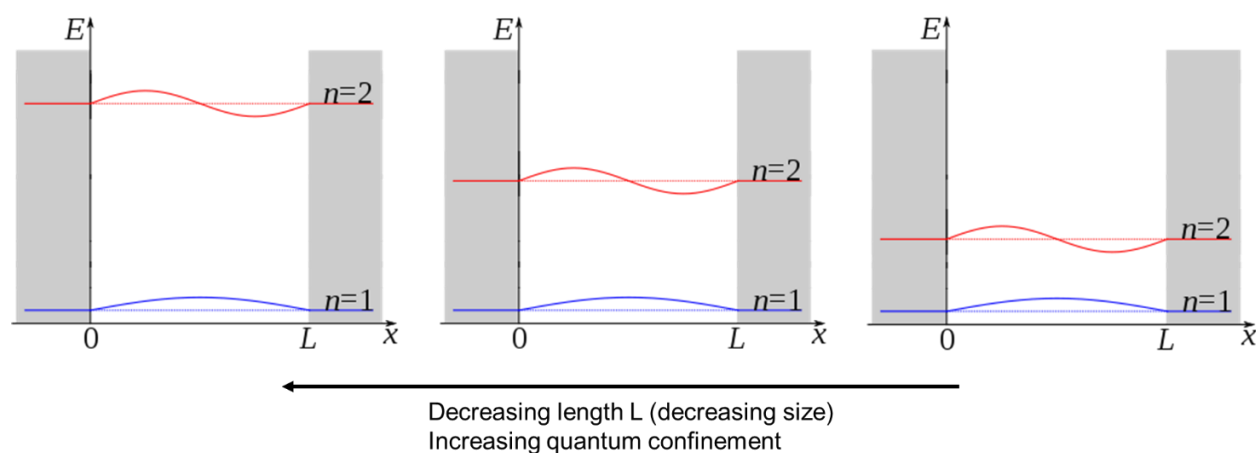
Figure 1.2. Relationship between the degrees of quantum confinement to the energy gaps.

High Absorption Cross Sections in NPLs

The absorption cross sections of nanocrystals increase with the particle size.[5-7] Although QDs possess naturally high absorption cross sections compared to standard organic dyes, their sizes are limited to values below the material's Bohr radius to keep the quantum confinement effects. NPLs are different in this regard, as they can continuously increase their lateral size to increase the absorption cross sections, while retaining the quantum confinement by keeping the thickness to a few nanometers. This makes it possible to have NPLs with absorption cross sections many folds of QDs (Figure 1.3). The same principle applies to the two-photon absorption cross section, making NPLs the material with the highest two photon absorption cross section to date.[7] This property is highly versatile for practical applications since it is possible to reach the same PL signals as QDs with lower excitation power or obtain greater signals with equal excitation power. The former case is potentially relevant in cases like in vivo microscopy or energy harvesting from sunlight while the latter for single particle detection or alike.
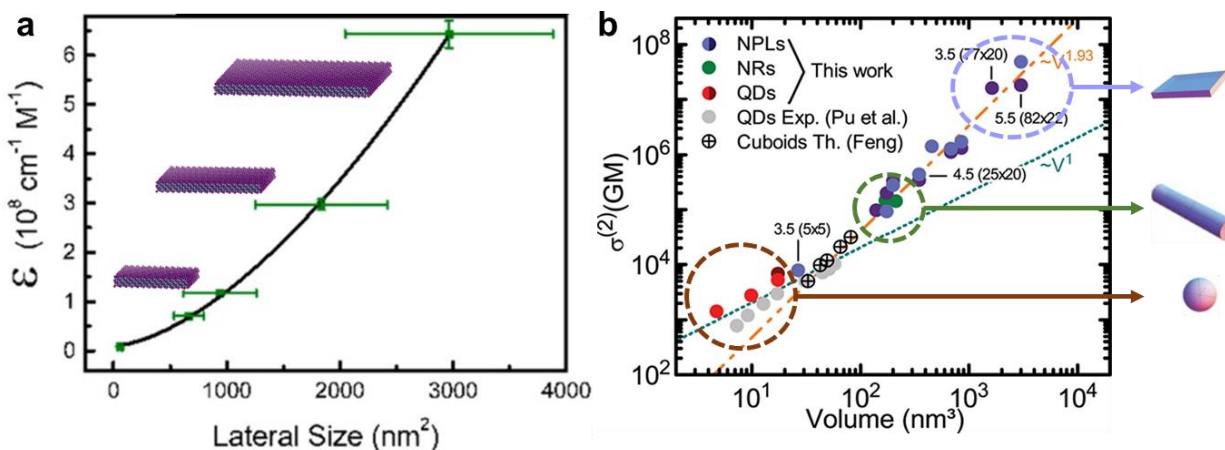
Figure 1.3. Absorption cross section of nanocrystals increase with their size. a) Lateral size dependent absorption cross section of 4ML NPLs. b) Two-photon absorption cross sections of various nanocrystal geometries. Absorption cross sections increase when the volume of the crystal increases i.e. their size. NPLs have greater scaling compared to other nanocrystal geometries and can therefore achieve the highest two-photon absorption cross section. Figure is adapted with permission from *The Journal of Physical Chemistry C* 2015 (47) 26768-26775[6] and *Nano Letters* 2015 (8) 4985-4992.[7]

Absolute Control of Energy Levels

Due to the formation mechanism of NPLs,[8] their thickness can be synthesized in an atomically precise manner. In the colloidal synthesis of CdSe NPLs, the 1 and 2 monolayer NPLs are unstable (discussed in later section, Figure 1.7.) so this starts off with 3 monolayer NPLs (4 layers of Cd, 3 layers of Se). The thickness can be increased to 4 monolayers, 5 monolayers and so on until 8 monolayers.[9] The effect of increasing the monolayer thickness is increasing the length of a quantum well (Figure 1.2).

By careful purification, it is possible to separate the different monolayer (ML) NPLs and obtain pure fractions of NPLs (Figure 1.4a-c). This is typically due to the lateral size difference of each ML fraction, for example the 3ML side product of 4ML NPL synthesis are much larger (edge length ~50 nm vs ~20 nm), so they agglomerate easier relative to 4ML NPLs. One may contrast this with quantum dots, where the next larger dot would only be less than a nanometer different in size, thus they are practically impossible to separate. The possibility of obtaining pure ML fractions

is a huge boon to the field of nanocrystals, as NPLs enables to an unprecedented degree of spectral purity – seen by the narrow emission peak (Figure 1.4a-c, FWHM ~10 nm) and caused by NPLs of equal thicknesses emitting the same way. An obvious application of this is to improve the color range of displays[10] (Figure 1.4d) but it can also be used to get homogeneous energy transfer from NPLs to small molecule acceptors as done in this work (chapter 2).
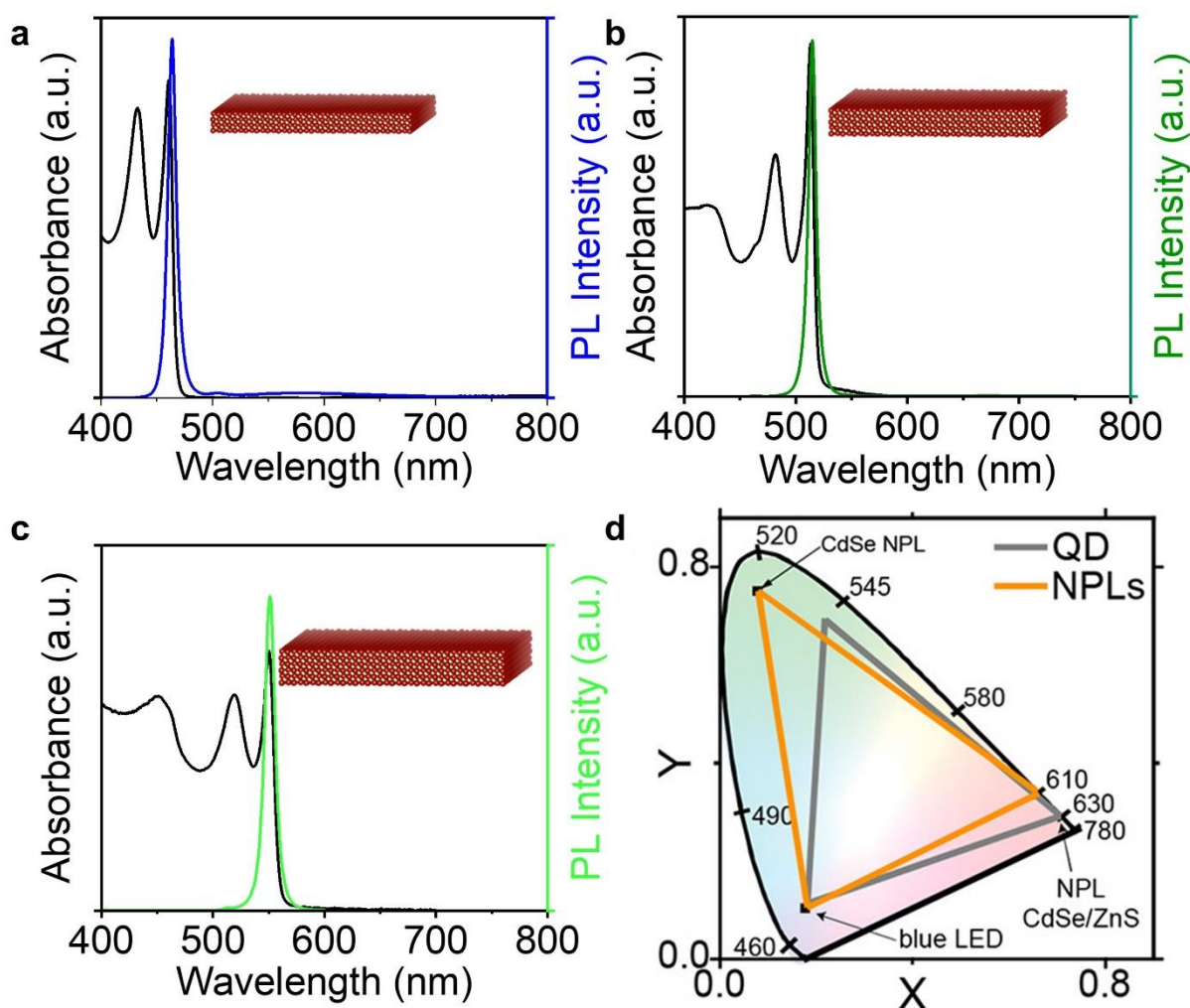
Figure 1.4. Absorption and emission properties of CdSe NPLs with 3MLs (a), 4MLs (b) and 5MLs (c). NPLs emit in a spectrally pure fashion, as seen by their narrow PL (FWHM ~8 nm). This property is interesting for application in large gamut displays, shown in the chromaticity diagram (d). Figure 1.4d is adapted with permission from *ACS Nano* 2019 (5) 5326-5334.[10]

Surface Functionalization and Ligand Coverage

Possessing Cd and Se atoms, we can expect that the surface chemistry of QDs and NPLs would follow traditional Cd and Se chemistry. To understand the whole picture however, we would have to look at the crystal facets of the nanocrystals. For typical CdSe QDs in a zincblende crystal structure, (100), (110) and (111) facets are exposed due to their quasi-spherical shape (Figure 1.5a). The (100) surface are Cd terminated, which leaves it with dangling bonds from the Cd atoms and can be thought of as a charged facet. These dangling bonds are in reality passivated by the fatty acid molecules introduced as the precursors in the synthesis.

The (111) facet contains exposed Cd and Se atoms and is therefore neutral. Since the COO⁻ group from the fatty acids are charged, they cannot simply interact with the (111) facets. Several studies showed that these facets are passivated by $Cd(RCOO^-)_2$ when the nanocrystals are just formed.[11-13] This surface is labile[12] and is prone to damage in case the Cd complex leaves, the Se gets exposed and oxidized.

For NPLs however, the picture is quite different since their surface only consists of (100) facets.[14] Thus, the ligands can only bind in one way to the Cd surface. This makes the ligand-NPL interactions much easier to control, since the behavior of the ligands is homogeneous in NPLs.
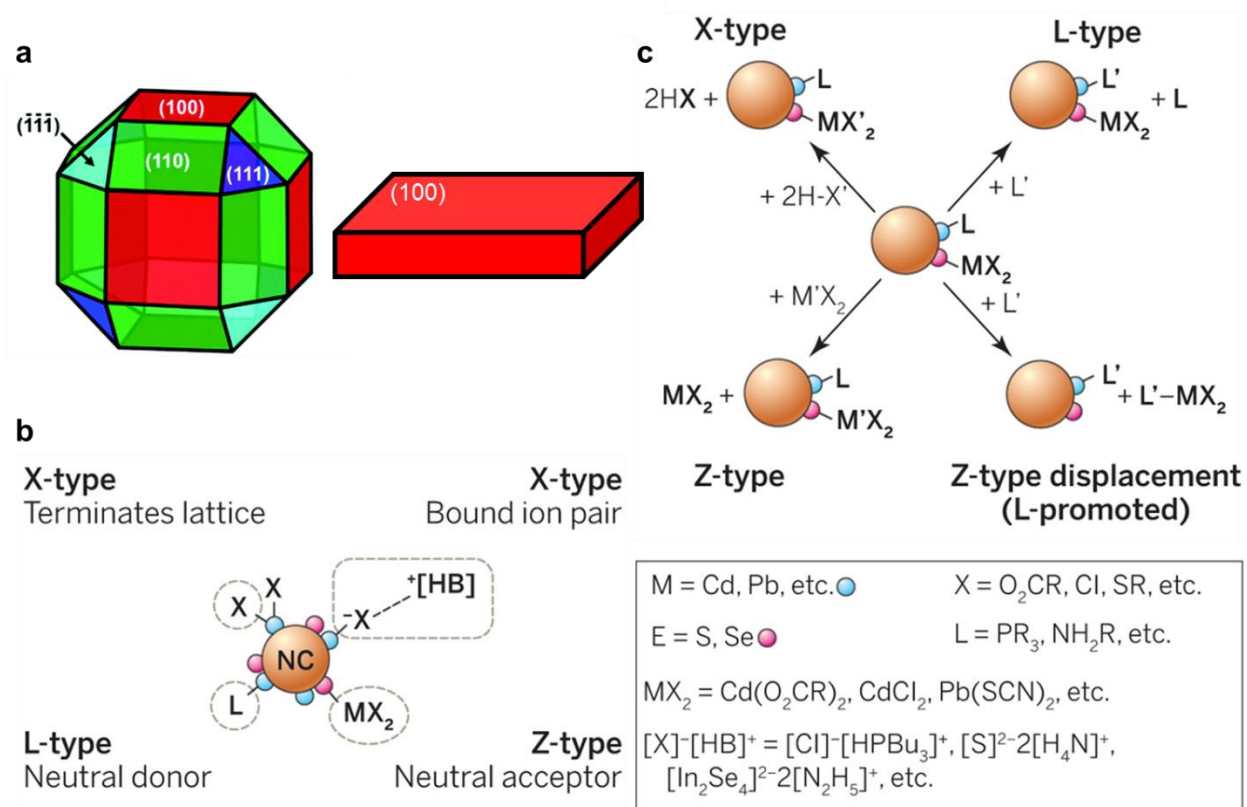
Figure 1.5. a) Comparison of crystal facets between QDs and NPLs. (100) facets are charged facets while (111) facets are neutral. b) Different possible binding modes of ligands to the nanocrystal facets. c) Different ligand displacement mechanisms. Figure is adapted and modified from *Chemical Communications* 2017 (53) 388-391[14] with permission from The Royal Society of Chemistry and *Science* 2015 (347) 615-616[13] with permission from AAAS.

Cd^{2+} is a metal ion with an intermediate hardness in the hard soft acid base principle.[15] Thus it can bind not only to $RCOO^-$ but also other common electron rich ligands like RS^- and R_3N. It also interacts with weak nucleophiles like the ROH in alcohols. These groups can all be plausibly used as anchor groups to attach functional ligands i.e. energy acceptors to the surface of NPLs. In scope of this work two of the groups are noteworthy, the COO^- and the S^-.

The exchange to COO^- is relatively mild in most cases so it could occur without significant quenching of the PL.[11] Quenching is very apparent in presence of N or S^- and could be commonly seen in the intermediate steps during the preparation of core/shell NPLs when octylamine or thioacetamide is added. The quenching effect is solely dependent on the surface of CdSe NPLs

since once the surface is protected (e.g. by synthesizing a shell of over the NPLs) addition of amines will no longer quenches the PL.

Due to the direct effect of the surface functionalization to the NPL's PL, the ligand exchange process can be monitored by observing the change in lifetime of the NPLs at increasing quencher concentrations. The result of this titration can be confirmed by an independent measurement of heat change during isothermal titration calorimetry. As the ligands interact with the surface of the NPLs, heat can be released or absorbed and this heat change from the binding event can be monitored. This result can then be compared to the quenching of fluorescence. These two titration techniques were demonstrated in chapters 2 & 3.

According to both titration methods, the large lateral size of NPLs allows hundreds of ligands to bind to the surface of NPLs. This result is a consequence of the easy binding to the charged (100) surface and allows all ligands to bind exactly the same way. It also supports the homogeneous energy transfer from NPLs to small molecule ligands.

1.2 Colloidal Stability of Nanoparticles

In the previous section we have seen how ligands can alter the surface of NPLs and how the geometry of the nanocrystal can affect the binding of the ligands to the surface. Another major aspect of ligands on NPLs is how they impact the colloidal stability of the dispersion. This is important when agglomeration needs to be avoided – for example when NPLs want to be uptaken by cells – or when agglomeration is needed – for example to separate NPLs from a mixture of colloids with different stability. To understand this, we will briefly review two concepts regarding nanoparticle stability.

DLVO Theory

The DLVO (Deryaguin and Landau,[16] Verwey and Overbeek[17]) theory combines the effect of van der Waals attraction and electrostatic repulsion to explain the agglomeration behavior of dispersions quantitatively. This was done by considering the energy-distance relationship of the two forces.

The van der Waals force is attractive (hence negative (-) energy) and calculated by summing the contribution from all interacting pairs of atoms that make up the particles. Shape needs to be accounted in this case, which is done by integrating over the total volume of the particle. By using the Derjaguin approximation,[18] the interaction energy $G(D)$ between two spheres and two flat surfaces are as follows:

Two spheres

$$G(D) = -\frac{A}{6D}\frac{R_1 R_2}{R_1 + R_2}\ (Eq.\ 1.1)$$

Two surfaces (per unit area)

$$G(D) = -\frac{A}{12\pi D^2}\ (Eq.\ 1.2)$$

Where R is the radius of the particle, D is the distance between the particle and A is the Hamaker constant given by:

$$A = \pi^2 C_{\rho 1 \rho 2}\ (Eq.\ 1.3)$$

Where C is a constant for interaction energy, which depends on the molecule's property and is distance independent, and ρ is the number density of the surface.

For the electrostatic repulsion, an electrical double layer is considered. The first layer is formed from the adsorption of charged molecules while the second layer is formed from the equilibrium of charged counterions around the first layer. This is given by:

Two spheres

$$G = \frac{64 k_B T R \rho_\infty \gamma^2}{\kappa^2} e^{-\kappa D}\ (Eq.\ 1.4)$$

Two surfaces

$$G = \frac{64 k_B T \rho_\infty \gamma^2}{\kappa} e^{-\kappa D}\ (Eq.\ 1.5)$$

Where k_B is the Boltzmann constant ($1.38{\times}10^{-23}$ J K^{-1}), ρ_∞ is the number density of ion in bulk solution, γ is the reduced surface potential given by:

$$\gamma = \tanh\left(\frac{ze\psi_0}{4k_B T}\right)(Eq.\ 1.6)$$

and the Debye screening length $1/\kappa$ is given by:

$$\kappa = \sqrt{\sum_i \frac{\rho_{\infty i} e^2 z_i^2}{\epsilon_r \epsilon_0 k_B T}} \quad (Eq.\,1.7)$$

Where z is the valency of the ion, ψ_0 is the potential on the surface, ε_0 is the vacuum permittivity and ε_r is the relative static permittivity.

To prevent the particles from overlapping, an additional term called the Born repulsion $(1/D^{12})$ is added to give the final equation as the sum of all contributions:

$$G(D) = -\frac{A}{6D}\frac{R_1 R_2}{R_1 + R_2} + \frac{64 k_B T R \rho_\infty \gamma^2}{\kappa^2} e^{-\kappa D} + \frac{1}{D^{12}} \quad (Eq.\,1.8)$$

The interactions and the contributions can be summarized in the plot in Figure 1.6.
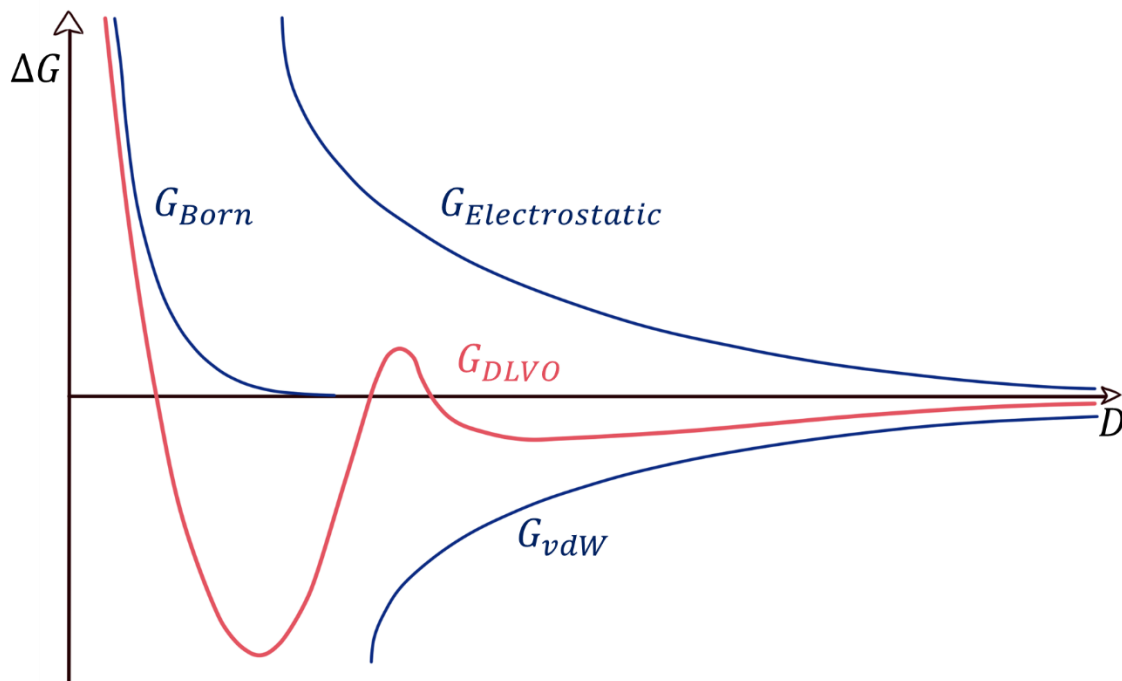
Figure 1.6. Total interaction predicted from DLVO theory at increasing distance (red curve).

Steric Stabilization

In addition to electrostatic stabilization, particles and droplets can be stabilized sterically by surfactants and polymers. This occurs by adsorption of the latter to the surface of the former.[19] Steric stabilization is widespread, because it can work in both aqueous and non-aqueous solvents, where the dielectric constant/relative permittivity ε_r of the latter is low and allows the use of non-ionic surfactants and polymers.[20] This makes the stabilization robust because it is insensitive to the electrolyte concentration.[19]

When the surfactant adsorbs to the surface of a particle, it creates an adsorbed layer with the thickness δ (Figure 1.7). If the solvent can dissolve the surfactant well, the surfactant's tail in the adsorbed layer may be strongly solvated.[20] The solubility of the tail is important because the tail forms a random coil on the surface.[21]
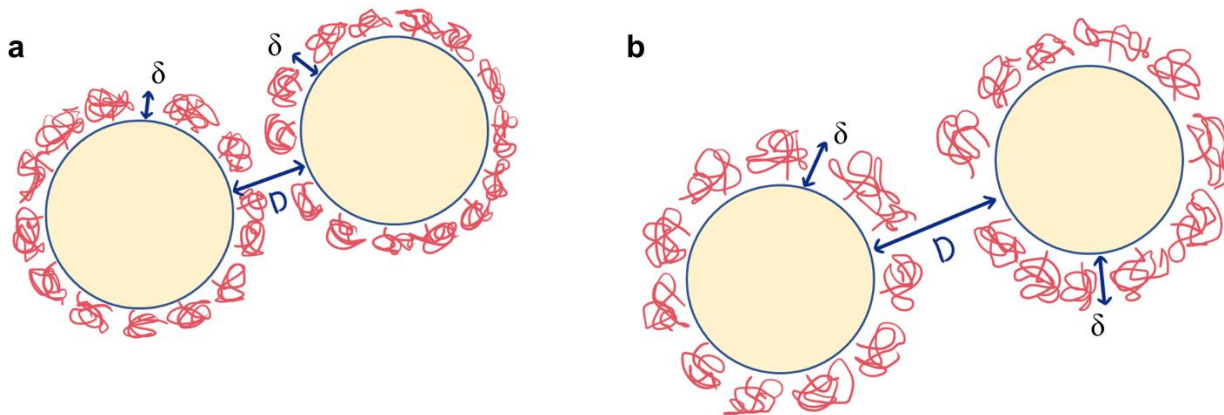
Figure 1.7. Particles in relatively a) poor solvated and b) well solvated conditions with adsorbed layer thickness δ and separation distance D.

The more solvated the tail, the larger the size of the random coil (radius of gyration).[21] This means an increase in the layer's thickness δ in well solvated conditions.

Two particles can approach one another until the separation D decreases to 2δ. In this case, the particles start to repel one another due to the compression of the adsorbed layers, relative to their ideal equilibrium conformation.[20] This repulsion arises from two effects, one of which is the

unfavorable mixing of the adsorbed layers when the layer is well solvated, and the other is the decrease in configurational entropy when the layers overlap.[20]

To create effective steric stabilization, the surface of the particle should be fully covered by the surfactant, as any uncovered area can induce agglomeration by van der Waals interaction. The surfactant should also be strongly bound to the surface to prevent any displacement when the particles approach one another. In addition, the surfactant's tail should be well solvated and would ideally form a layer with $\delta > 5$ nm. This would reduce the probability of weak flocculation.[20]

Depletion Attraction

For small solutes that do not interact with the particle surface (depletants), there is a region around the particle called the excluded volume. The solute cannot enter this volume due to loss of entropy. If the concentration of these solutes is high, osmotic pressure builds up and pushes the particles closer to one another to decrease the total excluded volume. This results in attraction of the particles to one another, hence agglomeration. For flat particles, the gain in excluded volume is greater than spherical particles, which makes NPLs agglomerate easily.

1.3 Colloidal Synthesis of CdSe NPLs

The synthesis of core only CdSe NPLs is done by a colloidal approach.[22, 23] This creates NPLs ranging from 3MLs up to 8MLs.[9] The thickness can be further increased by using a layer by layer approach on existing NPLs[24, 25] , which goes up to NPL thicknesses of 11 MLs.[25] However they typically lose out on the useful properties like PL due to the imperfection of the method that creates defect sites.[26] Thus core CdSe NPLs should be synthesized directly to the appropriate thickness practical applications.

Formation of Anisotropic NPLs instead of Isotropic QDs

In the colloidal synthesis of NPLs, short chain carboxylate cadmium salt is introduced to a mixture of long chain carboxylate cadmium salt and selenium. The difference in solubility creates a situation where the crystal growth is no longer limited by diffusion. As the crystal nuclei has its symmetry broken stochastically, crystal growth can occur in the wide facet or the narrow facet (Figure 1.8A). Growth in the narrow facet is kinetically much more favorable, hence the formation of NPLs. As a result of the energetics in the crystal formation of NPLs, the traditional synthetic method of NPLs from its cadmium carboxylate salt and selenium precursors can produce only 3, 4 and 5ML NPLs (Figure 1.8b).
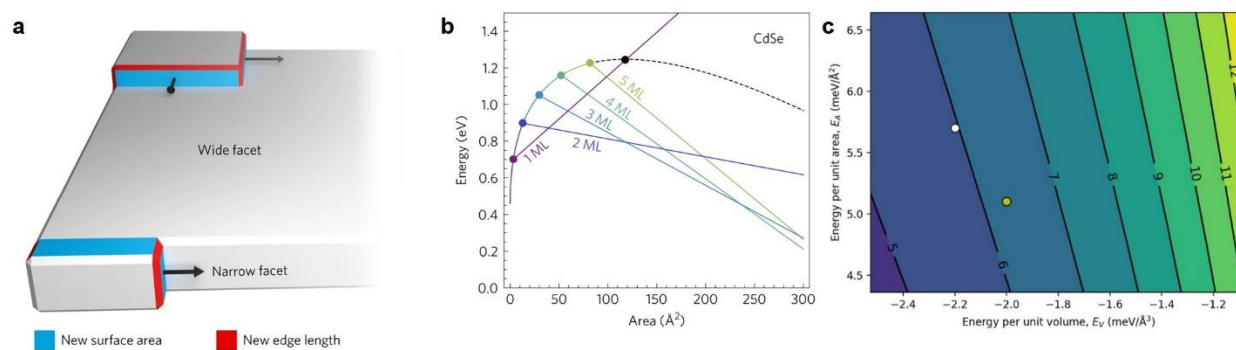
Figure 1.8. Energetics and formation mechanism of NPLs. a) Once the crystal nucleus has its symmetry broken stochastically, crystal growth can occur either in the wide facet or the narrow facet. In the experimental conditions for the formation of NPLs, the growth is much more favoured in the narrow facet, hence the formation of anisotropic nanocrystals. b) Energy barrier for the formation of different NPL MLs. c) Possible ways to tune the energies to achieve different ML thickness. White dot: synthesis without halides. Yellow dot: synthesis with halides. Figure is reprinted with permission and modified from *Nature Materials* 2017 (16) 743–748,[8] and *Chemistry of Materials* 2020 (1) 566-574.[26]

The selectivity of the reaction to the different ML products can be tuned by simply changing the reaction temperature. However, this approach is limited since the 3ML NPLs produced this way cannot reach high QYs and are always large. Furthermore, they tend to have more of a round geometry instead of a rectangle. This suggests that the NPLs may be formed rapidly, then etched at the corners due to rapid dissolution back to its monomers resulting in the rounded edges.[27, 28] The reason for this is the low reactivity of Se powder, which demands a high temperature (at least 180°C) to start forming NPLs.

The key to overcome this constraint is to modify the reactivity of the precursors. By using a more reactive Se precursor, the reaction could be done at a lower temperature. This affords slower growth and formation of high quality 3ML NPLs.[29] Meanwhile, changing the Cd precursor to include halides, the energetics of the NPL surface can be modified to produce 6, 7 and 8 ML NPLs.[9, 26, 30] (Figure 1.8c)

1.4 Colloidal Synthesis of Core/Shell NPLs

As mentioned in the earlier section, the surface of NPLs is highly sensitive to quenchers. In applications where high PL is desired, isolating this surface from potential quenchers is desirable. One typical way to do this for nanocrystals in general is by synthesizing a protective shell around the core. For applications in aqueous environments or biological medium for example, the introduction of a shell to CdSe NPLs is crucial to increase the robustness of NPLs by reducing their surface sensitivity. A variety of materials can be used as the shell but for purposes of protection, ZnS type I shell,[31] CdS quasi-type II shell[32-34] and the mixture CdZnS are most often used.

Energy | Type I   Reverse Type I   Type II
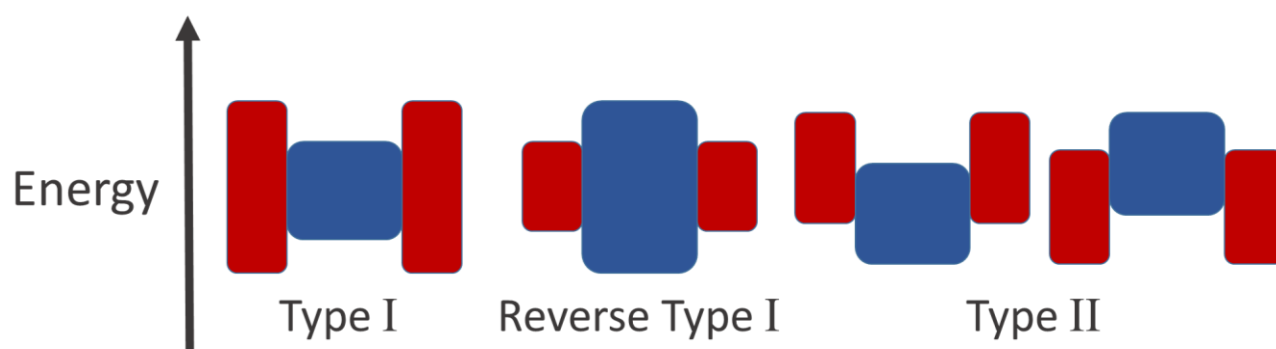
Figure 1.9. Band diagram of core (blue) shell (red) structures and their naming conventions.

Type I shells isolate the excited state within the core, which makes it difficult to quench after addition of 4-5 MLs of shell material (Figure 1.9). Meanwhile in the case of CdSe/CdS, there is a small conduction band offset, making it a quasi-type II structure where electrons delocalize and the hole remains in the core.[31]

The synthesis of a shell could be done by three main ways: atomic layer deposition[35], one pot synthesis[36, 37] and hot injection[38-41]. Although atomic layer deposition could form the shells layer by layer, making them useful for applications where thin shells are required, the shell synthesis used for this work are solely for the purpose of protection. Therefore, only the latter two methods are discussed.

One pot synthesis method could be done in open air at room temperature, making it highly convenient when the objective is simply to give the NPLs some protection. Unfortunately, the

method suffers from reproducibility issues in terms of quantum yield, hence should not be used for applications where the quantum yield is critical. As a result, the one pot synthesis approach did not find widespread use as one of the major selling points of NPLs is their potential to be bright emitters.

Just by looking at the similar reagents, it could be said that the hot injection method is the ideal evolution of the one pot synthesis. The major difference is the sulfur precursor is added slowly to the reaction mixture set at high temperatures (typically 300 °C). The high temperature facilitates the growth of high quality shell due to uniform growth and minimization of interfacial strains from atomic reorganizations.[38] NPLs with near unity QY can already be achieved through the use of a CdS shell.[38] Latest developments however opted to use a mixed shell CdZnS (Figure 1.10) because of the better colloidal stability of NPLs with Zn terminated surfaces.[41]
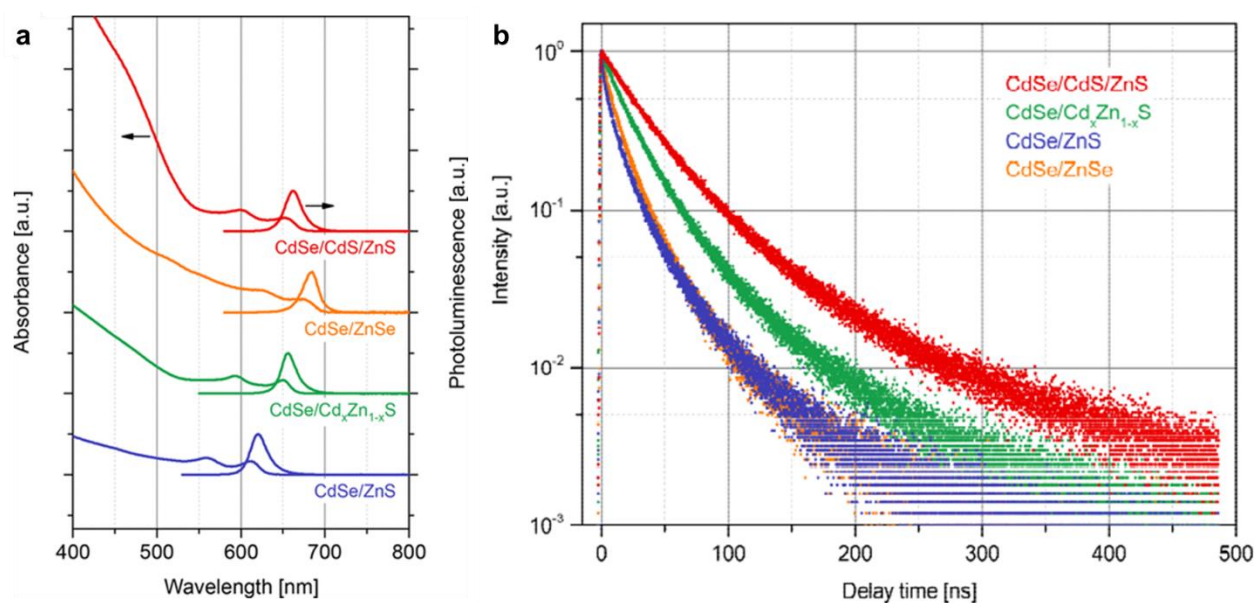
Figure 1.10. Steady state and time resolved spectra of some core/shell NPLs. a) PL of NPLs emit at wavelengths ~600 nm, greatly red-shifted compared to core NPLs shown in Figure 1.4. b) Time resolved PL of the core/shell NPLs changes with different shell composition. The NPL with the highest PLQY uses the CdSe/CdS/ZnS composition, which also exhibits the longest lifetime. This suggests that the shell has successfully isolated the excited state the most from its surroundings and promotes quenching mainly through PL. Figure is adapted and modified with permission from *Chemistry of Materials* 2019 (22) 9567-9578.[39]

1.5 Photoluminescence (Fluorescence)

Semiconductors are able to absorb photons with energy equal or greater to their bandgap. The absorption of photons promotes electrons from the valence band to the conduction band and leaves a hole in the valence band. Once in the conduction band, the energy can be released by going back into the valence band. The simplest way to release this energy is by the emission of photons with equal or lower energy to the excitation energy. Recall the band diagram in Figure 1.1 for the quantum dots. If the energy provided to the material exceeds the bandgap, the energy is dissipated quickly (usually thermally) until the excited state goes to the lowest part of the conduction band. Then it can re-combines with a hole in the valence band to emit a photon. The same could be observed for molecules with their molecular orbitals. The photon emission occurs mostly from the lowest excited state in accordance with Kasha's rule. Due to this behavior, the photon usually emits at longer wavelengths than the excitation wavelength. The shift in wavelength is called Stokes shift.

This emission process is in general described as photoluminescence. The term fluorescence is specific to the relaxation from an excited state to a ground state with the same spin, typically from singlet excited state to singlet ground state. Practically almost all photoluminescence events in organic molecules is the latter because of the low likelihood of a spin flip or crossover in the absence of heavy elements. In semiconductor nanocrystals, the spin of the excited state is ill defined,[42-44] thus to avoid confusion we refer to the process as the more general term photoluminescence (PL).

The PL lifetime of NPLs are in the range of $4 - 10$ ns ($<\tau>$ amplitude weighted average) and decreases at lower temperatures.[23] This is a relatively slow process compared to quenching mechanisms such as energy transfer, which happens in ps timescales. In other words, PL occurs if the energy of the excited state is not consumed by other faster quenching mechanisms discussed in the next sections. There are many applications where high PL is needed e.g. fluorescence microscopy, therefore in such cases the excited state should be protected from the possibility of going through alternative quenching mechanisms.

1.6 Photoluminescence Quenching via Defects and Trap States

In crystal structures, there are typically areas where there is some deviation from the perfect crystal. These areas are called defects and they can occur within the crystal or on the surface. The presence of these defects can influence the electronic levels of the semiconductor by, for example, creating sub band gap trap states (Figure 1.11).[45] These trap states can act as new quenching pathways, which may be non-radiative. The quenching process via a trap state tends to be much faster than PL, thus they usually lead to stark reduction in PL quantum yields.[46]
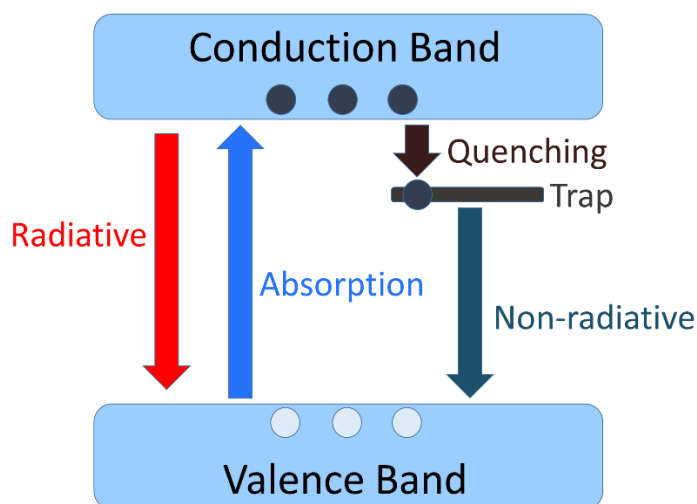
Figure 1.11. Energy level diagram of semiconductors in the presence of trap states. Upon excitation (blue arrow), the excited electron in the conduction band can re-combine with the hole as usual in the valance band and perform radiative recombination (PL, red arrow). However, it could also be quenched by sub-bandgap trap states which may result in nonradiative recombination or trap state emission in some cases.

Defects could be created upon the synthesis of a nanocrystal or changed later by processes which affect the nanocrystal surface. The contribution of defects could be roughly estimated by the PL quantum yield (QY) of the NPLs. After synthesis, PLQY of NPLs typically lies around 50%, unless the synthesis is well optimized. With these NPLs, several works have shown the possibility of making core/shell NPLs with near unity QYs.[38-41] Formation of a shell could passivate or repair surface and perhaps anneal defects out of the NPL core through the energy provided in the high temperature process.

On the other hand, the number of defects could be increased by simply introducing the NPLs to harsh environment e.g. acidic conditions. Introducing NPLs to harsh environments can etch the surface of NPLs and creates deviation from the perfect crystal surface, effectively denying the PL of NPLs by favoring non-radiative quenching. Thus, to best retain high PLQY, the surface of NPLs should be as isolated as much as possible from the external environment.

1.7 Photoluminescence Quenching via Energy Transfer

If the excited state is quenched by the presence of a suitable acceptor, energy transfer occurs. Energy transfer can take place through many different mechanisms which will be covered in the next sections. Each mechanism possesses different requirements for acceptors and distances thus the dominant energy transfer pathway can be deduced by measuring characteristic relationships of the transfer process (Figure 1.12).
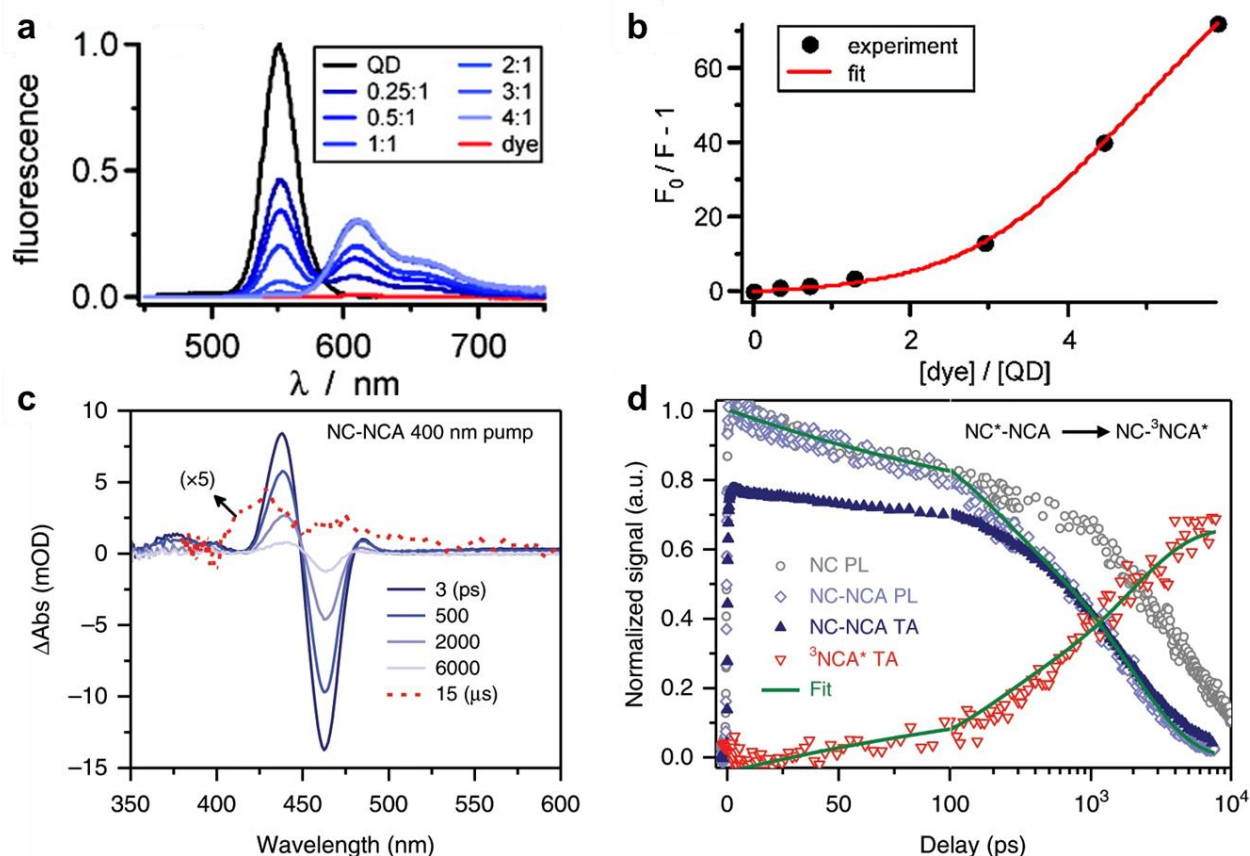
Figure 1.12. Examples of monitoring energy transfer process in a FRET system (a & b) and in a triplet energy transfer system (c & d). a) Steady state PL of QD decreases while PL of dye increases as more dye is added. b) Stern-Vollmer plot based on the quenching of QD indicating the increase in FRET efficiency with increasing dye ratio. c) Transient absorption of QD and dye at different times. Signal of QD decreases while signal of dye increases, suggesting triplet transfer. d) Changes in PL and transient absorption relative to the QD and dye. Figure a and b are adapted with permission from *Journal of the American Chemical Society* 2008 (51) 17242-17243[47] while figure c and d are adapted from *Nature Communications* 2020 (11) 28.[44]

Exciton Sizes in NPLs

Since energy transfers are distance dependent, one must know how exactly the distances are defined to fully understand the transfer process. The promotion of an electron to the valence band creates an electron-hole pair, which is one example of an exciton. Several studies showed that the exciton in NPLs are not delocalized over the entire platelet at room temperature and attempted to determine their size. [48-50] Transient absorption measurements done by Li *et al.* and

Morgan et al found the exciton is localized in an area of tens of nm^2. Meanwhile, magneto-optical spectroscopy by Brumberg *et al.* showed that the exciton is localized in a radius of 1 - 1.5 nm. These results have big implications for the energy transfer in NPLs since it means that the density of acceptor (ligands) per surface area should matter more than simply the number of acceptor (ligands) per NPL.

Dexter-like Energy Transfer for Triplet Transfer and Upconversion

Dexter energy transfer (also known as Dexter electron exchange) is a close range (~10Å)[51] energy transfer involving the interaction of orbitals (Figure 1.13). This mechanism conserves the spin of the electrons[52] and describes a variety of processes including triplet energy transfer.[53, 54]
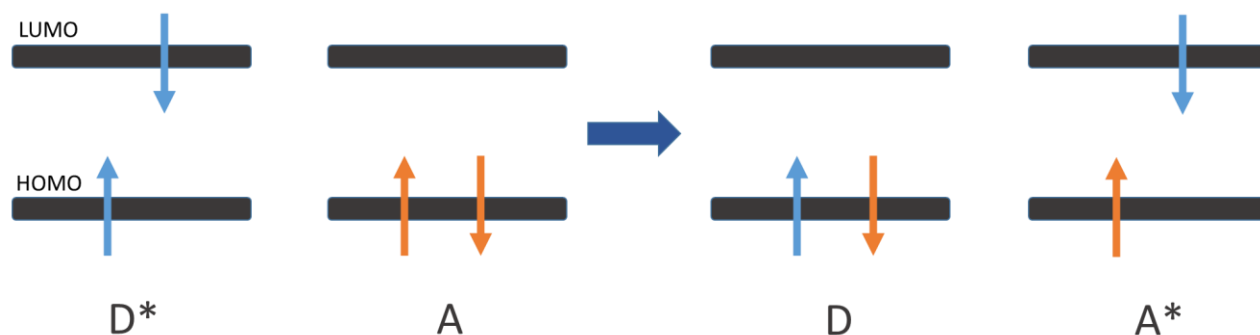
Figure 1.13. Dexter energy transfer in molecules. Note that the donor D and acceptor A do not gain or lose electrons, nor do the overall spin change.

The rate of a Dexter energy transfer (k_{ET}) is given by: [52]

$$k_{ET} \propto \frac{h}{2\pi} P^2 J e^{-\frac{2r}{L}} \ (Eq. \, 1.9)$$

Where h is the Planck's constant, P is an experimental constant, r is the separation from the donor to acceptor, L is the sum of the van der Waals radii of the donor and acceptor and J is the spectral overlap integral given by:

$$J = \int f_D(\lambda)\varepsilon_A(\lambda)\lambda^4 d\lambda \ (Eq. \, 1.10)$$

In the case of triplet energy transfer from nanocrystals to molecules, Mongin *et al.* discovered that the mechanism is also Dexter-like.[54] Triplet energy transfer has gained interest in the nanocrystal community due to the high absorption cross section of nanocrystals and the mixed spin state of the nanocrystal's exited state.[42-44] This potentially allows the possibility of increasing

the efficiency of triplet sensitization by reducing the energy losses in spin crossover found in traditional systems based on organic molecules and porphyrins.[55-60] The higher efficiency can play a significant role in applications like triplet-triplet annihilation (TTA) upconversion, a process that could aid harvesting the red regions of the solar spectrum to boost the blue region, which has application to improve the efficiency of solar cells.

Up to now, designs based on QDs focused on using polycyclic aromatic hydrocarbons (PAHs) as the surface ligand acceptor. The specific PAH used is customized to the nanocrystal by changing the number of aromatic rings[61-63] or the binding group[64, 65] to tune the triplet energy or improve the surface binding and transfer rate to the ligands (Figure 1.14).
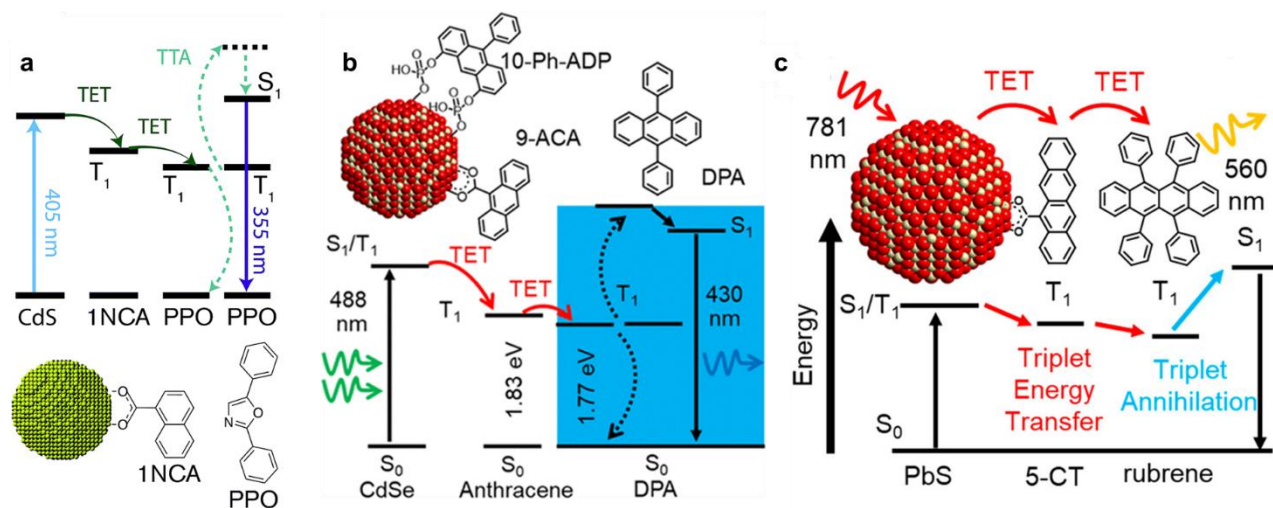
Figure 1.14. Examples of a variety of functionalized PAHs used as ligands for triplet energy transfer. PAHs were chosen based on their compatibility with the different QDs. Figures were taken and modified with permission from *Chemical Science* 2017 (8) 5488-5496,[63] *Chemistry of Materials* 2020 (4) 1461-1466,[65] and *Journal of the American Chemical Society* 2019 (25) 9769-9772,[61] respectively.

The most common and well-studied combination is perhaps using CdSe QDs with 9-anthracene carboxylic acid (CdSe-ACA).[54, 64-68] Recent results show that this system faces bottlenecks related to the fundamental properties of QDs, that is surface sensitivity, low number of ligands/QD and interference of trap states.

NPLs can undergo the ligand exchange with COO⁻ much more smoothly due to the identical charged (100) surface on all terminating facets. Some of these surfaces are large in comparison to QDs, which allows high number of ligands to bind/NPL. NPLs can also be more easily synthesized without mid-bandgap trap states, which can simplify the study of the energy transfer behavior to the surface acceptors.

Once the nanocrystal sensitizes triplets to the ACA (Figure 1.15), the triplets can be transferred to emitters like perylene or 9, 10 – diphenyl anthracene (DPA). Two emitters can use their triplet energy to do a triplet-triplet annihilation, emitting a photon from the singlet excited state with double of the triplet energy, thus resulting in upconversion.
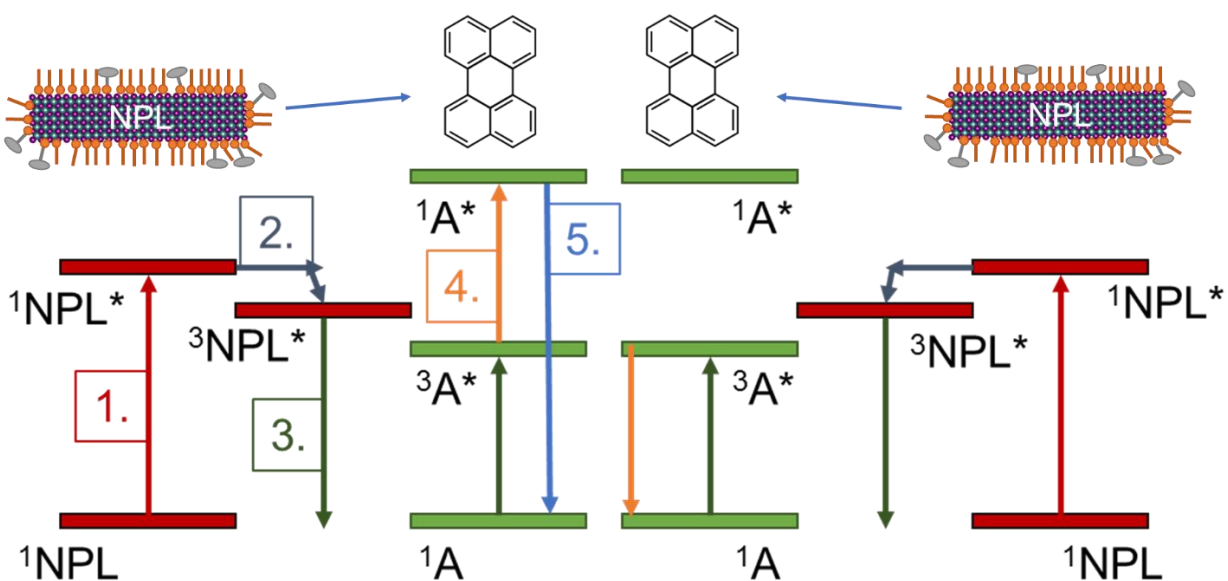
Figure 1.15. Energy level diagram for triplet-triplet annihilation upconversion process using NPL-ACA conjugate as donor and perylene as acceptor/emitter. 1) NPLs are excited to their singlet state. 2) Spin crossover occurs which changes the spin of the excited species to triplet. 3) Triplet transfer to perylene. 4) Two perylenes in triplet state combine to form one perylene in the singlet excited state and one perylene in ground state. 5) Perylene emits excited energy as blue photon.

This process happens in solution where the emitters are freely diffusing. For the TTA upconversion to occur, two of the excited emitters have to meet, which is difficult if the population of excited emitter is low. Thus, at low excitation power, there is a quadratic dependence of the upconversion intensity to the excitation power. This dependence switches to a linear one after a certain point. The point where the dependence switches from quadratic to linear is called the threshold intensity I_{th},[69] and it represents the efficiency of the upconversion system. The lower the I_{th}, the more efficient the system is, since it requires less excitation power to reach the point where the there are enough triplets present to consistently annihilate with one another. For an NPL-ACA-emitter system, this would mean that the first triplet transfer from NPL-ACA and the second triplet transfer from ACA-emitter will both have to be very efficient. The factors that make the transfer efficient is the focus of my project and will be discussed in detail in the upconversion chapter of this thesis (Chapter 3).

Electron / Hole Transfer for Photocatalysis

The same reasons to use NPLs for triplet generation could also be said for excited state generation. Photocatalysis could be done by using the excited electrons and holes generated in nanocrystals. Some work has been done with QDs (Figure 1.16), showing that they could be versatile photocatalysts at low loading concentrations and little optimization.[70]
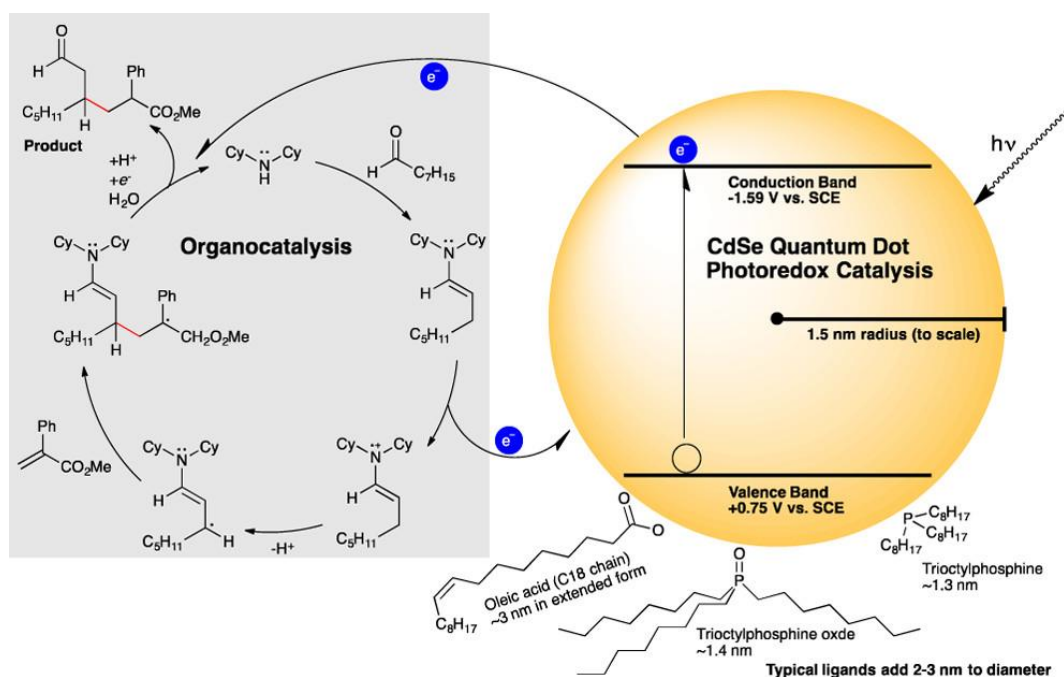
Figure 1.16. Generation of electron-hole pair in semiconductor nanocrystals allows photocatalysis by donating electrons or holes to the organic species and therefore acting as a one electron oxidant and a one electron reductant. Figure obtained from *Journal of the American Chemical Society* 2017 (12) 4250-4253,[70] and is reproduced with permission under the terms of *ACS AuthorChoice*.

The NPLs' absorption cross section scaling makes them able to reach very high absorption cross sections and absorb light easily at low molar concentrations. Furthermore, since the nanocrystals are colloids, they can be separated easily from the products and solvents by centrifugation, thereby acting as a dispersible heterogeneous catalyst with high surface areas. In this case NPLs have another advantage over QDs since NPLs are less colloidally stable. This means that they can be more easily separated from the reaction mixture at lower centrifugation speeds. Furthermore, the NPLs could theoretically be re-dispersed and re-used for another reaction, provided that the agglomeration is reversible and the re-dispersion step does not damage the

catalytic property of the NPLs. These features overall make NPLs attractive for a cost-effective alternative to traditional, previous metal-based photocatalysts.

Förster Resonance Energy Transfer (FRET)

FRET, sometimes referred to as fluorescence resonance energy transfer, is a non-radiative energy transfer that occurs through the resonance of dipoles between the donor and the acceptor. For FRET to occur, the dipoles must be able to interact with one another (Figure 1.17). This means that they must not be orthogonal and not too far apart (in nanometer range).[71] The emission of the donor must also match the energy of the absorption of the acceptor despite the non-radiative nature of the transfer.
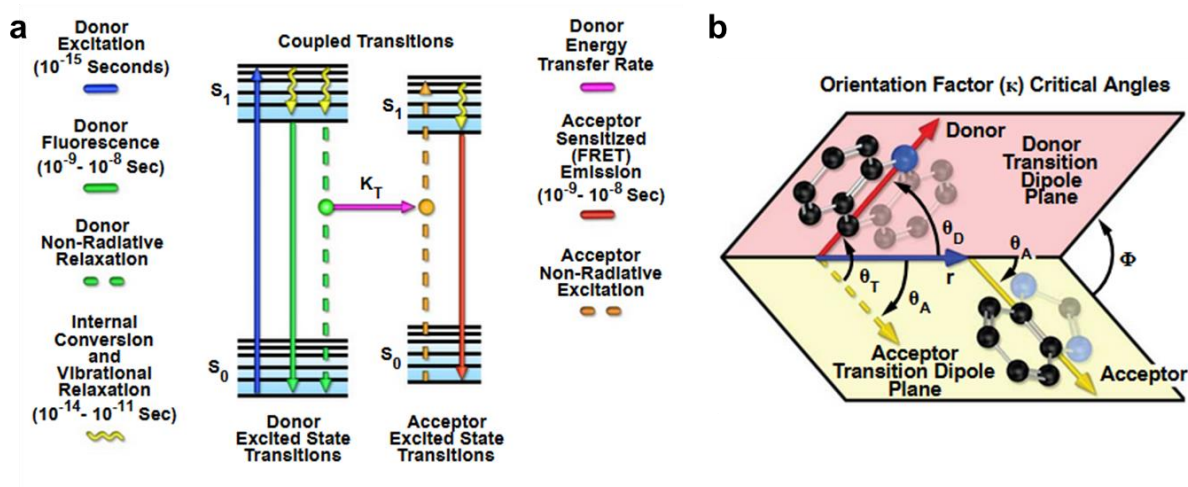
Figure 1.17. a) Jablonski diagram of the FRET process b) Dipole alignment between donor and acceptor. If dipoles are orthogonal, FRET will not take place. Figure is adapted and modified from Nikon.[72]

Due to the small stokes shift of NPL PL, NPLs undergo relatively high homo-FRET when the particles are close to one another.[73] This could happen in high dispersion concentrations or when the NPLs are dispersed in poor solvents. A common example could be seen when ethanol is added to an NPL dispersion in hexane.[74-76] In such case the PL is quenched but when the NPLs are precipitated and re-dispersed in pure hexane, the PL returns. This means that the ethanol did not quench the PL by damaging the surface of NPLs but instead induced agglomeration, which promotes self-quenching by homo-FRET to NPLs with defects.[73]

Organic molecules are prime candidates for FRET acceptors since their properties can be tailored to function by modifying their chemical structures. Using the tailored molecules directly for their intended function can be inefficient because organic molecules generally possess low absorption cross sections. This means that a high concentration of molecules is needed to accept the energy from donors or from direct excitation with light, which may not be feasible for practical applications if the molecule is difficult to synthesize in large amounts. Nanocrystals can assist the absorption process by acting as a sensitizer. QDs have been utilized often for this application therefore there has been many examples and studies, including some that shows the energy transfer follows a FRET model.[77-84]

When trying to mimic the same system with NPLs, two major differences must be considered. The first is related to the dipole moment. QDs have two-dimensional degenerated emission transition dipole moment of the lowest excitonic transition,[85] but the acceptors will orient themselves randomly relative to the spherical surface of the QDs. This makes the interaction of the dipoles between donor and acceptor randomly oriented. However, NPLs' dipole moment is fixed in the same plane as the lateral axes and their large lateral area compared to the narrow side facets makes interactions with the basal planes much more likely.[86] This makes a difference to the orientation factor (Figure 1.18) when the acceptor is on the basal planes of the NPLs or on the edges.[87]

$$\langle \kappa^2 \rangle = \frac{2 + 3sin^2\theta}{6} \qquad\qquad \langle \kappa^2 \rangle = \frac{5 - 3sin^2\theta sin^2\varphi}{6}$$
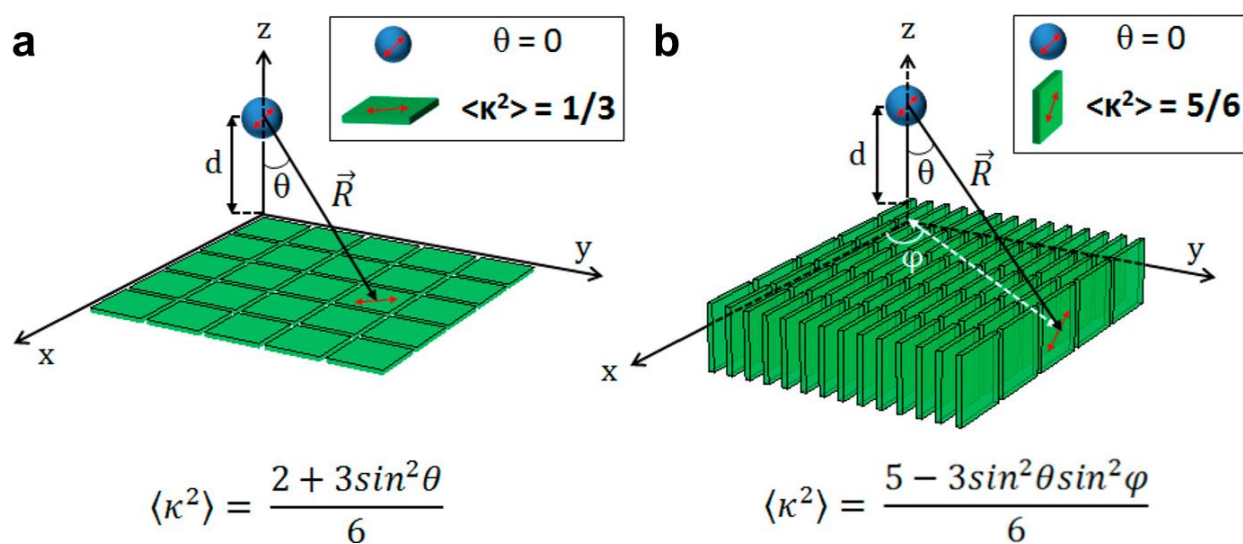
Figure 1.18. Dependence of orientation factor $<\kappa^2>$ when the interaction is to the basal planes of the NPLs (a) or the edge of the NPLs (b). Figure is taken and modified with permission from *Nano Letters* 2019 (7) 4297-4305.[87]

The second consideration is the surface binding of the acceptor to the NPLs. NPLs can be laterally large and allow binding of hundreds of acceptors on the surface. But at the same time the exciton in the NPLs was measured to be smaller than the size of the NPLs.[49] This suggests that the exciton are localized in areas of tens of nm,[2,50] or even in a smaller radius of $1 - 1.5$ nm,[48] depending on the measurement technique. If the localization is indeed so small in reality, it suggests that a high ligand coverage density is needed to get the acceptor near the exciton.

1.8 Imaging

Labelling is a common technique in imaging to detect samples with "unremarkable" characteristics. By labelling the target with a marker, we can distinguish it from the surroundings. This approach is routinely used in biology where samples are stained with fluorescent dyes and imaged with light microscopy. Although super resolution fluorescence microscopy is developing at a rapid pace, the resolution is still far from the resolution of electron microscopy.[88]

Furthermore, fluorescence microscopy is very difficult in deep-tissue due to the scattering and absorption of the short wavelength excitation beam (Figure 1.19). Near infra-red or infra-red absorbing organic molecules are rare and often absorb weakly. These reasons make it challenging to get high signal/noise ratio from the traditional fluorescent markers when using with one-photon excitation for deep-tissue fluorescence microscopy.
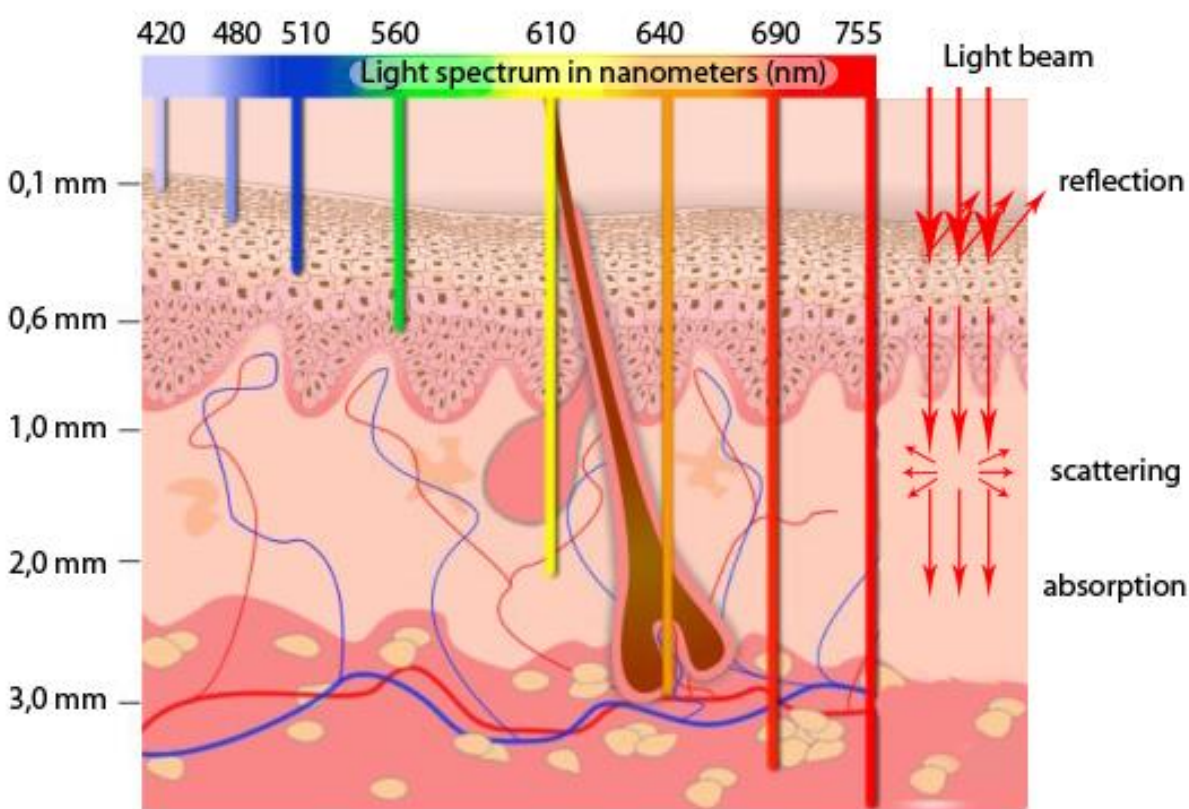
Figure 1.19. Tissue penetration depth for light at different wavelength. Figure adapted from University of Liège.[89]

Quantum dots can get around this problem, thus they have enjoyed increased usage in bioimaging. They can be easily excited by two or more photons in NIR or IR regions (Figure 1.20) which allows deep tissue imaging,[90, 91] and they can also be applied in cross correlation microscopy (known as correlated light electron microscopy or CLEM) to show the labelled samples in both fluorescence and electron microscopy.
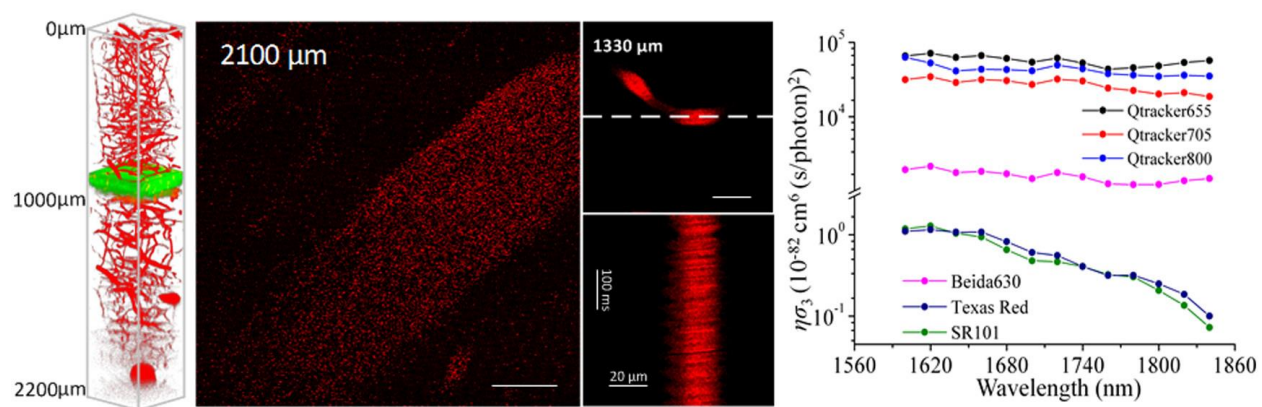
Figure 1.20. In vivo deep-brain structural multiphoton imaging using three-photon excitation. The three-photon fluorescence signal F_{3P} is given by $F_{3P} = C \times \eta\sigma_3 \times \varphi \times L_{Par}$, where C is the marker concentration, η is the fluorescence quantum yield, σ_3 is the three-photon absorption cross section, φ is the collection efficiency (photodetector), L_{Par} is a parameter determined by the excitation laser.[90, 92-95] Right plot shows the product of quantum yield and absorption cross section of QDs vs. organic dyes, which highlights the superior property of QDs for multiphoton absorption and fluorescence. Figure reprinted with permission from *Nano Letters* 2019 (8) 5260-5265.[95]

This achievement was enabled by the successful phase transfer of QDs from organic solvents to water. QDs can be transferred to water by ligand exchange or polymer coating.[96, 97] Commercially available water dispersed QDs tend to be in the polymer coated forms[98] due to their higher stability and the isolated surface[99] of the nanocrystals from potentially harsh environments and quenchers found in complex biological media.

NPLs have properties which are of great boon to this field, higher multi photon absorption cross section and rectangular geometry. Higher absorption cross sections mean the NPL markers

can be excited at lower powers to obtain the same fluorescent signals as other markers. This is highly beneficial because it reduces the background signals from auto fluorescence, and when measuring cells and tissues, lowers the possibility of photo-induced damage to the biological sample. Meanwhile the rectangular geometry makes them easy to spot in electron microscopy since they are distinguishable from the many spherical entities in cells. This unambiguous shape makes NPLs convenient markers in electron microscopy since their identity does not need to be confirmed by a complementary method like energy-dispersive X-ray spectroscopy (EDX).

Transferring NPLs have proven to be challenging due to the flat geometry. Lim *et al.* argues that the curvature of NPLs makes it challenging to directly use methods applied to QDs hence they specifically designed lipoproteins that could accommodate the rectangular geometries of NPLs.[100] Other examples use ligand exchange by 3-mercapto propionic acid (MPA)[101] or direct attachment of polymers with thiol groups to the surface of NPLs.[102] Though as seen in QDs' case, polymer coating would be the desirable approach for the phase transfer of NPLs in order to safely protect the surface of NPLs from the medium.

1.9 Cell Uptake and Protein Corona

Uptake of nanoparticles must be known in order to understand how nanoparticle markers interact with biological objects and when attempting to develop a nanocarrier based drug delivery system. The cell uptake process is rather complex, conducted by a machinery of proteins. To get an idea of the mechanism, the nanoparticle's properties like size and charge is correlated to the uptake result. However, this picture is incomplete as it does not take into account the protein corona.

Protein corona is a shell of proteins that adsorbs to the surface of nanoparticles upon entering biological medium. This is highly important because it changes the biological identity of the nanoparticle, affecting how the nanoparticle interacts with its surroundings. For example, the protein corona can cover transferrin functionalized nanoparticles and make them lose their targeting ability (Figure 1.21).
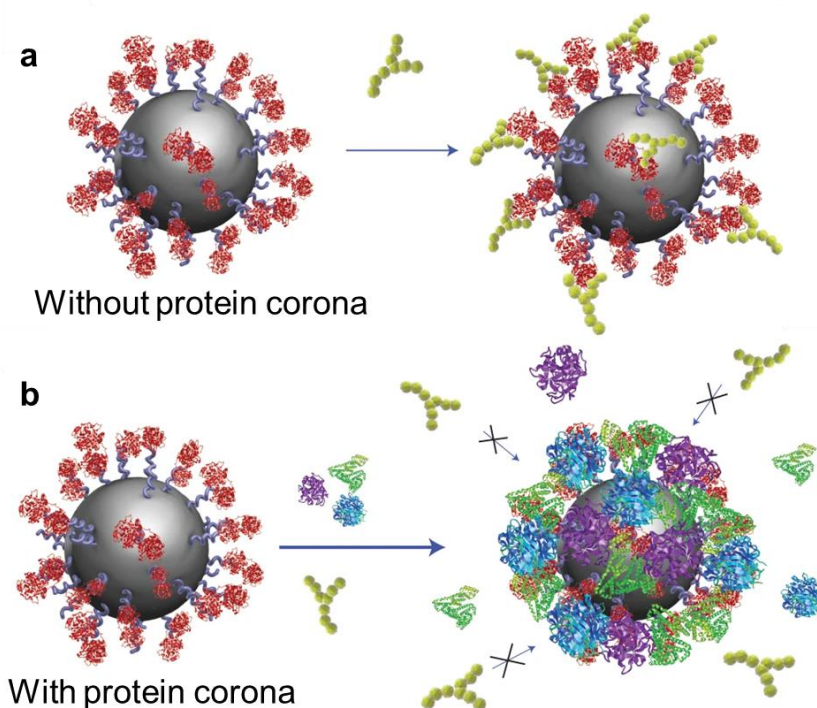
Figure 1.21. Effect of protein corona on the identity of nanoparticles. a) Nanoparticle surface is functionalized with transferrin which allows it to interact with antibody or targeted receptors on cells. b) Functionalized nanoparticle is exposed to protein, which changes its biological identity. The antibody can no longer recognize the nanoparticle. Figure adapted and modified with permission from *Nature Nanotechnology* 2013 (8) 137–143.[103]

The proteins in the cell uptake mechanism may also recognize the corona and decides based on this biological identity whether the nanoparticle may enter or not. Although the size and charge of nanoparticles may play big roles in the protein corona formation, there are other factors to consider such as the dynamics of protein adsorption to the surface.

Most nanoparticles and nanocapsules have ligands and surfactants on the surface which are dynamic surfaces, affected by equilibrium and changes in the environment. It is less often the case that a nanoparticle has a static surface. The influence of a dynamic surface versus a static surface to the protein corona composition will be covered in more detail in this thesis (Chapter 6) by comparing nominally equivalent nanoparticles with static and labile surface dynamics.

1.10 Motivation and Outline

Excitation by light is the ideal way to add energy into a sample or a system because of its high efficiency, spatial and temporal control. Light energy is also highly abundant and can be taken directly from sunlight, provided that the material can absorb a broad range of wavelengths. CdSe NPLs possess broadband and large absorption cross sections, which makes them very easy to excite with a variety of light sources. This advantage makes them very useful in situations where there are few NPLs available e.g. single particle fluorescence imaging, or when excitation intensities are low e.g. in vivo imaging (to avoid damage to cells) or in solar energy harvesting (especially in cloudy weather).

However, the absorption of light is just half the challenge when designing NPLs for practical applications. The other half is how we use the absorbed energy. For example, NPLs excited by sunlight can perhaps emit the photon by photoluminescence to sensitize a catalyst with a narrow absorption profile. Alternatively, it could transfer the energy directly to the substrate and act as a catalyst itself. If we would like to tailor the NPLs to a specific application e.g. bioimaging, FRET, photon upconversion, photocatalysis, etc. control of how the energy is used (in other words the quenching pathway) would be necessary to avoid wasting the harvested energy for unwanted processes.

Control over the quenching pathway gives us the ability to direct the energy transfer of a photoexcited NPL. As seen in the previous section, we can do this through the selection of surface ligands. Inert ligands prevent induced quenching of the excited state by sterically hindering access to the surface, given that the ligand packing is dense and the surface binding is not labile. This allows relatively slow decay pathways to occur, such as photoluminescence. On the other hand, reactive ligands and small molecules, which can directly interact or access the NPLs' surface, are bound to have strong interaction to the NPLs because of their close distance. This enhances interactions that are strongly distance dependent e.g. energy transfer and charge transfer. When the quencher ligand or small molecule is close, energy transfer is fast – therefore favored over simple photoluminescence. Furthermore, the interaction can even be enhanced by having multiple molecules near or bound to one NPL. Hence, detailed understanding of the NPLs' surface chemistry is critical for tailoring them towards specific applications.

I analyze in **chapter 2** the FRET transfer efficiency from different sized NPLs to conjugated fluorophores. FRET is well known for its sensitive distance dependence, which can be varied in NPLs by changing their lateral size since the exciton is localized. We confirm the localized exciton by the lateral size dependence in NPL-fluorophore FRET, instead of taking the pure spectroscopic approach on the NPLs alone in previous studies. Smaller NPLs can be quenched by fewer fluorophores/NPL, indicating the effectiveness of the energy transfer. This is because in small NPLs the randomly placed fluorophore and exciton are on average closer to one another. This consideration is important when designing efficient NPL-fluorophore system since fewer fluorophore/NPL on the surface will reduce unwanted self-quenching.

I utilize the photoexcited NPLs in a similar manner in **chapter 3**, where the energy transfers into ligands capable of triplet sensitization. The NPL-ligand conjugate sensitized freely diffusing emitters in solution and enabled triplet-triplet annihilation upconversion. We reveal how the interaction of the ligands on the surface of the NPLs can create unwanted loss mechanisms, which can explain the low upconversion efficiency of NPL based sensitizers in literature. Here we show the close ligand packing on the surface played a critical role, since it adjusts the energy levels and dictates the direction of energy transfer of the system. The packing decreased the triplet energy of the sensitizer, leading to back transfer from the emitter with similar triplet energy. It also appears to promote some triplet-triplet annihilation on the surface, leading to back transfer. Our findings aid future design of NPL based upconverters by showing which loss mechanisms contribute to the low efficiency of the current system.

In **chapter 4**, I describe how we looked into the chemical transformation of freely diffusing substrates catalyzed by NPLs. The surface of the NPLs allows free access of the small substrates to the photoexcited catalyst, as they are covered by the native fatty acid ligands. NPLs absorb light very well with their high absorption cross section and broad absorption spectra, which makes them effective catalysts at low mol% loadings. To demonstrate the viability of NPL catalysts, we chose the reduction of nitrobenzene to azoxybenzene, which the NPLs can catalyze without completely reducing it to aniline. All 3ML, 4ML and 5ML NPLs can catalyze the reaction thanks to their near-constant conduction band energy. But the conversion of nitrobenzene increases by using thicker NPLs, which we attributed mainly to the broader absorption spectrum and higher

photoluminescence quantum yields, enhancing the absorption of light from the white LED excitation and the consecutive electron transfer. This example shows the potential of NPLs to catalyze commodity small molecules to high value products in an energy efficient manner.

Conversely in **chapter 5**, I show an effective method to disperse NPLs in water, isolate it from its surroundings and deny surface access through a combination of a polymer coating and a CdZnS shell. This contrasts existing methods to disperse NPLs in water that relies on ligands and leaves the surface accessible. The key to this method is the interaction between the surface ligands and the polymer coating. Surface ligands alone are subject to equilibrium so without the polymer coating, NPL surface may be accessible due to detachment of ligands or simply insufficient ligand coverage density. I selected oleic acid ligands, which interacts favorably to the side chains of an amphiphilic polymer, forming a robust polymer coating. A polymer coating creates a hydrophobic barrier against the hydrophilic surrounding and makes the NPLs both colloidally and chemically stable.

I affirm this idea through a comparative study in **chapter 6** where I compare the photoluminescence and colloidal stability of ligand exchanged NPLs and polymer coated NPLs in biological medium. Exposure of the NPLs to the medium forms a coating of proteins around the nanoparticle, known as the protein corona. The protein corona analysis shows different set of proteins binding to the NPL samples, despite the similarity in particle shape, size, surface charge and functional groups (COO^-) – the commonly studied parameters for nanoparticle cell uptake. Our study implies that the protein corona is affected by the dynamics of the ligand binding, where they are free to equilibrate in the ligand exchanged case, while in contrast "locked" by interaction to the polymer in the polymer coated case. The difference in surface chemistry dynamics ultimately influences the uptake of NPLs into cells. This again highlights the benefit of understanding the surface when developing materials for specific applications.

Finally, I show in **chapter 7** an ongoing collaboration project using our platform in bioimaging. Here we marked bio-polymeric nanocapsules with NPLs and localized by correlated light and electron microscopy (cLEM). Rectangular NPLs can be unambiguously identified by transmission electron microscopy alone, unlike existing spherical markers resembling cellular

components. The polymer coating protects the photoluminescent properties of the NPL during the encapsulation step and their high dispersibility in water keeps them in the aqueous phase during the miniemulsion process. This makes the encapsulation of NPLs straightforward and thus readily used as a cLEM marker for bio-polymeric nanocarriers in general.

Chapter 2: Lateral Size-Dependence in FRET between Semiconductor Nanoplatelets and Conjugated Fluorophores

This chapter is based on the following publication:

Lateral Size-Dependence in FRET between Semiconductor Nanoplatelets and Conjugated Fluorophores. Henry Halim, David Trieb, Niklas Huber, María Martínez-Negro, Lars-Arne Meyer, Thomas Basché, Svenja Morsbach, Kai A. I. Zhang and Andreas Riedinger. *Journal of Physical Chemistry C.*, 2020, 45, 25028-25037. Reproduced with permission under the ACS AuthorChoice Creative Commons Attribution 4.0 International license.

My contributions to the project were: Data analysis and application of the FRET model to the data, development of an estimate to predict the optimal size of NPLs for FRET and our fluorophore, additional spectroscopy measurements. NPL synthesis and spectroscopic data recording was done by David Trieb. The synthesis of the fluorophore was done by Niklas Huber. The synthesis of bis(stearoyl)selenide was done by Angelika Manhart. The synthesis of cadmium myristate was done by Paul Kolpakov. The ITC experiments were done by María Martínez-Negro.

2.1 Introduction

Organic fluorophores play an indispensable role in a variety of applications, including bioimaging, sensing, and photocatalysis.[104-108] Their versatility arises from the fact that their properties can be fine-tuned by changing their molecular structures. However, their absorption cross-sections are lower and of narrow band-width compared to inorganic materials.[109] This limits the choice of excitation wavelengths and requires higher excitation powers for image acquisition with organic fluorophores in (bio) imaging applications, and an increased loading of the photocatalyst and/or high excitation powers in photocatalysis with organic fluorophores. Semiconductor nanocrystals possess size-tunable absorption bands and absorption cross-sections,[5-7] are relatively photostable[110] and can act as sensitizer for molecules in their proximity.[77-84] Therefore, the combination of semiconductor nanocrystals with organic fluorophores could be useful for applications where excitation intensities are low, e.g. absorption of sunlight without concentrators. To make this principle work, the energy absorbed by the nanocrystals must be transferred to the organic fluorophore, e.g. via FRET.[111]

FRET occurs when the nanocrystal and the organic fluorophore are in close proximity, oriented in a suitable angle and if there is a sufficient spectral overlap between the nanocrystal emission with the fluorophore absorption band. Since the absorption and emission bands of quasi-spherical nanocrystals (quantum dots, QDs) are size-dependent, concurrent and independent tuning of the absorption cross-section (by the size) and the spectral overlap (also by size) is problematic. Anisotropic semiconductor nanoplatelets (NPLs),[22] also known as colloidal quantum wells, overcome this issue. The atomically precise thickness of few atomic layers of NPLs (e.g. made from CdSe) is smaller and the lateral extension larger than the Bohr exciton radius.[23] Due to this highly anisotropic structure, NPLs exhibit large absorption cross sections and the spectral position of the absorption and emission bands only depend on the thickness, while the lateral extensions determine the absorption cross-section.[6] Furthermore, their flat and well-defined surfaces should simplify their surface chemistry.

This implies that it should be beneficial to conjugate NPLs with organic fluorophores in a donor-acceptor FRET couple. This arrangement would allow to significantly broaden the absorption bandwidth and boost the absorption cross-section of the conjugate by using laterally large NPLs as the sensitizer.

However, recently Brumberg *et al.* measured the size of the exciton in NPLs via magneto-optical spectroscopy and concluded that excitons are not delocalized across the lateral dimensions of the NPL but rather localized within a radius in the range of 1.0-1.5 nm.[48] By employing transient absorption spectroscopy Li *et al.*[49] and Morgan *et al.*[50] have reported much larger exciton sizes in the range of several tens of nanometers. While the discrepancies of the various measurements are still under debate, a common finding is exciton localization at room temperature. Thus, in laterally extended NPLs, the fluorophore would have to be in close proximity to the localized exciton in order to allow for efficient energy transfer. For FRET, this would mean a distance not much further than the Förster radius. Based on this, it would be important for practical applications to know the largest possible NPL size one can use as a sensitizer, without losing too much of the FRET efficiency due to large exciton-acceptor separation distance.

Here I present our findings on the FRET between 3 mono-layer (ML, defined as the number of Se layers in zinc blende CdSe across the thickness) thick CdSe NPLs and a carboxyl-functionalized diethienyl benzothiadiazole derivative [DBTCA, 5-(7-(thiophen-2-yl)benzo[c][1,2,5]thiadiazol-4-yl)thiophene-2-carboxylic acid]. DBTCA has an excellent spectral overlap with 3ML CdSe NPLs' photoluminescence (PL) and its derivatives found applications in the field of photovoltaics[112, 113] and photocatalysis.[114, 115] Therefore, we used it as a model system for our study, using the carboxyl group of DBTCA as anchor for the Cd-terminated NPL facets. By varying the DBTCA coverage on the surface of differently sized NPLs, we found a relationship between the size and the FRET efficiency. The analysis of the FRET behaviors observed in this work confirms that excitons are indeed of a small radius and stochastically distributed in CdSe NPLs. This shows that an optimum lateral size and fluorophore coverage exists and simply increasing the absorption cross-section by using larger NPLs is detrimental to the sensitization efficiency of small organic molecules. This finding will serve as a useful guideline for developing more efficient nanocrystal sensitizer systems for FRET based photocatalysis and fluorescent imaging.

2.2 Results and Discussion

Synthesis and Functionalization of 3ML NPLs

In order to get a good spectral overlap between the NPLs and DBTCA, 3 ML thick CdSe
NPLs were selected as the donor (Figure 2.1a). The emission peak of 3ML NPLs lies at 462 nm,
close to the absorption maximum of DBTCA at 446 nm. This results in a large overlap integral J
of 2.2 x 10^{15} $nm^4M^{-1}cm^{-1}$.
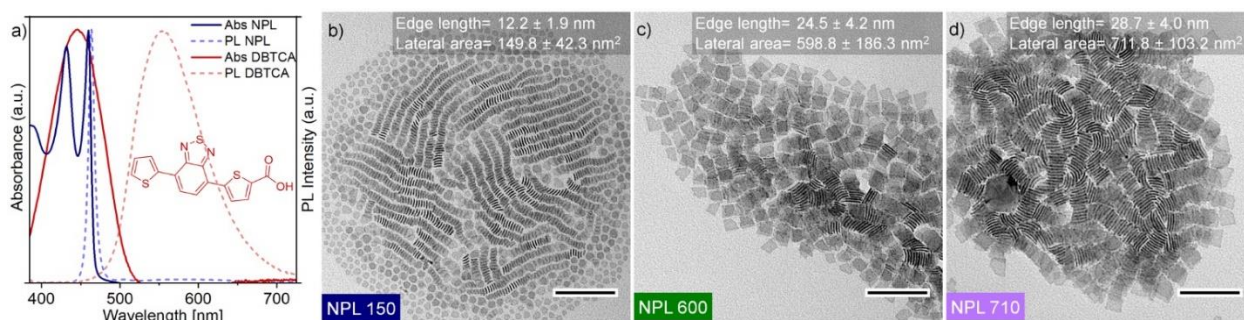
Figure 2.1. Properties of 3ML CdSe NPLs and DBTCA. a) Absorption (dark blue/red line) and PL
spectra (pale blue/red dotted line) of NPLs/DBTCA in toluene. Inset shows the structure of
DBTCA. The overlap integral J between the NPL's PL emission and DBTCA's absorption is 2.2 ×
10^{15} $nm^4M^{-1}cm^{-1}$. b) TEM image of the small NPLs with average lateral area of 150 nm^2. c) TEM
image of the medium NPLs with average lateral area of 600 nm^2. d) TEM image of the large NPLs
with average lateral area of 710 nm^2. Scale bars correspond to a length of 100 nm.

To study the influence of the lateral size in the FRET with DBTCA we first had to develop
a synthesis pathway for high quality 3ML NPLs of adjustable lateral dimensions. First, we
synthesized laterally small NPLs (surface area of ~ 150 nm^2, Figure 2.1b "NPL 150") with a
modified protocol from the work of Riedinger *et al.*[29] These NPLs were laterally extended with a
seeded growth synthesis based on the method developed by Tessier *et al.*[116] in order to obtain a
series of laterally larger NPLs (Figure 2.1 c & d, "NPL 600" and "NPL 710").

Using our modified procedure, we were able to produce three differently sized NPLs with
narrow lateral size distribution and a relatively regular shape (Figure 2.1 b-c). As expected, the
lateral size extension increased the absorption of the NPLs linearly with the lateral area (Figure
2.2), which agrees with previous findings in 4ML and 5ML NPLs.[6]
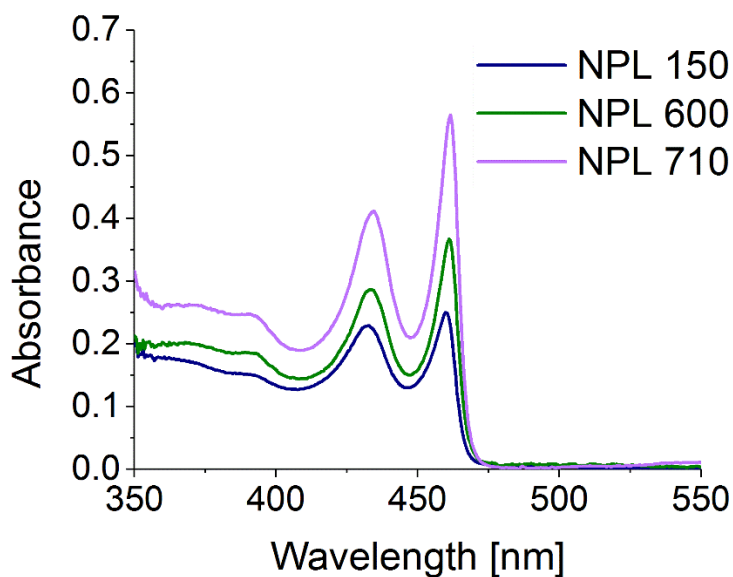
Figure 2.2. Absorption spectra of pure 3ML NPLs in hexane at equal molar concentration. Larger
NPLs exhibit higher absorbance due to their larger absorption cross sections.

After having a series of differently sized 3ML NPLs at hand, we first had to look into the
chemistry of DBTCA with the NPL surface. Since FRET is strongly distance dependent, it is
important to know whether the DBTCA, when mixed with NPLs in toluene, is freely diffusing or
directly bound to the surface of the NPLs.

We analyzed this by isothermal titration calorimetry (ITC). If the binding of DBTCA to the
surface atoms is favored by equilibrium, addition of DBTCA to NPLs will result in a heat release
or absorption upon interaction of the carboxylic group with the Cd-terminated NPL surfaces. Note
that the lack of carboxylic group results in no binding (Experimental section Figure 2.13). If the
equilibrium disfavors binding, no appreciable heat change will occur due to few products. In our
experiments, the binding of DBTCA to NPLs' surface indeed absorbs heat (Figures 2.3), which
shows that binding is favored and could also be used to quantify the maximum number of DBTCA
per NPL. Based on the observed heat changes (negative Gibbs free energy, indicating surface
binding) we determined the thermodynamic reaction parameters of the titration by careful fitting.
We found that $\Delta H = 20.4 \pm 1.2$ kJ/mol, $\Delta S = 180.0 \pm 2.9$ J/molK, $\Delta G = -33.2 \pm 0.4$ kJ/mol and K_d
$= 1.6 \pm 0.2 \times 10^{-6}$ M. The negative Gibbs free energy in relation to positive enthalpy and entropy

indicates that the process is entropically driven, most likely due to unlocking of the rotational degrees of freedom of the myristic acid released into solution after exchange with DBTCA, further changes of the solvation shell, and inter-DBTCA π-π interactions in solution.[117, 118] Meanwhile, the small dissociation constant K_d indicates that the DBTCA binding to the NPLs is highly favored. Noteworthy, the entire NPL surface can participate in binding. This enhances the binding probability significantly, similar to the situation of macromolecules with multiple binding sites (for details see Experimental section Figure 2.15).[119]

We confirmed the favorable binding by kinetic experiments (Figure 2.4). This suggests that all DBTCA introduced to the system bind to the NPL until the surface is fully covered. Furthermore, we observed the inflection point (reaction stoichiometry) at a ligand coverage of 0.61 DBTCA/nm^2 (Figure 2.3). In terms of DBTCA/NPL, this corresponds to 1.8×10^2, 7.0×10^2, 8.4×10^2 DBTCA/NPL for NPLs 150, 600, 710, respectively. When the DBTCA/NPL ratio exceeds those values, we should only see changes resulting from free excess DBTCA in solution, in the steady state PL and time resolved PL measurements of the NPLs and the DBTCA.
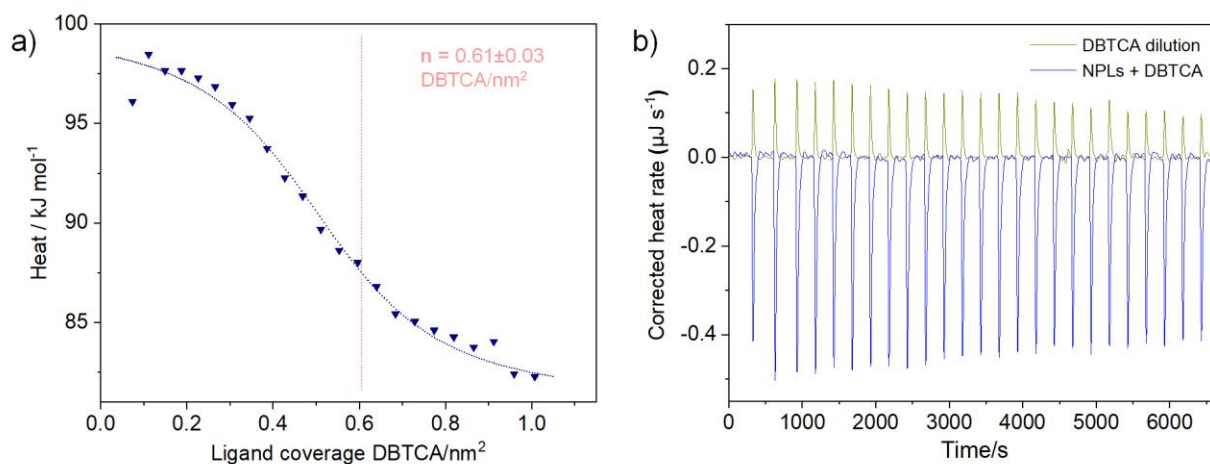
Figure 2.3. a) Exemplary ITC measurement of DBTCA titrated to NPL 450 in toluene. Results are shown in DBTCA coverage per nm^2. Data shows integrated heats after subtraction of dilution heats together with an independent binding model fit. Molar ratio at full coverage corresponds to 0.61 $DBTCA/nm^2$. b) Corrected heat rates of the titration of DBTCA to NPLs and into pure toluene (dilution experiment).

Table 2.1. Thermodynamic parameters from ITC.

K_d (M)	K_a (M^{-1})	ΔH (kJ/mol)	ΔS (J/molK)	ΔG (kJ/mol)	n/NPL	n/nm^2
$(1.6 \pm 0.2)*10^{-6}$	$(6.7 \pm 1.2)*10^{5}$	20.4 ± 1.2	180.0 ± 2.9	-33.2 ± 0.4	556 ± 29	0.61 ± 0.03
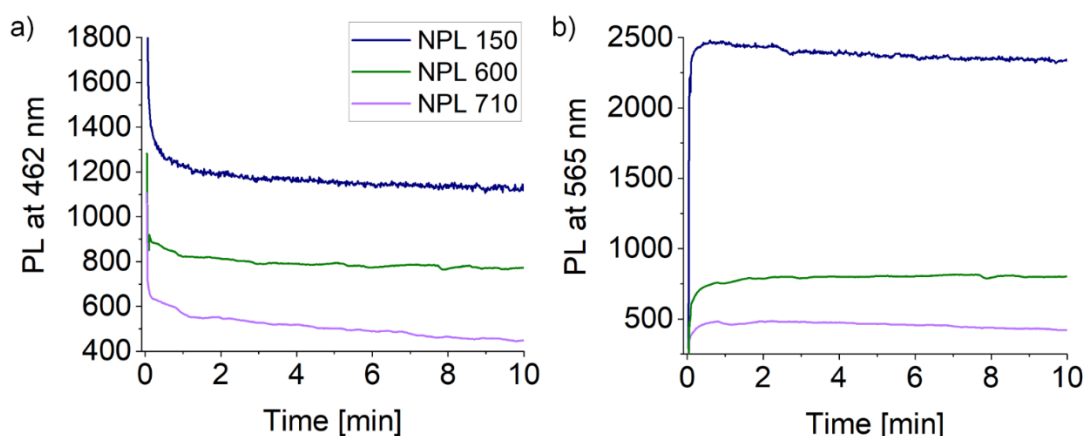
Figure 2.4. Kinetics of DBTCA binding to 3ML NPLs. a) NPL PL at 462 nm rapidly decreases as DBTCA is added. b) DBTCA PL at 565 nm rapidly increases as DBTCA is added. After the initial decrease/increase, the PL stays constant.

Estimation of Förster Radius Based on FRET Equation

The energy transfer from photoexcited semiconductor nanocrystals to suitable organic
ligands can often be described through FRET based mechanisms[47, 79, 120, 121] with few exceptions.[83,
122] For NPLs, this will involve the interaction between the transition dipole of the exciton and the
transition dipole of the fluorophore. When the NPLs are excited, the position of the exciton on the
NPL is unknown.[87] This means that we cannot use the traditional assumption of center-center
distance of donor and acceptor since the donor (the exciton) exhibits a stochastic distribution of
residence within the NPL. Thus, the distance between the donor and the acceptor must be measured
from the center-to-center distance of the exciton and DBTCA rather than the center of NPLs
(Scheme 6.1). However, since the position of the generated exciton is unknown, we must estimate
this by statistical means by using the DBTCA surface coverage. As the surface coverage increases,
the likelihood of the exciton to be near to DBTCA increases.
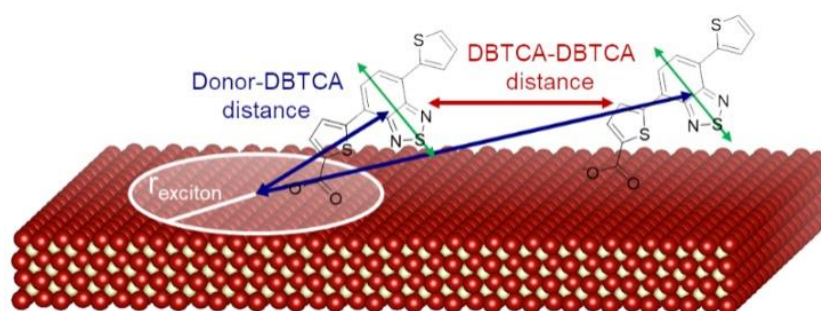
Figure 2.5. Surface binding of DBTCA on the (100) basal planes of 3ML CdSe NPLs. The left
DBTCA is positioned within the exciton radius while the right is positioned outside the radius.
Red atoms represent Cd while yellow atoms represent Se. Atomic sizes are not to scale. Green
arrows indicate the dipole moment of DBTCA.

Energy transfer *via* FRET can occur efficiently as long as the DBTCA lies within the
Förster Radius (R_0) of the NPL-DBTCA and the orientation factor κ^2 for the conjugate is non-zero.
Once the energy is transferred to the DBTCA, the molecule can relax back to its ground state by
emission of a photon. However, this process could be complicated by the possibility of (partial)
self-quenching from dimerization/oligomerization of nearby DBTCA molecules[123] on the surface
of NPLs at high ligand coverage (refer to Figure 2.6).
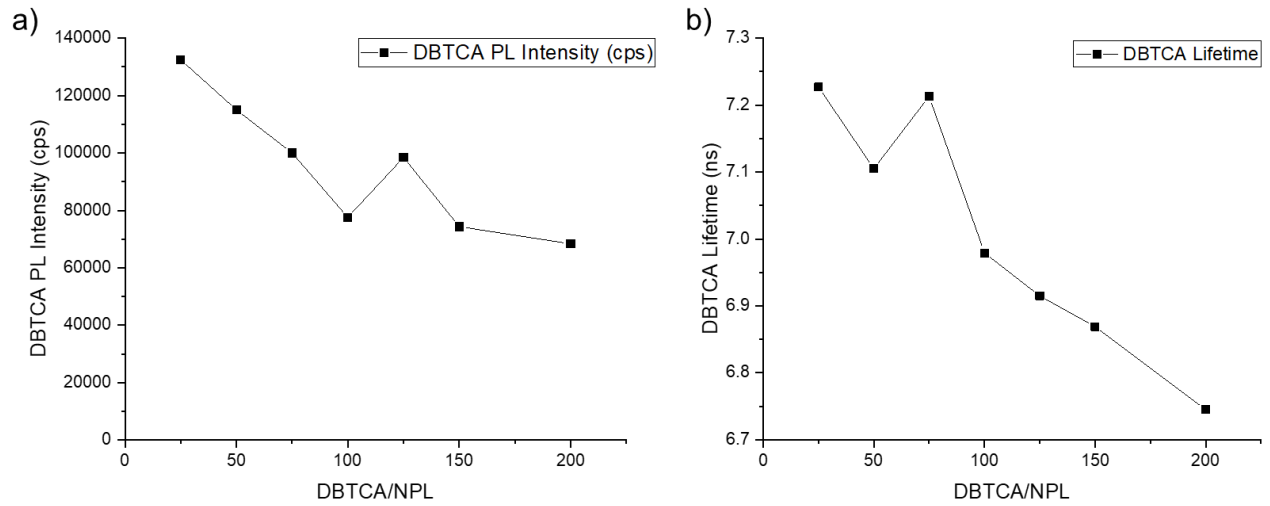
Figure 2.6. a) DBTCA PL Intensity at increasing DBTCA/NPL ratio using NPL 150 with direct excitation to DBTCA (500 nm). Ratio was adjusted by keeping DBTCA concentration constant and varying NPL concentration to facilitate comparison. Decreasing intensity suggests increasing contribution of self-quenching at high ligand coverage. b) DBTCA PL lifetime at increasing DBTCA/NPL ratio using NPL 150 with direct excitation to DBTCA (500 nm). Decreasing PL lifetime suggests DBTCA is more easily quenched at higher coverage, presumably due to closer distance of neighboring DBTCA.

Based on the properties of the three differently sized NPLs and DBTCA, R_0 can be estimated using Equation 2.1,[124] in order to estimate expected distances for efficient FRET (Table 2.2).

$$R_0^6 = 8.79 \times 10^{-11}(\text{nm}^2\text{Mcm}) \times \frac{\Phi J \kappa^2}{\text{n}^4} \quad (Eq.\,2.1)$$

Here, Φ is the quantum yield of the donor, κ^2 is the orientation factor between the donor-acceptor, n is the refractive index of the solvent and J is the overlap integral, given by Equation 2.2:[125]

$$J = \int f_{donor}(\lambda)\varepsilon_{acceptor}(\lambda)\lambda^4 \text{d}\lambda \quad (Eq.\,2.2)$$

Here, f is the normalized fluorescence intensity of the donor and ε is the molar extinction coefficient of the acceptor. Since the transition dipole moment in NPLs is mainly oriented in

plane[126], the orientation factor κ^2 will change when the DBTCA binds to the basal planes or the side facet. Erdem *et al.* demonstrated that κ^2 is 1/3 when a point-like donor dipole interacts with the basal plane of NPLs but is enhanced to 5/6 when it interacts with the side facet of the NPLs.[87] Since small NPLs have a greater contribution of side facet area compared to basal plane area (Table 2.3), we accounted for this difference for the determination of effective orientation factor κ_{eff}^2 (Table 2.2).

Table 2.2. Estimated κ_{eff}^2 and R_0 of the possible donor-acceptor pairs in this study. Estimation details are shown in Table 2.3.

	NPL 150	NPL 600	NPL 710	DBTCA
QY$_{Donor}$	0.48±0.048	0.05±0.005	0.02±0.002	0.80±0.080
$J_{Donor \to DBTCA}$ (nm^{4}M^{-1}cm^{-1})	2.20 x 10^{15}	2.20 x 10^{15}	2.20 x 10^{15}	5.36 x 10^{14}
Estimated κ_{eff}^2	0.40	0.37	0.37	0.67
$R_{0\ Donor \to DBTCA}$ (nm)	4.4	3.0	2.6	4.1

R_0 of the NPLs are calculated using Equation 2.1 and are found to lie in a similar range (Table 2.2). The differences are mainly due to the different QYs of the NPL samples (Experimental section Figure 2.14 and Table 2.6). Note that the distance dependence in this work is not ($1/r^4$), unlike in the study by Erdem *et al.*,[87] since the distance-dependence is determined by the dimensionality of the acceptor (DBTCA in our case) as shown by Martínez *et al.*[127]

Interestingly R_0 of the homo FRET between DBTCA molecules is in the same range as the FRET process between NPLs and DBTCA, which implies self-quenching will always be a possible decay pathway for the DBTCA when its surface-bound concentration is sufficiently high.

Table 2.3. Estimation of effective orientation factor $<\kappa_{eff}^2>$ and R_0 based on the different $<\kappa^2>$ when DBTCA is bound to the basal planes of NPLs or the side facets of NPLs.

Under the assumption that DBTCA acts as a point dipole, the orientation factor between NPLs and DBTCA changes from 1/3 when interacting with basal plane to 5/6 when interacting with side facets.[87] The contribution of each $<\kappa^2>$ depends on the population of DBTCA bound to the basal planes or the side facets. Taking this into account, $<\kappa_{eff}^2>$ can be calculated by **Equation 2.3**:

$$< \kappa_{eff}^2 > = \% \, surface \, basal \times basal \, planes \, < \kappa^2 > \, + \, \% \, surface \, side \, facets \, \times side \, facets \, < \kappa^2 >$$

$$(Eq. 2.3)$$

NPL 150	NPL 600	NPL 710	
0.48±0.048	0.05±0.005	0.02±0.002	**QY NPLs (±10%)**
2.20E15	2.20E15	2.20E15	**Overlap integral (J $_{NPL-DBTCA}$)**
1/3	1/3	1/3	**Basal planes $<\kappa^2>$[87]**
5/6	5/6	5/6	**Side Facets $<\kappa^2>$[87]**
6.2±0.6E3	6.4±0.6E2	2.6±0.3E2	**R_0^6 Basal planes (nm^6)**
1.5±0.2E4	1.6±0.2E3	6.4±0.6E2	**R_0^6 Side facets (nm^6)**
4.3±0.1	2.9±0.1	2.5±0.1	**R_0 Basal planes (nm)**
5.0±0.1	3.4±0.1	2.9±0.1	**R_0 Side facets (nm)**
150±42	598±186	712±103	**Average lateral area (nm^2)**
11±3	22±7	24±4	**Average Side facet area (nm^2)**
3.00±0.84E2	1.20±0.37E3	1.42±0.20E3	**Basal planes area (nm^2)**
44±12	89±28	97±16	**Side facets area (nm^2)**
0.87±0.08	0.93±0.06	0.94±0.03	**Contribution from Basal planes**
0.13±0.08	0.07±0.06	0.06±0.03	**Contribution from Side facets**
0.40±0.04	0.37±0.02	0.37±0.01	**$<\kappa_{eff}^2>$**
7.4±1.5E3	7.1±1.1E2	2.8±0.4E2	**R_0^6 Effective (nm^6)**
4.4±0.1	3.0±0.1	2.6±0.1	**R_0 Effective (nm)**

Lateral Size Dependent FRET

To assess size and concentration dependencies in NPL-DBTCA FRET couples experimentally, we conjugated various amounts of DBTCA with the NPLs by mixing the two components at different ratios in toluene. As shown in Figure 2.8 a-c, the PL intensities of the 3ML NPLs decrease with increasing concentrations of DBTCA while the DBTCA PL intensities increases first and decreases again after a certain critical surface coverage is reached. Furthermore, we observed subsequently decreasing NPL PL lifetimes upon binding of DBTCA (Figure 2.7). We confirm the FRET based nature of these phenomena by analyzing the quenching of the donor (NPL) PL and the concomitant enhancement of the acceptor (DBTCA) PL in Figure 2.9.
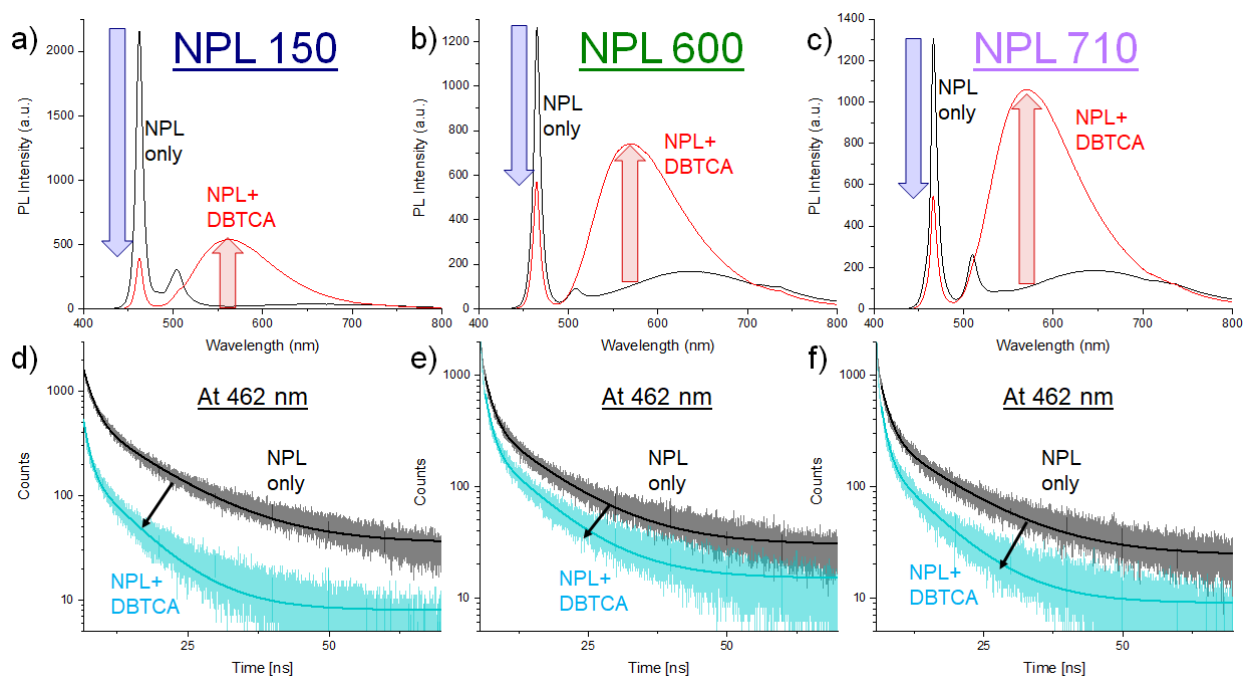
Figure 2.7. PL behavior of the three NPL sizes with and without DBTCA in steady state conditions (a-c) and time resolved conditions (d-f). DBTCA/NPL ratios were 66, 216 and 228 for NPL 150, 600 and 710 respectively, which is where max DBTCA PL occurs (refer to Table 2.4).
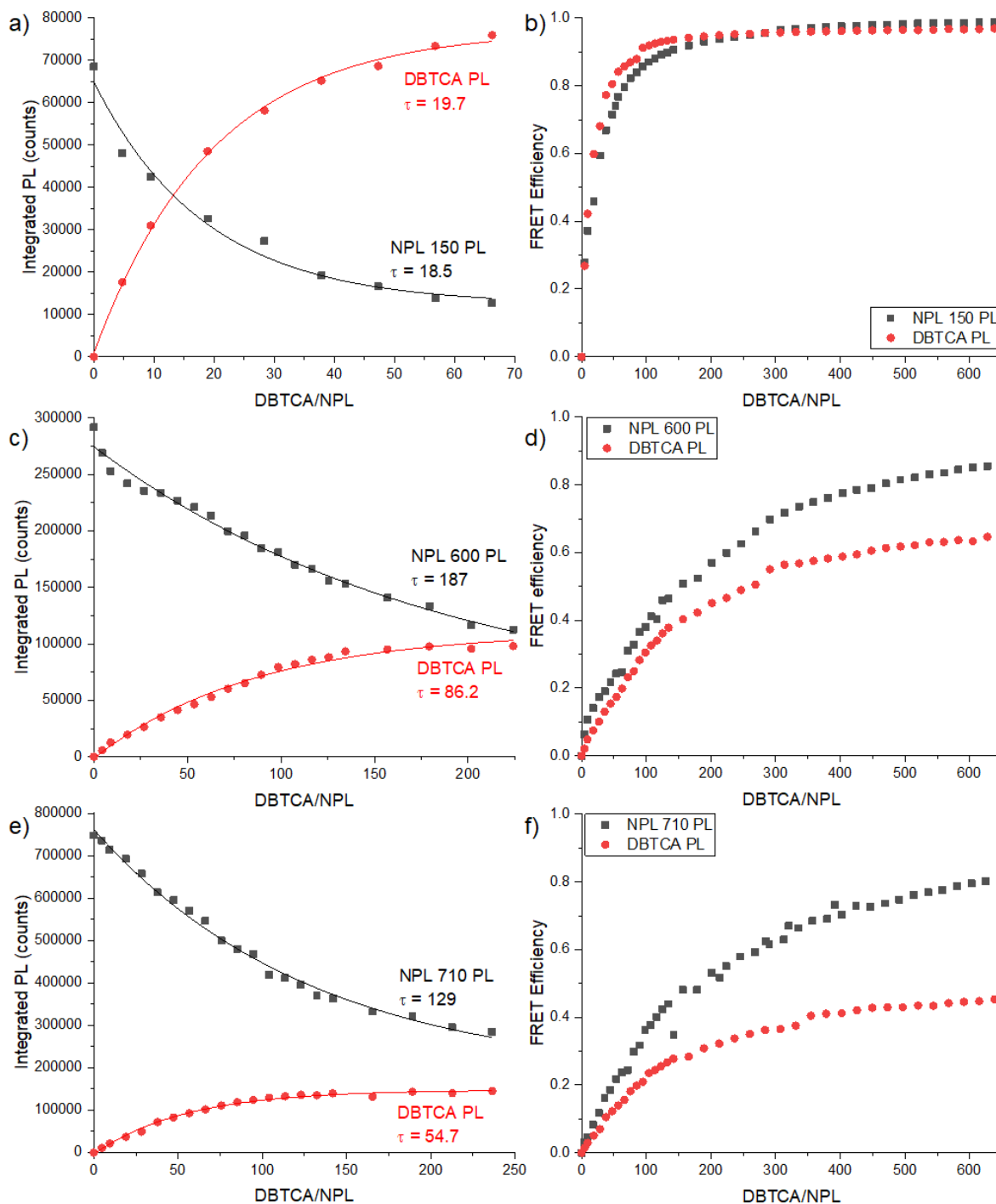
Figure 2.8. Left side: Plots of integrated PL intensities of NPL and DBTCA versus DBTCA/NPL
ratios. PL values are plotted after correction with respect to the quantum yield (Table 2.2) and
subtraction of predicted trap state contributions. Data points were fitted with exponential growth
and decay functions to quantify the rate of increase or decrease of PL using $|\tau|$. For NPL 150 (a),
energy transfer from the NPL donor to the DBTCA acceptors appears to proceed quantitatively up

to a DBTCA/NPL ratio = 66, indicating a FRET-type process with little influence of trap states and self-quenching. For NPL 600 (c) and NPL 710 (e) the influence of alternative quenching mechanisms becomes more dominant, leading to larger discrepancies of $|\tau|$. Right side: FRET efficiencies as a function of DBTCA/NPL ratios calculated according to equation 2.4 (see below) for DBTCA PL enhancement and Equation 2.5 for NPL PL quenching. For NPL150, FRET efficiencies for both NPL and DBTCA rise equally fast in early stages as seen in (b) and levels at near unity, supporting the notion of quantitative energy transfer. The losses of FRET efficiency when viewed from the DBTCA PL (d and f respectively) again indicate the contributions of trap states and self-quenching:

$$\eta_{FRET} = \frac{F_{DBTCA}/QY_{DBTCA}}{F_{NPL}/QY_{NPL} + F_{DBTCA}/QY_{DBTCA}} \quad (Eq.\,2.4)$$

As predicted from R_0 values of DBTCA-DBTCA homo FRET (Table 2.2), self-quenching starts to occur at high DBTCA/NPL ratios where the average DBTCA-DBTCA distance becomes increasingly shorter. As a result of self-quenching, the DBTCA PL intensity peaks at certain DBTCA/NPL ratios (Figure 2.9d, dotted arrows). Beyond this point, self-quenching starts to become the dominant relaxation pathway. The maximum PL intensity is reached at 66, 216 and 228 DBTCA/NPL ratios for NPLs 150, 600 and 710 (Table 2.4).
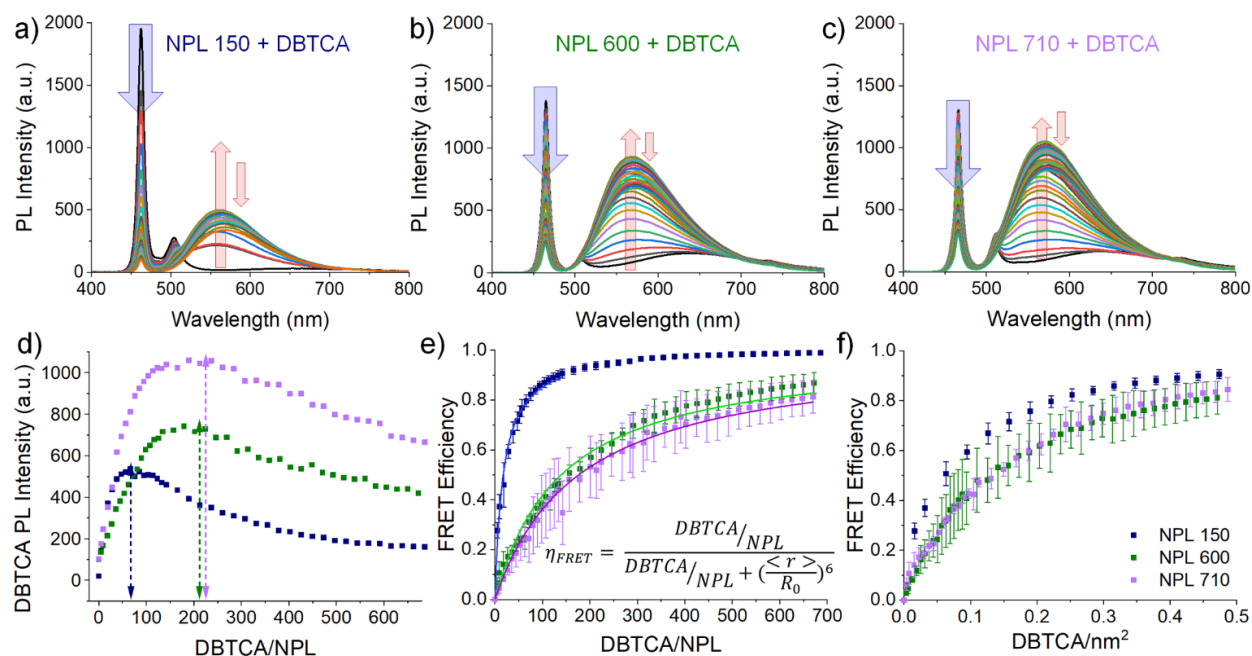
Figure 2.9. FRET between NPL and DBTCA at different DBTCA/NPL ratios. a – c) PL spectra of differently sized NPLs with increasing DBTCA concentrations. Samples were excited with a blue LED ($\lambda = 369$ nm, FWHM ~10 nm) where DBTCA weakly absorbs. NPL PL ($\lambda = 462$ nm) decreases as DBTCA concentration increases, while the DBTCA PL ($\lambda_{max} = 565$ nm) increases. The small peak at ~510 nm stems from a small amount of 4ML CdSe NPL impurities. d) Change of DBTCA steady state PL intensity. PL increases from near zero at low DBTCA and reaches a maximum at certain DBTCA/NPL ratio (dotted arrows) until the PL intensity decreases again. The position of the maximum PL shifts to higher DBTCA/NPL ratios for larger NPLs. e) FRET efficiency calculated from donor quenching (equation 2.5) of differently sized NPLs at different DBTCA/NPL ratios. Solid lines indicate fits with equation 2.6. f) FRET efficiency calculated from donor quenching of differently sized NPLs at equal DBTCA coverage.

The larger number of DBTCA required to reach this maximum on larger NPLs can be more easily understood by looking at the PL normalized to the number of ligands per surface area of each NPL in the series (DBTCA/nm²). As shown in Table 2.4 (third row), the coverage values for the three NPLs are in the same range, with smaller NPLs being more tolerant to higher coverage.

Table 2.4. DBTCA/NPL ratios and ligand coverage values for the three NPLs in different situations: maximum DBTCA PL intensity (from Figure 2.9d), maximum coverage (obtained from Figure 2.3, ITC turnover point). We approximate the NPLs surface area by considering only the planes.

	NPL 150	NPL 600	NPL 710
DBTCA/NPL at max. PL	66±5	216±13	228±18
DBTCA/NPL at max. coverage	$1.8\pm0.1\times10^2$	$7.3\pm0.4\times10^2$	$8.7\pm0.5\times10^2$
DBTCA/nm^2 at max. PL	0.22±0.02	0.18±0.01	0.16±0.01
DBTCA/nm^2 at max. coverage	0.61±0.03	0.61±0.03	0.61±0.03
Avg. DBTCA-DBTCA distance (nm) at max. PL	2.1	2.4	2.5
Avg. DBTCA-DBTCA distance (nm) at max. coverage	1.3	1.3	1.3

If we convert the coverage to the average separation distance of DBTCA-DBTCA (row 5), we obtain distances of 2.1-2.5 nm. These distances are clearly below the calculated R_0 of DBTCA-DBTCA (Table 2.2) and represents the point where self-quenching starts to dominate as relaxation pathway.

The shorter DBTCA-DBTCA distance for small NPLs implies that there is some tolerance to have the DBTCA close to one another before they efficiently quench. We attribute this to the higher relative amount of DBTCA ligands bound to the side facet that terminate the lateral expansion of the NPLs (Table 2.3). Binding to the small facets will change the orientation of the molecule, and thus the orientation factors κ^2 for DBTCA homo FRET and the desired NPL-DBTCA FRET. The orientation factor κ^2 of DBTCA-DBTCA will decrease for cases where one molecule is bound to the narrow and one is bound to the wide facets since they would be roughly orthogonally oriented to each other. Meanwhile, the NPL-DBTCA orientation factor will increase,[87] since the transition dipole moment of NPLs lie in their flat plane,[86] opening the possibility of (nearly) co-parallel transition dipole moment orientations in the best case. This difference, along with some unspecified losses observed in the large NPLs (Figure 2.8), could explain why NPL 710 need ~3.5× more DBTCA to only reach ~2× PL intensity compared to NPL 150.

The quenching of the NPL PL has been calculated by Equation 2.5 where η_{FRET} is the FRET efficiency. Moreover, in a first approximation, Equation 2.6[125] has been fitted to the data, keeping in mind that r as well as R_0 can be widely distributed:

$$\eta_{FRET} = 1 - \frac{F}{F_0} \quad (Eq.\,2.5)$$

$$\eta_{FRET} = \frac{DBTCA/NPL}{DBTCA/NPL + \left(\frac{<r>}{R_0}\right)^6} \quad (Eq.\,2.6)$$

We made a plot of FRET efficiency as function of DBTCA/NPL ratios (Figure 2.9e) and fitted the data with Equation 2.6. These fits yielded $<r>/R_0$ values of 1.62, 2.28 and 2.36 for NPL 150, 600 and 710, respectively. The lower $<r>/R_0$ values for smaller NPLs indicate that it is easier to reach high FRET efficiencies using small NPLs at equal DBTCA/NPL ratios.

By looking at the DBTCA coverage (DBTCA/nm^2) instead of DBTCA/NPL ratios, we found that the three NPLs exhibit similar FRET efficiencies at the same coverage (Figure 2.9f). This supports the idea that the excitons are localized rather than completely delocalized across the entire NPL, since the coverage shows the density of acceptors in the local proximity.

Interestingly, when DBTCA/nm^2 > 0.5, the FRET efficiency obtained by donor quenching converges to a value around 0.8 – 0.9. This happens close to when the surface of the NPLs is fully covered by the DBTCA $\approx$ 0.61 DBTCA/nm^2 (ITC, Figure 2.3 and Table 2.4). Based on this, we can conclude that the FRET efficiency between NPLs and DBTCA does reach its maximum at the highest possible ligand coverage.

However, if we compare the maximum DBTCA surface coverage to the surface coverage at maximum DBTCA PL (Table 2.4, row 1 and 2), we find the maximum PL at much lower surface coverage relative to the surface coverage where maximum FRET efficiency occurs. Therefore, we can conclude that although the energy is transferred to the DBTCA efficiently when the surface is fully covered, it will undergo subsequent (partial) self-quenching processes. In other words, when

using NPLs as sensitizers for fluorophores, it is best to minimize the self-quenching effects rather than maximize the FRET efficiency.

Qualitative Estimation of Ideal NPL Size for NPL-DBTCA FRET

Since the excitons in NPLs have a small radius and their location of residence is stochastically distributed, the size of NPLs must play an important role. With increasing ratio of DBTCA/NPL, the denser the DBTCA packing on the NPL surface becomes. At increasing ligand coverage, the probability of a DBTCA molecule to be situated near the exciton becomes higher. Therefore, if the FRET efficiencies are high at low DBTCA amounts, the DBTCA must already be placed where it can interact with the exciton efficiently. We evaluated this tentatively by looking at the steepness of the slopes in Figure 2.10.

a)

$$\eta_{FRET} = -0.808 \times e^{\frac{DBTCA/NPL}{-29.3}} + 0.895$$

b)

$$\eta_{FRET} = -0.843 \times e^{\frac{DBTCA/NPL}{-206}} + 0.895$$

c)

$$\eta_{FRET} = -0.848 \times e^{\frac{DBTCA/NPL}{-254}} + 0.895$$
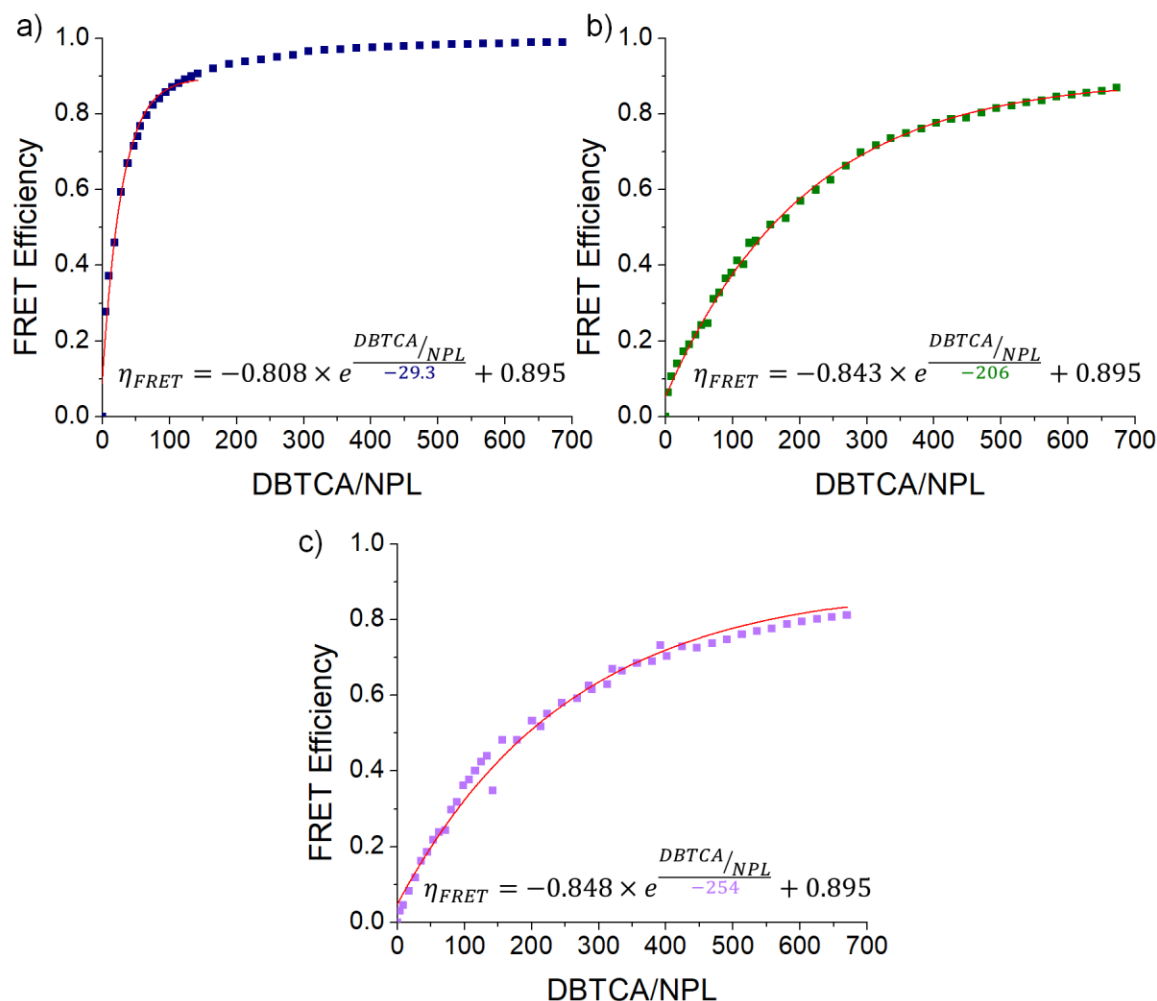
Figure 2.10. Exponential growth fits to the curves in Figure 2.9e. Exponential growth denominators obtained from fits are highlighted in dark blue, green and purple for NPL 150, NPL 600 and NPL 710 respectively.

The slope corresponds to the reciprocal probability of the DBTCA being positioned next to the generated exciton. To interpret this parameter qualitatively, we fitted the curves with an exponential growth function (Figure 2.10a-c). The steepness of the exponential growth is measured by the denominator of the exponent and scales linearly with the lateral area of the NPLs (Figure 2.11a, grey line). While this fit is not based on a physical model, a linear dependency could also be obtained by fitting the curves using equation 2.6 (Figure 2.11a, red line, refer to Figure 2.9e for the corresponding fits). This finding agrees well with the assumed uniformly distributed density of excitons in NPLs by Erdem *et al.*[87]
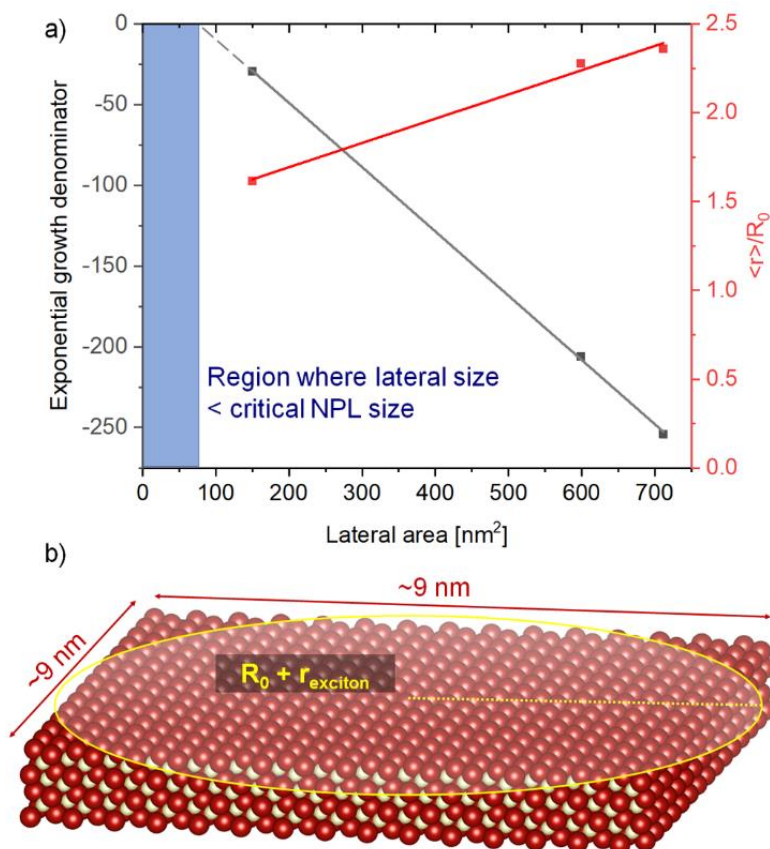
Figure 2.11. Determination of NPL size where DBTCA is always expected to be positioned close to the exciton. a) Extra-polation of the exponential growth denominator, determined from the fit of the slopes of Figure 2.10 using an exponential growth function. Result of the fits using Equation 2.6 are shown in red for comparison. The fits do not include Poisson statistics since it introduces negligible changes of the results, smaller than the error margin of the measurements (Table 2.7). The denominator approaches zero at lateral size of 78.5 nm^2. b) Sketch of square NPL with lateral size ≈78.5 nm^2, with illustration of the exciton radius and R_0.

When the exponential growth denominator approaches zero, the exponential growth function becomes infinitely steep. This means that the increase in FRET efficiency becomes infinitely fast as DBTCA binds to the NPLs' surface. In other words, DBTCA is always next to the exciton regardless of the binding site. By extrapolation we can obtain the critical NPL size where this phenomenon can occur (Figure 2.11a, blue region).

Since our study was done on roughly square NPLs, this size corresponds to square NPLs with dimensions of ~9 nm x 9 nm, slightly smaller than two times the sum of the exciton radius and average $R_{0, avg}$ (average over all R_0 in Table 2.2 = 3.3 nm) for the NPL-DBTCA FRET couple (Figure 2.11b). Although the localization of the exciton and the DBTCA binding are subject to statistical distributions, our qualitative estimation enables us to propose NPL sizes where high average FRET efficiencies could be reached without using high dye concentrations.

2.3 Conclusions

Our results on the FRET between 3ML CdSe NPLs to DBTCA ligands can be best described by dipole-dipole interactions between DBTCA and excitons in NPLs with radii in the range of few nanometers, exhibiting stochastically distributed locations of residence in the NPL. We observed the influence of this distribution by comparing the FRET efficiency of NPL-DBTCA pairs, using differently sized NPLs. For laterally small NPLs, FRET efficiencies increase rapidly at low DBTCA/NPL ratios, which indicates that the probability of DBTCA to be positioned near the exciton is high. Conversely for large NPLs, the FRET efficiency increases slowly until the conjugate reaches similar DBTCA surface densities, highlighting the dependence of FRET to surface coverage per unit area rather than DBTCA/NPL ratios. For smaller NPLs, there is a greater population of DBTCA that is positioned on the side facets, which experience less self-quenching compared to DBTCA positioned on the basal planes due to changes in the orientation factor. Therefore, increasing the absorption cross-section of NPLs by using large NPLs is accompanied with increased separation between exciton and the acceptors, the most critical parameter in FRET ($1/r^6$). Thus, optimal sensitization by NPLs should aim to use smaller NPLs to enhance FRET from exciton to acceptor molecule. Noteworthy, even small NPLs have significantly higher absorption cross sections compared to their spherical counterparts[128] the coupled system could benefit from. From our findings and estimations, these small NPLs should be isotropic in the lateral dimensions (e.g. square), with the edge length smaller than 9 nm to maximize the probability of the DBTCA to be located close to the exciton. The fluorophore density should also not be around 0.2 fluorophores/nm^2 on the surface, to minimize self-quenching. This result should aid the design of efficient NPL-fluorophore systems for sensing, imaging and photocatalysis.

2.4 Experimental Section

Chemicals. n-Hexane (95%) was purchased from Fischer scientific. Methyl acetate (99%) was purchased from Merck KGaA. 1-octadecene (ODE, 90%), cadmium acetate dihydrate (98%) were purchased from Acros organics. Selenium powder (99.999%), methanol (100%) were purchased from Alfa-Aesar. Toluene (99.8%) was purchased from VWR chemicals. Oleic acid (90%), cadmium nitrate tetrahydrate (98%), myristic acid (>98%) were purchased from Aldrich. All chemicals were used as received without further purification.

Synthesis of cadmium myristate. Cadmium myristate was prepared from its nitrate salt using standard literature methods.[129-131] Cadmium nitrate (1.23 g) was dissolved in 10 mL of methanol. Sodium myristate (3.13 g) was dissolved in 100 mL of methanol. The solutions were stirred well separately for 10 minutes until they are clear. Then, they were mixed together and stirred for 30 minutes at room temperature. The resulting white precipitate (Cd Myristate) was filtered, rinsed three times using cold methanol and dried under vacuum overnight. The white powder was stored at room temperature in the dark.

Synthesis of bis(steaoryl)selenide. Bis(stearoyl)selenide was prepared using LiAlHSeH as the selenating agent.[132] To prepare the LiAlHSeH, LiAlH$_4$ (0.76 g, 20 mmol) was added to a suspension of Se powder (1.92 g, 24 mmol) in 200 mL THF at -10 °C under argon atmosphere. The mixture was stirred for 30 min. The LiAlHSeH was formed *in situ* as a grayish dispersion. 80 mmol (27.2 mL) of stearoyl chloride was slowly added to the dispersion of 20 mmol LiAlHSeH. The mixture was stirred at -10 ºC under nitrogen atmosphere. After 2 h, 5 mL of deionized water was added to quench unreacted reagents. The organic reaction mixture was diluted with 300 mL of diethyl ether and washed four times with 100 mL brine. Bis(stearoyl)selenide was crystallized at 20 °C (12 h), filtered, and dried under high vacuum for 12 h. The resulting white flakes were stored in a nitrogen filled glove box.

Synthesis of laterally small 3ML NPLs (NPL 150).[29] In a three necked flask, 127.5 mg (0.225 mmol) of cadmium myristate and 17.3 mg (0.065 mmol) of Cd(OAc)$_2$·2 H$_2$O were dispersed in 15 mL ODE. This mixture was heated up to 100 °C and degassed under vacuum during 15 min. Afterwards the mixture was heated up to 140 °C under argon. At this temperature, a

solution of 45.8 mg (0.075 mmol) of bis(steaoryl)selenide dissolved in 1 mL of anhydrous toluene was added with a syringe. One minute later, 52 mg (0.195 mmol) Cd(OAc)$_2$·2 H$_2$O was added. The mixture was kept heated at 140 °C with an oil bath for five days. After five days, the mixture was cooled down to room temperature. Then 0.5 mL oleic acid was added. The reaction mixture was transferred to a centrifuge tube, the volume was filled up to 15 mL with hexane and the mixture was centrifuged at 5000 rpm (2599 g) for 10 min. The supernatant of this centrifugation was diluted with 15 mL of methyl acetate to induce agglomeration of the NPLs and centrifuged again at 8000 rpm (6654 g) for 10 min. The precipitate of this centrifugation was re-dispersed in 5 mL hexane. The resulting solution was clear yellow and contained pure 3 ML NPLs.

Preparation of 0.1M Se-ODE solution. 46.5 mL of ODE was introduced to a three necked flask and degassed under vacuum for 15 min at 100 °C. Afterwards, the ODE was heated up to 180 °C under argon and 393 mg (4.976 mmol) selenium dispersed in 3.3 mL toluene was added. The Se-ODE mixture was heated up to 205 °C during 25 min. During this period, the color of the mixture changed from grey to yellow. Then mixture was kept at 205 °C for 30 min. Then the solution was cooled to room temperature and transferred to a nitrogen-filled glovebox.

Seeded growth of 3ML NPLs to obtain larger lateral sizes (NPL 600, NPL 710). We synthesized NPL 600 and NPL 710 from lateral extension of NPL 150. 5 mL ODE, 2 mL NPL 150 (8.40×10^{-7} M, based on absorption), 12.8 mg cadmium myristate and 8.5 mg Cd(OAc)$_2$·2 H$_2$O were degassed at 100 °C for 15 min. Then the solution was heated up to 190 °C under argon. 1.0 mL/1.5 mL Se-ODE (for NPL 600/NPL710 respectively) was introduced using a syringe pump at speed of 50 μL/min. The reaction was stopped by cooling down to room temperature with a water bath. As the reaction was cooling, the syringe pump was stopped at 100 °C and 1 mL of oleic acid was added at 60 °C. After reaching room temperature, the reaction mixture was diluted with 5 mL methyl acetate to induce agglomeration of the NPLs and centrifuged at 8000 rpm for 10 min. The precipitate was re-dispersed with 5 mL hexane. No side products from the formation of new crystal nuclei or sample losses from loss of NPLs were found after purification.

Synthesis of 4,7-di(thiophen-2-yl)benzo[c][1,2,5]thiadiazole (DBT).[114]

4,7-Dibromobenzo[c][1,2,5]thiadiazole (1.15 g, 3.91 mmol), tributyl(thiophen-2-yl)stannane (2.73 mL, 8.61 mmol) were added to a previously dried Schlenk tube and dissolved in dry THF (40 mL). The solution was degassed with argon for 15 min, $PdCl_2(PPh_3)_2$ (55 mg, 0.08 mmol) was added and the mixture was heated to 70°C for 12h. After cooling to room temperature, THF was evaporated and the residue was taken up in DCM (50 mL). The organic phase was extracted with water (3 × 25 mL) and brine (25 mL). After drying with anhydrous $MgSO_4$ and filtration, the resulting solution was concentrated by evaporation. The crude product was recrystallized in methanol followed by washing with cold hexanes (100 mL). 4,7-Di(thiophen-2-yl)benzo-2,1,3-thiadiazole was obtained as red needles (1.07 g, 91%).

^{1}H NMR (300 MHz, CDCl$_3$) δ 8.10 (d, 2H), 7.83 (s, 2H), 7.45 (d, 2H), 7.21 (t, 2H) ppm.

^{13}C NMR (75 MHz, CDCl$_3$) δ 152.72, 139.47, 128.13, 127.62, 126.92, 126.07, 125.86 ppm.

N.B. DBT alone does not bind to NPL surface without the carboxylic acid group.
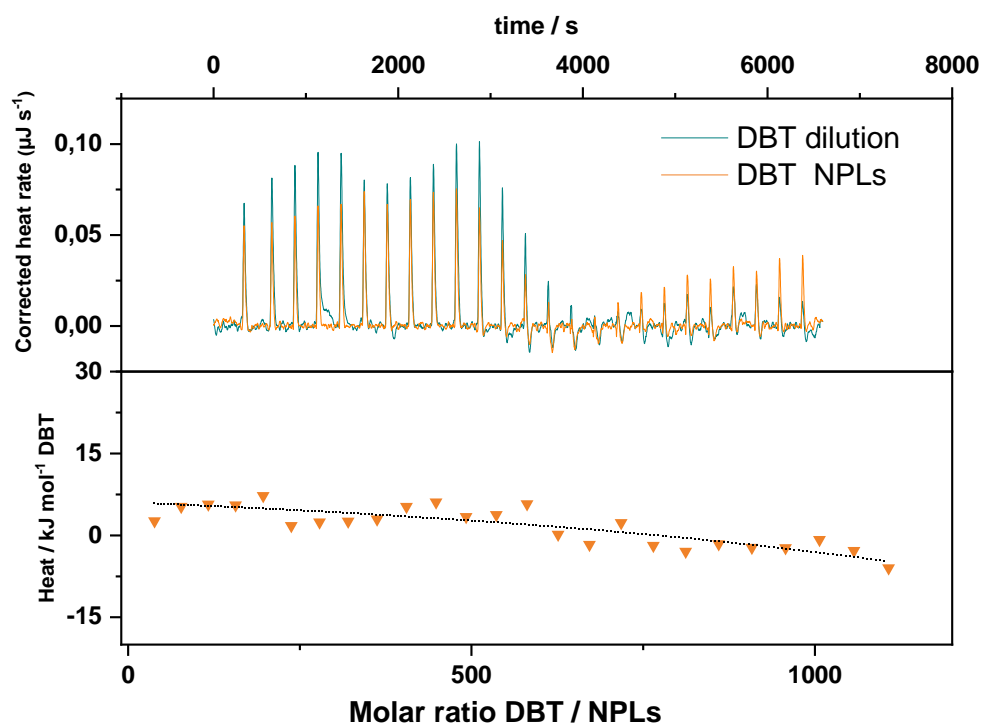
Figure 2.12. Control experiment using DBT (DBTCA without the carboxylic acid group). No binding occurs.

Synthesis   of   5-(7-(thiophen-2-yl)benzo[c][1,2,5]thiadiazol-4-yl)thiophene-2-carboxylic acid (DBTCA).

Step 1: In a dried Schlenk tube, DBT (650 mg, 2.16 mmol) and DMF (469 µL, 6.06 mmol) were dissolved in 1,2-dichloroethane (20 mL). $POCl_3$ (217 µL, 2.38 mmol) was slowly added to the solution. The mixture was stirred at 80 °C for 24 h. After cooling to room temperature, saturated ammonium acetate solution (20 mL) was added and left stirring for 30 min. DCM (20 mL) was added and the organic phase was extracted with water (3 x 20 mL) and brine (20 mL). The combined organic phases were dried over $MgSO_4$ and concentrated through rotary evaporation. The crude product was purified by column chromatography with hexanes/ethyl acetate (gradient from 2:1 to 0:1 v/v) and 5-(7-(thiophen-2-yl)benzo[c][1,2,5]thiadiazol-4-yl)thiophene-2-carbaldehyde (380 mg, 53%) was obtained as red powder.

^{1}H NMR (300 MHz, $CDCl_3$) δ 9.97 (s, 1H), 8.17 (s, 2H), 7.97 (d, 1H), 7.89 (d, 1H), 7.83 (d, 1H), 7.50 (d, 1H), 7.23 (t, 1H) ppm.

^{13}C NMR (75 MHz, $CDCl_3$) δ 183.14, 152.58, 152.52, 148.71, 143.52, 139.01, 136.93, 128.50, 128.35, 128.18, 128.06, 127.91, 127.51, 125.39, 124.46 ppm.

Step 2: In a dried Schlenk tube 5-(7-(thiophen-2-yl)benzo[c][1,2,5]thiadiazol-4-yl)thiophene-2-carbaldehyde (150 mg, 0.46 mmol) was dissolved in acetone (12 mL) and the solution was cooled to 0°C in an ice bath. Potassium permanganate (87 mg, 0.55 mmol) was added and the reaction was stirred at room temperature for 8h. The mixture was concentrated via rotary evaporation and the residue was dissolved in a solution of *N,N*-diisopropylethylamine in acetonitrile (10 vol%) and left stirring for 2h. A slurry of ion exchange resin (DOWEX IX8 chloride form 200-400 mesh) in acetonitrile was prepared and loaded into a short column. The product solution was then absorbed onto the column and washed several times with acetonitrile and DCM. For elution, trifluoroacetic acid in DCM (5 vol%) was passed through the column. After washing the resulting organic phase with brine and drying over $MgSO_4$, the solution was concentrated to dryness. 5-(7-(thiophen-2-yl)benzo[c][1,2,5]thiadiazol-4-yl)thiophene-2-carboxylic acid was obtained as red powder (139 mg, 89%).

^{1}H NMR (500 MHz, d6-DMSO, 373K) δ 8.14 (m, 2H), 8.05 (d, 1H), 8.04 (d, 1H), 7.79 (d, 1H), 7.71 (d, 1H), 7.25 (t, 1H) ppm.

^{13}C NMR (125 MHz, d6-DMSO, 373K) δ 162.27, 151.50, 151.49, 144.04, 137.98, 135.12, 132.87, 127.97, 127.64, 127.58, 127.12, 126.78, 126.28, 125.37, 123.87 ppm.

Sample preparation for FRET experiments. A stock solution of DBTCA was prepared by dissolving 1.6 mg pure powder in 33.78 mL toluene ([DBTCA] = 1.375×10^{-4}M). Dispersions of NPL 150, NPL 600 and NPL 710 were diluted with 600 µL toluene in a 700 µL quartz cuvette and adjusted to the same molar concentration of 4.87×10^{-8} M. The NPL samples were characterized with absorption, steady state and TCSPC (time correlated single photon counting) PL spectroscopy. Then 1 µL of the DBTCA stock solution was mixed to the NPL dispersion and the samples were characterized again by absorption, steady state and TCSPC PL spectroscopy. This process was repeated until a ratio of ~700 DBTCA/NPL was reached.

Sample preparation for kinetic experiments. NPL 150, NPL 600 and NPL 710 were diluted to a volume of 600 µL with toluene in a four sided cuvette to molar concentration of 1.95×10^{-7} M, 4.83×10^{-8} M and 4.0×10^{-8} M in order to reach the same absorption. Then 40 µL of the DBTCA stock solution (described in previous paragraph) was added. PL spectra was taken every second for a duration of 10 min.

Transmission electron microscopy (TEM). To provide the TEM images of the NPLs, 10 µL of a sample was diluted with hexane and drop-casted to a carbon coated copper TEM-grid. Within one minute, the hexane fully evaporated. Afterwards the sample was analyzed with a JEOL JEM-1400 TEM at an acceleration voltage of 120 kV. The sizes of the NPLs were measured from the TEM-images with ImageJ. The geometry of the NPLs were assumed to be perfect squares. For typical size determination, 100 to 200 NPLs were measured.

Steady state absorption spectroscopy. The absorption spectra were measured using an Agilent Cary 60 Spectrophotometer or Avantes spectrophotometer, consisting of Avantes AvaLight-DH-S-BAL as the UV-Vis light source passing through a neutral density filter (optical density = 2.0) and fiber-coupled to an Avantes SensLine AvaSpec-HSC-TEC detector.

Steady state photoluminescence (PL) spectroscopy. Photoluminescence spectra were recorded using an Avantes SensLine AvaSpec-HSC-TEC spectrophotometer in 90° geometry. A Prizmatix Silver high power LED was used as the excitation source (emission peak 369 nm, FWHM ~ 10 nm).

Time resolved PL spectroscopy / time-correlated single photon counting (TCSPC). PL lifetime measurements were conducted with a FluoTime200 time-correlated single photon counting setup. Samples were excited with a blue laser at 380 nm, which was controlled by PicoQuant PDL 800-D. The signal was detected using a micro-channel plate photomultiplier tube that was connected to PicoHarp 300 time-correlated single photon counting system. NPL PL signals were read at 462 nm while DBTCA signals were read at 565 nm. The instrument response function was measured using a dispersion of silica nanoparticles (LUDOX® HS-40 colloidal silica) in water. Lifetime of the NPLs were fitted with a double exponential function, while lifetime of DBTCA was fitted with a monoexponential function. The lifetimes of the pure components are shown below for reference.
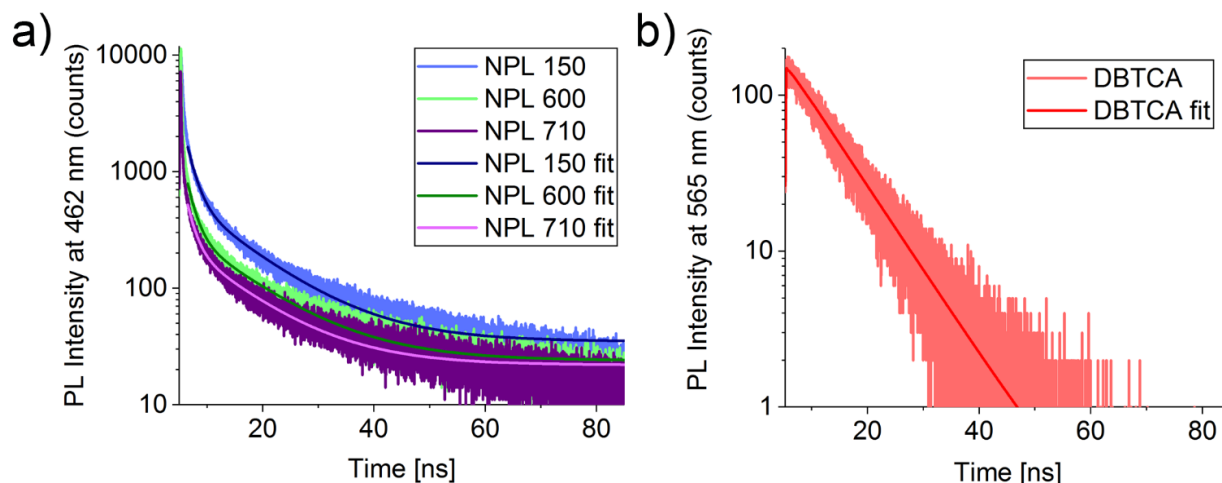
Figure 2.13. PL lifetimes of the NPLs and DBTCA with their corresponding double exponential (a) and monoexponential (b) fits. Lifetimes obtained from fits are shown in the table below.

Table 2.5. Lifetimes of the components obtained from exponential fitting (**Equation 2.7**).

$$I(t) = A_1 \cdot e^{-\frac{t}{\tau_1}} + A_2 \cdot e^{-\frac{t}{\tau_2}} \quad (Eq.\,2.7)$$

Sample	NPL 150	NPL 600	NPL 710	DBTCA
A1 /counts	510±20	320±20	260±10	160±10
τ_1 / ns	11.1±0.4	10.5±0.5	11.6±0.5	8.0±0.4
A2 / counts	1090±90	600±70	510±50	-
τ_2 / ns	1.6±0.1	1.4±0.2	1.5±0.2	-
Amplitude weighted <τ> / ns	4.6	4.6	4.8	8.0
Intensity weighted <τ> / ns	8.9	8.7	9.5	8.0

Determination of quantum yields (QYs). Quantum yields were determined relative to a reference dye[133] and conducted in open air. Rhodamine 6G was dissolved in absolute ethanol. 3ML CdSe NPLs were diluted in hexane until the sample absorption approached a value of 0.1 at the wavelength of 370 nm. The photoluminescence of the samples were recorded at that concentration using blue LED excitation at 369 nm (FWHM ~ 10 nm). Further dilution of the samples allowed us to obtain a linear fit between the sample absorption and the integrated photoluminescence,

which was compared to the Rhodamine 6G standard linear fit to obtain the quantum yield of the
samples.
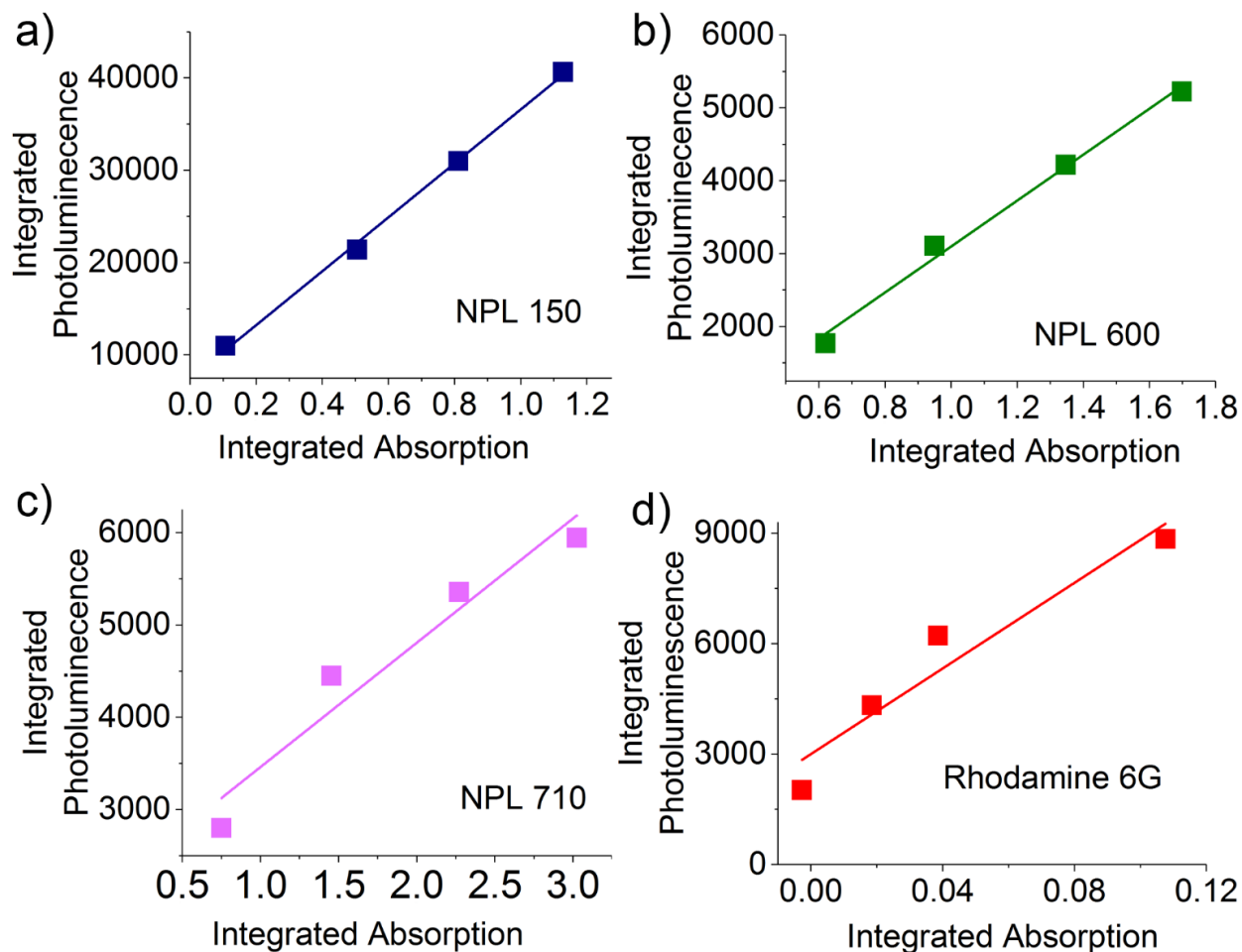
Figure 2.14. Linear fit of integrated absorption against integrated photoluminescence of NPLs and
Rhodamine 6G reference. Integrated absorption was measured between 364 – 374 nm, based on
the excitation wavelength and FWHM of the LED (369 nm, FWHM 10 nm). Slopes of the linear
fit and calculated QY are shown in the table below.

Table 2.6. Calculation of QYs of NPLs based on Rhodamine 6G and **Equation 2.8**.

Sample	NPL 150	NPL 600	NPL 710	Rhodamine 6G
Slope	29188	3151	1346	58124
Solvent	Hexane	Hexane	Hexane	Ethanol
n_D solvent	1.3272	1.3272	1.3272	1.3611
QY (±10%)	48	5	2	95

$$QY_{NPL} = QY_{Dye} \cdot \frac{slope_{NPL}}{slope_{dye}} \cdot \left(\frac{n_{D,NPL}}{n_{D,Dye}}\right)^2 \quad (Eq.\,2.8)$$

Isothermal titration calorimetry (ITC). ITC experiments were performed with a Nano ITC Low Volume from TA Instruments (Eschborn, Germany). The temperature was set to 25 °C during all measurements. The effective cell volume was 170 µL and a stirring rate of 350 rpm was chosen for all experiments. During each experiment 50 µL of the DBTCA ([DBTCA] = 1.0×10^{-4} M in toluene) were titrated into a toluene dispersion of NPLs with lateral size of 454 nm^2 (NPL 450, [NPL 450] = 3.3×10^{-8} M) with titration steps of 25 × 2 µL. Additionally, the same DBTCA solution was titrated into pure toluene to determine the heat of dilution. The temporal spacing between injections was set to 300 s. The integrated heats for each titration were analyzed with after subtraction of the heat of dilution using the NanoAnalyze software, version 3.5.0 by TA Instruments.[134] Measurements were performed in triplicate and fit parameter mean values and standard deviation were calculated from these measurements.

All obtained heat changes Δq were analyzed with a fit according to an independent binding model. [135, 136] (equation 2.9). This model assumes that a ligand L independently binds to one site of a NPL M without any cooperativity effects.

$$\Delta q = \left(\frac{(N[M]K_a+[L]K_a+1)-\sqrt{(N[M]K_a+[L]K_a+1)^2-4NK_a^2[M][L]}}{2K_a}\right) - [ML]_{n-1}\Delta H \Delta V_{cell} \quad (Eq.\,2.9)$$

From the fit, the stoichiometry N, association constant K_a and enthalpy change ΔH are obtained, whereas $[M]$ is the concentration of the NPLs, $[L]$ the concentration of the ligand, $[ML]$ the concentration of the formed complex and ΔV_{cell} the change of the total cell volume during the titration. To calculate the entropy change ΔS of the reaction, the reaction isotherm equation (equation 2.10) was combined with the Gibbs-Helmholtz equation (equation 2.11) and solved for ΔS (equation 2.12).

$$\Delta G = -RT \cdot \ln K_a \qquad \text{(Eq. 2.10)}$$

$$\Delta G = \Delta H - T \cdot \Delta S \qquad \text{(Eq. 2.11)}$$

$$\Delta S = R \cdot \ln K_a + \frac{\Delta H}{T} \qquad \text{(Eq. 2.12)}$$

Here ΔG is the Gibbs free energy, R is the universal gas constant and T the temperature, so that for known K_a and ΔH the entropy change can be calculated.
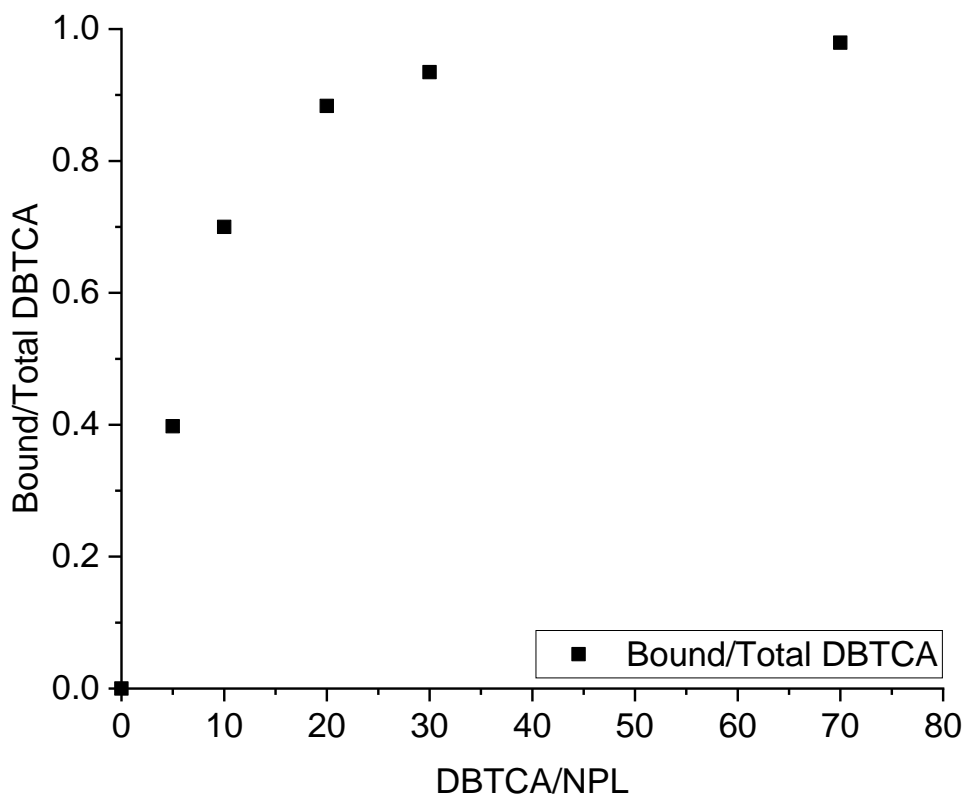
Figure 2.15. Ratio of bound DBTCA calculated from the dissociation constant from ITC. Here a model of macromolecules with multiple binding sites was used.[137]

$$r = \frac{\sum_{i=1}^{n} i \binom{n}{i} \left(\frac{[L]}{K_d}\right)^i}{1 + \sum_{i=1}^{n} i \binom{n}{i} \left(\frac{[L]}{K_d}\right)^i} \qquad (Eq. \, 2.13)$$

Where r is the ratio of bound ligands: unbound ligands, [L] is the initial ligand concentration and Kd is the dissociation constant. And:

$$Bound/Total\ DBTCA = \frac{Bound\ DBTCA}{Bound\ DBTCA + Free\ DBTCA} = \frac{r}{r+1} \quad (Eq.\,2.14)$$

Poisson statistics applied to 5 selected scenarios using NPL 150

$$\eta_{FRET} = \sum_{k=0}^{\infty} P(\lambda,k) \frac{d}{d + \frac{r^6}{R_0}} \quad (Eq.\,2.15)$$

Equation 2.15: Equation 2.6 with Poisson statistics. d = DBTCA/NPL

Where $P(\lambda,k) = \frac{\lambda^k e^{-\lambda}}{k!}$

Rearrange for r/R$_0$

$$\frac{r}{R_0} = \sum_{k=0}^{\infty} P(\lambda,k) \sqrt[6]{\frac{d}{\eta_{FRET}} - d} \quad (Eq.\,2.16)$$

Table 2.7. Comparison of r/R$_0$ obtained from equation 2.6 vs. equation 2.15.

DBTCA/NPL	η_{FRET}	r/R$_0$ w/o Poisson	r/R$_0$ w/ Poisson	% error
5	0.222	1.61(2)	1.57(7)	2.1
10	0.367	1.60(8)	1.59(2)	1.0
20	0.535	1.61(0)	1.60(0)	0.6
30	0.634	1.60(9)	1.60(1)	0.5
70	0.801	1.61(0)	1.60(3)	0.4

Noteworthy, the DBTCA/NPL ratio of interest in our study starts at 66 DBTCA/NPL, where the maximum PL intensity of DBTCA occurs. At such a high ratio, the error introduced by excluding Poisson statistics is between 0.4 – 0.5%, hence we excluded the analysis due to the large number of data points in our data set and the tedious nature of the summation.

Chapter 3: Intermolecular Interactions Between Anthracene Ligands on CdSe Nanoplatelet Surfaces Create Loss Mechanisms in Triplet-Triplet Annihilation Upconversion by Back Transfer

In the previous chapter I showed how organic fluorophores can be sensitized by NPLs by a FRET mechanism. This chapter uses an anthracene-based ligand, which is sensitized by a Dexter-like mechanism instead in order to receive the energy as a triplet. The anthracene ligand in the triplet state transfers the energy to emitters in solution allowing annihilation upconversion. This chapter is based on an unpublished paper draft.

My contributions to the project were: Synthesis of CdSe nanoplatelets, initial condition screening, characterization and optimization of the upconversion system, and data analysis. Further characterization and data analysis were done by Alessandra Ronchi. Transient absorption measurements were done by Ricardo Baez. ITC experiments were done by Dr. María Martínez-Negro. Cadmium myristate was synthesized by Paul Kolpakov.

3.1 Introduction

Sensitized triplet-triplet annihilation upconversion (sTTA-UC) [42, 43, 57, 58, 62, 138-156] is a strategy to improve the current UC process,[58, 139, 148, 157-163] which has applications in in photovoltaics,[157, 160] anti-counterfeit,[164, 165] fluorescence bioimaging,[166-168] and high sensitivity oxygen detection.[169, 170] Traditional sensitizers based on organic molecules can reach high UC quantum yields (QYs) as high as 30%, close to the maximum theoretical value of 50%.[145] To continue improving the UC-QYs, loss mechanisms in sTTA-UC pathway must be identified and removed from the process.

A recent development in sTTA-UC uses nanocrystals as sensitizers because of their broad absorption range, high absorption cross sections and more importantly, mixed triplet-singlet excited states.[152-154] This mixed state minimizes the energy loss when generating triplets since intersystem crossing is no longer necessary. Unfortunately, using nanocrystals comes with their own set of problems, hence current nanocrystal sensitizers using quantum dots have yet reached the same efficiency as the traditional sensitizers. Ronchi et al. recently showed that quantum dots

have intrinsic limitations due to how their surfaces interact with the surface ligands, leading to quenching via surface defects and hole withdrawal.[171] Hence it is challenging to achieve efficient sTTA with quantum dot sensitizers.

Colloidal quantum wells or quasi 2D nanoplatelets (NPLs) is an alternative nanocrystal that serve as a promising solution. Due to their geometry, zinc blende NPLs only have one type of crystal facet (100) on their surface, unlike quantum dots which has more than two different types of facets. This makes surface-ligand interactions simpler because binding of ligands on (100) facets is favourable on charged (100) surface,[11-13] reducing formation of surface defects during ligand exchange. Moreover, Zhou *et al*. showed that ligands shift the absolute band energies of NPLs,[172] alter the driving force of hole transfer.[173] This feature can be tuned to favour triplet energy transfer and suppress competition from hole withdrawal.

Recently, VanOrman *et al*. demonstrated modest green-blue TTA-UC-QYs using NPLs and diphenylanthracene (DPA) emitters.[174] They attribute the modest UC-QYs due to the NPLs having higher oscillator strengths, which is beneficial to absorb the excitation wavelength but will also strongly absorb the upconverted photons. Stacking of NPLs also hindered the effectiveness of their system since it effectively lowered the number of accessible ligands to generate triplets for the emitter molecules. However, these explanations are incomplete since they do not account for possible loss mechanisms related to surface chemistry. Although NPLs exhibit simpler surface-ligand interactions compared to QDs, the influence of a flat surface on the ligand-ligand interaction complicates the overall surface chemistry. Thus, it is crucial to know if the new surface chemistry introduces new loss mechanisms and determine whether there are ways to avoid them.

In this work, we showed multiple mechanisms that limit the sTTA-UC efficiency in hybrid decorated NPL and emitter dispersion. We also confirmed that the binding of 9-anthracence carboxylic acid (9-ACA) ligands is strong and facile, facilitating fast and efficient triplet transfer from NPL to 9-ACA. By studying the triplet transfer to the surface ligands ET^1 as a function of the nanocrystal coverage with the ligands, we found that intermolecular interactions between ligands play a crucial role that affects both the surface coverage dynamics and the ET^1 efficiency. These interactions induce competitive ultra-fast energy losses. Moreover, the formation of ligand

aggregates on NPLs' surface induce a shift of the ligand triplet exciton energy and affects the TTA in solution depending on the emitter's triplet level. This energy shift must be considered to optimize the triplet transfer ET^2 towards the annihilator moiety. The ligand aggregates also open a new relaxation pathway by TTA on the surface of NPLs, evidenced by delayed PL from NPLs. Our results therefore indicate intermolecular ligand interactions must be considered to avoid competitive processes for the design of NPL based hybrid triplet sensitizers. Accounting for these mechanisms would allow nanocrystal sTTA UC to match the UC performances of full organic counterparts, while benefitting from broad absorption range and high absorption cross sections.

3.2 Results and Discussion

To best account for the NPL-ligand surface interactions, we first quantified the ligand binding behaviour to NPL surfaces via isothermal titration calorimetry (ITC). We titrated a 2×10^{-3} M solution of ACA into a 2×10^{-7} M dispersion of NPLs and measured the heat change resulting from the ligand exchange process (Figure 3.1C, bottom). For this process, we used a 80:70:15 hexane:toluene:THF solvent mixture that we utilized later for the UC system (refer to Figure 3.1a). This solvent composition improves the solubility of all components, particularly the ACA due to their low solubility in pure toluene. Thus, we were able to identify the turnover point for the ligand binding where the surface of the NPLs is fully covered (1.4 ACA/nm^2), assuming homogeneous coverage of NPL surfaces. This value is a significant reduction of coverage (Σ) compared to the native fatty acid ligands, having a footprint of ~0.3 nm^2 and $\Sigma > 3.3$ nm^{-2}.[12, 156]

We calculated the thermodynamic parameters by fitting the triplicated measurement to determine how favourable ACA binding is to the surface over the native ligands. The binding of ACA to the NPLs exhibits a positive enthalpy (ΔH) and entropy (ΔS). At room temperature this results in a negative Gibbs free energy (ΔG), which means the ligand exchange is entropically driven. The entropy gain likely comes from the detachment of the native myristic acid ligands that gain rotational degrees of freedom in the solvent, changes in the solvent shell and the inter 9-ACA π-π interactions in solution.

The negative ΔG also means a small dissociation constant ($K_d = 3.0\times10^{-6}$ M), which indicates the equilibrium favours the exchange to 9-ACA over the native ligands. Using this

dissociation constant, we determined the ratio of bound ligands for a given 9-ACA/NPL ratio by assuming a model of a macromolecule with identical independent binding sites.[119] In this study, the lowest Σ we used was 0.5 ACA/nm^2, which corresponds to 127 ACA/NPL. At this ratio, the model predicts that >99.1% are bound to the surface of the NPLs (see Experimental section. Equation 3.1 and 3.2 for details). Therefore, it is safe to assume that every 9-ACA introduced in the mixture binds to the NPLs surface until saturation.
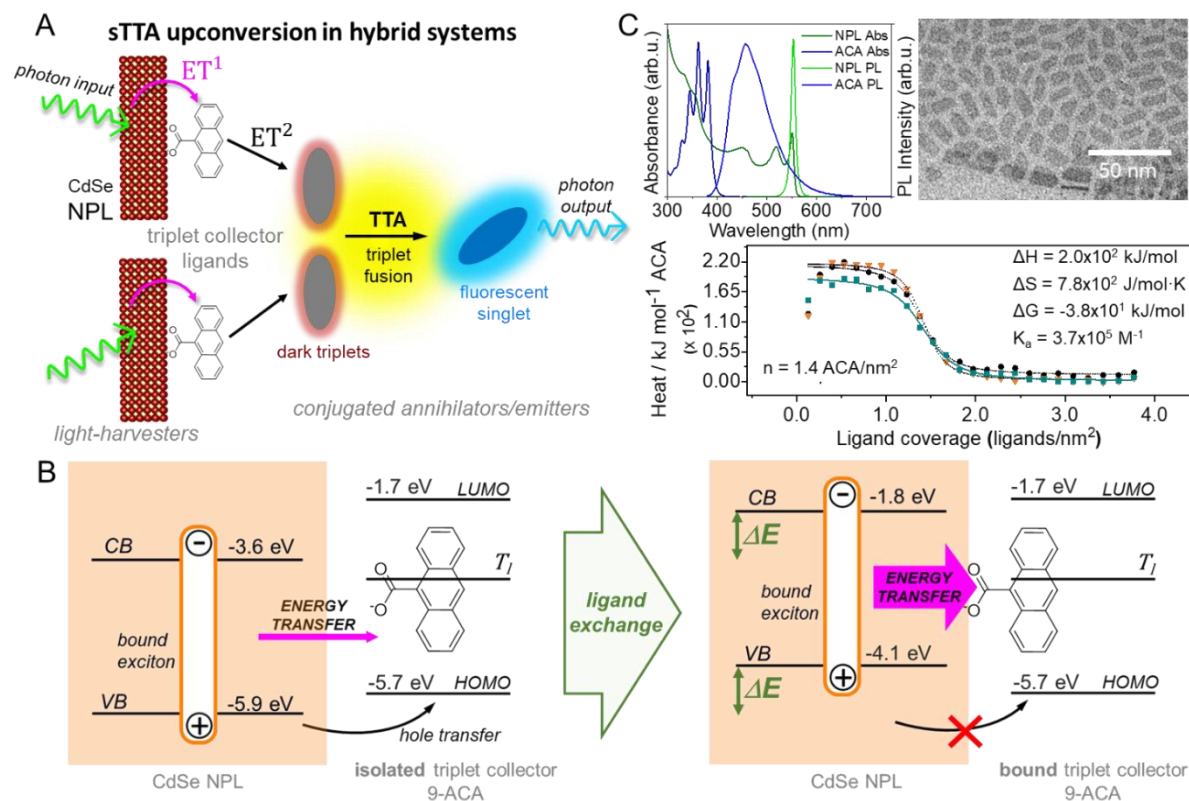
Figure 3.1. (a) Energy flux in the *s*TTA upconversion process in hybrid systems. Upon absorption of a green photon by the NPLs, the exciton energy is transferred via energy transfer ET^1 to the triplet collector ligand that then populates the triplet state of the emitter via ET^2. The annihilation of two emitter triplets (TTA) results in the formation of a high-energy fluorescent singlet state responsible for the upconverted blue luminescence. (b) Energy diagram and mechanistic picture of the CdSe NPL electronic energies shift due to the presence of 9-ACA surface ligands, as calculated by Weiss and co-workers[172] (c) *Top*. Absorption and photoluminescence (PL) spectra of pristine NPLs dispersed in hexane and TEM microscopy image of drop casted nanocrystals. Average lateral size is 15.5 nm × 8.2 nm (127.1 nm^2). *Bottom*. ITC of NPLs with ACA ligands measured in three different runs. The average inflection point occurs at 1.4 ACA/nm^2.

We studied the effect of the ligand exchange on the NPL emission and the ET^1 dynamics (triplet transfer from NPL to ligand, Figure 3.1a) by *cw* and time resolved photoluminescence spectroscopy as function of Σ. Figure 3.2a shows how the NPL photoluminescence intensity decreases by increasing Σ. To gain a better understanding of the process involved in the emission quenching, we looked into the time resolved spectra at 550 nm (Figure 3.2b). The pristine NPLs show an almost single exponential emission intensity decay with a characteristic lifetime of 8.5 ns. By changing the solvent from hexane to the solvent mixture, we observe a dramatic drop of the zero-time intensity I_0 of about one order of magnitude, as well an acceleration of the emission lifetime (Figure 3.2b, horizontal dashed line). This suggests some introduction of defects, quenching of the optical exciton by ultrafast electron trapping and/or the creation of an NPL sub-population which are non-emissive.[175-178] Interestingly, adding 9-ACA to the NPLs partially recovers I_0 at partial surface coverage ($\Sigma = 0.5$ nm^{-2}) and slightly accelerates the emission lifetime, due to the ET^1 to ligands.

By further increasing the 9-ACA content in the solution up to have nominal ligand densities above the full coverage values ($\Sigma > 1.4$ nm^{-2}), we observed a progressive acceleration of the decay time, in agreement with an enhanced ET^1 rate and yield. Figure 3.2c shows ET^1 reaches maximum value of 90% at nominal $\Sigma = 24$ nm^{-2}. Transient absorption (TA) experiments further confirm the occurrence of ET^1. Figure 3.2e shows the TA in the nanosecond time range for a dispersion with and without surface-bound ACA ($\Sigma = 24$ nm^{-2}).
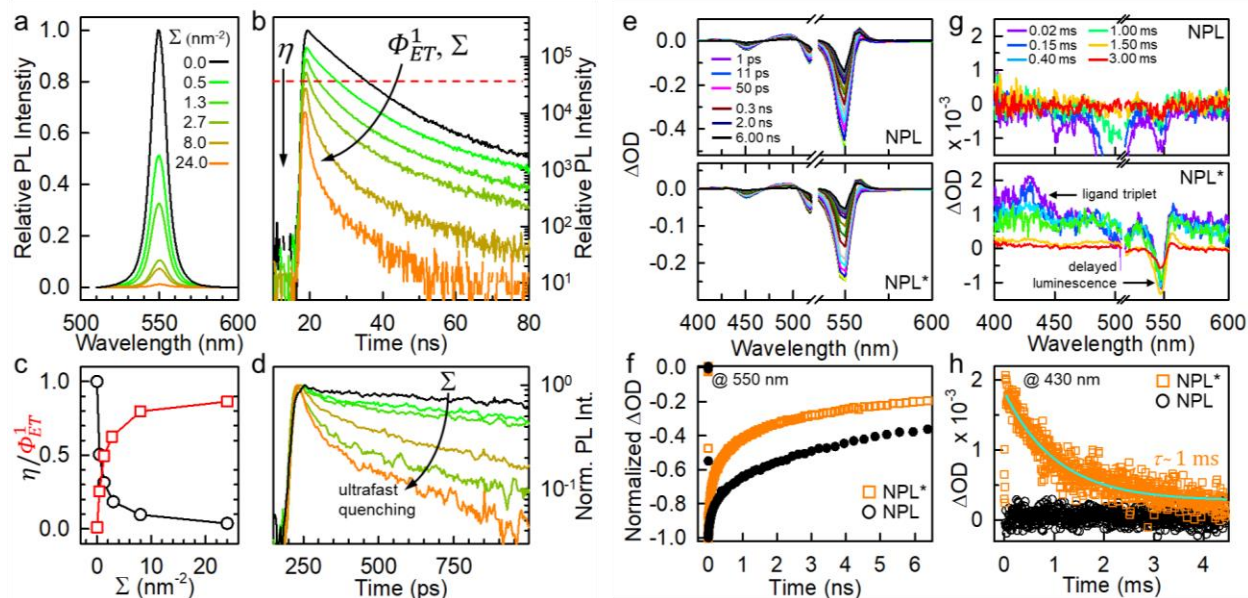
Figure 3.2. (a) Relative photoluminescence (PL) spectrum of CdSe nanoplatelets (NPLs) dispersion as function of the nominal ligand density Σ and (b) corresponding time resolved PL spectra recorded at 550 nm under pulsed excitation at 532 nm (pulse width 1 ns, repetition rate 10 MHz). The dashed horizontal line marks the zero-time loss of the PL intensity when pristine NPLs are move form native solved hexane to the mixture employed for the ligands exchange. (c) Zero-time intensity (I_0) and energy transfer efficiency (Φ_{ET}^1) as a function of Σ derived from the time resolved data in panel b. (d) Time resolved spectrum of the NPLs dispersion series recorded at 550 nm under pulsed excitation at 450 nm (pulse width 150 fs, repetition rate 76 MHz). (e) Transient absorption (TA) spectrum in the nanoseconds time scale of a NPLs and decorated NPLs (NPL*, Σ = 24 nm^{-2}) under pulsed excitation at 510 nm (repetition rate 200 Hz). (f) Time resolved TA spectrum recorded at 550 nm. (g) TA spectrum in the milliseconds time scale. (h) Time resolved TA spectrum at 430 nm. The solid line is the fit of data with a single exponential decay function with characteristic lifetime t= 0.9 ms.

We did not detect substantial differences in the wavelength-resolved spectrum, which is dominated by the NPL band edge photoluminescence at 550 nm. Conversely, the time resolved spectrum at this wavelength reported in Figure 3.2f again shows an acceleration of emission lifetime, in agreement with the dynamics observed in the photoluminescence experiments previously discussed. On the other hand, the decorated nanostructures show an absorption peak at

430 nm in the milliseconds time range (Figure 3.2g), absent in the pristine NPLs, which corresponds to the energy of the T_1-T_n transition in the 9-ACA ligand.[179] Moreover, the time resolved spectrum at 430 nm in Figure 3.2h indicates an excited state lifetime of about 1 ms, in good agreement with the lifetime of the 9-ACA triplet state T_1.[54] These findings unambiguously demonstrate efficient ET[1] from the NPL exciton to 9-ACA ligand triplets pivotal for the sTTA upconversion process.

Parallel to the exciton lifetime acceleration, the experiments also show a progressive reduction of I_0 at high Σ. This suggests the occurrence of ultrafast processes that reduce the fraction of active NPLs for UC. As discussed above, the addition to small amount of 9-ACA allow a substantial recovery of the I_0 loss due to the solvent change. This suggests 9-ACA can passivate the trap sites where fatty acids were removed. However, the PL recovery is not complete. We ascribe this fact to two factors. First, the steric hindrance of 9-ACA is significantly larger than of the native ligands. Surface passivation is effective with high density native fatty acids, but the same passivation is not possible with 9-ACA because of its larger size despite their low K_d Thus, the ligand exchange introduced defects and the time zero loss with $\Sigma = 0.5$ nm^{-2} can be quantified as $\eta = {I_\Sigma}/{I_0} = 0.5$, where I_Σ is the zero-time intensity at the given Σ and I_0 is the value in pristine NPLs. This loss cannot be ascribed to the charge transfer to ligands, since ultrafast time resolved measurements reported in Figure 3.2d, do not show any significant quenching in the hundreds of ps time scale. Electron transfer to ligands can also be excluded given the ligand-induced energy level shift reported by Zhou et al.[172] that disables hole transfer from NPLs to attached 9-ACAs. Further increase of 9-ACA induces an additional zero-time loss bringing η down to 0.03 at $\Sigma = 24$ nm^{-2} (Figure 3.2c). Time resolved measurements suggest the appearance of an additional exciton quenching process, with increasing efficiency at larger Σ, characterized by a rate constant in the order of tens of picoseconds.

In order to shed light on the ligand exchange dynamics and on this unexpected quenching at ultrashort times, we performed a series of absorption measurements on decorated NPLs. Figure 3.3a shows the calculated average intermolecular distance R between attached 9-ACA molecules on the NPLs surface estimated by assuming a homogeneous distribution. The calculation shows

that for $\Sigma < 3$ nm^{-2}, R takes values much larger than the typical $\pi-\pi$ stacking intermolecular distance between two anthracene moieties of 3.5 Å.[180] Thus, for $\Sigma > 3$ nm^{-2}, we should expect the appearance of the interaction between close packed anthracene cores of the ligands. However, the absorption data in Figure 3.3b suggest a completely different scenario. The 9-ACA absorption spectrum in the solvent mixture is reported for reference.
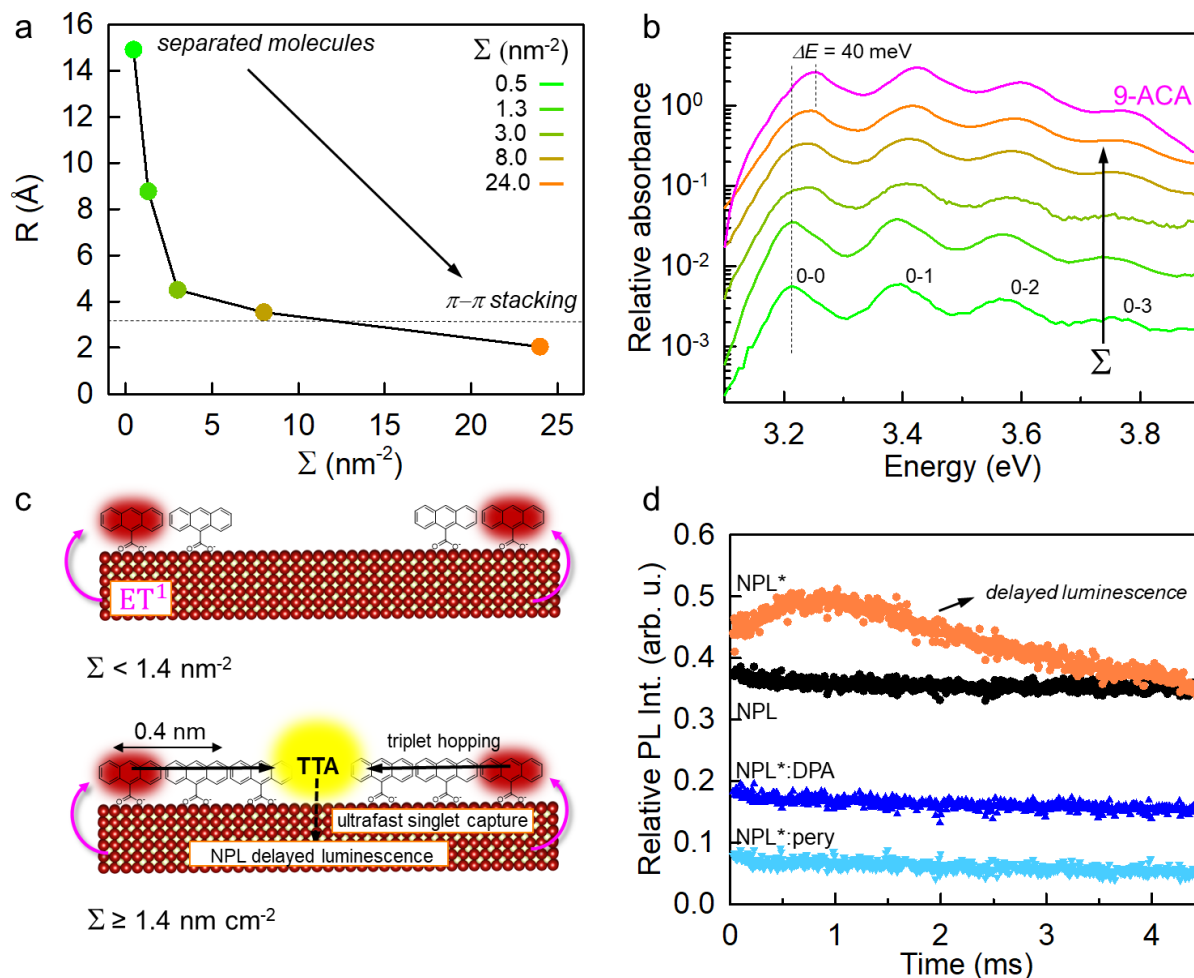
Figure 3.3. (a) Intermolecular distance R between ligands attached on the CdSe nanoplatelet (NPL) as function of the nominal surface density Σ of ligands. The dotted horizontal line indicated the distance $R = 3.5$ Å at which the $\pi-\pi$ stacking interaction is effective between two 9-ACA conjugated ligand molecules. (b) Absorption spectrum of the 9-ACA ligand in 80:70:15 hexane:toluene:THF (10^{-6} M) and of the decorated NPLs dispersions as a function of Σ. The dotted vertical lines mark the energy of the 0-0 vibronic transition at lowest coverage level

($\Sigma = 0.45$ nm^{-2}) and in the ligand isolated molecule. (c) Sketch of the decorated NPLs at low (top)

and high (bottom) coverage level. In the high-coverage configuration the close packed ligands

allow for diffusion of triplets generated by energy transfer (ET') enabling TTA and the production

of delayed luminescence from the NPL upon quenching of the upconverted singlets created by

TTA. (d) Time resolved photoluminescence (PL) spectrum at 550 nm of NPL, decorated NPL

($\Sigma = 24.0$ nm^{-2}) and decorated NPLs in solution with emitters DPA and perylene, respectively,

under pulsed excitation at 532 nm (200 Hz) in hexane:toluene:THF.

Each spectrum features the typical vibronic replicas series of the anthracene core, due to

the coupling of the electronic transition with C-H stretching modes. Importantly, we notice that

the absorption maxima positions in decorated NPLs with $\Sigma \leq 1.4$ nm^{-2} is red shifted with respect

to the free ligand of about 40 meV, which corresponds to reorganization energy value measured

for anthracene molecules condensation by means of $\pi-\pi$ stacking.[181] At larger Σ values, the

absorption peaks becomes broader as the result of the convolution of the spectra of both anchored

and free ligands in solutions, in agreement with the maximum coverage level achievable discussed

above. These results suggest the formation of an island of ligands, as sketched in Figure 3.3c, with

9-ACA bonded on the nanocrystal surface in an aggregated form.

The formation of the aggregated ligand islands allows us to explain the observed ET^1

dynamics. At low Σ, the 9-ACAs do not attach uniformly to NPLs but prefer to bind on regions

where other 9-ACAs are present. This results in the formation of 9-ACA islands on the surface of

NPLs and can be rationalized by the gain in free energy from $\pi-\pi$ interactions. The low ET^1 yield

and the time zero loss at low Σ (Figure 3.2c.) further supports this because ACA aggregates will

not extract localized NPL excitons[48] as efficiently as uniformly distributed ACA. At higher Σ, the

average ET^1 rate and yield measured on the nanocrystal ensemble increase because NPLs are

effectively covered by more aggregated 9-ACAs that at some point should form a layer of stacked

molecules (Figure 3.3c).

Time resolved photoluminescence experiments supports our hypothesis of dense ACA

coverage on NPL surfaces. The intermolecular distances between stacked anthracenes are small

enough to allow the diffusion of the ligand triplet exciton on the NPLs surface within the 9-ACA ensemble. Therefore, if two triplet excitons are sensitized simultaneously on the same nanocrystals, they can experience TTA and generate an upconverted high energy singlet state. In this case, the singlet is promptly quenched by the NPLs through fast Förster resonance ET because of their extreme proximity and of the complete resonance between the energy of the ligand's singlet and the NPL absorption. In such a scenario, the NPL can show delayed (~ms) fluorescence emission by TTA, which is kinetically ruled by the triplet diffusion by hopping within the ligand of the NPLs. As hinted by the TA experiments in Figure 3.2g, the presence of a delayed fluorescence form NPLs is confirmed by the data shown in Figure 3.3d, which reports a slow emission at 550 nm from decorated NPLs in dispersion. The slow build-up of the emission intensity and its slow recombination dynamics in millisecond time range suggest a slow diffusion of long living triplets within the layer of stacked ligands, enabling *in situ* TTA on a single nanocrystal. Though it may be possible that the TTA can occur between 9-ACA on different NPLs, we found the diffusion constant of NPLs to be in the order of $\sim 2\times 10^{-11}$ m^2/s[37] and the collision rate to be approximately 0.6 collisions/s for a NPL concentration of 5×10^{-8} M, which should be too slow relative to the triplet diffusion within a single NPL. We may also rule out the possibility of back transfer via thermally activated delayed PL due to the large energy gap between the NPLs and the triplet state of ACA (2.25 − 1.83 = 0.42 eV). This gap is further enhanced by the aggregation of ACA on the surface of NPLs, which further disfavors this back transfer pathway.

Conversely, no emission is detected in native NPLs and, remarkably, no emission can be detected after adding annihilators/emitters to the solution. The presence of annihilators deplete the ligand triplet population by ET[2]. This result demonstrate that the delayed fluorescence is directly related to the presence of unquenched ligand triplets on the NPLs surfaces. This finding suggests the possibility to drive and control bi-molecular interactions directly on the light harvester surface, thus allowing the possibility of an artificial photochemical nano-reactor. On the other hand, the clear presence of aggregates close to the NPLs surface can also results in the creation of additional quenching dark states, which can be responsible of the additional observed ultrafast losses. Further experiments are ongoing in this direction in order to point out the global effect of the ligand's interactions on the NPLs excited states properties.

To observe the consequence from the redshift of triplet electronic energy of ACA on ET^2, we measured the performance of decorated NPLs as sensitizers for sTTA upconversion in solution with two emitters, namely the DPA and perylene. Specifically, ET^2 should be slightly exothermic in order to avoid back transfer of triplets. Considering the energy of DPA triplet (1.77 eV) and the red shift from 1.83 eV to 1.80 eV of the surface-bound 9-ACA, the energy difference between aggregated ACA and DPA is only 30 meV. This means that at room temperature, ligand and annihilators triplets are nearly isoenergetic. Therefore, ET^2 to DPA may be disfavored from the lack of a forward driving force.[44] On the other hand, triplet energy difference is 170 meV in the case of perylene, large enough to prevent any back-transfer upon collision between excited perylenes and decorated NPLs. (Figure 3.4a)

Plotting the UC PL intensity vs. excitation power density reveals lower threshold intensity for perylene annihilators compared to DPA. This observation agrees with our hypothesis, since if DPA triplets are being back transferred to the ACA, a higher excitation density would be needed to generate a high enough population of DPA triplets. Meanwhile for perylene, back transfer is thermodynamically difficult, therefore it would be easier to excite enough perylene for them to start TTA. We note that this loss mechanism is unique to NPLs since the energy shift of aggregated ACA is a result of the facile aggregation of ACA on a flat surface. This example truly highlights the impact surface chemistry can have on the sTTA-UC process.
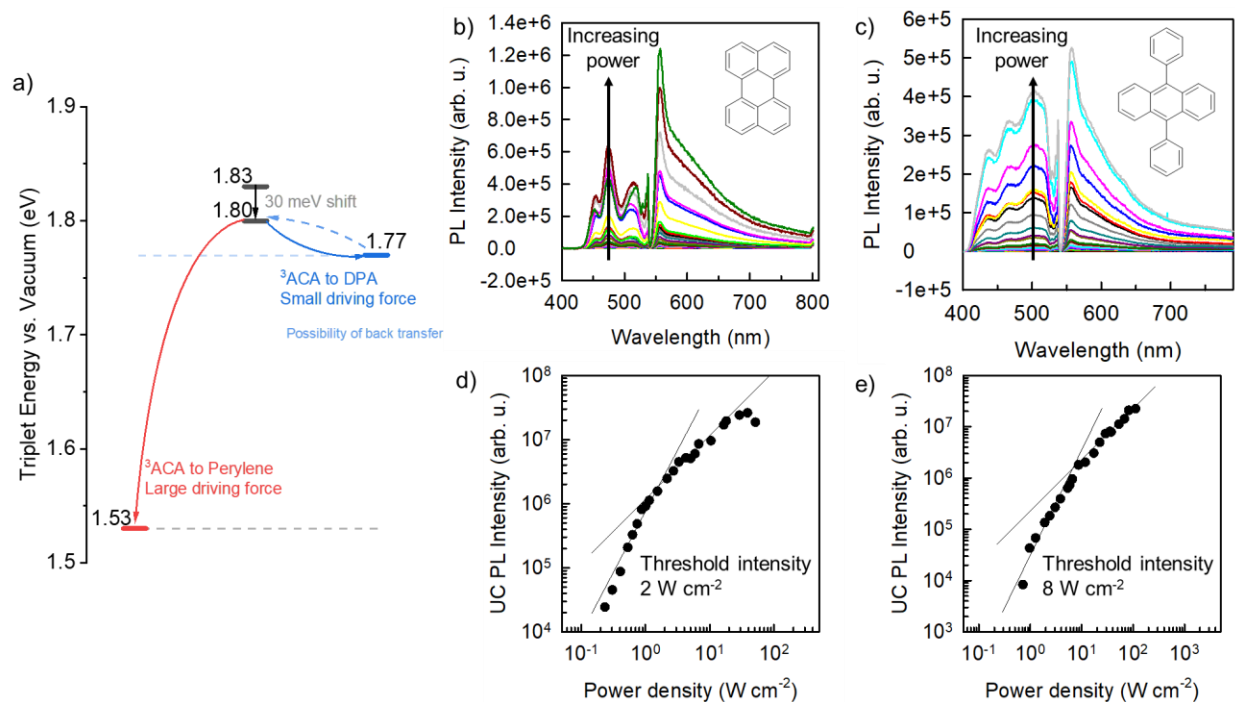
Figure 3.4. (a) Misalignment of triplet levels. (b-e) TTA-upconversion with NPLs + ACA using perylene and DPA as acceptors. Samples were excited with a 532 nm green laser. b) Power dependent PL spectra of the system with perylene acceptors. c) Power dependent PL spectra of the system with DPA acceptors. d) Upconversion PL intensity of perylene as a function of power density demonstrating the predicted quadratic to linear trend. Threshold intensity was found to be 2 W/cm^2. e) Upconversion PL intensity of DPA as a function of power density demonstrating the predicted quadratic to linear trend. Threshold intensity was found to be 8 W/cm^2. Loss of upconversion signal was observed in both cases at excitation power ~25 W/cm^2.

3.3 Conclusions

By studying the surface chemistry and binding of 9-ACA to NPLs in detail, we identified loss mechanisms in NPL sTTA-UC process. The first loss mechanism is due to the introduction of surface defects from ligand exchange. 9-ACA can partially passivate the NPL surface after ligand exchange but due to their bulk, they cannot passivate the surface as well as the native fatty acid ligands. The second and third loss mechanism stems from the aggregation of 9-ACA promoted by the flat surface of NPLs. By the energy shifts in the absorption spectrum, we showed that 9-ACA binds to the surface of the NPLs through the formation of islands rather than a homogeneous surface distribution. This has two major effects, one of which is allowing the possibility of TTA

on the surface of NPLs when the triplets are not quenched by emitters (DPA/perylene), resulting in delayed NPL luminescence. We are currently running experiments to confirm the TTA mechanism by studying the power dependence of this back transfer. The second effect is the shift of 9-ACA triplet energy level, which has a major impact when using emitters with similar triplet energies e.g. DPA, as it facilitates undesirable back transfer and increases the TTA-UC threshold efficiency. Based on our findings we believe that sTTA-UC with NPLs still has much potential to improve. Future research should focus on tuning the steric properties of surface ligands and the electronic properties of the emitter to get the optimal band alignment.

3.4 Experimental Section

Materials

1-Octadecene (technical grade 90%, O806-1L), oleic acid (technical grade 90%, 364525-1L), Cadmium acetate dihydrate ($Cd(OAc)_2(H_2O)_2$, 98%, 317131000) was purchased from Acros Organics. Selenium powder -200 mesh (Se, 99.999%, 36208) was purchased from Alfa Aesar. Hexane (95% n-hexane, analytical reagent grade, H/0355/21), toluene (analytical reagent grade ≥ 99.8%, T/2300/17) and tetrahydrofuran (THF, analytical reagent grade 99.99%, T/0701/17) was purchased from Fisher Chemical. 9-Anthracene carboxylic acid (99% A8,940-5), perylene (≥99%) and 9,10-diphenylanthracene (DPA) were purchased from Aldrich. Absolute ethanol (20821.330) was purchased from VWR chemicals.

All molecules were used as received. All samples for photophysical studies were prepared and sealed in a glove box under nitrogen atmosphere, with oxygen concentration below 0.1 ppm and water concentration below 0.5 ppm (unless otherwise stated).

Preparation of Cadmium Myristate [Cd(myristate)$_2$]

Cadmium myristate was synthesized following a modified protocol by Hendricks et al.[182] Briefly, 5.75 g CdO and 20 mL acetonitrile were combined in a 100-mL round-bottom flask and the mixture was stirred and cooled in an ice bath. Then, 0.7 mL trifluoroacetic acid and 6.2 mL of trifluoroacetic anhydride were added. After 10 min, the ice bath was removed and the flask heated at 50 °C until the solution turned white. In a 500-mL Erlenmeyer flask, 20.6 g myristic acid, 180 mL 2-propanol, and 14.0 mL of triethylamine were mixed and stirred. The cadmium

trifluoroacetate solution was then slowly added to the myristic acid solution while stirring. The resulting white precipitate was vacuum filtered through a fritted glass funnel and rinsed thoroughly with methanol. The final product was dried in a vacuum oven at 40 °C and stored under ambient conditions.

Synthesis of 5-monolayer-thick (5 ML) CdSe Nanoplatelets (NPLs)

Our CdSe NPL synthesis was slightly modified from a protocol by Tessier *et al.*[75] Briefly, 170 mg Cd(myristate)$_2$, 12 mg Se powder, and 15 mL ODE were added to a 100-mL round-bottom flask and degassed under vacuum for 30 min. Then, the mixture was heated up to 240 °C under N$_2$. At 200 °C, 80 mg Cd(acetate)$_2$ dihydrate was added. The mixture was kept at 240 °C for 8 min. Afterwards, the reaction flask was cooled using an air gun to 150 °C. During this cooling step, 0.5 mL OA was added when the temperature reached 180 °C. Once at 150 °C, the flask was placed in a water bath and cooled to room temperature (RT), and then 5 mL hexane was added. The mixture was centrifuged at 7500 rpm (5849 g) at 25 °C for 10 min. The precipitate was re-dispersed in 5 mL hexane and centrifuged at 7000 rpm (5095 g) for 8 min. Unwanted 3-monolayer-thick NPLs were removed as the precipitate. The 5-monolayer thick NPLs in the supernatant were then stored in the dark under ambient conditions until needed.

Transmission Electron Microscope (TEM)

Samples were prepared by dropcasting a hexane dispersion of the NPLs onto a carbon coated copper TEM grid. The grid sat on filter paper during the dropcasting to assist the drying of solvent. TEM imaging was done using JEOL1400 TEM with an acceleration voltage of 120 kV.

Centrifugation

Centrifugation was done using a Sigma spin control 3-30k centrifuge. Centrifugations were done with the 19776 rotor (6 x 50 mL tubes, fixed angle).

Preparation of Samples for Photophysical Studies and ITC

To maximize the dispersibility/solubility of NPLs, ACA and perylene/DPA, the sample was dissolved in a solvent mixture of hexane, THF and toluene (ratio 80:15:70). For the upconversion experiments, stock solutions of each component were prepared in a glove box (NPLs in hexane,

ACA in THF and perylene/DPA in toluene) and the three components were mixed to the desired ratio right before each measurement. Samples were loaded into cuvettes and sealed with glue and parafilm to prevent oxygen from entering. For the titration experiments (fluorescence lifetime and ITC), each component was dispersed in the mixed solvent before mixing to avoid changing the ratio of the solvent mixture during the titration process.

UV-Vis Absorption Measurements

To measure the absorption spectra we used either an Agilent Cary 60 Spectrophotometer or Avantes spectrophotometer, consisting of Avantes AvaLight-DH-S-BAL as the UV-Vis light source passing through a neutral density filter (optical density = 2.0) and fiber-coupled to an Avantes SensLine AvaSpec-HSC-TEC detector.

Quantum Yield Measurement

Quantum yield measurements were made relative to reference dyes[133] and conducted in open air. Rhodamine 6G was dissolved in absolute ethanol. CdSe core only NPLs were diluted in hexane until the absorbance approaches a value of 0.1 at the wavelength of 370 nm. The photoluminescence of the samples was recorded at that concentration using blue LED excitation at 369 nm (full-width half maximum, FWHM ~ 10 nm). Further dilution of the samples allowed us to obtain a linear fit between the sample absorption and the integrated photoluminescence, which was compared to the Rhodamine 6G standard linear fit to obtain the quantum yield of the samples.

Upconversion Study and Power Dependence

For the steady-state continuous wave (CW) photoluminescence (PL) measurements, a Coherent Verdi CW laser at 532 nm was used as excitation source, coupled with a portable spectrometer (USB2000+VIS-NIR, Ocean Optics) with bandpass of 1 nm for signal detection. The excitation laser beam is Gaussian shaped, with a spot diameter of 194 μm. Shape and spot size were measured following the knife-edge method.

Time Resolved PL Measurement

The time-resolved PL measurements were carried out using the 532 nm II harmonic of a Nd:YAG pulsed laser (LaserExport Co. LSC-DTL-374QT, pulse width 5 ns), while the signal of up-converting sample was recorded modulating the 532 nm laser with a TTi TG5011 wavefunctions generator, with a time resolution better than 0.1 µs (5 ns pulse width). For signal detection, a Triax 190 from J-Horiba monochromator with 0.5 nm bandpass was used with a Hamamatsu R94302 photomultiplier coupled with an Ortec 9353 multichannel scaler, with a temporal resolution of 0.1 ns.

Transient absorption (TA)

Transient absorption at picosecond timescale was done with the HELIOS Ultrafast System spectrometer. Millisecond timescale measurements was done with the EOS Ultrafast System spectrometer using excitation wavelength of 510 nm, power 22 mW and repetition rate of 200 Hz.

Isothermal Titration Calorimetry (ITC)

ITC experiments were performed with a Nano ITC Low Volume from TA Instruments (Eschborn, Germany). The temperature was set to 25 °C during all measurements. The effective cell volume was 300 µL, and a stirring rate of 350 rpm was chosen for all experiments. The data of heat vs. molar ratio were analyzed with an independent binding model using NanoAnalyze software, version 3.5.0 by TA Instruments.

Table 3.1 Full thermodynamic parameters obtained from ITC

	NPLs + 9-ACA - a	NPLs + 9-ACA - b	NPLs + 9-ACA - c	Average
ΔH (kJ/mol)	200.8	184.3	215.0	200.1 $\pm$ 12.5
ΔS (J/mol·K)	779.1	722.8	830.8	778.0 $\pm$ 44.1
ΔG (Kj/mol)	-31.46	-31.16	-32.68	-37.8 $\pm$ 0.6
K_d (M)	3.07E-06	4,05E-06	1,88E-06	3E-6 $\pm$ 8E-8
K_a (M^{-1})	3.25E5	2.88E5	5.32E5	3.7E5 $\pm$ 1.0E5
n (M)	1224	1249	1234	1235 $\pm$ 10

[NPLs] = 2E-7 M

[9-ACA] = 0.002 M

Independent Binding Model

To predict the ratio of bound ligands to the unbound ligands at a given K_d and ligand/NPL ratio, we applied the following equation:

$$r = \frac{\sum_{i=1}^{n} i\binom{n}{i}(\frac{[L]}{K_d})^i}{1 + \sum_{i=1}^{n} i\binom{n}{i}(\frac{[L]}{K_d})^i} \quad (Eq\ 3.1)$$

Where r is the ratio of bound ligands/unbound ligands, [L] is the initial ligand concentration and K_d is the dissociation constant.

For the lowest 9-ACA coverage in our study (0.5 9-ACA/nm^2), there are approximately 127 9-ACA/NPL, given the average lateral size of our NPLs is 127.1 nm^2. This results in r= 113.6:1. Converting this into percentage:

$$Bound/Total\ 9-ACA = \frac{Bound\ 9-ACA}{Bound\ 9-ACA + Free\ 9-ACA} = \frac{r}{r+1} \quad (Eq\ 3.2)$$

Gives a value of 99.1% bound 9-ACA.

Chapter 4: White Light Photoredox Catalysis of Nitrobenzene to Azoxybenzene Using Semiconductor Nanoplatelets

In the previous chapter I showed how dispersed colloidal NPLs can transfer their energy to freely diffusing small molecules, causing them to be excited to their triplet states and ultimately releasing the energy as light. Here the NPLs transfer their energy in the form of electrons, allowing a chemical transformation in the form of photocatalysis. Thanks to the large absorption cross sections of the NPLs, they can be used at minute mol% loadings, which makes them highly cost effective photocatalysts as they also absent of expensive metals. This chapter is based on an unpublished paper draft.

My contributions to the project were: Synthesis, purification and characterization of 3, 4, 5 monolayer nanoplatelets. Synthesis of bis(stearoyl)selenide was done by Angelika Manhart. Synthesis of cadmium myristate was done by Paul Kolpakov. Cyclic voltammetry measurements, photocatalysis experiments and conversion product quantification were done by Niklas Huber.

4.1 Introduction

White light photocatalysis is challenging due to the narrow spectrum and low absorption of organometallic and organic molecular photocatalysts. This means high catalyst loadings are necessary to absorb enough light, which is uneconomical since organometallic catalysts use precious metals, while organic photocatalysts can be difficult to synthesize and are typically less photostable. Cadmium chalcogenide nanoplatelets (NPLs) can be easily synthesized without any precious metals, are highly photostable, possess broad absorption spectra and extremely high absorption cross sections.[6, 7] Thanks to these properties, they have found applications in photocatalysis fields for example H_2 generation.[183] Here we demonstrate the potential of CdSe NPLs as photocatalysts by the transformation of nitrobenzene to azoxybenzene using NPLs of different monolayer (ML) thicknesses under white LED excitation.

By varying the NPL thickness, we modify the bandgap of the NPL to be 2.68/2.43/2.25 eV for 3/4/5 ML NPLs. Interestingly, this has a minor effect on the conduction band of the NPLs and changes only the valence band. Thus, the catalysis proceeds at low catalyst loadings (70 µmol%)

for all 3/4/5 ML NPLs, without over-reduction of the nitrobenzene to aniline. 5ML NPLs results in the highest conversion after 24 h, which we attribute mainly to the broader absorption spectrum and the higher photoluminescence quantum yields, effectively absorbing and using more of the while light. After the reaction, the NPLs can be easily separated from the mixture by simple centrifugation or by trapping the NPLs inside a dialysis tube. We also demonstrate the scalability of the reaction by conducting the photocatalysis in gram-scale. Our work clearly shows the potential of NPLs as a new class of cost effective photoredox catalyst.
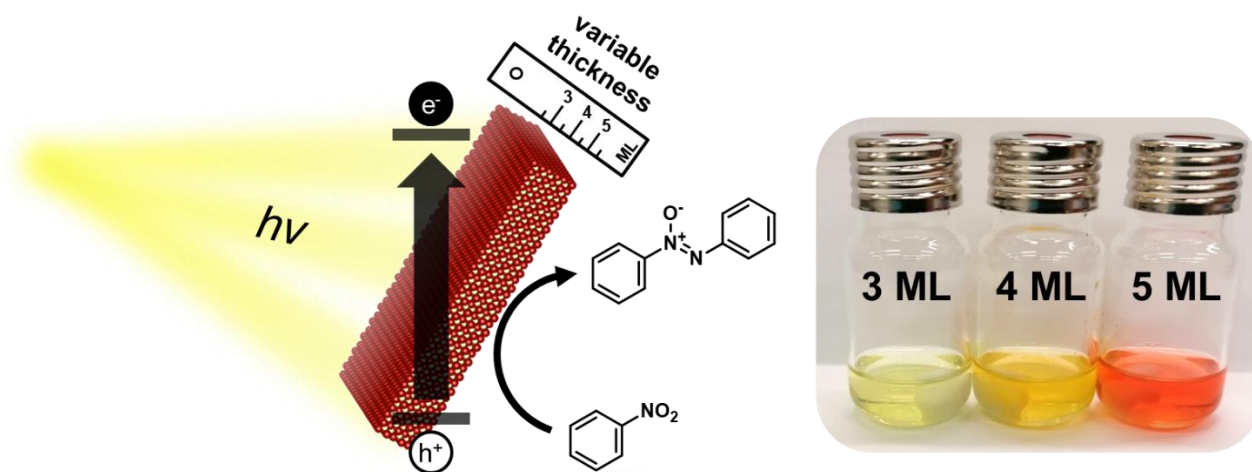
Figure 4.1. Schematic of the reaction and photographs of the NPL samples at equal molar concentration.

4.2 Results and Discussion

To prepare NPLs suitable for photocatalysis, we synthesized 3, 4, 5 ML NPLs using cadmium myristate precursors. This yielded NPLs dispersed in hexane, stabilized with myristate-passivated surfaces. To ensure that the excited state of the NPLs live long enough for reaction, we measured the time resolved photoluminescence (PL) of the NPLs (refer to Experimental Section Figure 4.7 for details). By fitting the decay curves with a double exponential fitting, we determined the effective lifetime of the NPLs to be in a range between 5.3 to 7.1 ns (Experimental Section Table 4.2). There are no major differences between the different ML thicknesses, suggesting that the recombination rate of the electrons and holes in the NPLs are also similar.
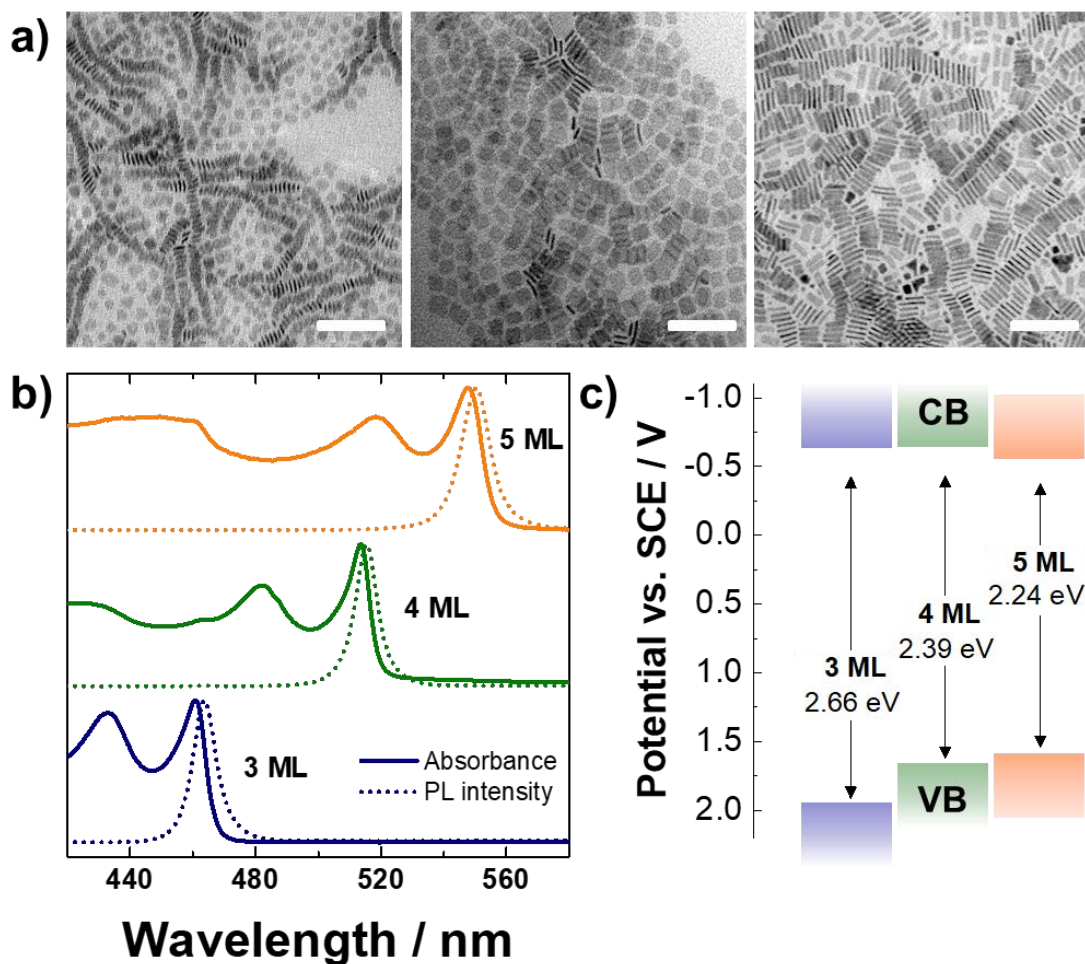
Figure 4.2. Properties of the CdSe NPLs with different monolayer (ML) thickness. TEM images of a) 3ML (left), 4ML (middle) and 5ML (right) NPLs. Scalebar corresponds to a length of 100 nm. NPLs are rectangular in shape with average lateral area of 130 ± 10 nm^2, 190 ± 40 nm^2, 170 ± 20 nm^2 for 3, 4 and 5 ML NPLs respectively. b) Absorption and photoluminescence (PL) spectra of the NPLs. c) valence, conduction band energies and the bandgap of NPLs with different ML thicknesses obtained by cyclic voltammetry (CV).

Due to the broader absorption range of thicker NPLs, 5ML NPLs can absorb more yellow-green light (Figure 4.2b). This gives a significant advantage when using the white LED source (Figure 4.3) since the region between 510 nm – 550 nm is a large part of the white spectrum. In addition, from TEM measurements (Figure 4.2a), the lateral areas of the NPLs are 130/190/170 nm^2 for 3/4/5 ML NPLs respectively. For the same NPL thickness, the lateral area of the NPLs

increase the molar absorption cross sections linearly.[6] This means that the larger 4ML and 5ML NPLs has a slight advantage in absorption cross section over the 3ML NPLs as well.
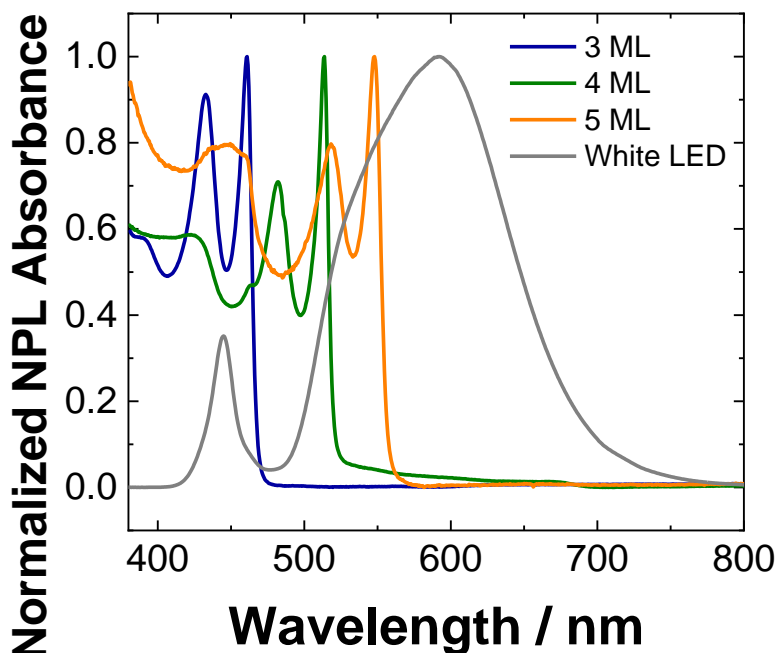
Figure 4.3. Spectrum of white LED emission used in the reactions (grey line). Colored lines show relative regions where the 3, 4, and 5 ML NPLs absorb. For relative integration areas, see experimental section Table 4.1.

To do a reduction using a photocatalyst, the energy of the conduction band must be appropriate to the substrate. We determined the energy of the valence band and the conduction band by cyclic voltammetry. Inamdar *et al.*[184] and Kucur *et al.*[185] have previously measured similar quantum dot systems using cyclic voltammetry, while Spittel *et al.*[186] showed that they could also identify the band edge positions of CdSe quantum dots and NPLs with potential-modulated absorption spectroscopy (EMAS) – albeit the complications with the bleach model for the NPLs resulting in discrepancies. By cyclic voltammetry measurements, we found that the conduction bands of the NPLs match the energy for this reaction and are very similar across different thicknesses (Figure 4.2c). Meanwhile the valence bands change through the different bandgaps, which allows us to study the effect of the bandgap to the performance of the photocatalyst. Based on our measurement, we opted for the photoreduction of nitrobenzene for our NPL system. This reaction is challenging because the nitrobenzene could easily be reduced to aniline, which is a common and low value product relative to azoxybenzene. Dai *et al.* has demonstrated this reaction

at room temperature using graphitic C_3N_4, where they were able to do selective conversion to azobenzene (~1000 Euros/kg) or azoxybenzene (2800 Euros/kg), without over-reduction to aniline (~10 Euros/kg).[187] However, their photocatalyst's absorption is restricted to mainly in the violet (410 nm) and blue (450 nm) regions, which hampers their usage in sunlight (peak emission λ_{max} ~500 nm).[188, 189] In contrast, NPLs have broad absorption spectra and they are able to absorb in green (4ML NPLs lowest-energy exciton peak = 510 nm, 5ML NPLs = 549 nm). More recently, Wang *et al.* showed that the reaction could also be catalyzed by a nanocomposite of $CQDs/ZnIn_2S_4$, which does absorb light at a broad range of wavelengths.[190] However, quantum dot absorbers do not possess as high of absorption cross section as NPLs and the requirement for a nanocomposite makes the catalyst preparation more complex.

As a result of the similar conduction band energies, all 3, 4 and 5 ML NPLs were able to catalyze the reduction. We monitored the conversion of the nitrobenzene at different time points using GC over a period of 24 h (Figure 4.4).
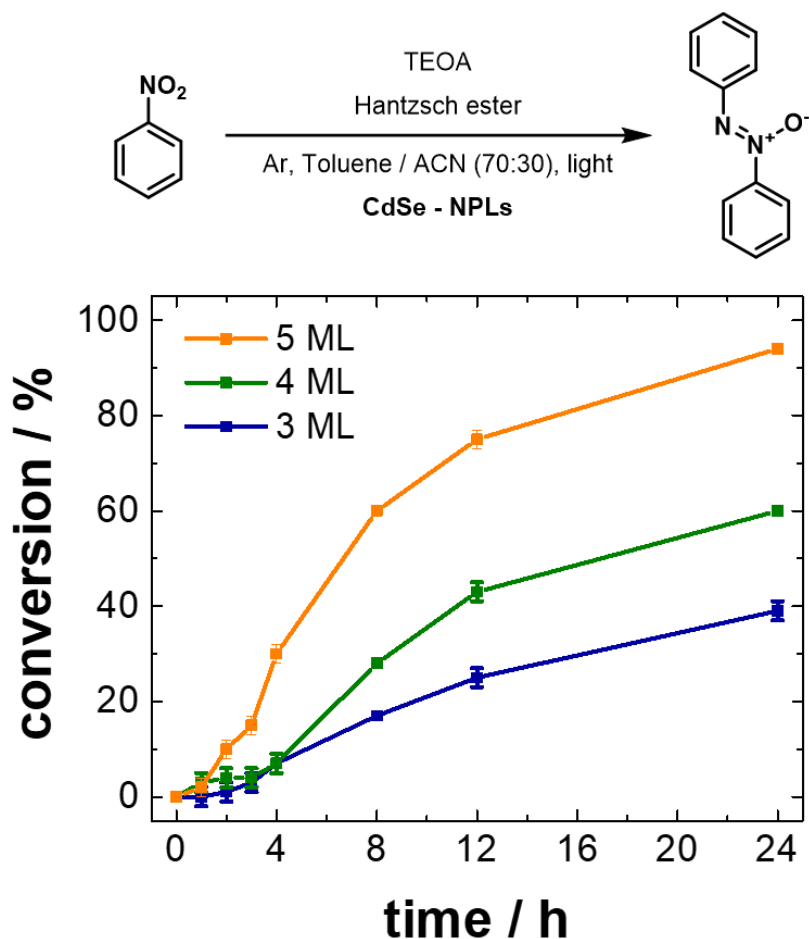
Figure 4.4. Conversion of nitrobenzene to azoxybenzene at different time points, using NPL photocatalyst of different ML thicknesses and white LED excitation.

The conversion of the nitrobenzene to azoxybenzene is higher for samples catalyzed with thicker NPLs at all time points. We attribute this to the more efficient harvesting of white light of the thicker NPLs, amplified by the higher PL quantum yields of 5ML NPLs, which allows more photoexcited NPLs to catalyze the conversion over the same period. Note that this improved conversion cannot be explained by the increased PL quantum yields alone, as the increase in conversion is greater than the difference in quantum yield (e.g. 4ML vs. 3ML = ~1.5× conversion at 24 h, but 1.3× PL quantum yield). Interestingly, we observed a time offset at the start of the reaction where no conversion occurs with a duration of approximately 2 h.

To explain this phenomenon, we looked into the mechanism of the conversion (Figure 4.5a). Azoxybenzene gradually forms through a two-step reduction reaction where nitrobenzene is

converted to azoxybenzene and then may be reduced to azobenzene depending on the reaction
conditions.[187] During the initial stage of this mechanism, it is likely that there is a buildup of the
intermediates nitrosobenzene, N-phenylhydroxylamine and azoxybenzene, before they are further
reduced to azobenzene. Unfortunately, we were not able to detect the former two intermediates in
GC, likely due to the strong affinity of them to the GC columns.
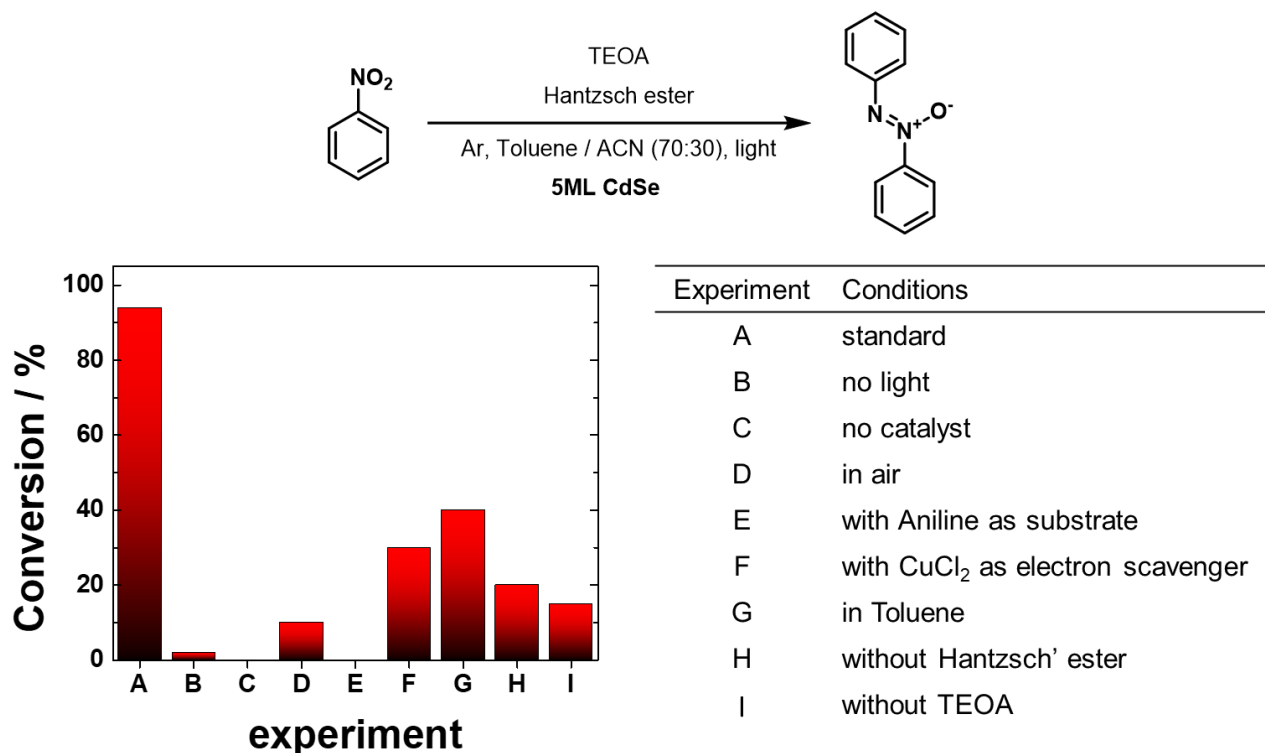
Figure 4.5. Changes in conversion related to different experimental condition.

The top scheme of Figure 4.5 shows the final optimized reaction condition using
acetonitrile toluene mixed solvent, TEOA as a base, and Hantzch ester as a hydrogen source.
Acetonitrile was necessary mix for the solvent to increase the polarity and stabilize the charge
separated state of the photoexcited NPLs. Without acetonitrile, the conversion drops from ~90%
to ~40% for a 24 h reaction, while addition of too much acetonitrile colloidally destabilizes the
NPLs and induces agglomeration. Agglomeration of NPLs reduces the free surface area of the
NPLs that are able to participate in the reaction. In addition, the excited states could be lost more
easily through homo-FRET between NPLs and quenching at defected NPL sub population.[73] We
verified the role of the NPLs by the control experiment C and showed no conversion in the absence
of NPLs. Similar to the findings of Dai *et al.*, we also observed loss of conversion in the presence

of air (control experiment D).[187] By using aniline as the substrate (control experiment E), we confirmed that the reaction does not reduce the nitrobenzene first to aniline then re-oxidize them to azoxy/azo-benzene. Lastly, we show that the conversion decreases; by using $CuCl_2$ as the electron scavenger, in the absence of Hantzch ester and TEOA, which supports the mechanism of an electron-initiated process and that our selection of reagents is optimal for the reaction conditions.

For the gram scale production of azoxybenzene, we utilized 6×10^{-8} M NPLs (80 µmol%) in a 500 mL flask (Figure 4.6). The photocatalysis proceeds, however at a lower conversion at 24 h compared to the small-scale experiments. This may be due to the lower intensity of the excitation source spread over the larger volume. We are currently finding ways to improve the yield of the product and confirming the reaction conditions suitable for the large-scale experiment.
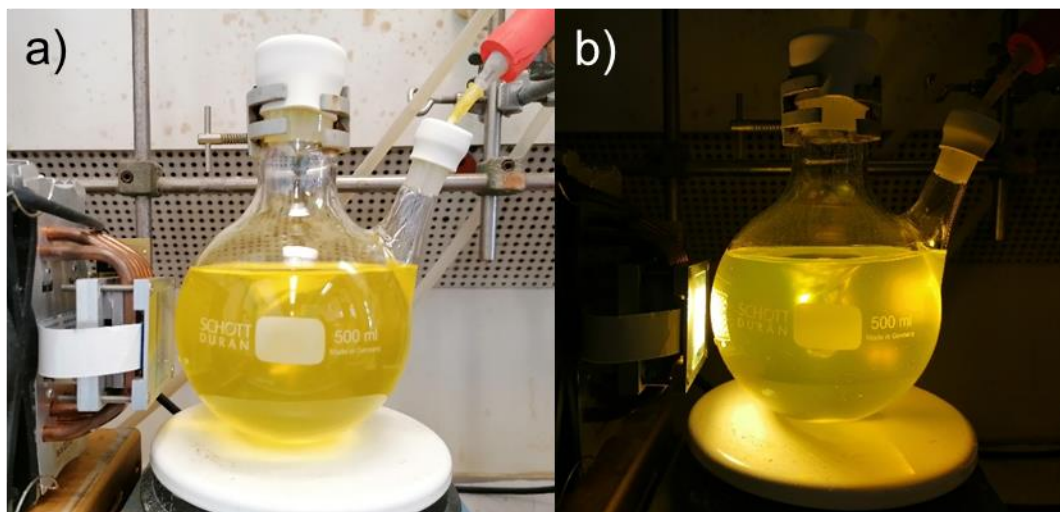
Figure 4.6. Photograph of the upscaled reaction setup. a) as mixed, b) under experimental condition.

4.3 Conclusions

We found that NPLs can photocatalyze the conversion of nitrobenzene to azoxybenzene using white light, with increasing conversion for thicker NPL MLs. This was possible due to the near-equivalent energies of the conduction band of the NPLs, despite the larger bandgaps of the thicker NPLs. The larger bandgaps enabled the 5 ML NPLs to absorb more photons, which explains their high conversion after 12 h. Our thicker NPLs also exhibited higher PL quantum

yields, which may have further helped the efficient transfer of electrons to the nitrobenzene substrates. The NPL catalysts can be used in large-scale reactions and are able to be separated easily by centrifugation. Further experiments are ongoing to improve the conversion of the large-scale reactions and to potentially recycle the precipitated photocatalyst, which should improve the viability of NPLs in future industrial applications. Investigation of functional group tolerance for the NPL photocatalysts are also under way.

4.4 Experimental Section

Chemicals. n-Hexane (95%) was purchased from Fischer scientific. Methyl acetate (99%) was purchased from Merck KGaA. 1-octadecene (ODE, 90%), cadmium acetate dihydrate (98%) were purchased from Acros organics. Selenium powder (99.999%), methanol (100%) were purchased from Alfa-Aesar. Toluene (99.8%) was purchased from VWR chemicals. Oleic acid (90%), cadmium nitrate tetrahydrate (98%), myristic acid (>98%) were purchased from Aldrich. All chemicals were used as received without further purification.

Synthesis of Cadmium myristate. Cadmium myristate was prepared from its nitrate salt using standard literature methods.[129-131] Cadmium nitrate (1.23 g) was dissolved in 10 mL of methanol. Sodium myristate (3.13 g) was dissolved in 100 mL of methanol. The solutions were stirred well separately for 10 minutes until they are clear. Then, they were mixed together and stirred for 30 minutes at room temperature. The resulting white precipitate (Cd Myristate) was filtered, rinsed three times using cold methanol and dried under vacuum overnight. The white powder was stored at room temperature in the dark.

Synthesis of Bis(steaoryl)selenide. Bis(stearoyl)selenide was prepared using LiAlHSeH as the selenating agent.[132] To prepare the LiAlHSeH, LiAlH$_4$ (0.76 g, 20 mmol) was added to a suspension of Se powder (1.92 g, 24 mmol) in 200 mL THF at -10 °C under argon atmosphere. The mixture was stirred for 30 min. The LiAlHSeH was formed *in situ* as a grayish dispersion. 80 mmol (27.2 mL) of stearoyl chloride was slowly added to the dispersion of 20 mmol LiAlHSeH. The mixture was stirred at -10 ºC under nitrogen atmosphere. After 2 h, 5 mL of deionized water was added to quench unreacted reagents. The organic reaction mixture was diluted with 300 mL of diethyl ether and washed four times with 100 mL brine. Bis(stearoyl)selenide was crystallized

at 20°C (12 h), filtered, and dried under high vacuum for 12 h. The resulting white flakes were stored in a nitrogen filled glove box.

Synthesis of 3ML NPLs.[29] In a three necked flask, 127.5 mg (0.225 mmol) of cadmium myristate and 17.3 mg (0.065 mmol) of $Cd(OAc)_2 \cdot 2\,H_2O$ were dispersed in 15 mL ODE. This mixture was heated up to 100 °C and degassed under vacuum during 15 min. Afterwards the mixture was heated up to 140 °C under argon. At this temperature, a solution of 45.8 mg (0.075 mmol) of bis(steaoryl)selenide dissolved in 1 mL of anhydrous toluene was added with a syringe. One minute later, 52 mg (0.195 mmol) $Cd(OAc)_2 \cdot 2\,H_2O$ was added. The mixture was kept heated at 140 °C with an oil bath for five days. After five days, the mixture was cooled down to room temperature. Then 0.5 mL oleic acid was added. The reaction mixture was transferred to a centrifuge tube, the volume was filled up to 15 mL with hexane and the mixture was centrifuged at 5000 rpm (2599 g) for 10 min. The supernatant of this centrifugation was diluted with 15 mL of methyl acetate to induce agglomeration of the NPLs and centrifuged again at 8000 rpm (6654 g) for 10 min. The precipitate of this centrifugation was re-dispersed in 5 mL hexane. The resulting solution was clear yellow and contained pure 3 ML NPLs.

Synthesis of 4ML and 5ML NPLs. Our CdSe NPL synthesis was slightly modified from a protocol by Tessier et al.[75] Briefly, 170 mg (0.3 mmol) Cd(myristate)$_2$, 12 mg (0.15 mmol) Se powder, and 15 mL ODE were added to a 100-mL round-bottom flask and degassed under vacuum for 30 min. Then, the mixture was heated up to 240 °C under N_2. At 200 °C, 80 mg (0.3 mmol) Cd(acetate)$_2$ dihydrate was added. The mixture was kept at 240 °C for 8 min. Afterwards, the reaction flask was cooled using an air gun to 150 °C. During this cooling step, 0.5 mL OA was added when the temperature reached 180 °C. Once at 150 °C, the flask was placed in a water bath and cooled to room temperature (RT), and then 5 mL hexane was added. The mixture was centrifuged at 7500 rpm (5849 g) at 25 °C for 10 min. The precipitate was re-dispersed in 5 mL hexane and centrifuged at 7000 rpm (5095 g) for 8 min. Unwanted 3-monolayer-thick NPLs were removed as the precipitate. The 4-monolayer or 5-monolayer thick NPLs in the supernatant were then stored in the dark under ambient conditions until needed.

Transmission Electron Microscope (TEM). Samples were prepared by drop casting a hexane dispersion of the NPLs onto a carbon coated copper TEM grid. The grid sat on filter paper during the drop casting to assist the drying of solvent. TEM imaging was done using JEOL1400 TEM with an acceleration voltage of 120 kV.

Estimation of Cd atoms/NPL. Average sizes of NPLs were determined from the TEM images using ImageJ. The NPLs were modelled using VESTA, accounting for the zinc blende crystal structure and the lattice parameters. The total number of atoms in a NPL was obtained from the model and the number of Cd was calculated by: Total number of atoms × (Monolayer of Cd / Total number of monolayers). Cd atoms/NPL = 2950, 5470, 5750 Cd/NPL for 3, 4, 5ML NPLs respectively.

Steady state absorption spectroscopy. The absorption spectra were measured using an Agilent Cary 60 Spectrophotometer or Avantes spectrophotometer, consisting of Avantes AvaLight-DH-S-BAL as the UV-Vis light source passing through a neutral density filter (optical density = 2.0) and fiber-coupled to an Avantes SensLine AvaSpec-HSC-TEC detector.

Steady state photoluminescence (PL) spectroscopy. Photoluminescence spectra were recorded using an Avantes SensLine AvaSpec-HSC-TEC spectrophotometer in 90° geometry. A Prizmatix Silver high power LED was used as the excitation source (emission peak 369 nm, FWHM ~ 10 nm). Relative PL quantum yield of the NPL samples were found to be approximately 30%, 40% and 80% for 3, 4, and 5 ML NPLs respectively.

Photocatalysis at 2 mL scale. 15 µL Nitrobenzene (0.15 mmol), 27 µL TEOA, 25 mg Hantzsch Ester, 300 µL NPLs (stock concentration 3.4E-7 M), 510 µL Acetonitrile was added to 1190 µL toluene (final catalyst concentration 5.0E-8 M = 0.00007 mol%). The mixture was bubbled with argon and then sealed and stirred under white LED exposure for 24 h. Aliquots were taken and assessed with GC.

Table 4.1. Relative integral covered from the white LED based on the absorption range of the NPLs.

Sample	Absorption range		Relative white LED integral
3ML	-	470 nm	1
4ML	-	520 nm	2.2
5ML	-	559 nm	5.8

Time-Resolved PL Spectroscopy/Time-Correlated Single-Photon Counting (TCSPC).
PL lifetime measurements were conducted with a FluoTime200 time-correlated single-photon counting setup. Samples were excited with a laser at 380 nm, which was controlled by PicoQuant PDL 800-D. The signal was detected using a microchannel plate photomultiplier tube that was connected to a PicoHarp 300 time-correlated single-photon counting system. NPL PL signals were read at 462 nm, 510 nm and 550 nm for 3ML, 4ML and 5ML NPLs respectively. The instrument response function was measured using a dispersion of silica nanoparticles (LUDOX HS-40 colloidal silica) in water. Lifetimes of the NPLs were fitted with a double exponential function.
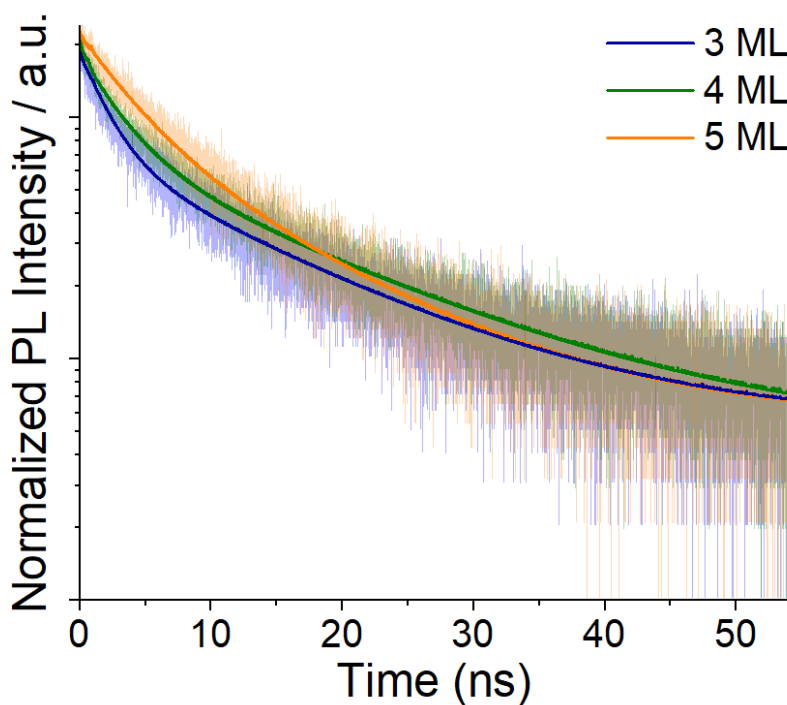
Figure 4.7. Normalized PL lifetimes of NPLs with different ML thicknesses.

Table 4.2. Lifetimes of the components obtained from double exponential fitting (Equation 4.1).

	A_1	T_1 (ns)	A_2	T_2 (ns)	Intensity Weighted $<T>$	Amplitude Weighted $<T>$
3ML	75.6	14.1	207	2.1	10.6	5.3
4ML	96.8	15.7	202	3.0	12.1	7.1
5ML	54.2	12.9	260	3.7	7.6	5.3

$$I(t) = \int_{\infty}^{t} IRF(t') \sum_{i=1}^{2} A_i e^{-\frac{t-t'}{\tau_i}} \, dt' \quad (Eq. \, 4.1)$$

Where:

IRF   Instrument response function

A_i Amplitude of the ith component, in counts

τ_i Lifetime of the ith component, in nanoseconds

Fit results gave X^2(reduced) of 1.0653, 1.0343 and 1.0570, which confirms a good fit to the data points.

Cyclic Voltammetry (CV). Cyclic voltammetry measurements were carried out on a Metrohm Autolab PGSTAT204 potentiostat/galvanostat with a three-electrode-cell system, glassy carbon electrode as the working electrode, Hg/HgCl$_2$ electrode as the reference electrode, platinum wire as the counter electrode.
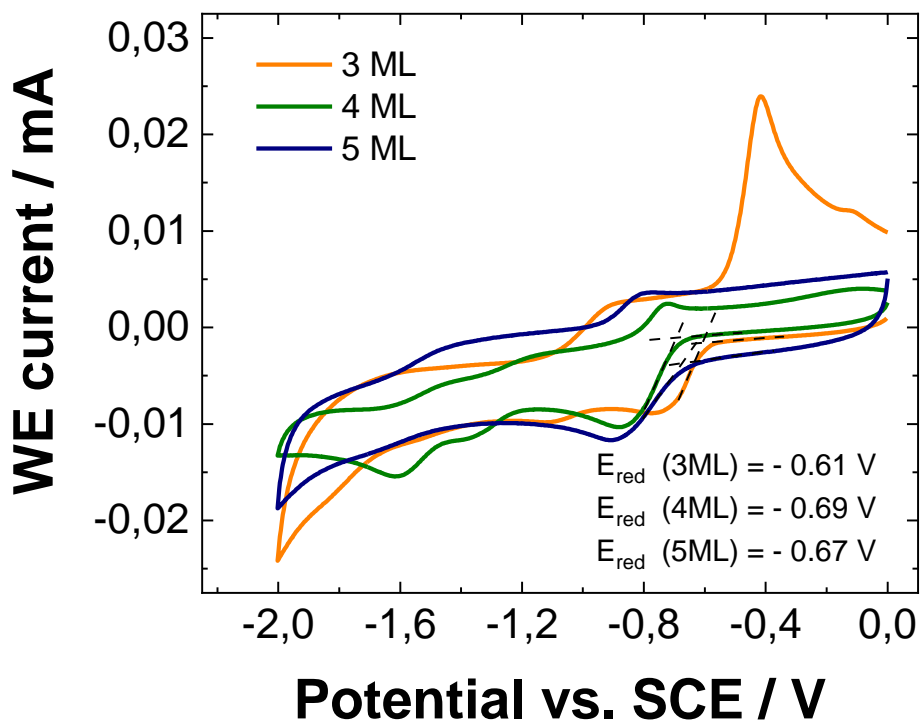
Figure 4.8. Cyclic voltammograms of NPLs with different ML thicknesses.

Chapter 5: Water-Dispersed Semiconductor Nanoplatelets with High Fluorescence Brightness, Chemical and Colloidal Stability

In the previous three chapters, I showed how NPLs are useful for energy transfer when the acceptor molecules can access the surface. Now I move on to the application for imaging, where the energy stays with the NPLs until it decays as photoluminescence.

This chapter is based on the following publication:
Water-dispersed semiconductor nanoplatelets with high fluorescence brightness, chemical and colloidal stability. Henry Halim, Johanna Simon, Ingo Lieberwirth, Volker Mailänder, Kaloian Koynov and Andreas Riedinger. *Journal of Materials Chemistry B*., 2020, 8, 146-154. Reproduced with permission under a Creative Commons Attribution 3.0 Unported Licence.

My contributions to the project were: The synthesis of CdSe NPLs, synthesis and optimization of the CdZnS shell synthesis, synthesis of the amphiphilic polymer for the coating, development and optimization of the polymer coating method, characterizations by spectroscopy and standard TEM. High resolution TEM was done by Dr. Ingo Lieberwirth, FCS was done by Dr. Kaloian Koynov. Cell experiments were done by Dr. Johanna Simon.

5.1 Introduction

Semiconductor nanocrystals are the ideal fluorescent light emitters in terms of spectral properties and long-term stability.[191-194] Quasi-two dimensional semiconductor nanoplatelets (NPLs) are the new generation of these nanocrystals, having unique physical properties compared to the traditional quasi-spherical semiconductor nanocrystals, known as quantum dots (QDs).[22, 23, 32] CdSe NPLs can by synthesized by colloidal methods so that every particle in the ensemble has exactly the same thickness of an integer number of atomic layers, while being extended in the other two dimensions.[8, 29] As a result, every NPL experiences the same level of quantum confinement (across their thickness) and the ensemble and single particle spectral properties are nearly identical.[76] The absence of inhomogeneous broadening leads to exceptionally narrow line widths.[23] In conjunction with high fluorescence quantum yield (QY)[32] and large one and two-photon absorption cross section,[7] NPLs make promising fluorescent markers in biological systems where

often more than one fluorescent label is used at the same time. Labels with high spectral brightness facilitate multiplexed imaging by reducing spectral cross-talk.

However, as with many semiconductor nanocrystals, cadmium chalcogenide NPLs are synthesized in organic solvents but biological studies are conducted in aqueous media. Whilst there are numerous literature on the phase transfer of QDs to water,[191] there exist only a limited number of examples to date of the transfer of NPLs into water.[100-102] This may relate to the specific geometry of the NPLs imposing additional challenges during the phase transfer. In particular, the higher agglomeration tendency of NPLs during coating procedures relative to QDs originates from large contact area between the flat surfaces of NPLs. This makes it challenging to transfer individual NPLs into aqueous phase without accidentally inducing agglomerative stacking of NPLs instead.[195] Even if the transfer could be done by simple ligand exchange,[196] the fluorescence properties of the NPLs still need to be considered since such a process usually damages the surface of the NPLs and quenches the fluorescence. Simple ligand exchange also leaves the surface of the NPLs exposed and accessible to chemical attacks. This makes them more prone to surface damage and subsequent loss in fluorescent brightness.

In the first example of NPL phase transfer, Lim *et al.* carefully considered the geometry of the NPLs.[100] They used a combination of phospholipids, detergents and membrane scaffold proteins that match the geometry of NPLs in order to wrap them around the NPLs. Before the transfer process, they grew a shell of CdS around the CdSe core NPLs to maintain some of the fluorescence of the NPLs through the transfer (QY 4.3% in hexane, 1.6% in water).[100] The biomolecular encapsulation material gave their NPLs specific characteristics in cellular environment, enabling e.g. rapid cellular uptake. However, this encapsulation technique relies on costly protein synthesis limiting the scalability of this method.

Following the ligand exchange approach, two developments were made to improve the properties of the final product.[102, 101] Kechkeche *et al.* used a two-step ligand exchange to first transfer the NPLs into aqueous phase using simple, small molecular ligands followed by attachment of tailor made, water soluble polymer as the final coating to disperse the NPLs in a aqueous environments of high ionic strength.[102] The advantage of this method is that the polymers

could be customized to contain useful functional groups and the transfer method is scalable. However, the requirement for a special, finely tuned polymer and being a two-step method perhaps hampers the wide use of this method in the community. Meanwhile, Shendre *et al.* focused on the retention of fluorescent properties and synthesized core/crown/shell NPLs applying only the ligand exchange method to transfer the NPLs to water.[101] Although they were able to reach very high QYs, Kechkeche *et al.* pointed out that ligand exchange with small hydrophilic thiol ligands can only stabilize the NPLs for a short term due to the oxidation of the thiol groups and the weak binding of monodentate ligands.[101]

To simplify the encapsulation and water transfer of NPLs we exploited a commonly used polymer coating strategy previously applied to a wide range of nanoparticles of isotropic geometry.[197, 97] Here, the hydrophobic side-chains of dodecyl-grafted-poly(isobutylene-*alt*-maleic acid) interacts via hydrophobic forces with the hydrophobic ligands of nanocrystals, while the anhydride units provide a large number of negatively charged carboxylate group on the outer surface after water transfer. Importantly, this one-step procedure utilizes only cheap and commercially available starting materials, making this method easy to use and also scalable. Furthermore, by generating a hydrophobic inter-layer between the nanoparticles and the hydrophilic backbone of the dodecyl-grafted-poly(isobutylene-*alt*-maleic acid) (Figure 5.1), the nanoparticles are able to withstand harsh conditions (e.g. low pH ~4.7 as found in some cellular compartments like the lysosome).[99, 198] This polymer coating has also been shown to make nanocrystals accumulate selectively in the liver sinusoidal endothelial cells, which may be useful for studies related to regulatory T-cell based therapies.[199] Thus, bringing this well established and studied polymer coating to the NPLs certainly could foster their widespread use in bioimaging. To do this, the aforementioned agglomeration challenge related to the flat, anisotropic shape of NPLs must be solved.
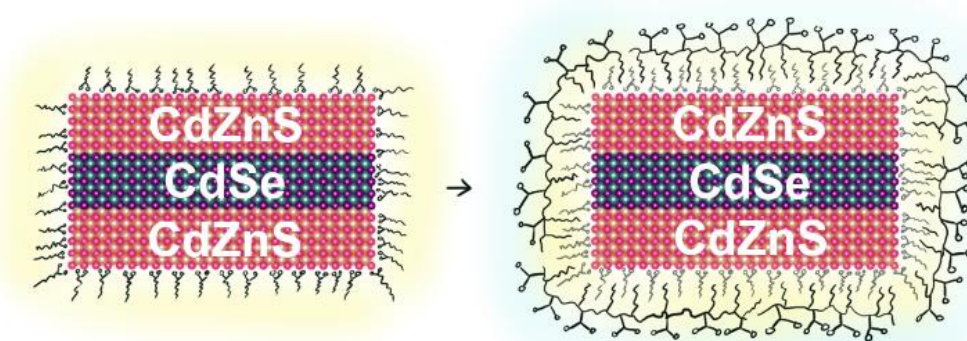
Figure 5.1 Illustration of polymer coating. Hydrophobic regions are highlighted in yellow.

5.2 Results and Discussion

Much like the existing attempts to transfer the NPLs into water, we employed core/shell NPLs for the water transfer. Applying our polymer coating method to core only CdSe NPLs resulted in degradation of the NPLs when we added the borate buffer (pH 12) to the polymer-NPLs mixture as seen by the change in absorption and PL spectra (Figure 5.2).
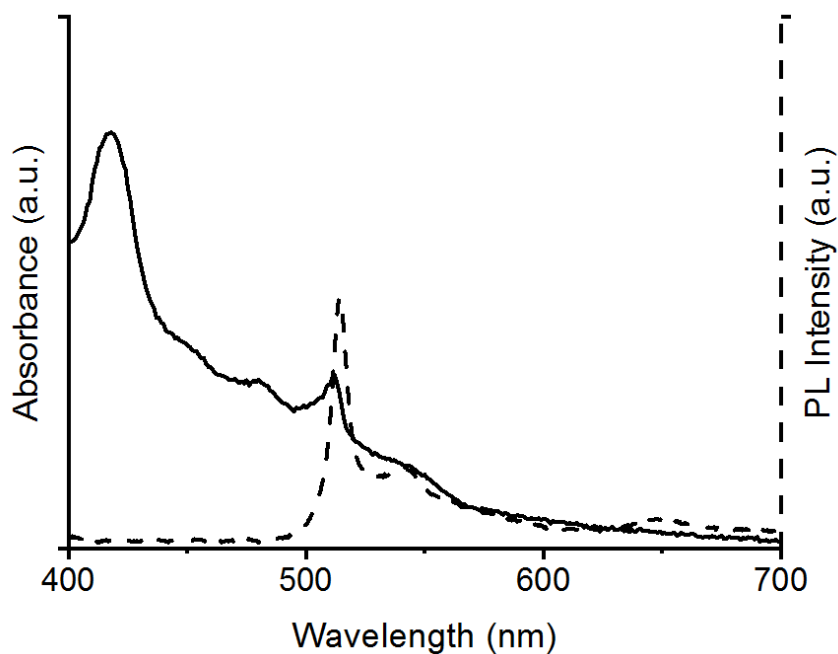
Figure 5.2. Absorption and fluorescence spectrum of water transferred 4ML core only NPLs. The broadened peaks suggest the NPLs were damaged during the water transfer.

To overcome this issue, 4 monolayer (ML, number of selenium atoms across the thickness) thin CdSe NPLs with lateral sizes of 43±8 nm ×12±2 nm and oleic acid surface ligands were coated with a graded CdZnS shell according to a procedure described by Mahler *et al.*[36] The spectral properties of the NPLs before and after shell growth are shown in Figure 5.3 together with the corresponding transmission electron microscopy (TEM) micrographs. At the end of the core/shell synthesis, the NPLs were precipitated from the reaction mixture and re-dispersed in chloroform. In some published protocols a post treatment step consisting of the addition zinc nitrate and oleic acid is applied to stabilize the properties of the NPLs.[36] The zinc nitrate improves the spectral properties of the NPLs by passivating S dangling bonds[200] while the oleic acid helps to preserve the colloidal stability.
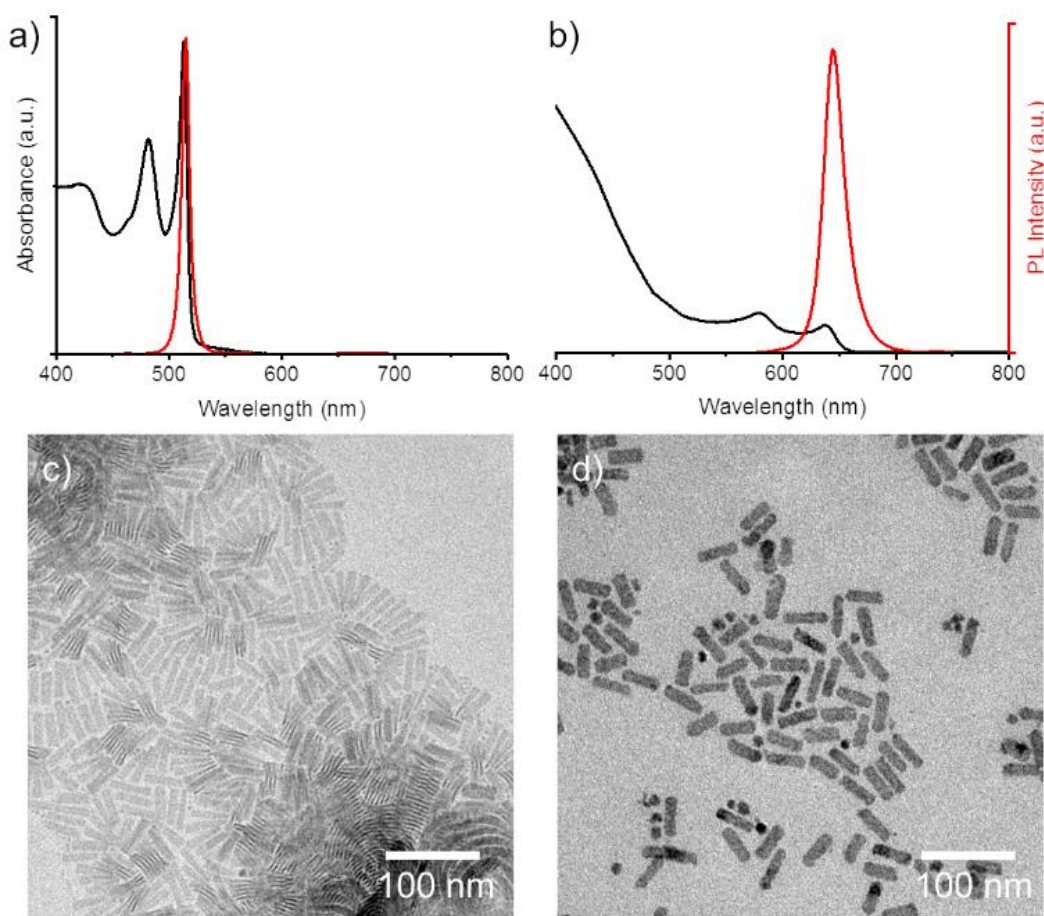
Figure 5.3. Characterization of the NPLs. (a) Absorption spectrum (black) and fluorescence spectrum (red) of 4ML CdSe NPLs in hexane. (b) Absorption spectra (black) and fluorescence spectra (red) of CdSe/CdZnS core/shell NPLs in chloroform. (c) TEM image of 4ML NPLs. (d) TEM image of core/shell NPLs.

Interestingly, we found that this post treatment step is crucial for successful phase transfer of NPLs from non-polar solvents to water. To do the phase transfer,[97] the core/shell NPLs in chloroform are mixed with a solution of amphiphilic polymer (dodecyl-grafted-poly(isobutylene-*alt*-maleic acid), with 75% of the anhydride rings opened by dodecylamine and the rest remains closed as anhydride groups). The mixture is dried with a rotatory evaporator and re-dispersed in chloroform through several cycles to ensure even coating. After the final evaporation, boric acid buffer (pH 12) is added to the dried film to open all the anhydride rings. NPL samples which did not undergo the $Zn(NO)_3$/oleic acid post-treatment do not phase transfer after polymer coating, while NPLs that received the post-treatment undergo the phase transfer. To understand this phenomenon, we conducted a test with and without the zinc nitrate and oleic acid to figure out whether the effect is due to the zinc nitrate, the oleic acid or both components (Figure 5.4).
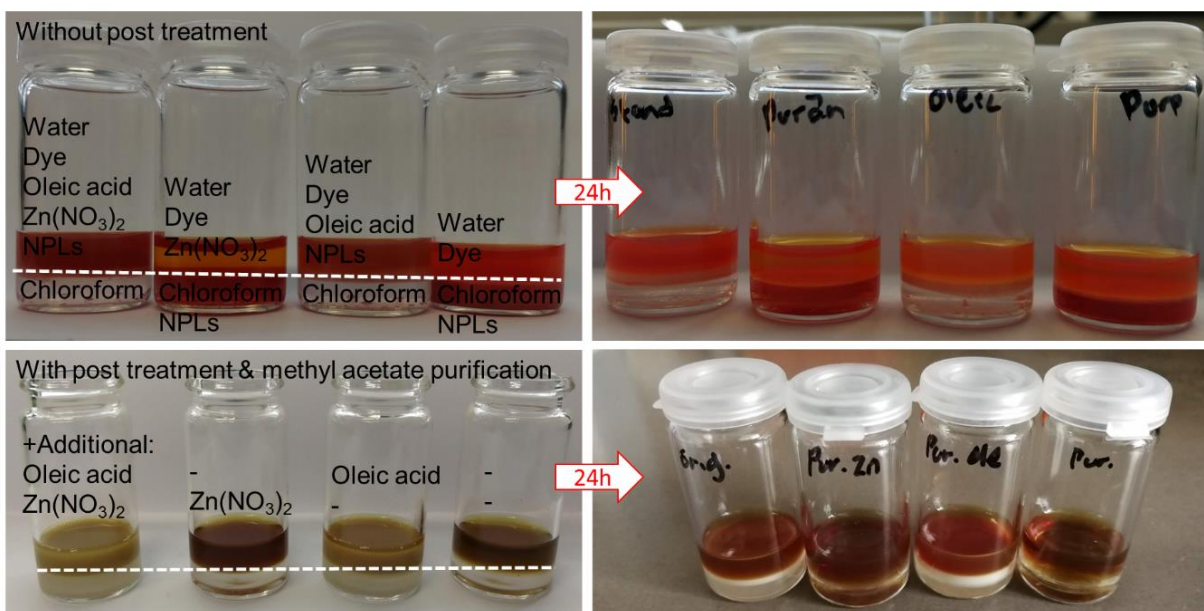
Figure 5.4. Study of the effect of oleic acid and zinc nitrate on the phase transfer of core/shell NPLs. Top photographs show the study conducted on the system without post treatment after the core/shell synthesis. Bottom photographs show the study conducted on the system with post treatment and methyl acetate purification to remove the excess oleic acid introduced in the post treatment step.

In the case without post treatment, samples without oleic acid addition shows red colour in the bottom chloroform layer. This indicates that the NPLs preferentially stays in the organic solvent instead of the aqueous solvent. The samples with oleic acid addition show a colourless chloroform layer. This indicates that the NPLs prefers to stay in the aqueous layer (dyed orange with fluoresceinamine). This effect is independent of the presence or absence of zinc nitrate.

In the post treatment, oleic acid was introduced (bottom row). The oleic acid should bind to the surface of the NPLs and exchange with the octylamine ligands introduced in the core/shell synthesis. The excess oleic acid is removed by precipitating the NPLs with methyl acetate and re-dispersing the NPLs in chloroform. To determine whether an excess of oleic acid is needed for the phase transfer, additional oleic acid was added to two of the four samples containing in the presence and in the absence of zinc nitrate. After the polymer coating and the addition of the basic buffer, all samples dispersed in water. Addition of chloroform layer is colourless which indicates that the NPLs prefer to stay in the aqueous layer.

Note the effect of excess oleic acid on the samples: with excess oleic acid the aqueous layer is cloudy while without the layer is clear. Overnight storage of the samples shows the cloudy aqueous layer become clear with the generation of a white interlayer between the two phases. The white substance is likely to be the precipitated excess polymer mixed with oleic acid micelles. The same is observed for the samples without post treatment.

The results clearly show that oleic acid plays a key role in the polymer coating step and phase transfer while zinc nitrate alone does not work. However, the effect of oleic acid at this point was ambiguous since it could have changed the system in two different ways. Firstly, free oleic acid at high concentrations could act as a solvent at low pressure during the chloroform evaporation step since it does not evaporate. Avoiding complete dryness in the system could keep the NPLs dispersed, which could prevent irreversible agglomeration. Secondly, surface-bound oleic acid could facilitate the polymer coating if it acts as a ligand that interacts better with the dodecyl side chain of the polymer coating compared to the octylamine ligands introduced in the core/shell synthesis step. To determine whether the excess oleic acid plays a role in the phase transfer, we removed the excess oleic acid by precipitating the core/shell NPLs with methyl acetate before the

polymer coating. This way, during the chloroform evaporation, the NPLs do not stay as a viscous liquid at 1 mbar pressure, but rather are embedded in a solid polymer film. It turns out that removing the excess oleic acid not only allows phase transfer (Figure 5.4) but also makes the transfer happen faster. For samples with excess oleic acid it takes a few hours to fully disperse polymer coated NPLs in water while the samples precipitated with methyl acetate acid transfers completely within a few minutes.

After dispersion in water, the samples contain polymer coated NPLs and excess polymer in the form of micelles which can be detected by either gel electrophoresis (Figure 5.5) or TEM (Figure 5.6).
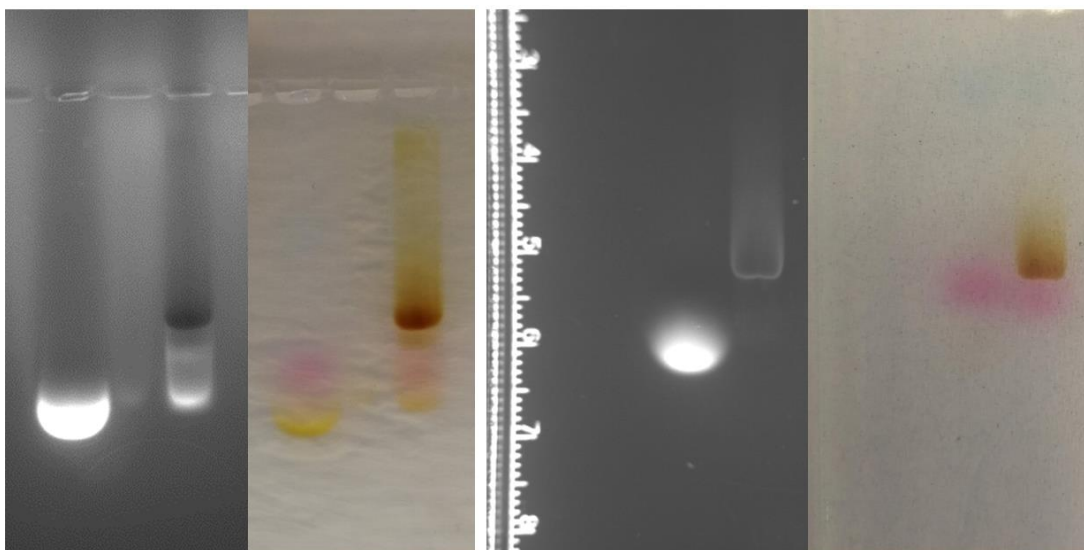
Figure 5.5. Photographs of samples after gel electrophoresis taken under UV (greyscale) and under ambient conditions (coloured). Brown spots are polymer coated NPLs. Purple spots are standard gel loading dye (purple 6x, typically used for DNA staining). Yellow spots are fluoresceinamine labelled polymer. In the left image, NPLs before sucrose gradient separation in the right lane was compared to the polymer only in the left lane. Based on the image under UV, excess polymer is present. In the right image, the same test was done with NPLs after sucrose gradient separation. Excess polymer was not observed in this case.
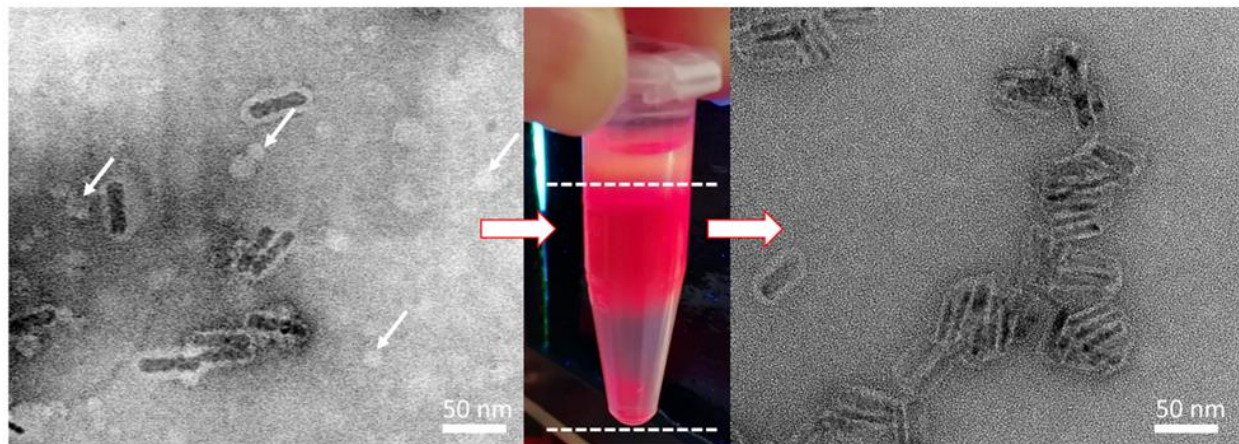
Figure 5.6. TEM images of core/shell NPLs after polymer coating and phase transfer with uranyl acetate staining. Left TEM image shows NPLs before sucrose gradient purification. White arrows indicate bright circles, which are remains of the excess polymer in the sample in the form of spherical micelles. Middle photograph shows the section of NPLs taken from the sucrose gradient separation. Right image shows sample purified with sucrose gradient centrifugation. Micelles are no longer present in this sample. Additional high resolution TEM images of the NPLs can be found in Experimental section Figure 5.17. The absence of micelles was also confirmed by polymer coating the NPLs with fluoresceinamine labelled polymer and checking the fluorescence signal in gel electrophoresis (Figure 5.5).

To remove the excess polymer, we purified the NPLs with a sucrose density gradient (Figure 5.6).[201] Here, we note that purification by gel electrophoresis may be too harsh as we observed a drastic loss in QY for NPLs purified this way. Purification of NPLs by sucrose gradient yields NPLs with negligible loss in QY (see Table 5.1).

Table 5.1. Quantum yields measured in this study. Samples in the first row are the standards used.

Sample	QY ± 10%	Sample	QY ± 10%
Rhodamine 6G (Ethanol)	94%	Sulforhodamine 101 (Ethanol)	95%
Core only NPLs (Hexane)	50%	Core/Shell NPLs (Water)	21%
Core/Shell NPLs (Hexane)	30%	QDs (Water)	65%
Core/Shell NPLs (Water)	25%		

To demonstrate the effect of the polymer coating to the chemical stability of the NPLs, we
monitored the fluorescence spectrum of the NPLs at pH 1.8 – 12.2 environments (Figure 5.7). We
observed minor changes in fluorescence intensity from the NPLs. This suggests that the polymer
coating indeed protects the NPLs from the external aqueous environment (detailed information in
Experimental section, Figure 5.15 and 5.16). For salt concentrations in physiological conditions
(< 14 g/L), no increase in scattering signals were observed which suggests the absence of
agglomerates.
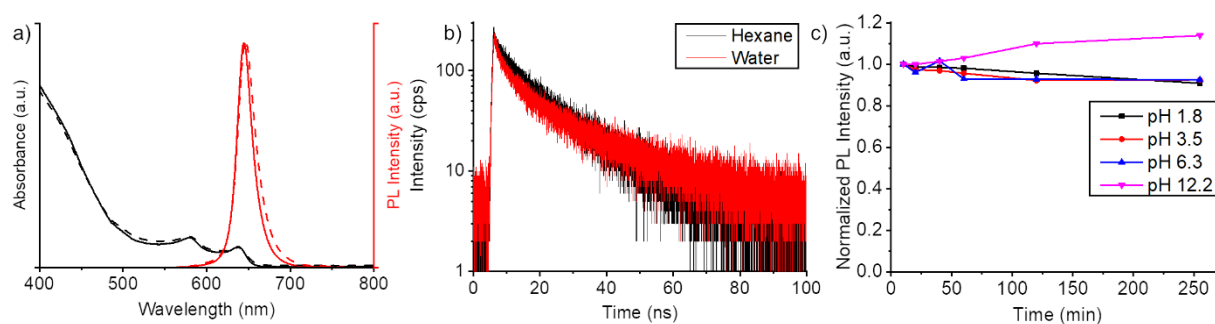
Figure 5.7 Basic properties of core/shell NPLs. a) Absorption spectra (black) and fluorescence
spectra (red) of CdSe/CdZnS core/shell NPLs in chloroform (solid line) and water (dashed line).
b) Fluorescence lifetime measurements of core/shell NPLs before phase transfer (in hexane, black
decay curve) and after phase transfer (in water, red decay curve). Double exponential fitting
(Figure 5.14) of the fluorescence decay gave lifetimes of 14.1 ns and 1.0 ns for NPLs in hexane
and 13.7 ns and 1.3 ns for NPLs in water. c) Fluorescence intensities of polymer coated NPLs in
different pH environments. pH values were adjusted by adding hydrochloric acid for the acidic
conditions and by adding sodium hydroxide for the basic conditions. The full absorption and PL
spectra of the samples are found in Figure 5.15.

Overall, we have achieved a water transfer process, which largely preserves the spectral
shape (Figure 5.7a) and the QY of the NPLs (Table 5.1). To gain further understanding of the
optical properties, we conducted fluorescence lifetime measurements of the core/shell NPLs in
hexane and polymer coated core/shell NPLs in water. From these experiments, we have found that
there are only minor changes in the fluorescence lifetime of the NPLs before and after the phase
transfer (Figure 5.7). In the double exponential fitting (Figure 5.14), we found only slight

variations in the short and long-lived components. Thus, water transfer did not introduce surface defects to a significant extent. The negligible change in lifetime also shows that the thick CdZnS shell and polymer coating efficiently shield excitons from the dielectric of the solvent.

To ensure the quality of our phase transfer and purification, we studied the properties of our water dispersed NPLs with TEM (Figure 5.6) and fluorescence correlation spectroscopy (FCS)[202] (Figure 5.8) and compared them to commercially available Quantum Dots (QDs, Thermo Fisher Qdot™ 655 ITK™ Carboxyl Quantum Dots, see Figure 5.9). From the TEM images and the FCS data, we confirmed that we transferred NPLs individually to water rather than as agglomerates. This is also reflected in the fluorescence intensity time trace (inset in Figure 5.8) that shows no spikes, which would be expected if agglomerates were present.
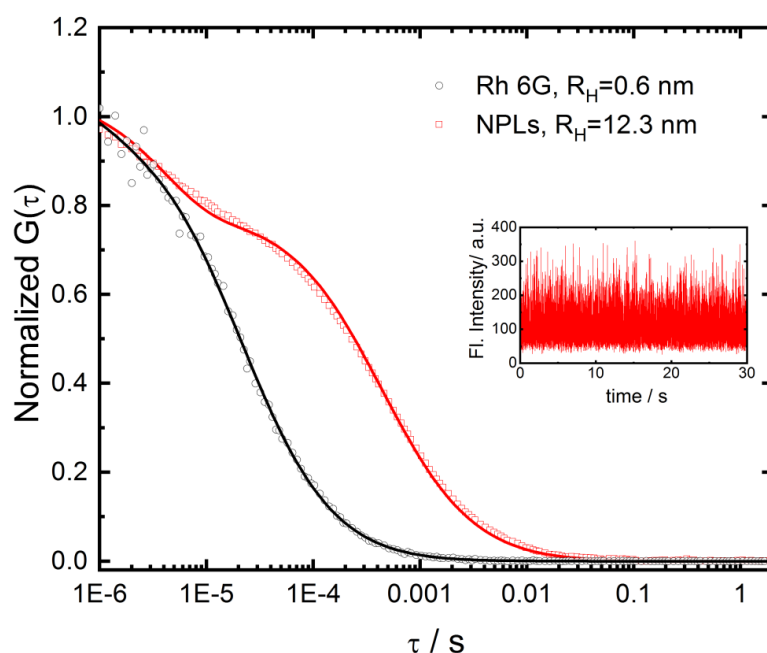
Figure 5.8. FCS data of core/shell NPLs and Rh 6G used as reference standard. Normalized experimental autocorrelation curves of the NPLs (red squares) and Rh 6G (black circles) measured upon one photon excitation at 488 nm in water. The solid lines represent the corresponding fits with equation (5.2). Inset shows the fluorescence intensity time trace of the NPLs with no spikes from agglomerates.
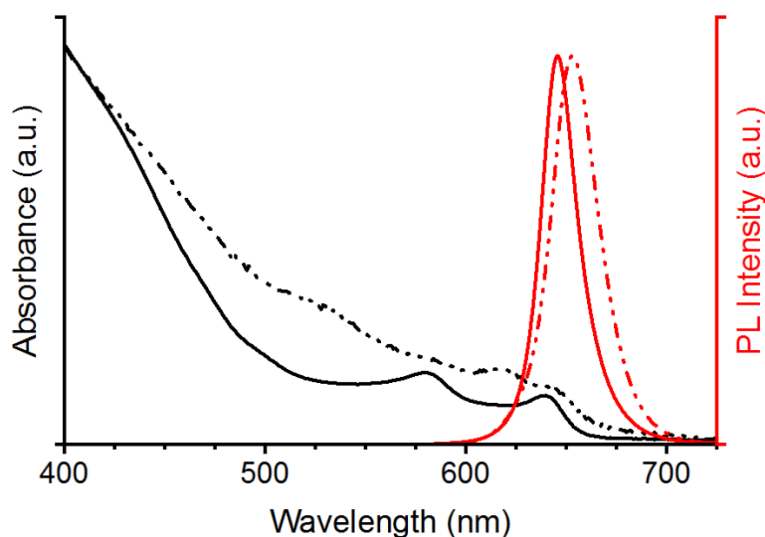
Figure 5.9. Absorption spectra (black) and fluorescence spectra (red) of CdSe/CdZnS core/shell NPLs (solid line) and commercial Qdot™ 655 ITK™ Carboxyl QDs (dotted line) in water.

To use the NPLs for bioimaging, we would need to confirm that the NPLs also do not aggregate (agglomerate) in biological medium. Thus, we also tested the behaviour of the NPLs under physiological conditions by performing FCS studies in human serum. Typical autocorrelation curve of the NPL dispersed in human serum is shown in Figure 5.10. A fit with equation (5.2) yielded a hydrodynamic radius of ≈16.5 nm after accounting for the plasma viscosity as in earlier studies.[203] This value that is only ~ 4 nm larger than the one measured in water, probably due to protein corona formation,[204] indicates that the NPLs are still well dispersed and show no aggregation in human serum. This is further confirmed by the fluorescence intensity time trace (inset in Figure 5.10) that shows no spikes caused by aggregates.
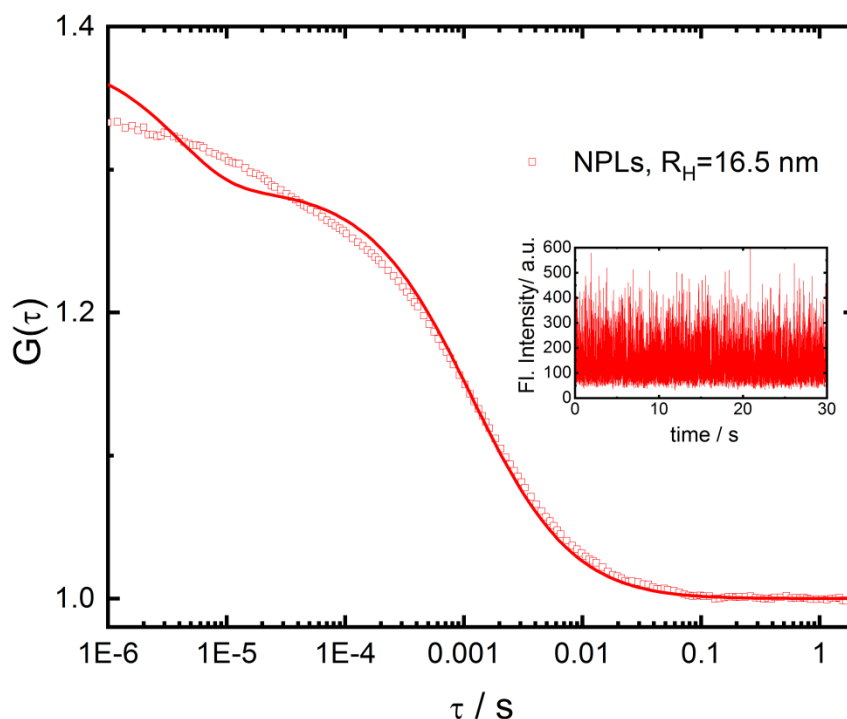
Figure 5.10. FCS data of core/shell NPLs in human serum. Experimental autocorrelation curve of the NPLs (red squares) measured upon one photon excitation at 488 nm in human serum. The solid line represents the corresponding fit with equation (5.2). The deviation at short lag times is probably caused by a more complex photo-physics (blinking behaviour) of the NPLs upon formation of protein corona that cannot be described well with the single exponent term in equation (5.2). Inset shows the fluorescence intensity time trace of the NPLs with no spikes from agglomerates.

In bioimaging experiments, a good fluorophore should be as bright as possible to increase the signal-to-noise ratio that inherently suffers from autofluorescence.[205] The fluorescence brightness of a sample is given by equation 5.1:

$$FB \propto \varepsilon \cdot \varphi \qquad \text{eq. 5.1}$$

Where FB is fluorescence brightness, ε is the molar extinction coefficient and φ is the quantum yield. Given the very high absorption cross section of NPLs,[7] the brightness of our samples should be extremely high, even at moderate quantum yields. We assessed this by comparing the FB of our NPLs to commercially available QDs in FCS (Figure 5.11).
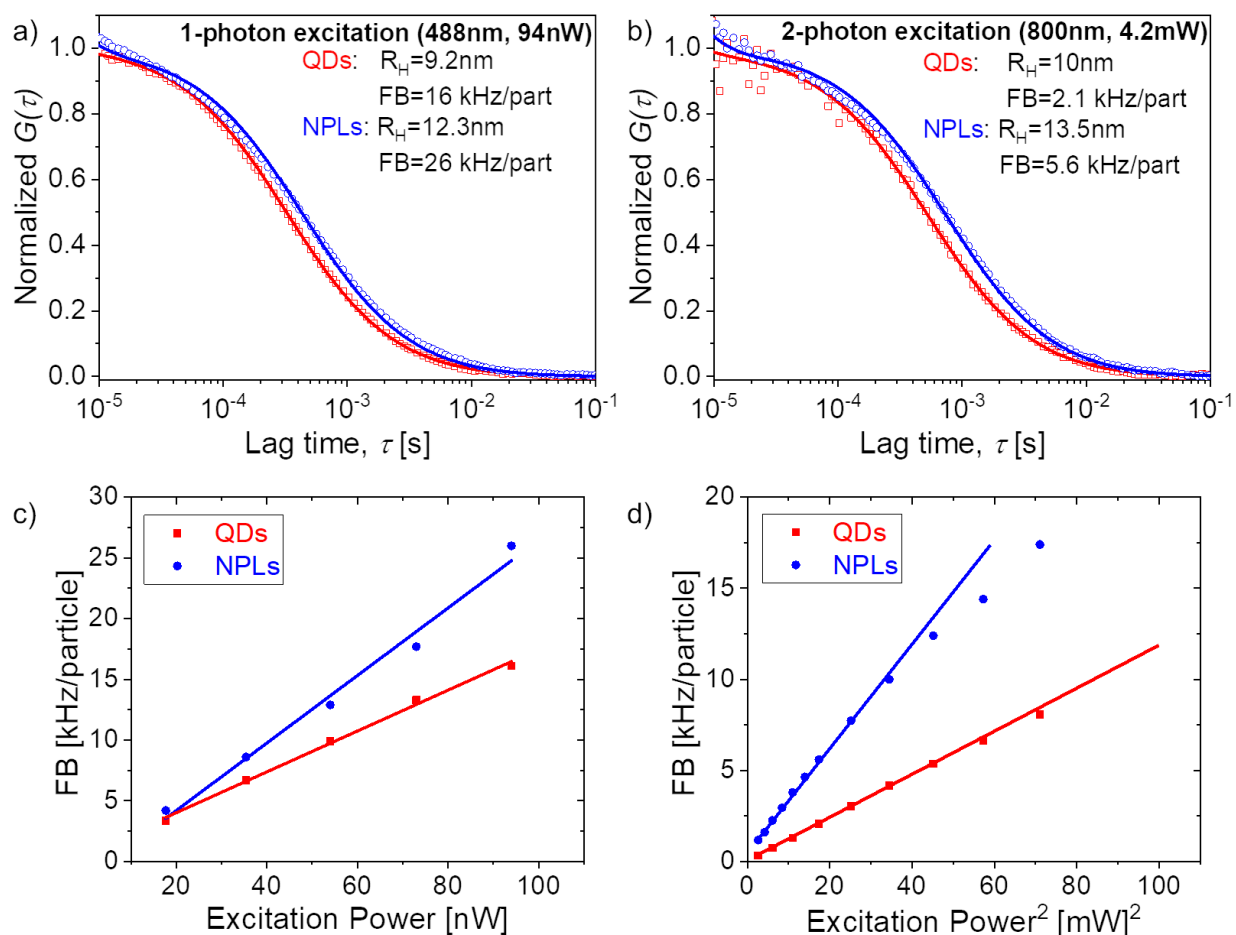
Figure 5.11. FCS studies of QDs and NPLs dispersed in water. a) Normalized experimental autocorrelation curves of the two samples (symbols) measured upon one photon excitation at 488 nm (a) and two photon excitation at 800 nm (b). The data points were fitted. The solid lines represent the corresponding fits with equation (5.2). The fluorescent brightness (FB) was 16 (QDs) and 26 kHz/particle (NPLs) with excitation at 488nm and 2.1 (QDs) and 5.6 kHz/particle (NPLs) with excitation at 800 nm. c, d) Power dependence of the FB of the QDs and NPLs at an excitation wavelength of 488 nm (c) and of 800 nm (d).

Despite the modest QYs of our core/shell NPLs (QY ~20%), we found that the core/shell NPLs exhibit around two-to-three-fold higher FB (26 vs. 16 kHz/particle for 1-photon excitation and 5.6 vs. 2.1 kHz/particle for 2-photon excitation as measured by FCS under same experimental conditions in each case) compared to the QD standards (QY ~70%). This increase in fluorescence brightness is consistent with the higher molar extinction coefficient of our NPLs

$(1.72 \times 10^7$ M^{-1}cm$^{-1})$ in comparison to the QDs $(3.00 \times 10^6$ M^{-1}cm^{-1}, see Figure 5.12). The effect is especially apparent for the two photon excitation case where the NPLs are known to have huge two photon absorption cross section.[7] We would like to note that, with more advanced shell growth methods[206] the QY of future NPL samples could be brought close to unity, which should allow for a further 3-5 fold increase of their fluorescence brightness.
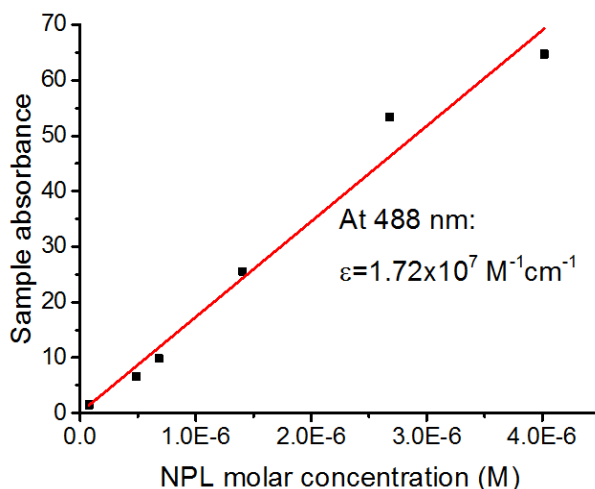
Figure 5.12. Calibration curve used to determine the molar extinction coefficient of the NPLs at 488 nm. The concentrations were calculated from ICP-OES data.

$$FB \propto \varepsilon \cdot \varphi$$

$$Estimated\ ratio\ of\ FB = \frac{\varepsilon_{NPL}}{\varepsilon_{QD}} \times \frac{\varphi_{NPL}}{\varphi_{QD}} = \frac{1.72 \times 10^7}{3.00 \times 10^6} \times \frac{0.2}{0.7} = 1.64$$

The measured ratio of fluorescence brightness obtained from FCS = 26/16 = 1.63, which agrees well with the calculation.

To investigate the performance of NPLs in bioimaging experiments, we incubated different concentration of NPLs (18-150 µg/mL) with RAW264.7 macrophages in the absence (0%) or presence of 10% FBS. Cellular uptake of NPLs into macrophages was quantitatively analysed by flow cytometry (Figure 5.13a, b) and verified by confocal laser scanning microscopy (Figure 5.13c).
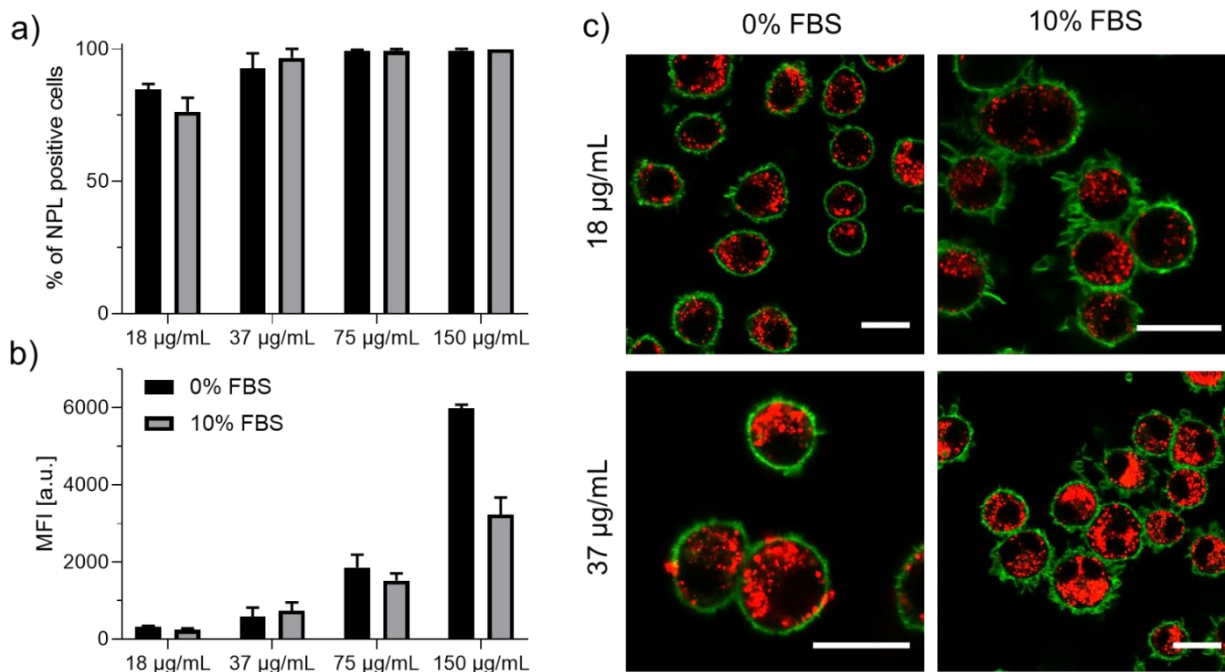
Figure 5.13. Cellular uptake of CdSe/CdZnS core/shell NPLs by RAW264.7 macrophages. Different concentrations of NPLs (18-150 µg/mL) were added to RAW264.7 cells in cell culture medium containing 0% FBS or 10% FBS for 24 h. Cellular uptake was quantified by flow cytometer and the amount of NPL positive cells in % (a) or the median fluorescence intensity (MFI) is shown (b). (c) The intracellular localization of the NPLs was confirmed by confocal laser scanning microscopy (cLSM). RAW264.7 cells were treated with NPLs for 24 h. The cell membrane was stained with CellMask Green and is pseudo-colored in green and NPLs are pseudo-colored in red. The scale bars correspond to 20 µm.

To prove that the fluorescence intensity of the NPLs is not quenched after cell uptake, NPLs were added to RAW264.7 cells for 24 h. Twenty-four hours after NPLs incubation, the NPLs were localized in phagolysosomes, which have an acidic pH between 4.5-6.5.[207, 208] Our stability experiments (see Figure 5.7, additionally Experimental section 5.15 and 5.16) suggest that the NPL photoluminescence is not quenched under these harsh conditions, due to the robust polymer coating.

With flow cytometry, we determined a concentration dependent cellular uptake of the NPLs by RAW264.7 macrophages after 24 h. Additionally, we saw that the presence of FBS in the cell

culture medium slightly reduced the cellular uptake. This effect has also been observed in literature for spherical nanoparticles and is attributed to the adsorption of serum proteins towards the NPLs surface (protein corona formation).[209, 210] Finally, with confocal laser scanning microscopy (cLSM), we could verify the intracellular localization of the NPLs in the presence or absence of serum after 24 h. Internalized NPLs had a bright, fluorescent signal, were distributed inside the cell and did not accumulate on the cell membrane. Overall, these results indicate that the NPLs are highly suitable for bio imaging.

5.3 Conclusions

In this work, we have demonstrated the phase transfer of NPLs into aqueous medium using a cheap, one-step polymer coating method. The main challenge of applying this method to NPLs was the agglomeration problems inherent to the flat platelet shape, which was overcome by the post treatment of the core/shell NPLs with oleic acid. This method not only offers practical advantages over the other existing NPL phase transfer methods[102, 100] but also application advantages in terms of a hydrophobic protection layer between the NPL and the aqueous environment. The protection layer provides high chemical stability (pH 1.8 – 12.2) and colloidal stability in high ionic strength media ([NaCl] 5.8 – 11.7 g/L) and in human serum. We have shown the NPLs retain their fluorescent properties also inside a cell, as shown in the bioimaging experiments. From these results, we believe that the combination of the superior chemical stability and colloidal stability of these NPLs in biological media along with the extremely high FB will foster the widespread use of these NPLs for all sorts of imaging applications.

5.4 Experimental Section

Materials

1-Octadecene (technical grade 90%, O806-1L), oleic acid (technical grade 90%, 364525-1L), cadmium nitrate tetrahydrate ($CdNO_3(H_2O)_4$, 98%, 642045-100G), zinc nitrate hydrate ($ZnNO_3(H_2O)$, 99.999%, 230006-25G), poly(isobutylene-alt-maleic anhydride) (85%, average Mw ~6000, 12-200 mesh, 531278-250G), Dulbecco's Phosphate Buffered Saline and sodium chloride were purchased from Aldrich. Cadmium acetate dihydrate ($Cd(OAc)_2(H_2O)_2$, 98%, 317131000) was purchased from Acros Organics. Selenium powder -200 mesh (Se, 99.999%, 36208) and 1-octylamine (99%, B24193) was purchased from Alfa Aesar. Hexane (95% n-hexane, analytical reagent grade, H/0355/21) and tetrahydrofuran (THF, analytical reagent grade 99.99%, T/0701/17) was purchased from Fisher Chemical. Chloroform, stabilized with amylene (100%, 83627.290), absolute ethanol (20821.330), and sodium hydroxide (NaOH, 1 mol/L 1N, UN1824) were purchased from VWR Chemicals. Thioacetamide (TAA, >98%, T0187) and 1-dodecylamine (>97%, D0980) was purchased from TCI. Boric acid (>99.8%, 6943.1) was purchased from Carl Roth GmbH and Qdot™ 655 ITK™ Carboxyl Quantum Dots were purchased from Thermo Fisher. Human blood serum was obtained from six healthy donors at the Transfusion Center of the University Clinic of Mainz, Germany, in accordance with the Declaration of Helsinki. For serum generation, blood was clotted overnight and centrifuged according to the standard procedure. All serum batches were pooled together and stored at -20 °C. For the serum preparation, blood is naturally coagulated so there were no additives used.

Synthesis of 4 Monolayer (4ML) Thick CdSe NPLs

The 4ML CdSe NPLs were prepared modifying the procedure published by Mahler et al.[36] Briefly, 60 mL of 1-octadecene, 320 mg (1.20 mmol) of $Cd(OAc)_2(H_2O)_2$, and 879 µL (787 mg, 2.79 mmol) of oleic acid were added into a 100 mL three-neck flask. The mixture was degassed under vacuum while stirring at 110 °C for 90 min. After stopping the vacuum and putting the flask to argon, 48 mg (0.607 mmol) of Se powder was swiftly added into the flask and the temperature was set to 240 °C. When the temperature reached 205 °C, 160 mg (0.600 mmol) of $Cd(OAc)_2(H_2O)_2$ was introduced into the reaction mixture and the reaction proceeded for 15 min at 240 °C. The mixture was then cooled to room temperature using a water bath and 6.7 mL of

oleic acid was added. The mixture was centrifuged for 10 min at 5000 rpm (2599 g), the supernatant was discarded and the precipitated NPLs were re-dispersed in 12 mL hexane.

Synthesis of $Cd_{0.33}Zn_{0.67}S$ Shell

The shell synthesis to create core/shell NPLs was done by modifying an existing procedure.[36] Briefly, 6 mL of the as-synthesized 4ML NPLs (optical density at 510 nm was 30) were added into a 50 mL round bottom flask. In a separate flask, 300 mg (3.99 mmol) of TAA, 3 mL (18.2 mmol) of octylamine and 9 mL of chloroform were combined, stirred for a few seconds and then sonicated in an ultrasound bath until the TAA dissolved. The TAA solution was added to the NPL solution while stirring. The mixture was stirred further for a couple of minutes. Then 500 µL of $CdNO_3$ solution (0.2 M in ethanol) and 1000 µL of $ZnNO_3$ solution (0.2 M in ethanol) were added into the mixture while stirring. The flask was capped and left to stir for 24 h in ambient conditions.

To stop the reaction and obtain the product, the mixture was first concentrated by evaporating some of the solvent using a rotatory evaporator at approximately 280 mbar, 40 °C for a couple of minutes. Then the concentrated mixture (volume approx. 15 mL) was centrifuged for 10 min at 8000 rpm (6654g), the supernatant was discarded, and the precipitated NPLs were suspended in 15 mL chloroform. To better stabilize the NPLs and to facilitate the polymer coating, 300 µL of $ZnNO_3$ solution (0.2M in ethanol) and 600 µL of oleic acid were added into the solution while stirring and the solution was kept at ambient conditions for a couple of days for PL recovery.

To remove the excess oleic acid introduced in this step, methyl acetate was added to the chloroform dispersion of core/shell NPLs (chloroform:methyl acetate = 1:1 v/v). The NPLs were precipitated by centrifugation and re-dispersed in chloroform.

Synthesis of Dodecyl-Grafted-Poly(isobutylene-alt-maleic acid)

The amphiphilic polymer was synthesized according to the method described elsewhere.[97] Briefly, 105.3 mg (0.662 mmol monomer units /$1.10x10^{-5}$mmol polymer) of poly(isobutylene-alt-maleic anhydride), 4.6 mg (0.013 mmol, equivalent to 2% of monomer units) of fluoresceinamine, 92.0 mg (0.497 mmol, equivalent to 75% of monomer units) of 1-dodecylamine and 25 mL of THF

were combined in a 50 mL round bottom flask containing a magnetic stir bar. Note that the fluoresceinamine is used as a label to visualize the polymer and can be left out if unnecessary. Then a reflux condenser was attached and the mixture was heated to reflux. After approximately 10 minutes, the solution turned clear and it was kept refluxing for 18 hours. Then the solution was brought back to room temperature and the THF was removed using a rotatory evaporator. 13.24 mL of chloroform was then added to the solid polymer film to make a 0.05 M solution (based on monomer concentration).

Preparation of Boric Acid Buffer

To prepare the buffer, 80 mL of distilled water and 245.6 mg (3.972 mmol) of boric acid were mixed until the boric acid dissolved. Then a 1 N solution of NaOH was added into the boric acid solution until it reached pH 12.

Polymer Coating of NPLs and Phase Transfer

To coat the NPLs with the polymer, 7.5 mL of the core/shell NPLs (optical density = 2.574 at lowest-energy exciton peak) was added into a 2.125 mL polymer solution in a 50 mL round bottom flask. The flask was gently shaken for a few seconds and the mixture was then evaporated gently using a rotatory evaporator until all the solvent is removed (approx. 10 min, 40°C water bath). The remains were re-dispersed in chloroform, re-evaporated again for a total of three times to ensure even coating. Then 30 mL of boric acid buffer (pH 12) was added to open the remaining anhydride rings of the polymer in the dried polymer and NPLs mixture. The flask was gently shaken for 10 min for complete dispersion in water.

Sucrose Gradient Separation

To remove the excess polymer introduced in the polymer coating step, the NPLs were run through a sucrose density gradient. Water dispersed core/shell NPLs were concentrated with Amicon® Ultra-15 Centrifugal Filter (M_w cutoff 100k) by centrifuging the sample at 6.9k rpm (5000g) for 15 min. This step also removes small molecule impurities e.g. free fluorescienamine if the labelled polymer coating is used. Sucrose solutions with 30/35/40/45/50/55% sucrose were prepared by dissolving 338.1/402.9/470.6/541.3/614.8/691.9 mg sucrose in 1 mL water each. Sucrose gradients were prepared by taking 200 µL sucrose solutions (highest % first) and adding

them layer by layer into a 1.5 mL Eppendorf tube without shaking. After six layers of different sucrose concentrations, 100 µL of concentrated core/shell NPLs was added to the top and the tube was centrifuged at 16.6k RPM (20000g) for 45 min at room temperature. The NPLs penetrate into the sucrose gradient (see Figure 5.6), therefore the sucrose above the NPLs was discarded. The sucrose gradient containing the NPLs was diluted with water and concentrated with Amicon filters to wash off the sucrose. The washing was repeated three times to ensure that the sucrose is removed.

Centrifugation

Centrifugation was done using a Sigma spin control 3-30k centrifuge. Centrifugation for the sucrose gradient separation was done with the 12110 – H rotor (12 × 1.5 mL tubes, fixed angle) while all other centrifugations were done with the 19776 rotor (6 × 50 mL tubes, fixed angle).

UV-Vis Absorption Measurements

To measure the absorption spectra we used either an Agilent Cary 60 Spectrophotometer or Avantes spectrophotometer, consisting of Avantes AvaLight-DH-S-BAL as the UV-Vis light source passing through a neutral density filter (optical density = 2.0) and fiber-coupled to an Avantes SensLine AvaSpec-HSC-TEC detector.

Photoluminescence Measurements

Photoluminescence spectra were recorded using an Avantes SensLine AvaSpec-HSC-TEC spectrophotometer in 90° geometry with a Prizmatix Silver high power LED as excitation source (emission peak 369 nm, FWHM ~ 10 nm).

Quantum Yield Measurements

Quantum yield measurements were made relative to reference dyes.[133] Rhodamine 6G and Sulforhodamine 101 were dissolved in ethanol. CdSe core only NPLs and CdSe/CdZnS core/shell NPLs were diluted in hexane. Polymer coated CdSe/CdZnS core/shell NPLs were diluted in distilled water. Samples were diluted until the absorbance approaches a value of 0.1 at the wavelength of 370 nm. The photoluminescence of the samples were recorded at that concentration using blue LED excitation at 369 nm (full-width half maximum, FWHM ~ 10 nm). Further dilution of the samples allowed us to obtain a linear fit between the sample absorption and the integrated

photoluminescence, which was compared to the Rhodamine 6G/Sulforhodamine 101 standard linear fit to obtain the quantum yield of the samples.

Fluorescence Lifetime Measurements

Fluorescence lifetime measurements were conducted with a FluoTime200 time-correlated single photon counting setup. Samples were excited with a green LED at 500 nm which was controlled by PicoQuant PDL 800-D. The signal was detected using a micro-channel plate photomultiplier tube that was connected to PicoHarp 300 time-correlated single photon counting system. The instrument response function was measured using a dispersion of silica nanoparticles (LUDOX® HS-40 colloidal silica) in water.
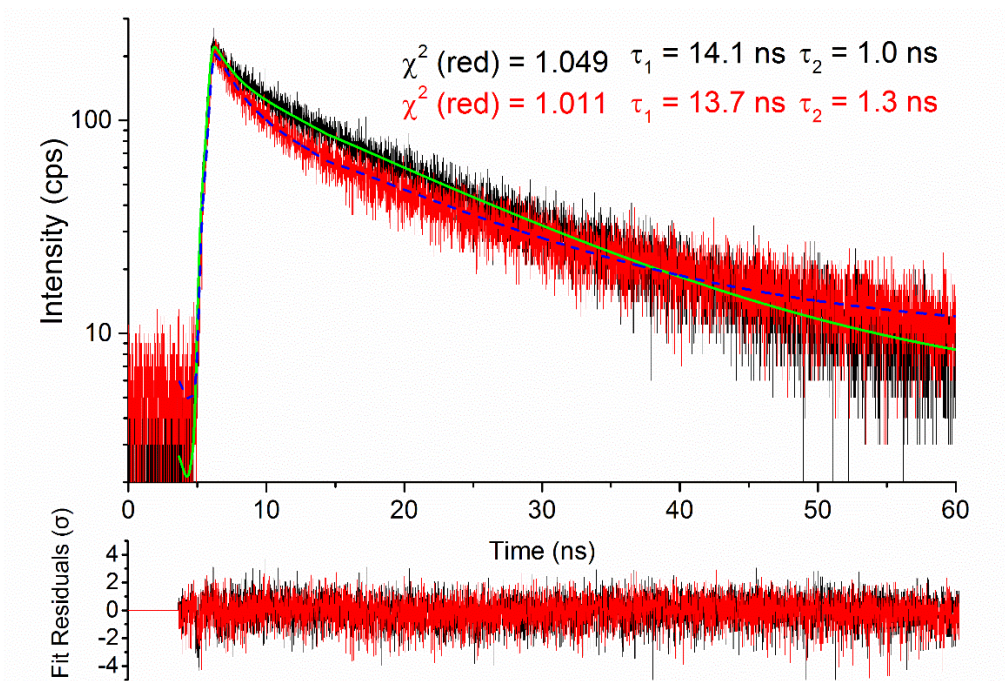
Figure 5.14. Fluorescence lifetime measurements of core/shell NPLs before phase transfer (in hexane, black) and after phase transfer (in water, red). Green solid line shows double exponential fitting of the fluorescence decay of the core/shell NPLs in hexane. Lifetimes obtained from fit were 14.1 ns and 1.0 ns. Blue dashed line shows double exponential fitting of the fluorescence decay of the core/shell NPLs in water. Lifetimes obtained from fit were 13.7 ns and 1.3 ns.

The fitting was done with the following equation:

$$I(t) = \int_{\infty}^{t} IRF(t') \sum_{i=1}^{2} A_i e^{-\frac{t-t'}{\tau_i}} \, dt'$$

Where:

IRF   Instrument response function

A_i Amplitude of the ith component, in counts

τ_i Lifetime of the ith component, in nanoseconds

X^2 Quality of fitting

Sample	X^2(reduced) [σ]	A_1 [counts]	τ_1 [ns]	A_2 [counts]	τ_2 [ns]
Core/Shell NPLs in hexane	1.049	169.0	14.1	126.7	1.0
Core/Shell NPLs in water	1.011	129.1	13.7	142.6	1.3

Stability of NPLs at Different pH and Salt Concentrations Over Time
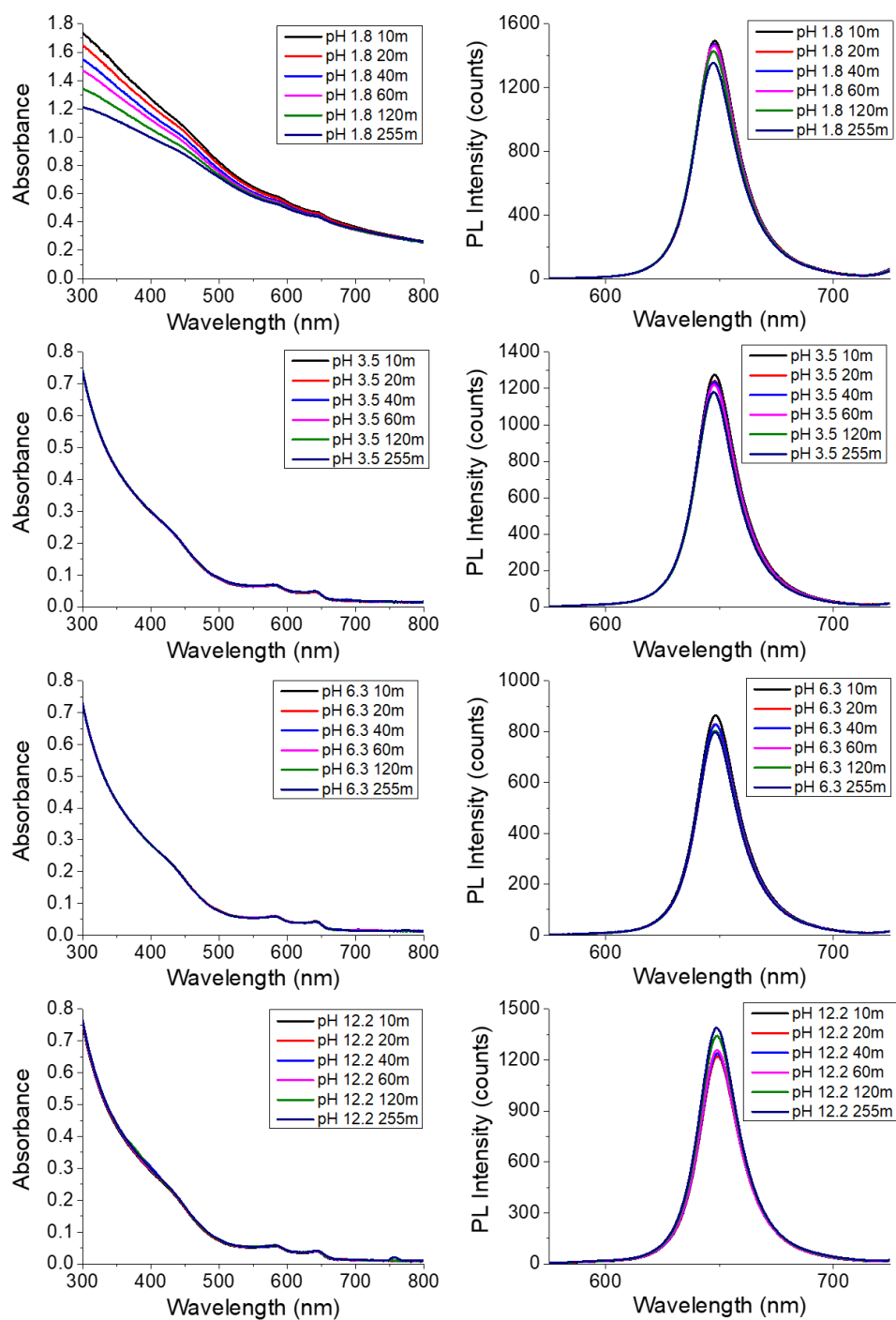
Figure 5.15. Absorption and PL spectra of water dispersed core/shell NPLs at different pH environments. The spectra remain stable for over 3 hours except in the case in pH 1.8 due to the agglomeration of NPLs over time, caused by the protonation of the COO- groups on the polymer coating.
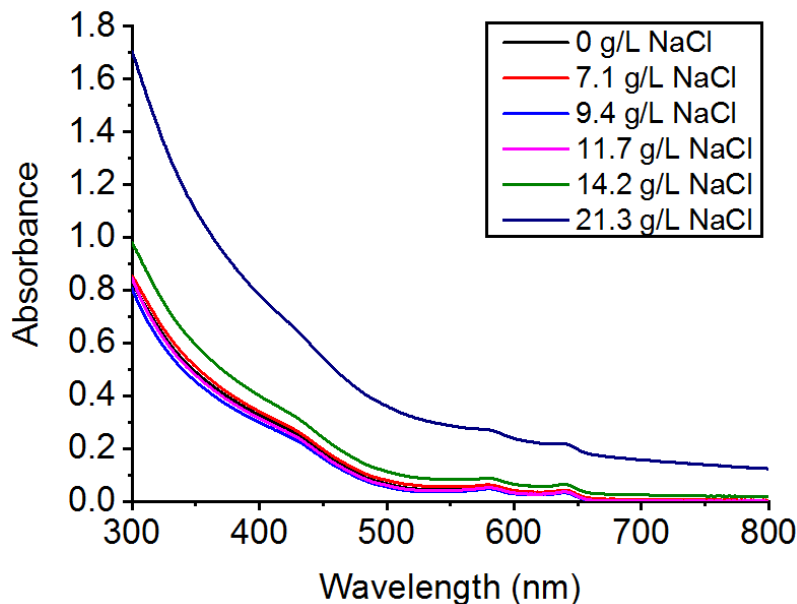
Figure 5.16. Absorption spectra of NPLs dispersed in Dulbecco's phosphate buffered saline (PBS) buffer at different NaCl concentrations. Signals from scattering are not visible until the NaCl concentration goes over 14 g/L.

Gel Electrophoresis

Gel Electrophoresis was conducted in 1% agarose gel and tris acetate-EDTA (TAE) buffer (pH 8.3). The voltage applied was 10 V/cm for duration of 40 min. Typical sample loading used 10 µL of concentrated core/shell NPLs per well.

Transmission Electron Microscope (TEM)

Samples were prepared by dropcasting a hexane/chloroform/water solution of the NPLs onto a carbon coated copper TEM grid. The grid sat on filter paper during the dropcasting to assist the drying of solvent. Routine TEM imaging was done using JEOL1400 TEM with an acceleration voltage of 120 kV. Microstructural characterization was done using a FEI Tecnai F20 TEM with an acceleration voltage of 200 kV.
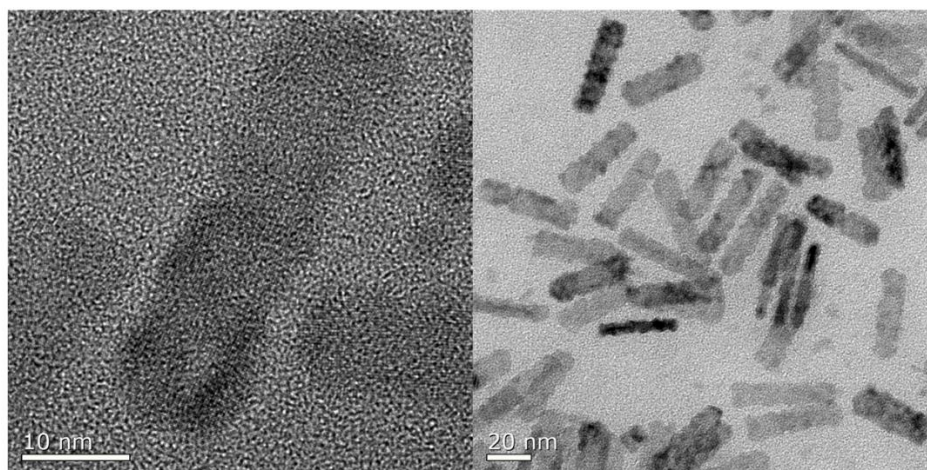
Figure 5.17. Transmission electron microscopy image of polymer coated core/shell NPLs after phase transfer. NPLs are well distributed which indicates that the NPLs are individually coated (see also FCS in Figure 5.8).

Fluorescence Correlation Spectroscopy (FCS)

Serum containing samples were prepared 30 min prior to the experiments by diluting 1 part of NPL stock solution with 20 parts serum. Experiments were performed on a commercial setup LSM 880 (Carl Zeiss), with a Zeiss C-Apochromat 40×/1.2W water immersion objective. The one photon excitation was done by an Argon Laser (488 nm) and the two photon excitation by a Ti:Sa laser (Spectra Physics) operating at wavelength of 800 nm and providing ~ 100 fs long pulses at repetition rate of 80 MHz. In both cases the emission in the range 550-700 nm was detected using a Quasar spectral detection unit (Carl Zeiss) operating in single-photon counting mode. The excitation power given in Figure 5.11 refers to the power after the objective. Eight-well polystyrene-chambered cover glass (Nunc™ Lab-Tek™, Thermo Fisher Scientific) was used as a sample cell. For each solution, a series of 10 measurements with a total duration of 5 min were performed at room temperature (23 °C). The fluctuations of the fluorescent intensity *δI(t)=I(t)-<I(t)>* were recorded and analyzed by an autocorrelation function *G(τ)=1+<δI(t)δI(t+τ)>/<I(t)>²*. For an ensemble of identical freely diffusing fluorescence species, *G(τ)* has the following analytical form (Equation 5.2)

$$G(\tau) = 1 + \left[1 + \frac{f_T}{1-f_T}e^{-t/\tau_T}\right]\frac{1}{N}\frac{1}{\left[1+\frac{t}{\tau_D}\right]\sqrt{1+\frac{t}{S^2\tau_D}}} \qquad \text{eq. (5.2)}$$

Here, N is the average number of diffusing fluorescence species in the observation volume, f_T and τ_T are the fraction and the decay time of the triplet state or blinking contribution, τ_D is the lateral diffusion time and S is the so-called structure parameter, $S = z_0/r_0$, where z_0 and r_0 represent the axial and radial dimensions of the observation volume. Furthermore, the lateral diffusion time, τ_D, is related to the respective diffusion coefficient, D, through $\tau_D = r_0^2/4D$. The experimentally obtained $G(\tau)$ were fitted with eq. (5.2), yielding the corresponding diffusion times and subsequently the diffusion coefficients of the fluorescent species. Finally, the hydrodynamic radii R_H were calculated using the Stokes-Einstein relation: $R_H = k_B T/6\pi\eta D$, where k_B is the Boltzmann constant, T is the temperature, and η is the viscosity of the solvent. Furthermore, FCS yielded also the fluorescent brightness (FB) of the studied species defined as the ratio between the detected average fluorescent intensity and the mean number of fluorescent species in the observation volume, $FB = <I(t)>/N$. As the value of r_0 depends on the specific characteristics of the optical setup, a calibration was performed using a reference standard with known diffusion coefficient, namely Rhodamine 6G, $D = 4.14 \times 10^{-10} \text{m}^2/\text{s}$ in water at 25°C.

Inductively Coupled Plasma - Optical Emission Spectrometry (ICP-OES)

All measurements were performed with an ACTIVA M spectrometer (Horiba Jobin Yvon, Bernsheim, Germany) equipped with a Meinhardt-type nebulizer, a cyclone chamber, and controlled by ACTIVAnalyst 5.4 software. The following conditions were applied: 1200 W forward plasma power, $12 \text{ L} \cdot \text{min}^{-1}$ Ar flow and 15 rpm pump flow. The water dispersed NPLs were diluted in MilliQ water prior to measuring to reach ion concentrations in the range of 2-20 mg/L. The carbon emission line at 193.026 nm (for the Cd measurements) and the argon emission line at 404.442 nm (for the Zn measurements) were used as the reference lines. Measurements were performed three times per emission line, using three different elemental emission lines. As baseline correction, a dynamic underground correction provided by the software was used. The emission lines chosen for the characterization of the respective elements were: Cd: 326.105 nm, 346.620 nm, 361.051 nm; Zn: 202.548 nm, 206.200 nm, 213.857 nm.

The concentration of the NPLs was determined by the following equation:

$$NPL\ concentration = \frac{Measured\ Cd^{2+} concentration}{Number\ of\ Cd^{2+} per\ NPL}$$

Where the number of Cd2+ per NPL was found by calculating the theoretical number of Cd2+ per NPL. This value was obtained by using a crystal structure model with thickness of 5ML/4ML/5/ML shell/core/shell thickness and lateral sizes measured from TEM. The theoretical value was confirmed from the stoichiometry between Cd and Zn: the predicted Cd:Zn ratio in one platelet was found to match well with the actual ratio of Cd:Zn measured by ICP.

Cell Culture

RAW 264.7 cells (DZMS, Germany) were maintained in Dulbecco Modified Eagle Medium (DMEM) supplemented with 10% FBS, 100 IU/mL penicillin and 100 µg/mL streptomycin. All components were obtained from Thermo Fisher, USA. The cells were splitted at 80% confluency two or three times per week.

Flow Cytometry

RAW264.7 cells were seeded out in 24-well plates (100 000 cells/well) in DMEM with all supplements. The next day, the medium was removed and NPLs were added to cells at a concentration between 18-150 µg/mL in DMEM with all supplements or DMEM without FBS. After 24 h, cells were detached with trypsin-EDTA (Gibco, Germany), centrifuged (500 g, 5 min) and resuspended in PBS (1 mL). Flow cytometry measurements were performed on an Attune NxT flow cytometer (Thermo Fisher, USA).

Confocal Laser Scanning Microscopy (cLSM)

RAW 264.7 cells (50 000 cells/well) were seeded in Ibidi iTreat-dishes (IBIDI, Germany). The next day, the medium was removed and NPLs were added to cells at a concentration of 18 or 37 µg/mL in DMEM with all supplements or DMEM without FBS. After 24 h, the NPLs were removed and the cell membrane was stained with CellMask Green (dilution 1:5000 in PBS, Thermo Fisher, USA). Images were acquired on a Leica TCS SP5 II microscope with an HC PL

APO CS 63x/1.4 oil objective using the LAS AF 3000 software. NPLs are pseudo-colored in red

and the cell membrane is pseudo-colored in green.

Chapter 6: Surface Dynamics of Nominally Equivalent Nanoparticles Governs Cell Uptake Behaviour

In the previous chapter I showed that a polymer coating can disperse core/shell NPLs in water and protect them from harsh conditions. Here I compare the polymer coated NPLs with ligand exchanged NPLs, another approach to disperse NPLs in water. Remarkably, the two methods allow NPLs to be dispersed in aqueous medium without changing their shape, size and surface charge. This allows a comparison between the two different phase transfer methods and study the influence of surface dynamics where the ligands are more labile and the polymer coating is more static. This chapter is based on an unpublished paper draft.

My contributions to the project were: Synthesis and characterization of water dispersed nanoplatelets using polymer coating and ligand exchange. Cell experiments and protein corona analysis were done by Dr. Johanna Simon. FCS measurements were done by Dr. Kaloian Koynov. DLS measurements were done by Christine Rosenauer.

6.1 Introduction

Nanoparticles have incredible potential as a platform for bio-applications such as drug delivery and bioimaging, however their uptake mechanism into cells is highly complex and relies on many parameters. To understand their uptake mechanism systematically, studies have simplified the parameters into major groups, for example the particle size, charge and functional groups.[211] These parameters influence the interaction with the proteins in the biological medium, hence dictates; the protein corona surrounding the nanoparticle, its biological identity and ultimately its cell uptake mechanism. However, such parameter studies assume that the parameters are static, which may be problematic since the parameters depend on the particles' surface consisting of ligands subject to dynamic equilibrium. Here we show the influence of surface dynamics to the cell uptake of nanoparticles by designing a nominally equivalent system in terms of size, shape, charge and functional groups but different in their surface dynamics.

As the platform for this study we selected CdSe/CdZnS nanoplatelet as the nanoparticle model, which can be dispersed in water by ligand exchange with hydrophilic ligands or

amphiphilic polymer coating. Both methods have minor influence in the shape and size of the nanoparticle, possess the same terminal functional groups (COO⁻) thus similar surface change. The ligand exchanged surface is subject to dynamic equilibrium while the polymer coating contains multiple alkyl side chains that creates a static surface by multiple hydrophobic interaction with the native surface ligands.

Analysis of the protein corona revealed major differences in protein compositions surrounding the ligand exchanged and polymer coated nanoplatelets after exposure to human serum and human plasma. Photoluminescence spectroscopy implies the proteins in serum and plasma can interact directly with the Cd surface of the ligand exchanged NPLs instead of just the COO⁻ functional groups, while the same does not happen to the polymer coated NPLs due to the static nature of the polymer coating. The difference in protein interaction led to differences in colloidal stability of the nanoplatelets in human serum and the cell uptake amount. This data highlights the unnoticed potential of surface dynamics as a major parameter of study when determining the uptake mechanism of nanoparticles into cells.

6.2 Results and Discussion

To determine the effect of surface dynamics on the uptake of nanoplatelets (NPL), we designed a system with equivalent particle size, chemical groups and surface charge. Polymer coated NPLs (POLY) were prepared based on our previous findings[37] while 3-mercaptopropionic acid ligand exchanged NPLs (MPA) were prepared based on a recent publication by Shendre et al.[101] A static surface is achieved by the polymer coating due to the multiple interaction of a single polymer chain to multiple fatty acid ligands on the surface of the NPLs while a dynamic surface is achieved instead when the interaction of a MPA ligand takes place through just a monodentate binding mode. The two-phase transfer method did not alter the size and shape of the CdSe/CdZnS NPLs as shown in Figure 6.1A and B respectively.

In both cases, the NPLs are dispersed by the negative charge coming from the hydrophilic COO⁻ groups on the surface of the polymer coating and on the ends of the MPA ligands. (Figure 6.1C and D) Based on the zeta potential measurements (Figure 6.1E), both NPLs are negatively charged, with zeta potential around - 40 mV. This indicates that the COO⁻ group density is also similar.
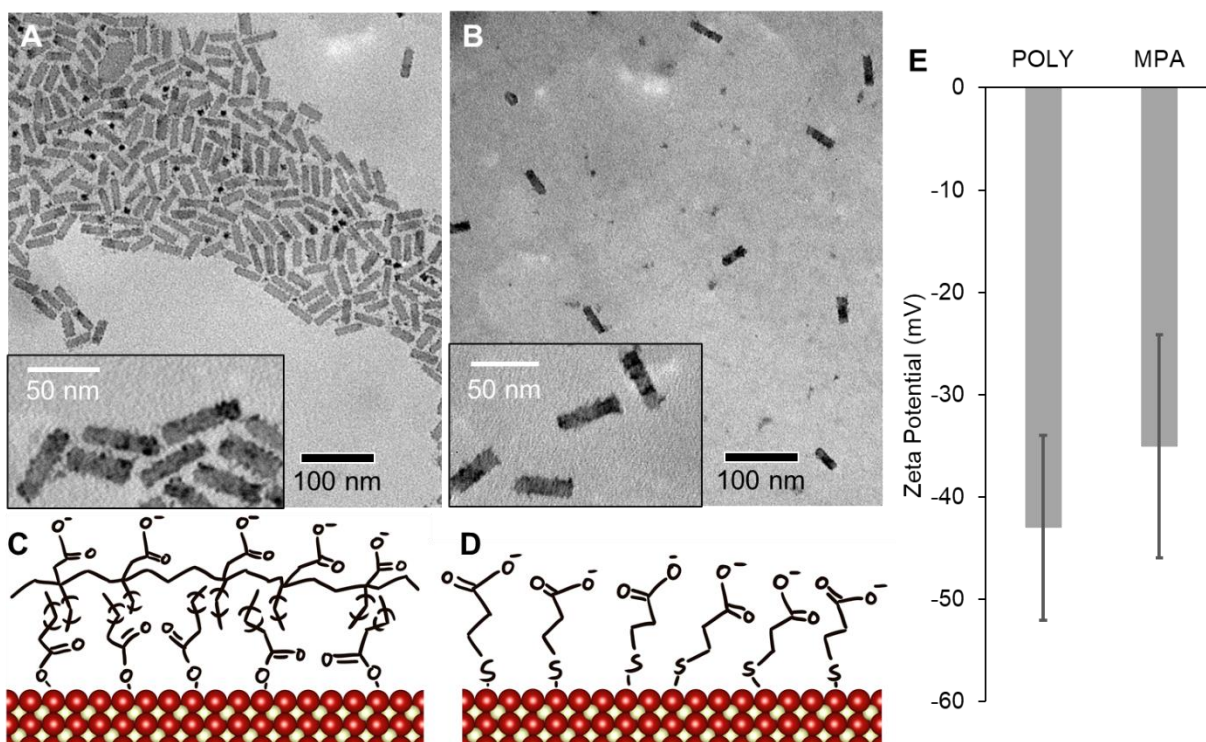
Figure 6.1. Particle size and surface charge characterization of NPLs dispersed by COO⁻ groups. TEM image of A) polymer coated and B) MPA ligand exchanged NPLs used in this work. Average lateral size of the NPLs are 600 nm². Details of size measurement are shown in Table 6.1. Simplified sketch of the surface functionality for C) polymer coated and D) MPA ligand exchanged NPLs. Long fatty acid chains are shortened by brackets for clarity. E) Zeta potential at pH 7 in 0.001 M KCl solution. Error bars indicate the zeta deviation.

Using both types of NPLs, we performed cell uptake experiments with cancer cells (HeLa). Without incubation in human serum, both NPLs are strongly binding to HeLa cells (Figure 6.2A, black bars and Figure 6.2B). However, in the presence of human serum, the cell uptake behaviour is significantly altered. The uptake of MPA NPLs is strongly decreased, while the uptake of POLY NPLs remain relatively constant (Figure 6.2B grey bars).
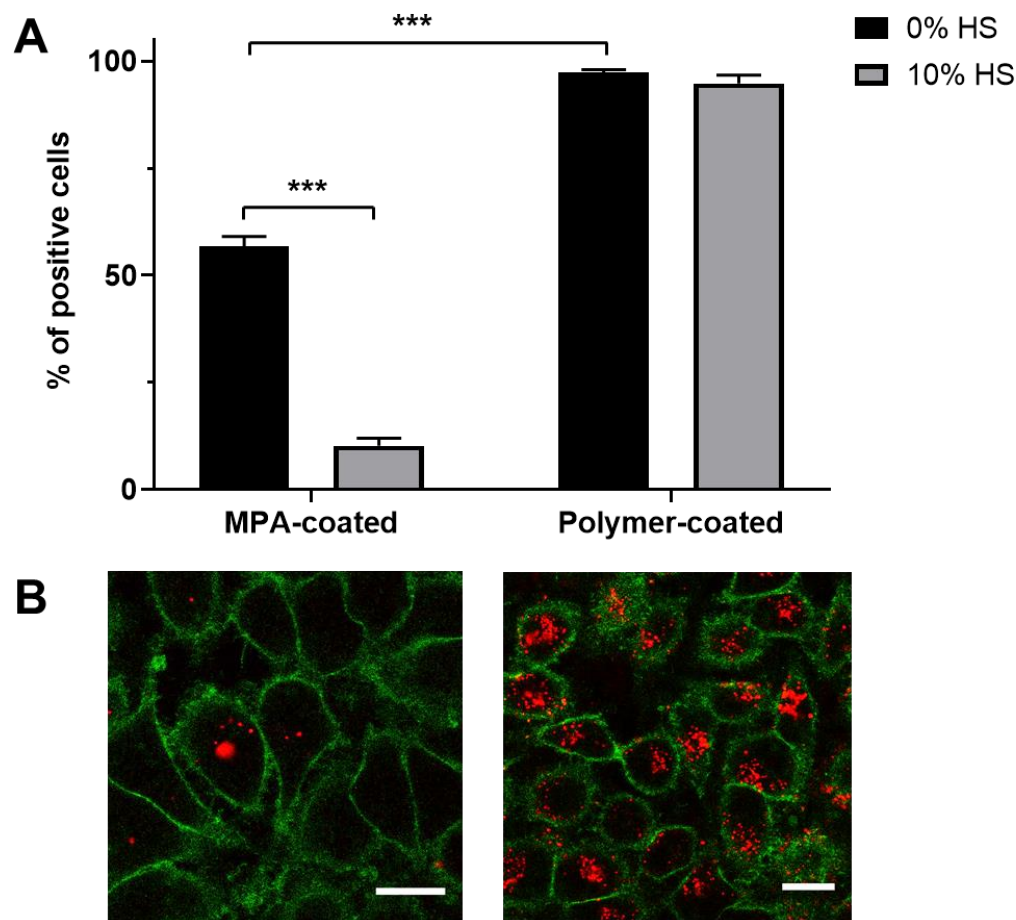
Figure 6.2. Cell interaction of NPLs with HeLa cells in the absence of serum (0% HS) or with serum (10% HS) after 24 h. A) The amount of NPL fluorescent positive cells was determined by flow cytometry. B) Confocal laser scanning microscopy images of the cells after incubation of MPA-coated NPLs (left) and Polymer coated NPLs (right) in the absence of serum (0% HS). The cell membrane is pseudo-coloured in green while the NPLs are pseudo-coloured in red.

This indicates that there is a clear difference in the interaction of MPA NPLs in contrast to POLY NPLs with serum proteins. To explain this phenomenon, we looked at the surface dynamics of the MPA and POLY NPLs. As shown in Scheme 1, the interaction of MPA ligands to the Cd/Zn surface of NPLs is held by a monodentate Cd-S or Zn-S bond. Previous studies have shown that the interaction of MPA to the Cd/Zn surface of nanocrystals is labile.[212] The reason that the bond is labile is partly due to the monodentate nature, which does not benefit from any chelate effect, meaning that it loses more entropy of disorder compared to ligands which can chelate e.g. proteins with multiple thiol groups. Another reason is that the thiol group can be prone to oxidation which

will prevent it from interacting with the Cd surface over time. This lability results in a dynamic surface, which is in constant equilibrium with the surrounding environment. Proteins and small molecules often contain nucleophilic groups (e.g. amine, thiol), which can potentially participate in this equilibrium and interact directly with the surface of NPLs.

Meanwhile, the surface of POLY NPLs is static[213] since the backbone of the polymer has multiple interaction with the fatty acid ligands on the surface. Both the fatty acid ligands and the backbone are hydrophobic, which forces the COO⁻ groups to stay on the outside and the hydrophobic groups to be buried to minimize interaction with water. As a result, spontaneous detachment of the polymer is very unlikely,[213] since it will expose the hydrophobic groups to the aqueous environment. Furthermore, the Cd surface of the NPLs is concealed, which means that the thiol groups of proteins can hardly interact with POLY NPLs.

Dynamic surface
- Ligands are labile
- Relatively facile equilibrium to surroundings
- Potentially free access to NPL surface

Static surface
- Hydrophobic chains buried to minimize energy
- Equilibrium favours polymer coating
- Sterically hindered access to NPL surface

— C / C-C / C=C / C-N
● S⁻
● COO⁻
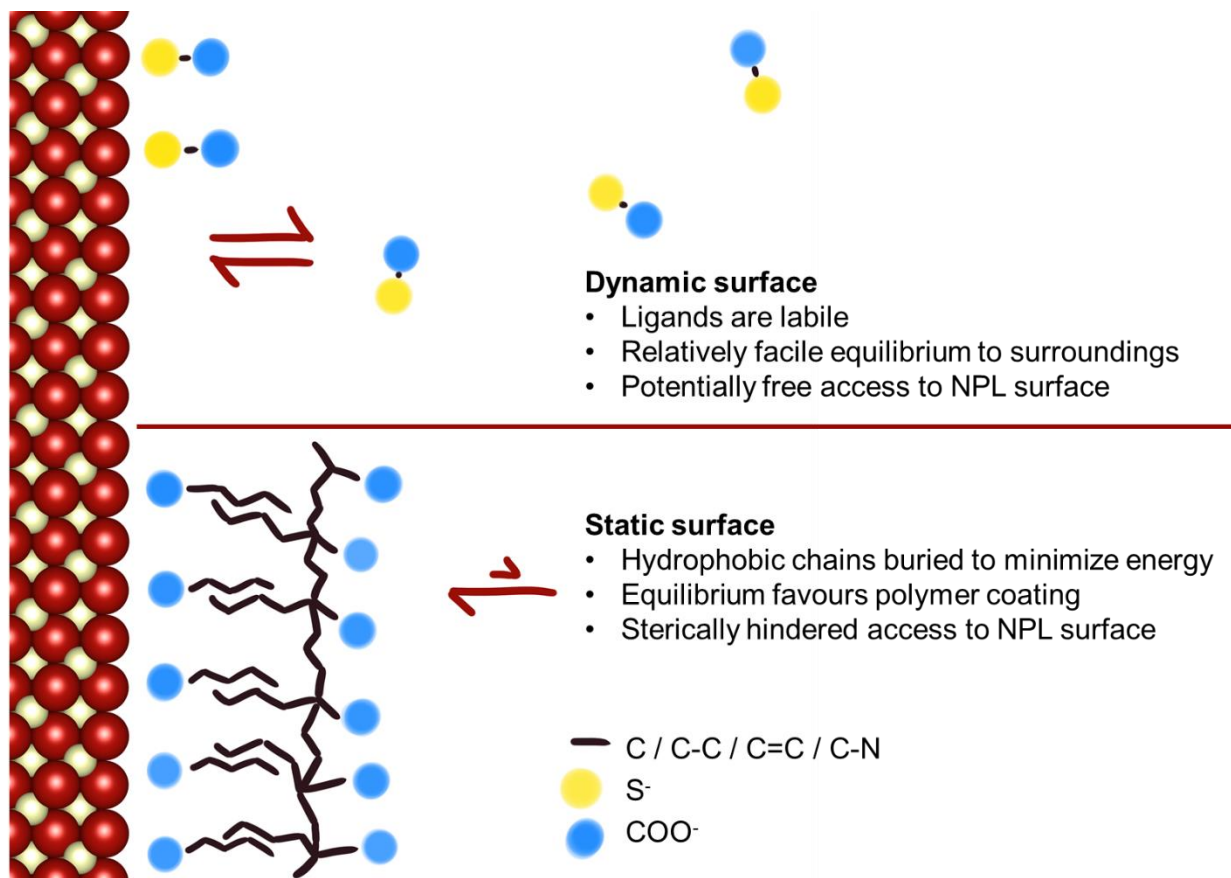
Scheme 6.1. Surfaces of NPLs for MPA ligand exchanged (top) and polymer coated (bottom). Red spheres represent Cd/Zn atoms in the NPLs' shell, pale yellow spheres S atoms.

By using photoluminescence (PL) spectroscopy, we rationalised our hypothesis illustrated in scheme 1. Figure 6.3A and B shows that changes in PL of both MPA NPLs and POLY NPLs respectively. First, we compared the PL of NPLs in water and saline dispersion, which stayed relatively constant. This indicates that the PL change is not influenced by salt. In the presence of serum, the PL intensity of MPA NPLs is quenched significantly while for POLY NPLs it remains constant. This suggests that the proteins do have a more direct interaction for MPA NPLs.

We rationalized the quenching in PL by considering two scenarios. The first possibility is if the quenching is caused by direct surface damage to the NPLs. Nucleophilic groups in serum could influence the equilibrium of the NPL ligands and strip them off the surface. This would lead to improper passivation of the NPLs, therefore PL quenching. Another possibility is quenching from agglomeration. The interaction of NPLs to serum proteins could destabilize the NPLs and

induce agglomeration. When NPLs are stacked and close to each other (distance < ~5 nm), they
can undergo homo-FRET.[73, 214] In a batch of NPLs with QY<100%, homo-FRET from bright NPLs
to dark NPLs would overall lead to quenching of PL intensity.[73] Since the agglomeration is
dependent on the protein interaction to NPLs, the PL quenching is also indicative of the surface
binding selectivity of serum protein to MPA NPL and POLY NPL.
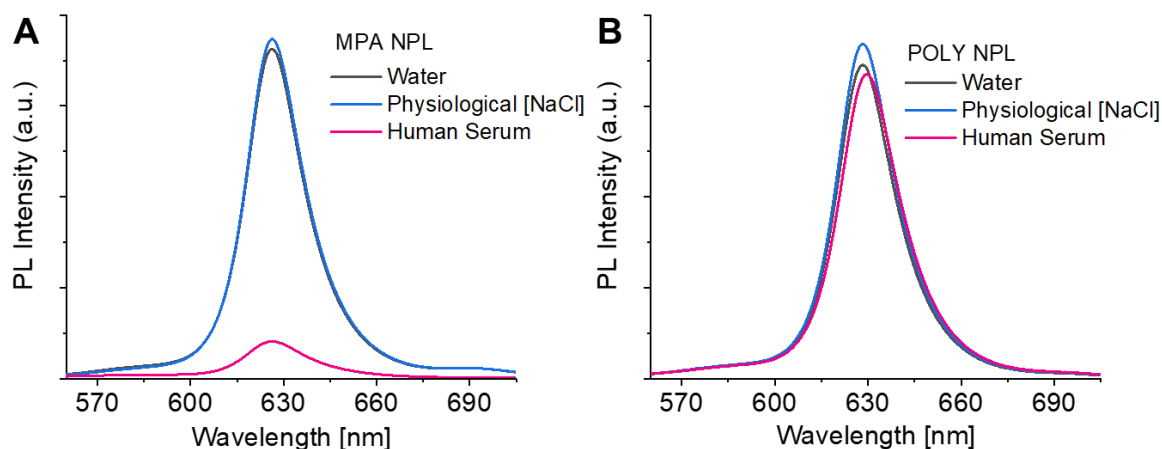
Figure 6.3. PL spectra of NPLs in water (grey lines), NaCl solution at physiological salt
concentration (blue lines) and in human serum (pink lines). A) MPA ligand exchanged NPLs. B)
Polymer coated NPLs.

To further assess, the interaction of serum and plasma proteins with NPLs having a static
polymer or a more dynamic MPA surface coating, a thorough protein corona analysis was
conducted (Figure 6.4). Therefore, NPLs were incubated with serum/plasma for 1 h at 37 °C.
Subsequently, free or loosely bound proteins were removed via several washing steps. The amount
that was strongly attached to surface of the NPLs was determined by Pierce Assay and the proteins
were identified via high resolution mass spectrometry measurements (LC-MS). The Pierce assay
shows that both NPLs strongly adsorb serum/plasma proteins whereas MPA NPLs adsorbed more
protein material compared to POLY NPLs (Figure 6.4A). Based on LCMS protein classification,
we discovered that the types of protein that interact with MPA NPLs and POLY NPLs vary
significantly. In particular, the MPA NPLs have high contribution from coagulation proteins
(Figure 6.4B). The differences in proteins was also demonstrated in the heat map (Figure 6.4C),

showing a high contribution from kininogen-1 for MPA NPLs. In contrast to that, a higher number of immunoglobulins (Ig gamma 1 and 2) and serum albumin adsorbs to POLY NPLs.
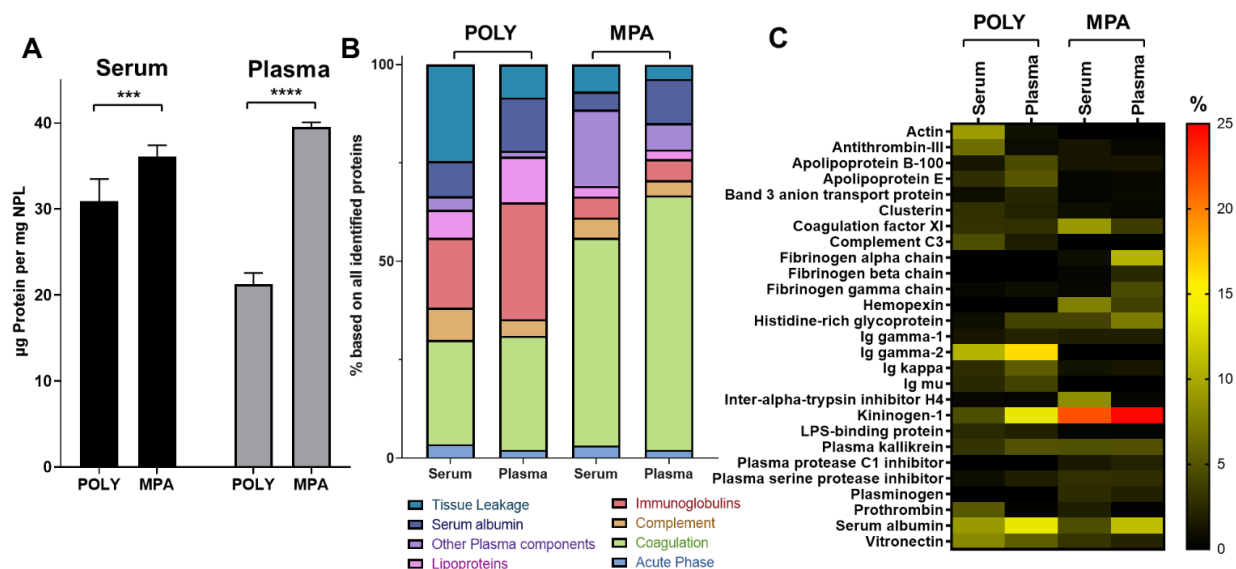
Figure 6.4. Protein corona analysis of polymer coated NPLs (POLY) and ligand exchanged NPLs (MPA) after incubation in human serum and human plasma. A) Quantification by pierce assay of samples, showing amount of proteins in µg/mg NPL. B) LCMS protein classification. C) Heat map illustrating the relative quantity of the most abundant proteins found in LCMS protein identification.

Induced by this selective protein binding, the colloidal stability in serum and plasma varies greatly between the two samples. For POLY NPLs, the particles remain stable in the presence of serum proteins as we observed in DLS (Experimental section Figure 6.5) and fluorescence correlation spectroscopy (FCS) (Experimental section Figure 6.6). Consistent with our previous study,[37] the hydrodynamic radii increase slightly in the presence of proteins, likely due to the formation of protein corona (Figure 6.6 and Table 6.2). Furthermore, we observed no agglomerates of POLY NPLs in FCS and retention of the particle brightness, which agrees with the PL measurements in Figure 6.3. Although the results of the fitting[215] show that aggregates are present in the DLS measurements (Table 6.1), our FCS experiment show that these aggregates are non-fluorescent. This suggests that the presence of POLY NPLs induced some aggregation of the serum proteins.

In contrast, MPA NPLs sediment over time in presence of human serum. Using fluorescence microscopy (Experimental section Figure 6.7), we observed the formation of micron sized agglomerates of MPA NPLs. Considering that coagulation proteins contribute to a large proportion to the MPA NPL's protein corona, we hypothesize that these proteins promote agglomeration of MPA NPLs and drastically alter the uptake behaviour of the particles. Our findings highlight that the interaction between nanoparticles and proteins in solution is determined not only by the size, the shape, the surface charge and the type and concentration of surface chemical groups, but also by surface dynamics. We show that surface dynamics is a determining factor for the interaction of nanoparticles with proteins and thus must be considered as critical parameter in the formation of protein corona and cellular uptake.

6.3 Conclusions

We showed how surface dynamics can influence the cell uptake of nanoparticles by using water dispersed NPLs as a model system. Our model allows us to isolate the influence of surface dynamics by keeping the commonly studied parameters the same, particularly the size, shape, surface change and chemical functionality. Ligand exchanged NPLs exhibited high surface dynamic and participated in equilibrium with the surrounding complex environment. This induced the formation of different protein corona around the NPL samples and changed their biological identity and surface parameters. As a result, ligand exchanged NPLs were colloidally destabilized and agglomerated. Polymer coated NPLs remained stable after interaction with the surrounding proteins and can be taken up by cells. Our study encourages future research to have greater awareness of the surface dynamics of nanoparticles, especially for surfaces covered by ligands.

6.4 Experimental Section

Materials

1-Octadecene (technical grade 90%, O806-1L), oleic acid (technical grade 90%, 364525-1L), cadmium nitrate tetrahydrate ($CdNO_3(H_2O)_4$, 98%, 642045-100G), zinc nitrate hydrate ($ZnNO_3(H_2O)$, 99.999%, 230006-25G), poly(isobutylene-alt-maleic anhydride) (85%, average Mw ~6000, 12-200 mesh, 531278-250G), ethylenediamine absolute ($H_2NCH_2CH_2NH_2$, >99.5%, 03550-250ML) and 3-mercaptopropionic acid ($HSCH_2CH_2CO_2H$, 99+%, M5,80-1) were purchased from Aldrich. Cadmium acetate dihydrate ($Cd(OAc)_2(H_2O)_2$, 98%, 317131000) was purchased from Acros Organics. Selenium powder -200 mesh (Se, 99.999%, 36208) and 1-octylamine ($CH_3(CH_2)_7NH_2$,99%, B24193) was purchased from Alfa Aesar. Hexane (95% n-hexane, analytical reagent grade, H/0355/21) was purchased from Fisher Chemical. Chloroform, stabilized with amylene (100%, 83627.290), absolute ethanol (20821.330) and sodium hydroxide (NaOH, 1 mol/L 1N, UN1824) were purchased from VWR Chemicals. Thioacetamide (TAA, >98%, T0187) and 1-dodecylamine (>97%, D0980) was purchased from TCI. Boric acid (>99.8%, 6943.1) was purchased from Carl Roth GmbH.

Synthesis of 4 Monolayer (4ML) Thick CdSe NPLs

4ML thick CdSe NPLs were synthesized by a modified procedure published by Mahler *et al.*[36] Briefly, 60 mL of 1-octadecene, 320 mg (1.20 mmol) of $Cd(OAc)_2(H_2O)_2$, and 879 μL (787 mg, 2.79 mmol) of oleic acid were combined inside a 100 mL three-necked flask attached to a water-cooled condenser. The mixture was stirred and degassed under vacuum at 110 °C for 90 min. After stopping the vacuum line, the flask was filled with argon and 48 mg (0.607 mmol) of Se powder was swiftly added into the flask. Then the temperature of the heating mantle was set to 240 °C. When the temperature in the flask reached 205 °C, 160 mg (0.600 mmol) of $Cd(OAc)_2(H_2O)_2$ was added into the mixture and the reaction proceeded for 15 min at 240 °C. Afterwards the flask was cooled to room temperature using a water bath and 6.7 mL of oleic acid was injected. The mixture was centrifuged for 10 min at 5000 rpm (2599 g), the supernatant was discarded. Finally, the precipitated NPLs were re-dispersed in 12 mL hexane.

Synthesis of $Cd_{0.33}Zn_{0.67}S$ Shell

The CdZnS shell was synthesized using a one-pot method, modified from an existing procedure.[36] Briefly, 6 mL of the as-synthesized 4ML NPLs (with optical density at 510 nm = 30) were added into a 50 mL round bottom flask containing a stir bar. In a separate flask, 300 mg (3.99 mmol) of TAA, 3 mL (18.2 mmol) of octylamine and 9 mL of chloroform were gently mixed and then sonicated in an ultrasound bath until all the TAA dissolved. The TAA solution was added to the NPL solution while stirring. After a couple of minutes, 500 µL of $CdNO_3$ solution (0.2 M in ethanol) and 1000 µL of $ZnNO_3$ solution (0.2 M in ethanol) were added into the mixture. The flask was sealed with a glass stopper and left to stir for 24 h in ambient conditions.

To be able to precipitate the NPLs, the mixture was first concentrated by evaporating a portion of the solvent using a rotatory evaporator at approximately 280 mbar, 40 °C for a couple of minutes. Then the concentrated mixture (volume approx. 15mL) was centrifuged for 10 min at 8000 rpm (6654 g), the supernatant was discarded, and the precipitated NPLs were re-suspended in 15 mL chloroform. To better stabilize the NPLs, 300 µL of $ZnNO_3$ solution (0.2 M in ethanol) and 600 µL of oleic acid were added into the NPL dispersion while stirring and the mixture was kept at ambient conditions for a couple of days for PL recovery.

To remove the excess oleic acid introduced in this step, methyl acetate was added to the chloroform dispersion of core/shell NPLs (in the ratio of chloroform:methyl acetate = 1:1 v/v). The NPLs were precipitated by centrifugation and re-dispersed in chloroform.

Synthesis of Dodecyl-Grafted-Poly(isobutylene-alt-maleic acid) (polymer)

The amphiphilic polymer was synthesized according to the method described by Riedinger et al.[97] Briefly, 105.3 mg (0.662 mmol monomer units /1.10×10^{-5} mmol polymer) of poly(isobutylene-alt-maleic anhydride), 92.0 mg (0.497 mmol, equivalent to 75% of monomer units) of 1-dodecylamine and 25 mL of THF were combined in a 50 mL round bottom flask containing a magnetic stir bar. Then a reflux condenser was attached and the mixture was heated to reflux using an oil bath. After approximately 10 min, the solution turned clear and it was kept refluxing for 18 h. Then the solution was brought back to room temperature and the THF was

removed using a rotatory evaporator. 13.24 mL of chloroform was then added to the solid polymer film to make a 0.05 M solution (based on monomer concentration).

Phase Transfer by Polymer Coating

The NPLs were coated with the amphiphilic polymer and subsequently transferred to water using a method developed by Halim *et al.*[37] To coat the NPLs with the polymer, 7.5 mL of the core/shell NPLs (optical density = 2.574 at lowest-energy exciton peak) was added into a 2.125 mL polymer solution in a 50 mL round bottom flask. The flask was gently shaken for a few seconds and the mixture was then evaporated gently using a rotatory evaporator until all the solvent is removed (approx. 10 min, 40 °C water bath). The remains were re-dispersed in chloroform, re-evaporated again for a total of three times to ensure an even coating. Then 30 mL of boric acid buffer (pH 12) was added to open the remaining anhydride rings of the polymer in the dried polymer and NPLs mixture. The flask was gently shaken for 10 min for complete dispersion in water.

The excess polymer was removed by sucrose gradient centrifugation and the sucrose was washed away by rinsing the NPLs with water while they were trapped in an Amicon filter ($M_{\text{w cutoff}}$ = 100k). The molar and weight concentration of the core/shell NPLs were determined from their relationship with the sample absorbance calculated in the previous study.[37]

Phase Transfer by 3-Mercaptopropionic Acid Ligand (MPA)

For the ligand exchanged NPLs, the NPLs were transferred to water by replacing the native oleic acid ligands with MPA based on a two-step method reported by Shendre *et al.*[101] First, a concentrated dispersion of core/shell NPLs (optical density = 9.0 at lowest-energy exciton peak) was added to a small 4 mL glass vial containing a stir bar. While the dispersion was stirring, 167 μL of ethylenediamine was added and the mixture was left to stir for 1 h. A fresh solution of MPA (0.15 M) was then prepared by diluting 13.1μL of MPA in 1mL milliQ water. 500 μL of the diluted MPA was added to the NPL dispersion. The mixture was left to stir for 20 min and was subsequently transferred to a 1.5 mL Eppendorf tube to allow phase separation of chloroform and water. To assist the phase separation, the tube was gently centrifuged at 800 g for 3 min. The top aqueous layer containing the NPLs was carefully removed using a mechanical pipette.

The excess MPA was washed away by rinsing the NPLs with water while they were trapped in an Amicon filter ($M_{w\ cutoff}$ = 100k). The molar and weight concentration of the core/shell NPLs were determined from their relationship with the sample absorbance calculated in the previous study.[37]

Dynamic Light Scattering (DLS) of Water Dispersed NPLs

All light scattering experiments were performed with an ALV-CGS 8F SLS/DLS 5022F goniometer equipped with eight simultaneously working ALV 7004 correlators and eight QEAPD Avalanche photodiode detectors (ALV, Langen, Germany). A HeNe laser (632.8 nm, 25 mW output power) was utilized as the light source. The dispersion medium (milliQ water, DMEM + 10% human serum, 100% human serum and 100% human plasma) were all filtered with 0.2 µm Millex-GS, 0.22 µm syringe filter before use. Concentrated NPL dispersions were diluted in the medium and incubated for 1 hour before measurement at 37 °C.
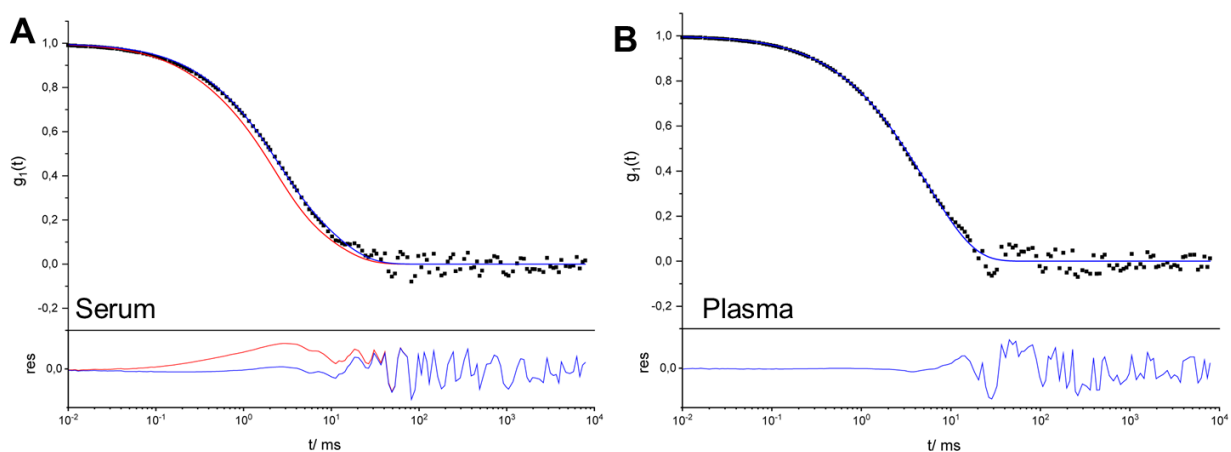
Figure 6.5. Size determination of polymer coated NPLs in serum and plasma by dynamic light scattering.

Autocorrelation function (black squares) of NPLs in A) human serum and B) human plasma. Scattering angle = 30°. The red line in A) represents the forced fit composed of the sum of individual components while the blue line in A) and B) represent the fits with an additional aggregation function.

Table 6.1. Hydrodynamic radii and intensity contributions of polymer coated NPLs in human serum and plasma.

	I% Protein	I% NPL	I% Prot. Aggr.	R_h Protein	R_h NPL	R_h Prot. Aggr.
Human Serum	79.2	9.6	11.2	20.7 nm	31.1 nm	117.2 nm
Human Plasma	96.6	3.4	0	35.2 nm	31.1 nm	N/A

Fluorescence Correlation Spectroscopy (FCS) of Water Dispersed NPLs
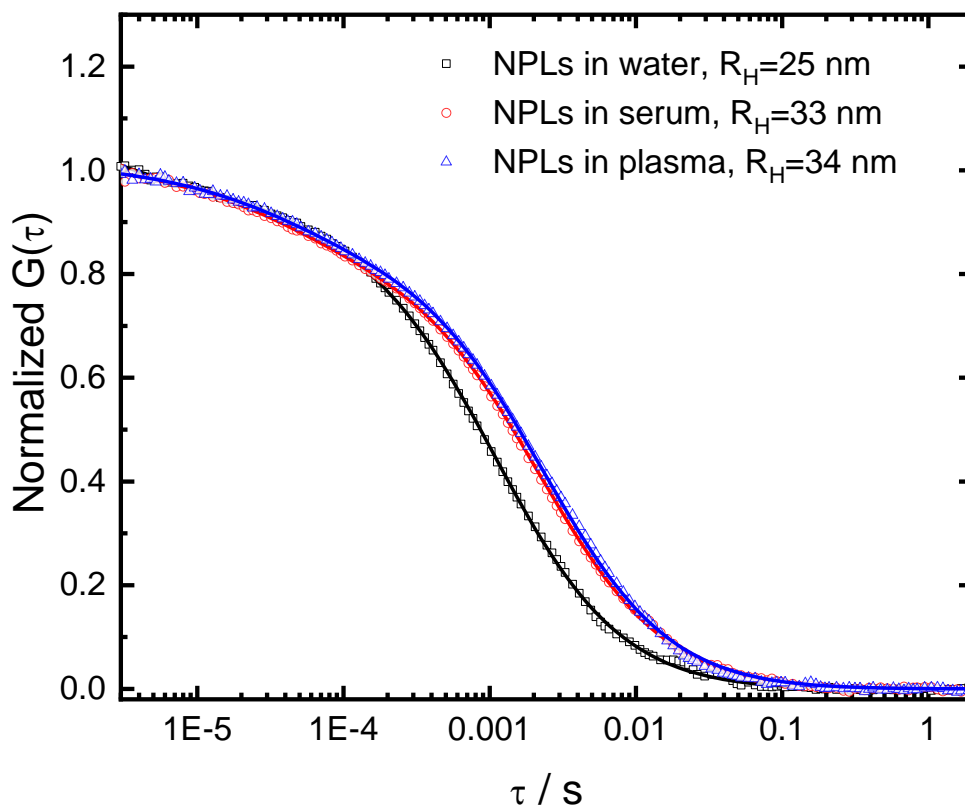
Figure 6.6. Normalized experimental autocorrelation curves of polymer coated NPLs dispersed in water (black), serum (red) and plasma (blue) obtained from FCS. Measurements were conducted using one photon excitation at 488 nm.

Table 6.2. FCS fit results of polymer coated NPLs in different media.

Polymer coated	T_D (μs)	R_h (nm)	FB (kHz/particle)
Water	1117	25	50
DMEM + 10% HS	1371	31	50
Human Serum	2246	33	40
Human Plasma	2371	34	40

Agglomeration of MPA Ligand Exchanged NPLs in Presence of Proteins Observed by Fluorescence Microscopy

Experiments were performed on a commercial setup LSM 880 (Carl Zeiss). Measurements were conducted using one photon excitation at 488 nm.
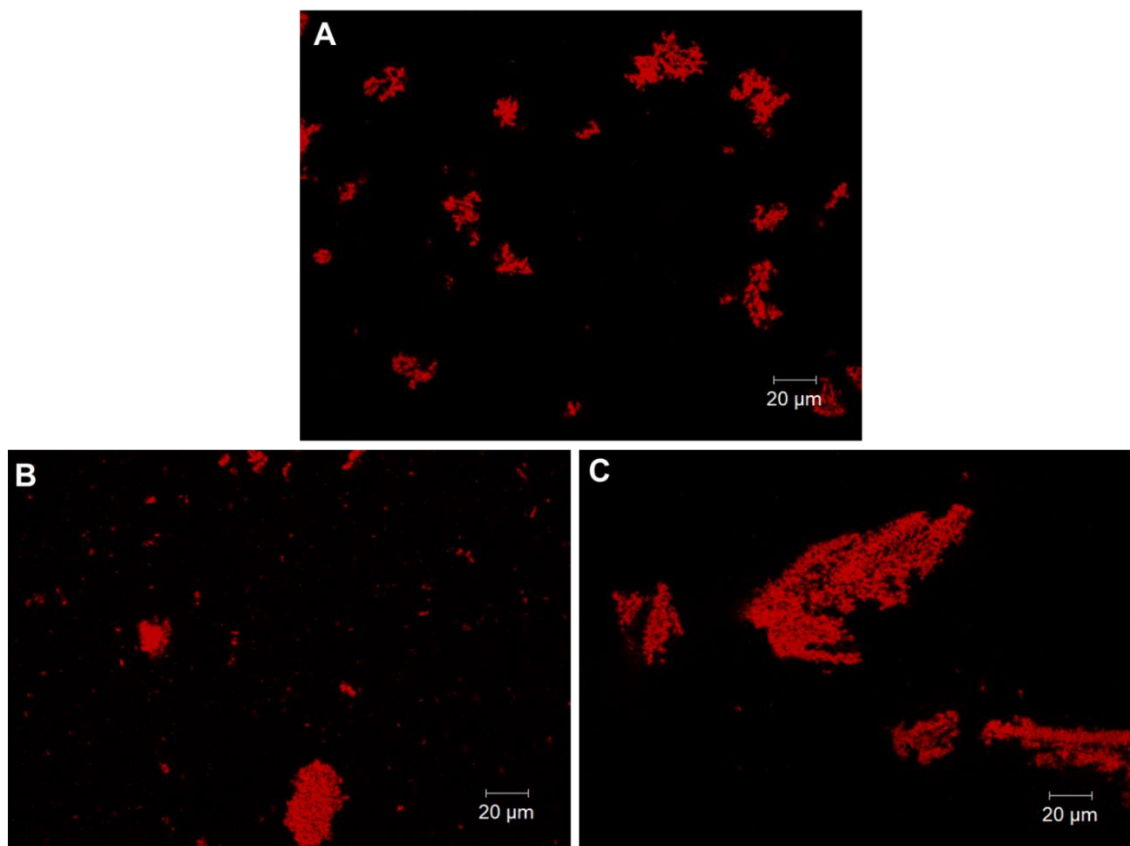
Figure 6.7. Protein mediated agglomeration of MPA ligand exchanged NPLs visualized by fluorescence microscopy. A) NPL agglomerates in DMEM + 10% serum. B) NPL agglomerates in 100% serum. C) NPL agglomerates in 100% plasma.

Zeta Potential of Water Dispersed NPLs

Zeta potential measurements were performed with a Zetasizer Nano Z (Malvern Instruments GmbH, Herrenberg, Germany) in a 10^{-3} M KCl sample dispersion. ξ-potentials of -41.9 mV and -36.2 mV were determined for the polymer coated and ligand exchanged NPLs respectively.

UV-Vis Absorption Measurements

To measure the absorption spectra we used either Agilent Cary 60 Spectrophotometer or Avantes spectrophotometer, consisting of Avantes AvaLight-DH-S-BAL as the UV-Vis light source passing through a neutral density filter [optical density, O.D. = 2.0] and fiber-coupled to an Avantes SensLine AvaSpec-HSC-TEC detector.

Photoluminescence Measurements

Photoluminescence spectra were recorded using an Avantes SensLine AvaSpec-HSC-TEC spectrophotometer in 90° geometry with a Prizmatix Silver high power LED (emission peak 368.65 nm, FWHM ~ 10 nm).

Transmission Electron Microscope (TEM)

Samples were prepared by dropcasting an aqueous dispersion of the NPLs onto a carbon coated copper TEM grid. The grid sat on filter paper during the dropcasting to assist the drying of solvent. Routine TEM imaging was done using JEOL1400 TEM with an acceleration voltage of 120 kV.

Cellular Uptake of Nanoplatelets by HeLa cells Using Flow Cytometry

HeLa cells (obtained from ATCC® CCL-2™) were cultured in Dulbecco Modified Eagle Medium (DMEM, Gibco, USA) supplemented with 10% fetal bovine serum (FBS), 100 U/mL penicillin, 100 mg/mL streptomycin and 2 mM glutamine (all from Thermo Fisher, Germany). Cells were split about two or three times a week at 80-90% confluency. For cell uptake studies, cells were detached with 2.5% trypsin (Gibco, Germany) and seeded out in 24-well plates (100 000 – 150 000 cells/well) in cell culture medium with 10% FBS. After overnight incubation, the medium was changed to serum-free medium. Nanoplatelets (37.5 µg/mL) were added to cells in serum-free cell culture medium (-HS) or cell culture medium containing 10% human serum (+HS) for 24 h at 37 °C. For flow cytometry analysis, cells were detached and measurements were performed on an Attune NxT flow cytometer (Thermo Fisher, USA).

Cellular Uptake of Nanoplatelets by HeLa cells Using Confocal Laser Scanning Microscopy (cLSM)

To visualize the intercellular localization of the nanoplatelets in Hela cells, confocal laser scanning microscopy (cLSM) images were taken. as employed. The cell membrane was stained with CellMask DeepGreen (stock solution: 5 mg/mL, Thermo Fisher). 50 000 cells in DMEM with 10% FBS were seeded out into 8-well μ-Slides (ibidi). After an overnight incubation, the cells were treated with the respective sample in medium with 0% HS or with 10% HS. After 24-hour incubation with the nanoplatelets at a concentration of 37.5 μg/mL, the wells were washed with PBS to remove unbound nanoplatelets. Afterwards, the cells were directly imaged. Cell membrane staining was conducted shortly before the cLSM analysis for 3-5 min in the dark using CellMask Deep Green (Dilution of stock solution: 1:1.000 in PBS). Confocal laser scanning microscopy images were taken on the LSM SP5 STED Leica Laser Scanning Confocal Microscope (Leica, Germany), composed of an inverse fluorescence microscope DMI 6000CS equipped with a multi-laser combination using a HCX PL APO CS 63 x 1.4 oil objective.

Purification of Protein Corona

Nanoplatelets (1 mg) were incubated with 1 mL of human serum or human plasma at 37 °C for 1 h. Protein coated nanoplatelets were centrifuged (20 000 g, 30 min, 4 °C), the supernatant was removed and the pellet was washed with 1 mL PBS solution. This step was repeated three times. Finally, the strongly attached corona proteins were desorbed from the surface with an aqueous solution containing 2 wt% SDS supplemented with 62.5 mM Tris-HCL and the sample was incubated for 5 min at 95 °C. After a last centrifugation step, the supernatant was taken, which contained the corona proteins. The protein concentration was analyzed using a Pierce 660 nm Protein Assay (Thermo Fisher, Germany) according to manufacturer's instructions.

SDS-PAGE of the Protein Corona

Corona proteins (1-2 μg in 26 μL) were incubated with sample buffer (10 μL) and reducing agent (4 μL) for 10 min at 70 °C. Further the solution was applied onto a 10% NuPAGE Bis-Tris Gel and the gel was run at 120 mV for ~1 h. The protein bands were visualized by the SilverQuest Silver Staining Kit according to the manufacturer's instructions.

In-solution Digestion

SDS was removed via Pierce detergent removal columns (Thermo Fisher, Germany) according to the manufactures´ instruction. Tryptic digestion was carried out according to former reports. [216] [217] [218] Briefly, proteins were precipitated using a ProteoExtract protein precipitation kit (Merck Millipore, Germany) overnight. After centrifugation, the protein pellet was resuspended in RapiGest SF (Waters, USA) dissolved in 50 mM ammonium bicarbonate (Sigma Aldrich, Germany) and the samples were incubated at 80 °C for 15 min. For reduction, dithiothreitol (5 mM, Sigma Aldrich, Germany) was added to the solution for 45 min at 56 °C. In the following, proteins were alkylated with iodoacetoamide (15 mM, Sigma Aldrich, Germany) for 1 h in the dark. In a last step, a protein:trypsin ratio of 50:1 was used for tryptic digestion (incubation time 15-18 h at 37 °C). The digestion was stopped with hydrochloric acid (Sigma Aldrich, Germany). Finally, resulting peptide sample was centrifuged (14 000 g, 15 min, 4 °C) to remove degradation products of RapiGest SF.

Liquid Chromatography-Mass Spectrometry (LC-MS)

Samples were diluted with 0.1% formic acid and spiked with 50 fmol of Hi3 EColi Standard (Waters, USA) for absolute protein quantification. LC-MS measurements were performed with a nanoACQUITY UPLC system coupled to a Synapt G2-Si mass spectrometer (Waters, USA). A nanoLockSpray source was used for electrospray ionization (ESI) in positive ion mode. The mass spectrometer was operated in resolution mode performing data-independent experiments (MS^E). Data was processed with MassLynx 4.1, proteins were identified with Progenesis QI and a reviewed human data base was downloaded from Uniprot. The absolute amount of each protein was calculated based on the TOP3/Hi3 approach.[219] A list of all identified proteins and the absolute amount in fmol or relative amount in % is given in a separated excel document.

Chapter 7: Polymeric Nanocarriers with Hydrophilic Nanoplatelet Markers

Unambiguously Localized by Correlative Light and Electron Microscopy

In the previous chapter I showed how NPLs can be taken up by HeLa cells and that they can be imaged by fluorescence microscopy. Here I present a study where we took advantage of the fluorescent property and the electron dense property of the NPLs. This allows complementary imaging using light and electron microscopy to track samples which are relatively challenging to visualize in electron microscopy such as polymeric nanocarriers. This chapter is based on an unpublished paper draft written for an ongoing collaboration.

My contributions to the project were: Synthesis and characterization of water dispersed nanoplatelets, spectroscopy of encapsulated nanoplatelets. Encapsulation and capsule analysis were done by Marie-Luise Frey. TEM was done by Shen Han and Yeliz Yangazoglu. Fluorescence microscopy was done by Anke Kaltbeitzel. Cell experiments were done by Dr. Johanna Simon.

7.1 Introduction

Polymeric nanocarriers are hard to track within cells since they cannot be clearly identified: they require either fluorescent markers to see with light microscopy (LM) or electron-dense markers to see with electron microscopy (EM). By using a marker visible in both EM and LM, one can track the marked nanocarrier in high resolution EM, at the same time highlighting the nanocarrier with color in LM from the grayscale surroundings generated by EM. This combination of techniques is called correlative light and electron microscopy (cLEM).[88] In cell biology, cLEM is often used to make proteins or cell interactions visible in organisms and cells, but also to track nanocarriers in a biological surrounding.[220-223] However current markers to track nanocarriers like quantum dots cannot be visualized readily – they are difficult to distinguish from cellular components, due to their small size (~5 nm) and spherical shape.[224, 225] This means additional elemental analysis (e.g. EDX or ESI) must be done to confirm the identity of the quantum dots to ultimately locate the nanocarrier.[226-228] Here we developed a convenient method to localize nanocarriers by using large (20-50 nm), highly absorbing,[7] rectangular nanoplatelets (NPLs), resulting in unambiguous identification of the markers.

We demonstrate the potential of our new marker by visualizing, hence localizing, a model system of NPL-marked polymeric nanocapsules (NCs) taken up by macrophages. We encapsulated NPLs into biocompatible NCs, a type of drug delivery vehicle, by a polyaddition at the droplet interface in inverse miniemulsion. The key to success of the NPL markers hinged on the protective coating on the NPLs that endows them with a hydrophilic surface. This coating makes NPLs both easy to disperse in aqueous medium and protects the NPLs' surface[37] from major damage during the encapsulation process, thus retaining high fluorescence after encapsulation. We used NCs made of hydroxylethyl starch (HES) or bovine serum albumin (BSA), crosslinked at the interface with toluene diisocyanate (TDI), forming a dense polymeric shell.[229, 230] The NPLs were added to the aqueous dispersed phase prior to the miniemulsion process, leading to the encapsulation of the NPLs into the NCs.

The NCs containing NPLs were then taken up by macrophages in a time-dependent manner. The NCs were easy to detect in EM and LM thanks to the NPLs' unique rectangular shape, large size and high absorption cross sections,[7] which lead to high sample brightness and easy detection in LM at low excitation powers. CLEM, as combination of both microscopy techniques, resulted in an unambiguous localization by visualization of NPL-containing NCs inside the cells (provided no degradation of capsules during the study). We are currently conducting further analysis on this data to reveal details of the fate of NCs, such as their distribution in the cell and the population of NCs in the late endosomes.

7.2 Results and Discussion

We accomplished encapsulation of the NPLs into biocompatible NCs by adding water-dispersible NPLs into the aqueous phase of a miniemulsion. Under the assumption of a Poisson distribution of the NPLs inside the NCs, we employed an excess of NPLs per expected NCs to achieve a labeling of all capsules. We calculated the number of NCs per mL using the hydrodynamic radius and the solid content of the expected NCs dispersion.

Table 7.1 Calculation of added NPLs for encapsulation into HES and BSA Nanocapsules (NCs)

NC diameter at 90°/ nm (sample 10:1 from table 1)	Radius/ nm	Volume of one NC/ m³
234	117	6.71×10^{-21}
Solid content of dispersion/ wt%	**mL NC in 1 mL dispersion, if density = 1 g/cm³**	**Volume of NC in dispersion/ m³**
0.714	0.00714	7.14×10^{-9}

$$\text{Amount of NCs/ mL} = \frac{\text{Volume of one NC/m}^3}{\text{Volume NCs in dispersion/m}^3}$$

$$= \frac{7.14 \times 10^{-9}}{6.71 \times 10^{-21}} = 1.064 \times 10^{12} \, NCs/mL$$

Since the total volume of the BSA NC dispersion is 16.55 mL, a total amount of NCs in dispersion is approximately 1.76×10^{13} NCs. NPLs concentration obtained was 1.99×10^{15} NPLs/mL. Therefore, for a 10:1 ratio 88.64 µL, for a 5:1 ratio 44.32 µL and for a 1:1 ratio 8.86 µL of NPLs dispersion needs to be added to the mixture. According to previously performed experiments and expected capsule diameters, 57.02 µL (10:1), 28.51 µL (5:1) and 5.70 µL (1:1) were added.

Then, HES or BSA respectively, were added into the aqueous dispersed phase and emulsified in cyclohexane with a surfactant. By adding the crosslinker toluene diisocyanate (TDI) to the generated miniemulsion, a polyaddition at the interface of the droplets is performed, leading to the formation of a polymeric shell. In order to use the NCs for cell experiments, they must be redispersed in aqueous solution. We analyzed sizes of the obtained BSA NCs (Table 7.2) and HES NC (Table 7.3) with encapsulated NPLs in three different ratios in cyclohexane as well as the zeta potentials after redispersion in water. Furthermore, we analyzed morphologies of the obtained BSA NCs in cyclohexane by TEM (Figure 7.1).

Table 7.2 Physicochemical properties of BSA NC with encapsulated NPLs in different ratios. Hydrodynamic radii where determined using multiangle DLS (30 – 150°) with a standard deviation of 10%. Dispersions were filtered with a PTFE syringe filter (pore size 5 μm) prior to measurement.

Ratio (NPLs:NC)	R_h/ nm (cyclohexane)	R_h/ nm (water)	PDI (90°) in cyclohexane	PDI (90°) in water	ζ-potential/ mV in water
10:1	200 ± 20	202 ± 20	0.248	0.207	-27.8 ± 4.42
5:1	226 ± 23	192 ± 19	0.179	0.202	-30.0 ± 3.86
1:1	218 ± 22	218 ± 22	0.183	0.219	-29.3 ± 4.11

Table 7.3 Size distributions of HES NC with different ratios of encapsulated NPLs measured at an angle of 90°.

Sample	R_h/ nm (cyclohexane)	PDI in cyclohexane
10:1 NPLs:NC	149 ± 67 nm	0.193
5:1 NPLs:NC	148 ± 101 nm	0.263
1:1 NPLs:NC	140 ± 103 nm	0.247
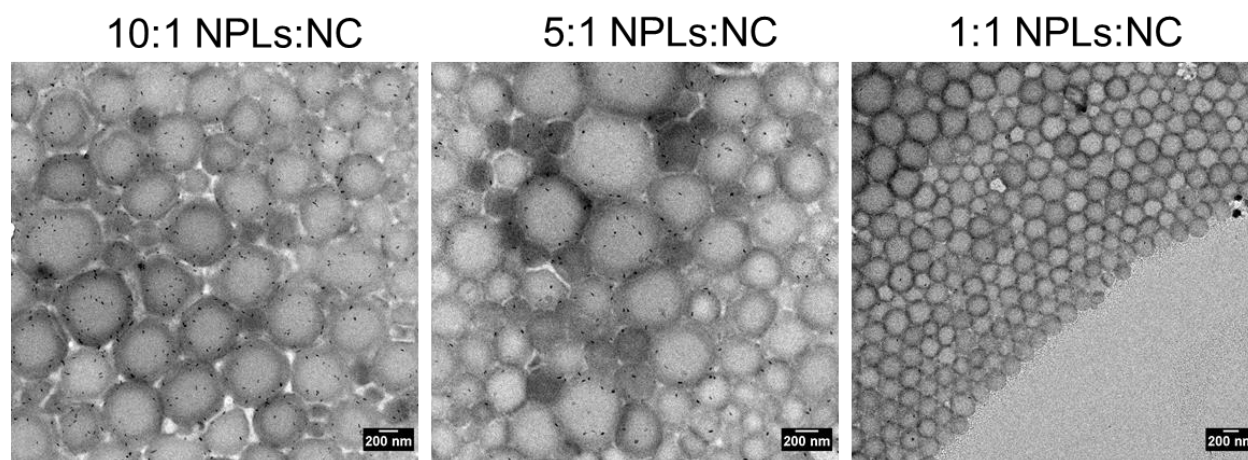
Figure 7.1 TEM micrographs of BSA NC listed in Table 1 in cyclohexane. White scalebars indicate a length of 200 nm.

The NCs obtained after encapsulation of different NPLs ratios, showed hydrodynamic radii of around 200 nm in cyclohexane as well as in water and a polydispersity index (PDI) of around 0.2. The ζ-potential of all capsules was negative. Table 1 demonstrates that there are no significant changes in size and surface charge upon encapsulation of different NPLs concentrations. A

reduction of the fluorescence intensity of the green fluorescent label FITC (fluorescein isothiocyanate) in dependency of the amount of encapsulated NPLs, confirmed successful encapsulation. FITC was attached to the surface of BSA NCs containing NPLs and it is assumed that the reduction of median fluorescence intensity (MFI) is caused by an absorption of the green fluorescence by the red one due to close proximity of both dyes (Figure 7.2) as measured by applying flow cytometry. Furthermore, we analyzed the morphology of the BSA NCs with NPLs (5:1) by cryo-TEM (Figure 7.3 C) and display the optical properties of the NCs with encapsulated NPLs (Fig. 7.3 A and B).
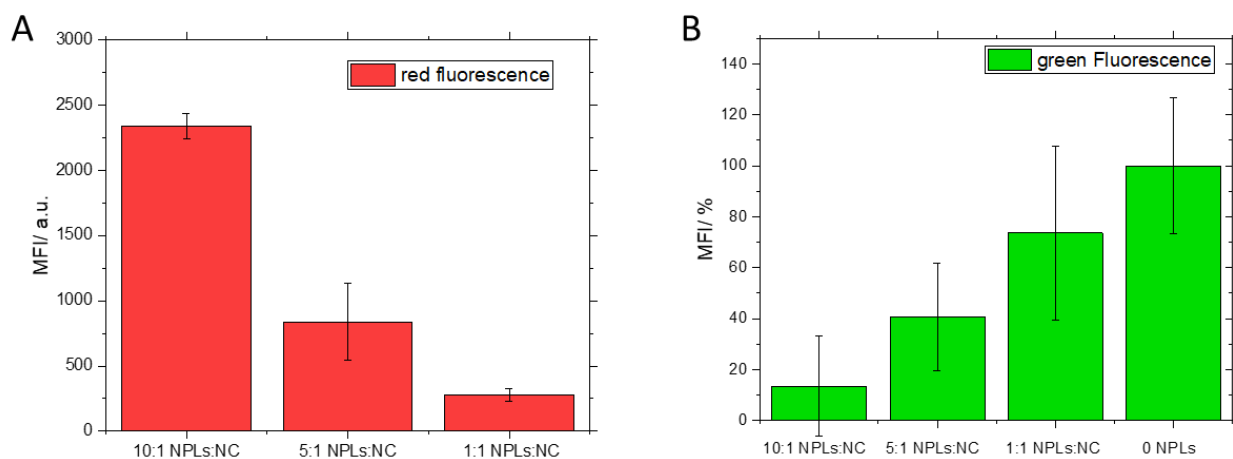
Figure 7.2 Flow cytometry measurements of FITC labeled BSA NC with encapsulated NPLs. A: MFI of red fluorescence of the NPLs. B: Reduction of FITC MFI in percent caused by encapsulation of NPLs.
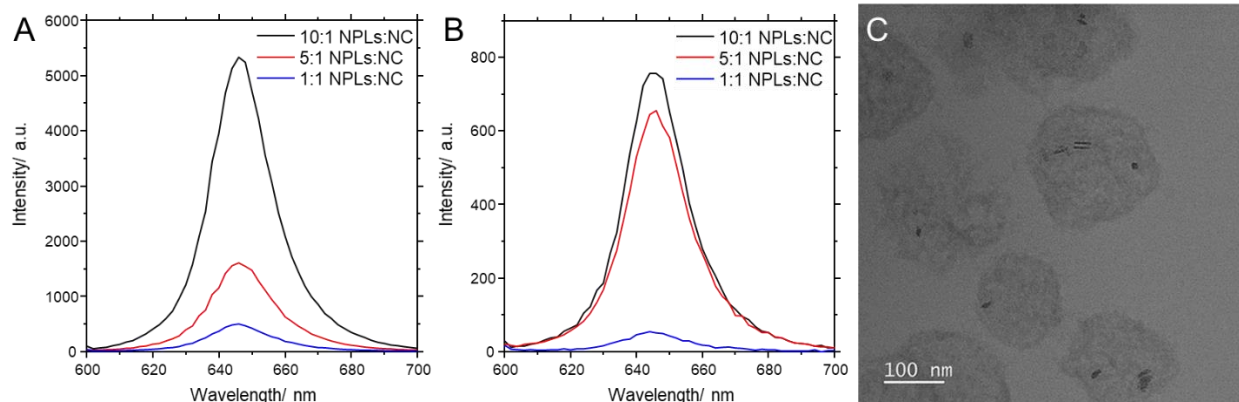
Figure 7.3 A) Fluorescence intensity measurements of BSA NC with encapsulated NPLs in different ratios in cyclohexane. B) Fluorescence intensity measurements of BSA NC with encapsulated NPLs in different ratios in water. C) cryo-TEM in water of BSA NC containing NPLs in a 5:1 ratio.

Figure 7.3 A demonstrates the fluorescence emission spectra of BSA NC containing different NPLs concentrations in cyclohexane. The NPLs inside the NC show an emission maximum at 646 nm at 590 nm excitation. As expected, the 10:1 ratio shows the strongest fluorescence signal, while the signal is decreasing for the other ratios. When the NCs are transferred to water, the fluorescence intensity decreases for all the ratios (Figure 7.3 B). For the emission spectra of the 1:1 ratio only a very weak signal can be detected. Figure 7.3 B also demonstrates that there is only a very small difference in fluorescence intensity between the 10:1 ratio and the 5:1 ratio after water transfer. The cryo-TEM micrograph in Figure 7.3 C shows that the BSA NCs are spherical and that they contain at least one NPL per NC encapsulated. Based on the cryo-TEM micrographs and the minimal gain of PL intensity for the 10:1 ratio (Figure 7.3 B), we selected the 5:1 ratio as the optimized ratio for labelling the NCs. After successful water transfer, RAW264.7 macrophages were incubated with different concentrations of BSA NCs containing NPLs (5:1) and different incubation times of the cells were compared (Figure 7.4).
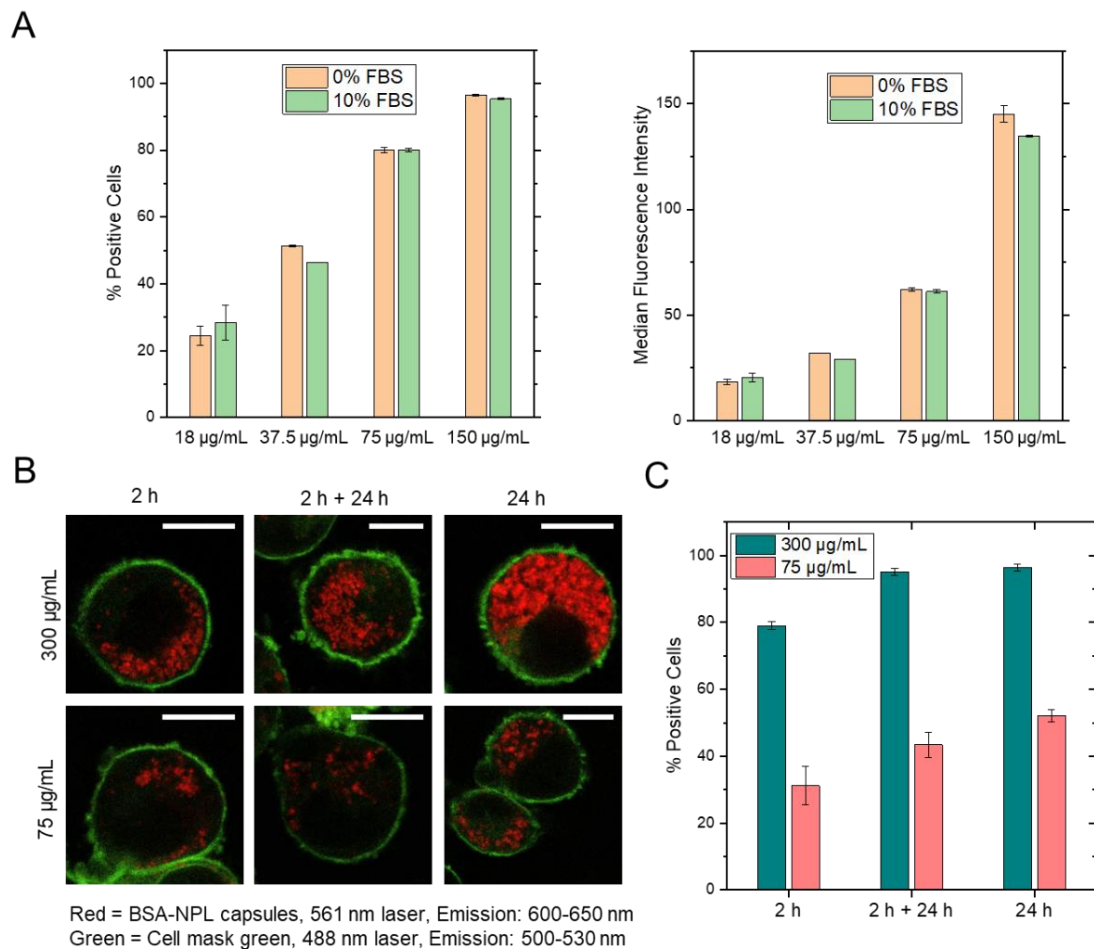
Figure 7.4 Cell uptake of BSA NCs + NPLs with and without incubation in fetal bovine serum (FBS) into RAW 264.7 macrophages for different concentrations and different time periods. A) Percentage of cells found containing NCs and median fluorescence intensity analyzed by flow cytometry with and without addition of 10% FBS. B) Confocal laser scanning microscopy images of the cell samples after uptake of BSA NCs for two concentrations and in a time-dependent manner. The cell membrane is pseudocoloured in green while the NPLs are shown in red. C) Percentage of positive cells found containing NCs after time-dependent incubation of 75 µg/mL and 300 µg/mL of NCs into RAW267.4 macrophages.

Figure 7.4 A shows that the uptake of NCs into macrophages appears to be concentration-dependent. We found one third of macrophages positive for NCs containing NPLs at a concentration of 18 µg/mL, while at 150 µg/mL NCs we found up to approximately 90% of macrophages positive. Addition of 10% fetal bovine serum (FBS) does not show a significant

difference in uptake behavior, either suggesting no formation of protein corona around the BSA NCs or that the FBS proteins are biologically similar or identical to the BSA proteins. Analysis of the median fluorescence intensity (MFI) of the same incubated cells, indicates a similar result.

Next to the concentration dependency of the uptake, we observed also a time-dependent uptake of the BSA NCs (Figure 7.4 B and C) and in addition, confocal laser scanning microscopy (cLSM) proves uptake of the NC containing NPLs (Figure 7.4 B). Comparison of three experiments with different incubation times which were performed simultaneously, revealed that the uptake into the macrophages was time-dependent. In a first experiment, we incubated macrophages with NCs containing NPLs for 2 h and we immediately analyzed the uptake by cLSM (Figure 7.4 B, left panel), while in a second experiment, after 2 h incubation, we interrupted incubation for 24 h and observed the cells afterwards by cLSM (Figure 7.4 B, middle panel). In a third experiment, we continuously incubated cells with NC containing NPLs for 24 h (Figure 7.4 B, right panel). These three experiments allow us to determine whether the cell uptake is slow (~24 h) of fast (<2 h) and monitor where the NCs may be localized or degraded in the cell once the cell stops taking up new capsules.

Furthermore, we determined the positive cells by flow cytometry (Figure 7.4 C). Figure 7.4 B again proves concentration-dependent uptake of NC into the cells, since higher fluorescence intensities can be observed for an incubation with 300 µg/mL of NCs than for the incubation with the same capsules at a concentration of 75 µg/mL. For the different time periods, we observed an increased fluorescence intensity after an incubation period of 24 h in comparison to a 2 h incubation time. As displayed in Figure 7.4 C, a slightly higher percentage of fluorescent cells is detectable after the NC uptake was stopped and kept for 24 h (2 h uptake + 24 h no uptake) than after immediate analysis of the cells (2 h uptake) at concentration of 75 µg/mL, which is clearly increased at a concentration of 300 µg/mL (2 h). Moreover, Figure 2 C demonstrates, that there is no significant increase of positive cells detectable after a 24 h incubation time in comparison to 2 h incubation with a 24 h period of no uptake, which suggests, that the macrophages already reached their maximum uptake capacity after 2 h of incubation. A period of 24 h after incubation could perhaps lead to degradation of the BSA NC inside the cells, resulting in the release of the encapsulated NPLs.

After analysis of the uptake behavior of the macrophages towards the NCs containing NPLs by cLSM and flow cytometry, we embedded the cells into a matrix and analyzed the slices by TEM. Figure 7.5 shows a macrophage containing BSA NCs with encapsulated NPLs in a 5:1 ratio.
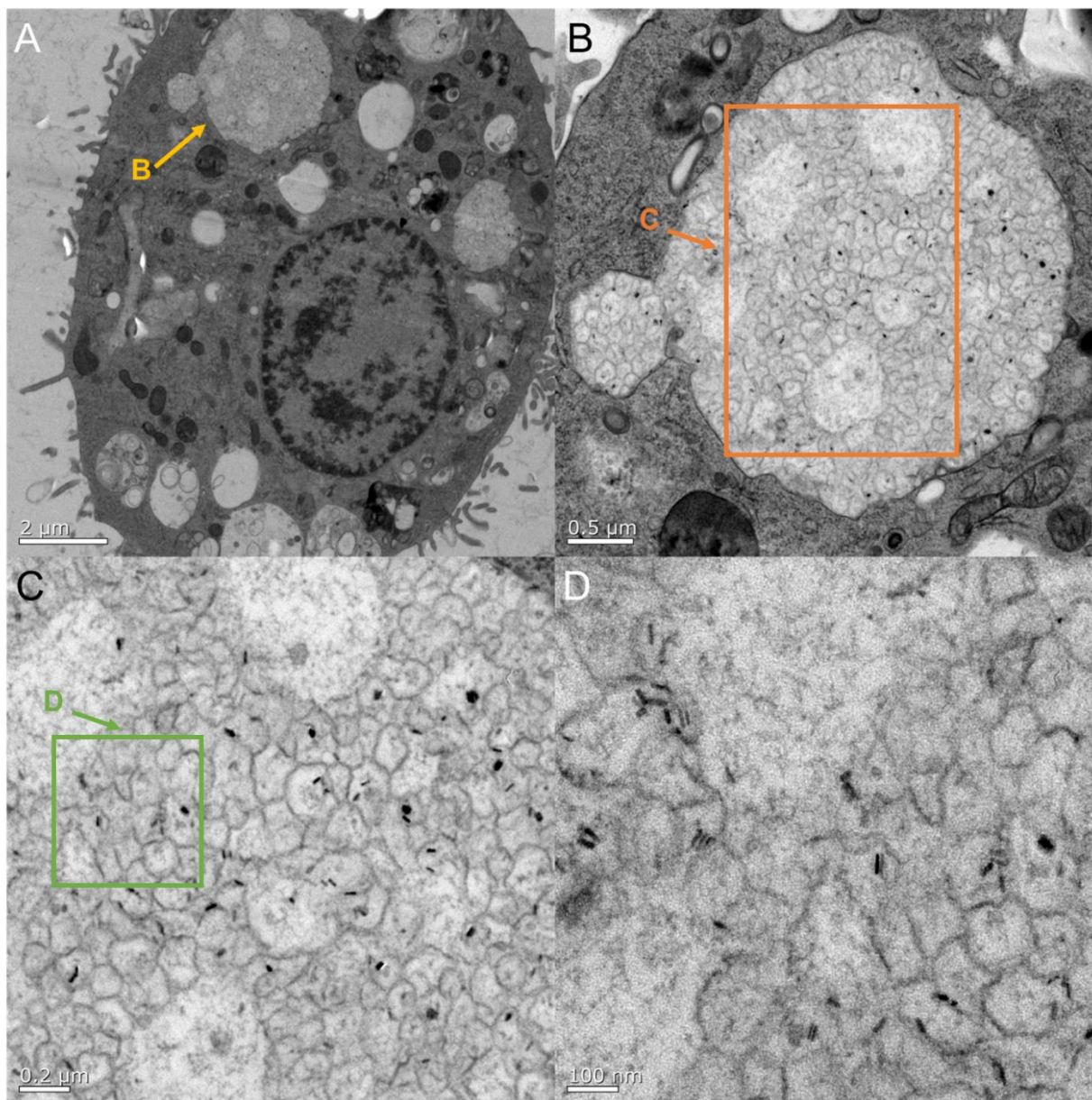
Figure 7.5 TEM images of the cellular uptake and intercellular localization of BSA NCs + NPLs. Cells were incubated with NC at a concentration of 300 µg/mL for 24 h. The cells were washed after 1 h with PBS and fresh cell growth medium without further NCs was added and incubated for 23 h. A) BSA NCs + NPLs in RAW 264.7 cells in vesicles, scale 2000 nm B) 500 nm C) 200 nm D) 100 nm.

Figure 7.5 B demonstrates, that the NCs are stored in vesicles inside the cells. The high cell loading of 300 µg/mL of NCs appears to overload the vesicles and deform the shape of the capsules, though it does not cause apoptosis to the cells, as shown in Figure 7.5 B. The NCs keep their core-shell structure during uptake and the encapsulated NPLs are visually clearly setting apart from the NCs due to their high electron-density and rectangular shape, thus clearly identifying the NCs inside the cell. In the different magnifications, the high concentration of NCs inside the vesicles is visible, while the NPLs are randomly distributed inside the NCs. A lot of NCs just contain one NPL, which again supports the assumption that at least a 5:1 ratio of NPLs in comparison to NCs is necessary to encapsulate at least one NPLs per NC.

To unambiguously identify the NCs containing NPLs inside the cell, we performed correlative light and electron microscopy (cLEM).
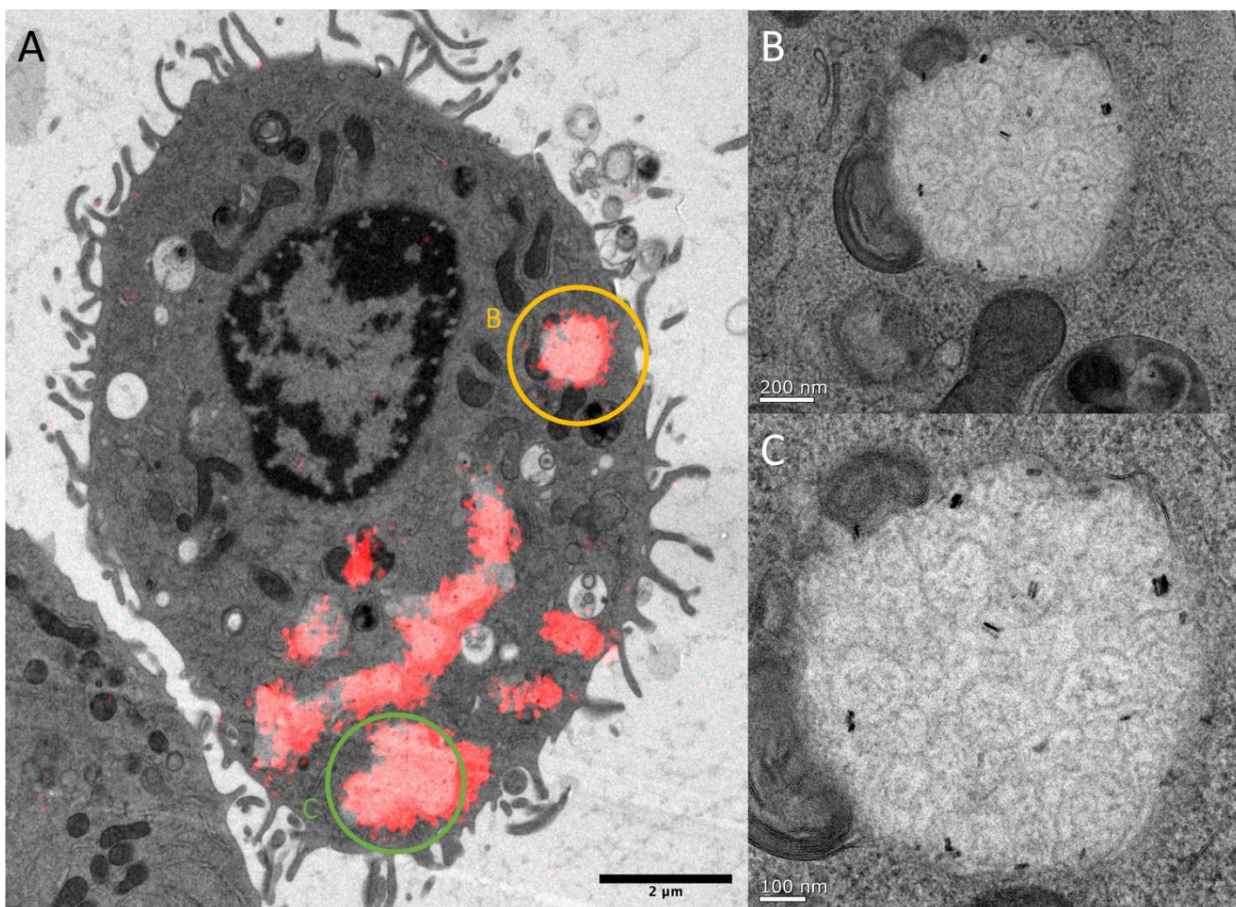
Figure 7.6 BSA NCs + NPLs in RAW 264.7 cells a.) CLEM Image (TEM and cLSM) of BSA NCs + NPLs (the BSA NCs with a concentration of 300 µg/mL, incubated for 1 hour with RAW 264.7 cells, washed and kept for 23 hours before measurement), scale bar 1µm b.) & c.) High magnification images of BSA NCs + NPLs.

Figure 7.6 reveals different parts of a macrophage which show red fluorescence. The red fluorescence is derived from the NPLs inside the NCs and is overlapping to a large extent with the optical findings of the NPLs in the electron microscopy images, thus clearly identifying the NCs inside the cell. Figure 7.6 b and c which represent magnifications of bright areas in the macrophage, demonstrate vesicles, filled with NC containing NPLs inside the cell. In this macrophage, it is again evident that the high uptake of NCs did not trigger apoptotic processes. This is confirmed by the performance of a cytotoxicity assay, which showed high cell viability of the macrophages incubated with different concentrations of NCs containing NPLs (5:1) in the presence of FBS (Figure 7.7).
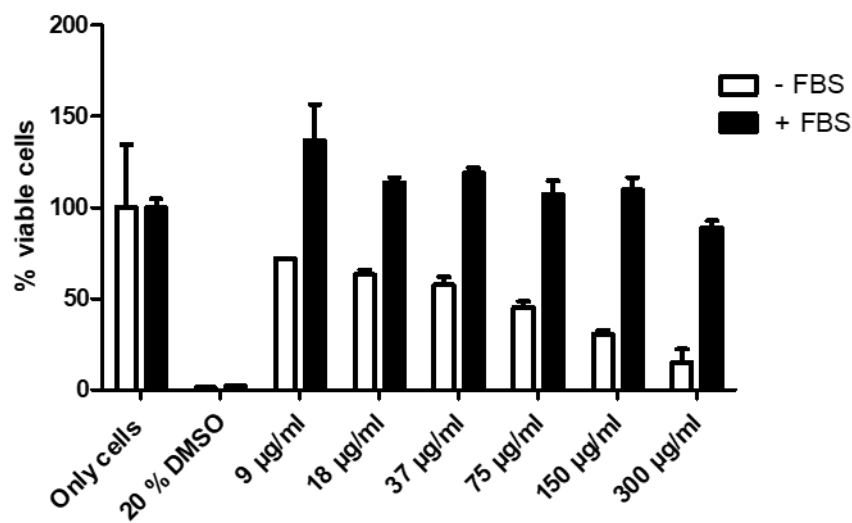
Figure 7.7 Cell viability of RAW264.7 macrophages after incubation with different concentrations of BSA NC containing NPLs (5:1) with fetal bovine serum (FBS) and without.

7.3 Conclusions

We demonstrated that NPL containing NCs can be detected and unambiguously localized by cLEM. The encapsulation of the NPLs into biocompatible NCs could be accomplished without disturbing the NC formation and damaging the NPLs' properties, obtaining a stable dispersion with high fluorescence intensity. We were able to adjust different NPL concentrations inside the NCs and obtained reproducible size distributions. The bright fluorescent signal indicated the NCs were taken up inside macrophages in a time-dependent manner. Combined with cLEM, we could even see the different parts of macrophages where the NCs are taken up.

With the help of our method, NCs with aqueous cores can be readily visualized by cLEM inside a cell using NPLs as markers. We are currently doing more detailed analysis on our images to better understand the role of uptake amount relative to the capsule degradation and the fate of the NCs inside the cells, in particular where they are localized at different times. This localization method should be extendable to polymeric nanocarriers in general, making it very important for future research on cell uptake mechanisms and may reveal the metabolic pathway of an encapsulated drug.

Final conclusions and outlooks

Through the works in this thesis I described how the surface of NPLs play a role in the optimization of their properties for applications in imaging and energy transfer. Chapter 2, 3 and 4 relates to the transfer of energy to small organic molecules, while chapter 5, 6 and 7 relates to retention of PL at different conditions so that the NPLs can become bright markers in biological applications. This work contributes to the understanding of how the nanocrystal geometry can influence their interaction with small molecules and polymer, which is helpful for their applications in bioimaging, photon upconversion and photocatalysis.

In chapter 2, we saw how NPLs transfer their energy to DBTCA fluorophores conjugated to the surface of the NPLs. The localized exciton in the NPLs means that the DBTCA coverage density mattered more than the DBTCA/NPL ratio to get high FRET efficiency. The flat geometry allowed the DBTCA to be close to each other at high coverage density, which results in self-quenching between DBTCA. To minimize this problem, fewer DBTCA needs to be on the surface of one NPL, while keeping the FRET from the exciton to the DBTCA high. Since FRET is highly distance dependent, we were able to estimate that smaller NPLs should be able to keep the high FRET efficiency at low DBTCA/NPL ratio and proposed this approach as one way to minimize energy loss from self-quenching.

We explored more about the energy losses in chapter 3, in the framework of triplet-triplet annihilation upconversion. Here the ACA ligands could aggregate on the flat surface of NPLs, shifting the energy level of ACA, which impacted the upconversion process by creating the possibility of back transfer. This highlights how important surface interaction is when designing energy transfer system as it can affect the energetic alignment. Knowing this opens new possibilities to prevent the energy loss e.g. bulkier ligands, or to utilize the energy shift for some intended application.

In chapter 4, we saw how NPLs can be used for white light photocatalysis though the model reaction of nitrobenzene to azoxybenzene. The near-equal conduction band energies of the 3, 4 and 5 ML NPLs allows the 5ML NPLs to take advantage of their broader absorption wavelengths,

leading to greater conversion. This was also supported by the higher quantum yields of the 5ML NPLs compared to the two thinner NPLs. From this study, we see the possibility of reduction photocatalysis with even thicker NPLs could further increase the white light absorption.

The development of the polymer coating in chapter 5 shows how the surface ligands can aid the interaction between the NPLs with the amphiphilic polymer. This helped to overcome the facile agglomeration of NPLs during the phase transfer to water. The polymer coated NPLs show high fluorescent brightness in one and two-photon excitation, despite their modest quantum yields, thanks to their high absorption cross sections. The polymer coating also makes the NPLs colloidally stable and chemically inert.

The robustness of the polymer coated NPLs is demonstrated in chapter 6, where they were compared to ligand exchanged NPLs. The PL of the polymer coated NPLs is more difficult to quench and they do not agglomerate as easily in protein containing medium. This was a result of the lower surface dynamics of the polymer coated NPLs compared to the ligand exchanged NPLs with higher surface dynamics. This difference – unrelated to the commonly studied parameters of particle, size, shape and charge – influenced the interaction with the protein corona and ultimately the uptake to the cells.

Additionally, we used the high brightness and high electron density of NPLs as microscopy markers, to localize polymeric nanocapsules and try to understand their uptake to cells in chapter 7. The rectangular geometry of NPLs and their large lateral size makes it possible to unambiguously identify them in the electron microscope, which circumvents the need of elemental analysis to confirm the identity of the marker. With this new marker, we can analyze the uptake of nanocapsules and other nanocarriers in detail and uncover their uptake mechanism.

Overall, this thesis showed how NPL properties and energy transfer processes can be tuned through the understanding of surface interactions. Future works can utilize this idea for a broader scope in the bioimaging field and photocatalysis field. This could lead to nanocrystal-based systems with higher performance (e.g. fluorescence brightness, photocatalytic conversion).

References

1. Atkins, P.; Overton, T., *Shriver and Atkins' Inorganic Chemistry*. 5 ed.; OUP Oxford: 2010.

2. Alivisatos, A. P., Semiconductor Clusters, Nanocrystals, and Quantum Dots. *Science* **1996,** *271* (5251), 933-937.

3. Quantum Dots | Sigma Aldrich. https://www.sigmaaldrich.com/technical-documents/articles/materials-science/nanomaterials/quantum-dots.html (accessed 27th May 2020).

4. Krauss, T. D.; Peterson, J. J., Electronic structure and optical transitions in colloidal semiconductor nanocrystals. In *Colloidal Quantum Dot Optoelectronics and Photovoltaics*, Sargent, E. H.; Konstantatos, G., Eds. Cambridge University Press: Cambridge, 2013; pp 59-86.

5. Leatherdale, C. A.; Woo, W. K.; Mikulec, F. V.; Bawendi, M. G., On the Absorption Cross Section of CdSe Nanocrystal Quantum Dots. *The Journal of Physical Chemistry B* **2002,** *106* (31), 7619-7622.

6. Yeltik, A.; Delikanli, S.; Olutas, M.; Kelestemur, Y.; Guzelturk, B.; Demir, H. V., Experimental Determination of the Absorption Cross-Section and Molar Extinction Coefficient of Colloidal CdSe Nanoplatelets. *The Journal of Physical Chemistry C* **2015,** *119* (47), 26768-26775.

7. Scott, R.; Achtstein, A. W.; Prudnikau, A.; Antanovich, A.; Christodoulou, S.; Moreels, I.; Artemyev, M.; Woggon, U., Two Photon Absorption in II–VI Semiconductors: The Influence of Dimensionality and Size. *Nano Letters* **2015,** *15* (8), 4985-4992.

8. Riedinger, A.; Ott, F. D.; Mule, A.; Mazzotti, S.; Knüsel, P. N.; Kress, Stephan J. P.; Prins, F.; Erwin, S. C.; Norris, D. J., An intrinsic growth instability in isotropic materials leads to quasi-two-dimensional nanoplatelets. *Nature Materials* **2017,** *16* (7), 743-748.

9. Christodoulou, S.; Climente, J. I.; Planelles, J.; Brescia, R.; Prato, M.; Martín-García, B.; Khan, A. H.; Moreels, I., Chloride-Induced Thickness Control in CdSe Nanoplatelets. *Nano Letters* **2018,** *18* (10), 6248-6254.

10. Dufour, M.; Qu, J.; Greboval, C.; Méthivier, C.; Lhuillier, E.; Ithurria, S., Halide Ligands To Release Strain in Cadmium Chalcogenide Nanoplatelets and Achieve High Brightness. *ACS Nano* **2019**.

11. Knauf, R. R.; Lennox, J. C.; Dempsey, J. L., Quantifying Ligand Exchange Reactions at CdSe Nanocrystal Surfaces. *Chemistry of Materials* **2016,** *28* (13), 4762-4770.

12. Anderson, N. C.; Hendricks, M. P.; Choi, J. J.; Owen, J. S., Ligand Exchange and the Stoichiometry of Metal Chalcogenide Nanocrystals: Spectroscopic Observation of Facile Metal-Carboxylate Displacement and Binding. *Journal of the American Chemical Society* **2013,** *135* (49), 18536-18548.

13. Owen, J., The coordination chemistry of nanocrystal surfaces. *Science* **2015,** *347* (6222), 615-616.

14. Ko, J.-H.; Yoo, D.; Kim, Y.-H., Atomic models for anionic ligand passivation of cation-rich surfaces of IV–VI, II–VI, and III–V colloidal quantum dots. *Chemical Communications* **2017,** *53* (2), 388-391.

15. Pearson, R. G., Hard and soft acids and bases, HSAB, part 1: Fundamental principles. *Journal of Chemical Education* **1968,** *45* (9), 581.

16. Derjaguin, B. V., Acta Physicochim. *USSR* **1941,** *14*.

17. Verwey, E. J. W.; Overbeek, J. T. G., Theory of the stability of lyophobic colloids. *Journal of Colloid Science* **1955,** *10* (2), 224-225.

18. Derjaguin, B., Untersuchungen über die Reibung und Adhäsion, IV. *Kolloid-Zeitschrift* **1934,** *69* (2), 155-164.

19.   Liz-Marzán, L. M.; Correa-Duarte, M. A.; Pastoriza-Santos, I.; Mulvaney, P.; Ung, T.; Giersig, M.; Kotov, N. A., Chapter 5 - CORE-SHELL NANOPARTICLES AND ASSEMBLIES THEREOF. In *Handbook of Surfaces and Interfaces of Materials*, Nalwa, H. S., Ed. Academic Press: Burlington, 2001; pp 189-237.

20.   Tadros, T., Steric Stabilization. In *Encyclopedia of Colloid and Interface Science*, Tadros, T., Ed. Springer Berlin Heidelberg: Berlin, Heidelberg, 2013; pp 1048-1049.

21.   DeArmitt, C.; Rothon, R., 22 - Dispersants and Coupling Agents. In *Applied Plastics Engineering Handbook (Second Edition)*, Kutz, M., Ed. William Andrew Publishing: 2017; pp 501-516.

22.   Ithurria, S.; Dubertret, B., Quasi 2D Colloidal CdSe Platelets with Thicknesses Controlled at the Atomic Level. *Journal of the American Chemical Society* **2008,** *130* (49), 16504-16505.

23.   Ithurria, S.; Tessier, M. D.; Mahler, B.; Lobo, R. P. S. M.; Dubertret, B.; Efros, A. L., Colloidal nanoplatelets with two-dimensional electronic structure. *Nature Materials* **2011,** *10* (12), 936-941.

24.   Ithurria, S.; Talapin, D. V., Colloidal Atomic Layer Deposition (c-ALD) using Self-Limiting Reactions at Nanocrystal Surface Coupled to Phase Transfer between Polar and Nonpolar Media. *Journal of the American Chemical Society* **2012,** *134* (45), 18585-18590.

25.   Chu, A.; Livache, C.; Ithurria, S.; Lhuillier, E., Electronic structure robustness and design rules for 2D colloidal heterostructures. *Journal of Applied Physics* **2018,** *123* (3), 035701.

26.   Meerbach, C.; Wu, C.; Erwin, S. C.; Dang, Z.; Prudnikau, A.; Lesnyak, V., Halide-Assisted Synthesis of Cadmium Chalcogenide Nanoplatelets. *Chemistry of Materials* **2020,** *32* (1), 566-574.

27.   Knüsel, P. N.; Riedinger, A.; Rossinelli, A. A.; Ott, F. D.; Mule, A. S.; Norris, D. J., Experimental Evidence for Two-Dimensional Ostwald Ripening in Semiconductor Nanoplatelets. *Chemistry of Materials* **2020,** *32* (7), 3312-3319.

28.   Ott, F. D.; Riedinger, A.; Ochsenbein, D. R.; Knüsel, P. N.; Erwin, S. C.; Mazzotti, M.; Norris, D. J., Ripening of Semiconductor Nanoplatelets. *Nano Letters* **2017**.

29.   Riedinger, A.; Mule, A. S.; Knüsel, P. N.; Ott, F. D.; Rossinelli, A. A.; Norris, D. J., Identifying reactive organo-selenium precursors in the synthesis of CdSe nanoplatelets. *Chemical Communications* **2018,** *54* (83), 11789-11792.

30.   Cho, W.; Kim, S.; Coropceanu, I.; Srivastava, V.; Diroll, B. T.; Hazarika, A.; Fedin, I.; Galli, G.; Schaller, R. D.; Talapin, D. V., Direct Synthesis of Six-Monolayer (1.9 nm) Thick Zinc-Blende CdSe Nanoplatelets Emitting at 585 nm. *Chemistry of Materials* **2018,** *30* (20), 6957-6960.

31.   Polovitsyn, A.; Dang, Z.; Movilla, J. L.; Martín-García, B.; Khan, A. H.; Bertrand, G. H. V.; Brescia, R.; Moreels, I., Synthesis of Air-Stable CdSe/ZnS Core–Shell Nanoplatelets with Tunable Emission Wavelength. *Chemistry of Materials* **2017,** *29* (13), 5671-5680.

32.   Tessier, M. D.; Mahler, B.; Nadal, B.; Heuclin, H.; Pedetti, S.; Dubertret, B., Spectroscopy of Colloidal Semiconductor Core/Shell Nanoplatelets with High Quantum Yield. *Nano Letters* **2013,** *13* (7), 3321-3328.

33.   van Embden, J.; Jasieniak, J.; Mulvaney, P., Mapping the Optical Properties of CdSe/CdS Heterostructure Nanocrystals: The Effects of Core Size and Shell Thickness. *Journal of the American Chemical Society* **2009,** *131* (40), 14299-14309.

34.   Kelestemur, Y.; Guzelturk, B.; Erdem, O.; Olutas, M.; Gungor, K.; Demir, H. V., Platelet-in-Box Colloidal Quantum Wells: CdSe/CdS@CdS Core/Crown@Shell Heteronanoplatelets. *Advanced Functional Materials* **2016,** *26* (21), 3570-3579.

35. Pelton, M.; Andrews, J. J.; Fedin, I.; Talapin, D. V.; Leng, H.; O'Leary, S. K., Nonmonotonic Dependence of Auger Recombination Rate on Shell Thickness for CdSe/CdS Core/Shell Nanoplatelets. *Nano Letters* **2017,** *17* (11), 6900-6906.

36. Mahler, B.; Nadal, B.; Bouet, C.; Patriarche, G.; Dubertret, B., Core/Shell Colloidal Semiconductor Nanoplatelets. *Journal of the American Chemical Society* **2012,** *134* (45), 18591-18598.

37. Halim, H.; Simon, J.; Lieberwirth, I.; Mailänder, V.; Koynov, K.; Riedinger, A., Water-dispersed semiconductor nanoplatelets with high fluorescence brightness, chemical and colloidal stability. *Journal of Materials Chemistry B* **2020,** *8* (1), 146-154.

38. Rossinelli, A. A.; Riedinger, A.; Marques-Gallego, P.; Knusel, P. N.; Antolinez, F. V.; Norris, D. J., High-temperature growth of thick-shell CdSe/CdS core/shell nanoplatelets. *Chemical Communications* **2017.**

39. Rossinelli, A. A.; Rojo, H.; Mule, A. S.; Aellen, M.; Cocina, A.; De Leo, E.; Schaeublin, R.; Norris, D. J., Compositional Grading for Efficient and Narrowband Emission in CdSe-Based Core/Shell Nanoplatelets. *Chemistry of Materials* **2019,** *31* (22), 9567-9578.

40. Altintas, Y.; Quliyeva, U.; Gungor, K.; Erdem, O.; Kelestemur, Y.; Mutlugun, E.; Kovalenko, M. V.; Demir, H. V., Highly Stable, Near-Unity Efficiency Atomically Flat Semiconductor Nanocrystals of CdSe/ZnS Hetero-Nanoplatelets Enabled by ZnS-Shell Hot-Injection Growth. *Small* **2019,** *15* (8), 1804854.

41. Liu, B.; Altintas, Y.; Wang, L.; Shendre, S.; Sharma, M.; Sun, H.; Mutlugun, E.; Demir, H. V., Record High External Quantum Efficiency of 19.2% Achieved in Light-Emitting Diodes of Colloidal Quantum Wells Enabled by Hot-Injection Shell Growth. *Advanced Materials* **2020,** *32* (8), 1905824.

42. Scholes, G. D., Controlling the Optical Properties of Inorganic Nanoparticles. *Advanced Functional Materials* **2008,** *18* (8), 1157-1172.

43. Garakyaraghi, S.; Castellano, F. N., Nanocrystals for Triplet Sensitization: Molecular Behavior from Quantum-Confined Materials. *Inorganic Chemistry* **2018,** *57* (5), 2351-2359.

44. Luo, X.; Han, Y.; Chen, Z.; Li, Y.; Liang, G.; Liu, X.; Ding, T.; Nie, C.; Wang, M.; Castellano, F. N.; Wu, K., Mechanisms of triplet energy transfer across the inorganic nanocrystal/organic molecule interface. *Nature Communications* **2020,** *11* (1), 28.

45. McCluskey, M. D.; Janotti, A., Defects in Semiconductors. *Journal of Applied Physics* **2020,** *127* (19), 190401.

46. Greaney, M. J.; Couderc, E.; Zhao, J.; Nail, B. A.; Mecklenburg, M.; Thornbury, W.; Osterloh, F. E.; Bradforth, S. E.; Brutchey, R. L., Controlling the Trap State Landscape of Colloidal CdSe Nanocrystals with Cadmium Halide Ligands. *Chemistry of Materials* **2015,** *27* (3), 744-756.

47. Ren, T.; Mandal, P. K.; Erker, W.; Liu, Z.; Avlasevich, Y.; Puhl, L.; Müllen, K.; Basché, T., A Simple and Versatile Route to Stable Quantum Dot−Dye Hybrids in Nonaqueous and Aqueous Solutions. *Journal of the American Chemical Society* **2008,** *130* (51), 17242-17243.

48. Brumberg, A.; Harvey, S. M.; Philbin, J. P.; Diroll, B. T.; Lee, B.; Crooker, S. A.; Wasielewski, M. R.; Rabani, E.; Schaller, R. D., Determination of the In-Plane Exciton Radius in 2D CdSe Nanoplatelets via Magneto-optical Spectroscopy. *ACS Nano* **2019,** *13* (8), 8589-8596.

49. Li, Q.; Liu, Q.; Schaller, R. D.; Lian, T., Reducing the Optical Gain Threshold in Two-Dimensional CdSe Nanoplatelets by the Giant Oscillator Strength Transition Effect. *The Journal of Physical Chemistry Letters* **2019,** *10* (7), 1624-1632.

50.   Morgan, D. P.; Kelley, D. F., Exciton Localization and Radiative Lifetimes in CdSe Nanoplatelets. *The Journal of Physical Chemistry C* **2019,** *123* (30), 18665-18675.

51.   Dexter   Energy   Transfer. https://chem.libretexts.org/Bookshelves/Physical_and_Theoretical_Chemistry_Textbook_Maps/ Supplemental_Modules_(Physical_and_Theoretical_Chemistry)/Fundamentals/Dexter_Energy_ Transfer.

52.   Verhoeven, J. W., Glossary of terms used in photochemistry (IUPAC Recommendations 1996). *Pure and Applied Chemistry* **1996,** *68* (12), 2223.

53.   Parker, C.; Hatchard, C., Delayed fluorescence from solutions of anthracene and phenanthrene. *Proceedings of the Royal Society of London. Series A. Mathematical and Physical Sciences* **1962,** *269* (1339), 574-584.

54.   Mongin, C.; Garakyaraghi, S.; Razgoniaeva, N.; Zamkov, M.; Castellano, F. N., Direct observation of triplet energy transfer from semiconductor nanocrystals. *Science* **2016,** *351* (6271), 369-372.

55.   Dzebo, D.; Moth-Poulsen, K.; Albinsson, B., Robust triplet–triplet annihilation photon upconversion by efficient oxygen scavenging. *Photochemical & Photobiological Sciences* **2017,** *16* (8), 1327-1334.

56.   Kim, J.-H.; Deng, F.; Castellano, F. N.; Kim, J.-H., High Efficiency Low-Power Upconverting Soft Materials. *Chemistry of Materials* **2012,** *24* (12), 2250-2252.

57.   Gray, V.; Moth-Poulsen, K.; Albinsson, B.; Abrahamsson, M., Towards efficient solid-state triplet–triplet annihilation based photon upconversion: Supramolecular, macromolecular and self-assembled systems. *Coordination Chemistry Reviews* **2018,** *362*, 54-71.

58.   Baluschev, S.; Miteva, T.; Yakutkin, V.; Nelles, G.; Yasuda, A.; Wegner, G., Up-Conversion Fluorescence: Noncoherent Excitation by Sunlight. *Physical Review Letters* **2006,** *97* (14), 143903.

59.   Amemori, S.; Sasaki, Y.; Yanai, N.; Kimizuka, N., Near-Infrared-to-Visible Photon Upconversion Sensitized by a Metal Complex with Spin-Forbidden yet Strong S0–T1 Absorption. *Journal of the American Chemical Society* **2016,** *138* (28), 8702-8705.

60.   Singh-Rachford, T. N.; Castellano, F. N., Photon upconversion based on sensitized triplet–triplet annihilation. *Coordination Chemistry Reviews* **2010,** *254* (21), 2560-2573.

61.   Huang, Z.; Xu, Z.; Mahboub, M.; Liang, Z.; Jaimes, P.; Xia, P.; Graham, K. R.; Tang, M. L.; Lian, T., Enhanced Near-Infrared-to-Visible Upconversion by Synthetic Control of PbS Nanocrystal Triplet Photosensitizers. *Journal of the American Chemical Society* **2019,** *141* (25), 9769-9772.

62.   Huang, Z.; Li, X.; Mahboub, M.; Hanson, K. M.; Nichols, V. M.; Le, H.; Tang, M. L.; Bardeen, C. J., Hybrid Molecule–Nanocrystal Photon Upconversion Across the Visible and Near-Infrared. *Nano Letters* **2015,** *15* (8), 5552-5557.

63.   Gray, V.; Xia, P.; Huang, Z.; Moses, E.; Fast, A.; Fishman, D. A.; Vullev, V. I.; Abrahamsson, M.; Moth-Poulsen, K.; Lee Tang, M., CdS/ZnS core–shell nanocrystal photosensitizers for visible to UV upconversion. *Chemical Science* **2017,** *8* (8), 5488-5496.

64.   Xia, P.; Huang, Z.; Li, X.; Romero, J. J.; Vullev, V. I.; Pau, G. S. H.; Tang, M. L., On the efficacy of anthracene isomers for triplet transmission from CdSe nanocrystals. *Chemical Communications* **2017,** *53* (7), 1241-1244.

65.   De Roo, J.; Huang, Z.; Schuster, N. J.; Hamachi, L. S.; Congreve, D. N.; Xu, Z.; Xia, P.; Fishman, D. A.; Lian, T.; Owen, J. S.; Tang, M. L., Anthracene Diphosphate Ligands for CdSe Quantum Dots; Molecular Design for Efficient Upconversion. *Chemistry of Materials* **2020**.

66.   Xu, Z.; Huang, Z.; Jin, T.; Lian, T.; Tang, M. L., Mechanistic Understanding and Rational Design of Quantum Dot/Mediator Interfaces for Efficient Photon Upconversion. *Accounts of Chemical Research* **2020**.

67.   Huang, Z.; Xia, P.; Megerdich, N.; Fishman, D. A.; Vullev, V. I.; Tang, M. L., ZnS Shells Enhance Triplet Energy Transfer from CdSe Nanocrystals for Photon Upconversion. *ACS Photonics* **2018**.

68.   Piland, G. B.; Huang, Z.; Lee Tang, M.; Bardeen, C. J., Dynamics of Energy Transfer from CdSe Nanocrystals to Triplet States of Anthracene Ligand Molecules. *The Journal of Physical Chemistry C* **2016,** *120* (11), 5883-5889.

69.   Monguzzi, A.; Mezyk, J.; Scotognella, F.; Tubino, R.; Meinardi, F., Upconversion-induced fluorescence in multicomponent systems: Steady-state excitation power threshold. *Physical Review B* **2008,** *78* (19), 195112.

70.   Caputo, J. A.; Frenette, L. C.; Zhao, N.; Sowers, K. L.; Krauss, T. D.; Weix, D. J., General and Efficient C–C Bond Forming Photoredox Catalysis with Semiconductor Quantum Dots. *Journal of the American Chemical Society* **2017,** *139* (12), 4250-4253.

71.   Jones, G. A.; Bradshaw, D. S., Resonance Energy Transfer: From Fundamental Theory to Recent Applications. *Frontiers in Physics* **2019,** *7* (100).

72.   Nikon   Basics   of   FRET   Microscopy. https://www.microscopyu.com/applications/fret/basics-of-fret-microscopy (accessed 26th May 2020).

73.   Guzelturk, B.; Erdem, O.; Olutas, M.; Kelestemur, Y.; Demir, H. V., Stacking in Colloidal Nanoplatelets: Tuning Excitonic Properties. *ACS Nano* **2014,** *8* (12), 12524-12533.

74.   Abécassis, B.; Tessier, M. D.; Davidson, P.; Dubertret, B., Self-Assembly of CdSe Nanoplatelets into Giant Micrometer-Scale Needles Emitting Polarized Light. *Nano Letters* **2014,** *14* (2), 710-715.

75.   Tessier, M. D.; Biadala, L.; Bouet, C.; Ithurria, S.; Abecassis, B.; Dubertret, B., Phonon Line Emission Revealed by Self-Assembly of Colloidal Nanoplatelets. *ACS Nano* **2013,** *7* (4), 3332-3340.

76.   Tessier, M. D.; Javaux, C.; Maksimovic, I.; Loriette, V.; Dubertret, B., Spectroscopy of Single CdSe Nanoplatelets. *ACS Nano* **2012,** *6* (8), 6751-6758.

77.   Schmelz, O.; Mews, A.; Basché, T.; Herrmann, A.; Müllen, K., Supramolecular Complexes from CdSe Nanocrystals and Organic Fluorophors. *Langmuir* **2001,** *17* (9), 2861-2865.

78.   Willard, D. M.; Carillo, L. L.; Jung, J.; Van Orden, A., CdSe−ZnS Quantum Dots as Resonance Energy Transfer Donors in a Model Protein−Protein Binding Assay. *Nano Letters* **2001,** *1* (9), 469-474.

79.   Clapp, A. R.; Medintz, I. L.; Mauro, J. M.; Fisher, B. R.; Bawendi, M. G.; Mattoussi, H., Fluorescence Resonance Energy Transfer Between Quantum Dot Donors and Dye-Labeled Protein Acceptors. *Journal of the American Chemical Society* **2004,** *126* (1), 301-310.

80.   Potapova, I.; Mruk, R.; Hübner, C.; Zentel, R.; Basché, T.; Mews, A., CdSe/ZnS Nanocrystals with Dye-Functionalized Polymer Ligands Containing Many Anchor Groups. *Angewandte Chemie International Edition* **2005,** *44* (16), 2437-2440.

81.   Fernández-Argüelles, M. T.; Yakovlev, A.; Sperling, R. A.; Luccardini, C.; Gaillard, S.; Sanz Medel, A.; Mallet, J.-M.; Brochon, J.-C.; Feltz, A.; Oheim, M.; Parak, W. J., Synthesis and Characterization of Polymer-Coated Quantum Dots with Integrated Acceptor Dyes as FRET-Based Nanoprobes. *Nano Letters* **2007,** *7* (9), 2613-2617.

82.   Zenkevich, E.; Cichos, F.; Shulga, A.; Petrov, E. P.; Blaudeck, T.; von Borczyskowski, C., Nanoassemblies Designed from Semiconductor Quantum Dots and Molecular Arrays. *The Journal of Physical Chemistry B* **2005,** *109* (18), 8679-8692.

83.   Dayal, S.; Lou, Y.; Samia, A. C. S.; Berlin, J. C.; Kenney, M. E.; Burda, C., Observation of Non-Förster-Type Energy-Transfer Behavior in Quantum Dot−Phthalocyanine Conjugates. *Journal of the American Chemical Society* **2006,** *128* (43), 13974-13975.

84.   Dworak, L.; Matylitsky, V. V.; Ren, T.; Basché, T.; Wachtveitl, J., Acceptor Concentration Dependence of Förster Resonance Energy Transfer Dynamics in Dye–Quantum Dot Complexes. *The Journal of Physical Chemistry C* **2014,** *118* (8), 4396-4402.

85.   Empedocles, S. A.; Neuhauser, R.; Bawendi, M. G., Three-dimensional orientation measurements of symmetric single chromophores using polarization microscopy. *Nature* **1999,** *399* (6732), 126-130.

86.   Gao, Y.; Weidman, M. C.; Tisdale, W. A., CdSe Nanoplatelet Films with Controlled Orientation of their Transition Dipole Moment. *Nano Letters* **2017,** *17* (6), 3837-3843.

87.   Erdem, O.; Gungor, K.; Guzelturk, B.; Tanriover, I.; Sak, M.; Olutas, M.; Dede, D.; Kelestemur, Y.; Demir, H. V., Orientation-Controlled Nonradiative Energy Transfer to Colloidal Nanoplatelets: Engineering Dipole Orientation Factor. *Nano Letters* **2019,** *19* (7), 4297-4305.

88.   de Boer, P.; Hoogenboom, J. P.; Giepmans, B. N. G., Correlated light and electron microscopy: ultrastructure lights up! *Nature Methods* **2015,** *12* (6), 503-513.

89.   Light against cancer. http://www.reflexions.uliege.be/cms/c_41432/en/light-against-cancer?portal=j_55&printView=true (accessed 28th May 2020).

90.   Larson, D. R.; Zipfel, W. R.; Williams, R. M.; Clark, S. W.; Bruchez, M. P.; Wise, F. W.; Webb, W. W., Water-Soluble Quantum Dots for Multiphoton Fluorescence Imaging in Vivo. *Science* **2003,** *300* (5624), 1434-1436.

91.   Miller, D. R.; Jarrett, J. W.; Hassan, A. M.; Dunn, A. K., Deep Tissue Imaging with Multiphoton Fluorescence Microscopy. *Curr Opin Biomed Eng* **2017,** *4*, 32-39.

92.   Cheng, L.-C.; Horton, N. G.; Wang, K.; Chen, S.-J.; Xu, C., Measurements of multiphoton action cross sections for multiphoton microscopy. *Biomedical optics express* **2014,** *5* (10), 3427-3433.

93.   Xu, C.; Webb, W. W., Measurement of two-photon excitation cross sections of molecular fluorophores with data from 690 to 1050 nm. *JOSA B* **1996,** *13* (3), 481-491.

94.   Liu, H.; Wang, J.; Peng, X.; Zhuang, Z.; Qiu, P.; Wang, K., Ex and in vivo characterization of the wavelength-dependent 3-photon action cross-sections of red fluorescent proteins covering the 1700-nm window. *Journal of Biophotonics* **2018,** *11* (7), e201700351.

95.   Liu, H.; Deng, X.; Tong, S.; He, C.; Cheng, H.; Zhuang, Z.; Gan, M.; Li, J.; Xie, W.; Qiu, P.; Wang, K., In Vivo Deep-Brain Structural and Hemodynamic Multiphoton Microscopy Enabled by Quantum Dots. *Nano Letters* **2019,** *19* (8), 5260-5265.

96.   Lin, C.-A. J.; Sperling, R. A.; Li, J. K.; Yang, T.-Y.; Li, P.-Y.; Zanella, M.; Chang, W. H.; Parak, W. J., Design of an Amphiphilic Polymer for Nanoparticle Coating and Functionalization. *Small* **2008,** *4* (3), 334-341.

97.   Riedinger, A.; Zhang, F.; Dommershausen, F.; Rocker, C.; Brandholt, S.; Nienhaus, G. U.; Koert, U.; Parak, W. J., Ratiometric optical sensing of chloride ions with organic fluorophore-gold nanoparticle hybrids: a systematic study of design parameters and surface charge effects. *Small* **2010,** *6* (22), 2590-7.

98.   Invitrogen™ Qdot™ 655 ITK™. https://www.thermofisher.com/order/catalog/product/Q21321MP#/Q21321MP.

99. Lartigue, L.; Alloyeau, D.; Kolosnjaj-Tabi, J.; Javed, Y.; Guardia, P.; Riedinger, A.; Péchoux, C.; Pellegrino, T.; Wilhelm, C.; Gazeau, F., Biodegradation of Iron Oxide Nanocubes: High-Resolution In Situ Monitoring. *ACS Nano* **2013,** *7* (5), 3939-3952.

100. Lim, S. J.; McDougle, D. R.; Zahid, M. U.; Ma, L.; Das, A.; Smith, A. M., Lipoprotein Nanoplatelets: Brightly Fluorescent, Zwitterionic Probes with Rapid Cellular Entry. *Journal of the American Chemical Society* **2016,** *138* (1), 64-7.

101. Shendre, S.; Delikanli, S.; Li, M.; Dede, D.; Pan, Z.; Ha, S. T.; Fu, Y. H.; Hernández-Martínez, P. L.; Yu, J.; Erdem, O.; Kuznetsov, A. I.; Dang, C.; Sum, T. C.; Demir, H. V., Ultrahigh-efficiency aqueous flat nanocrystals of CdSe/CdS@Cd1−xZnxS colloidal core/crown@alloyed-shell quantum wells. *Nanoscale* **2019,** *11* (1), 301-310.

102. Kechkeche, D.; Cao, E.; Grazon, C.; Caschera, F.; Noireaux, V.; Baron Niel, M.-L.; Dubertret, B., Semiconductor Nanoplatelets: A New Class of Ultrabright Fluorescent Probes for Cytometric and Imaging Applications. *ACS Applied Materials & Interfaces* **2018,** *10* (29), 24739-24749.

103. Salvati, A.; Pitek, A. S.; Monopoli, M. P.; Prapainop, K.; Bombelli, F. B.; Hristov, D. R.; Kelly, P. M.; Åberg, C.; Mahon, E.; Dawson, K. A., Transferrin-functionalized nanoparticles lose their targeting capabilities when a biomolecule corona adsorbs on the surface. *Nature Nanotechnology* **2013,** *8* (2), 137-143.

104. Lavis, L. D.; Raines, R. T., Bright Ideas for Chemical Biology. *ACS Chemical Biology* **2008,** *3* (3), 142-155.

105. Fan, J.; Hu, M.; Zhan, P.; Peng, X., Energy transfer cassettes based on organic fluorophores: construction and applications in ratiometric sensing. *Chemical Society Reviews* **2013,** *42* (1), 29-43.

106. Heilemann, M.; van de Linde, S.; Mukherjee, A.; Sauer, M., Super-Resolution Imaging with Small Organic Fluorophores. *Angewandte Chemie International Edition* **2009,** *48* (37), 6903-6908.

107. Umezawa, K.; Citterio, D.; Suzuki, K., New Trends in Near-Infrared Fluorophores for Bioimaging. *Analytical Sciences* **2014,** *30* (3), 327-349.

108. Romero, N. A.; Nicewicz, D. A., Organic Photoredox Catalysis. *Chemical Reviews* **2016,** *116* (17), 10075-10166.

109. Silvi, S.; Credi, A., Luminescent sensors based on quantum dot–molecule conjugates. *Chemical Society Reviews* **2015,** *44* (13), 4275-4289.

110. Bruchez, M.; Moronne, M.; Gin, P.; Weiss, S.; Alivisatos, A. P., Semiconductor Nanocrystals as Fluorescent Biological Labels. *Science* **1998,** *281* (5385), 2013-2016.

111. Clapp, A. R.; Medintz, I. L.; Mattoussi, H., Förster Resonance Energy Transfer Investigations Using Quantum-Dot Fluorophores. *ChemPhysChem* **2006,** *7* (1), 47-57.

112. Zhou, E.; Yamakawa, S.; Zhang, Y.; Tajima, K.; Yang, C.; Hashimoto, K., Indolo[3,2-b]carbazole-based alternating donor–acceptor copolymers: synthesis, properties and photovoltaic application. *Journal of Materials Chemistry* **2009,** *19* (41), 7730-7737.

113. Zhang, X.; Steckler, T. T.; Dasari, R. R.; Ohira, S.; Potscavage, W. J.; Tiwari, S. P.; Coppée, S.; Ellinger, S.; Barlow, S.; Brédas, J.-L.; Kippelen, B.; Reynolds, J. R.; Marder, S. R., Dithienopyrrole-based donor–acceptor copolymers: low band-gap materials for charge transport, photovoltaics and electrochromism. *Journal of Materials Chemistry* **2010,** *20* (1), 123-134.

114. Wang, L.; Huang, W.; Li, R.; Gehrig, D.; Blom, P. W. M.; Landfester, K.; Zhang, K. A. I., Structural Design Principle of Small-Molecule Organic Semiconductors for Metal-Free,

Visible-Light-Promoted Photocatalysis. *Angewandte Chemie International Edition* **2016,** *55* (33), 9783-9787.

115. Wang, L.; Rörich, I.; Ramanan, C.; Blom, P. W. M.; Huang, W.; Li, R.; Zhang, K. A. I., Electron donor-free photoredox catalysis via an electron transfer cascade by cooperative organic photocatalysts. *Catalysis Science & Technology* **2018,** *8* (14), 3539-3547.

116. Tessier, M. D.; Spinicelli, P.; Dupont, D.; Patriarche, G.; Ithurria, S.; Dubertret, B., Efficient Exciton Concentrators Built from Colloidal Core/Crown CdSe/CdS Semiconductor Nanoplatelets. *Nano Letters* **2014,** *14* (1), 207-213.

117. Turcu, I.; Mic, M., Size Dependence of Molecular Self-Assembling in Stacked Aggregates. 2. Heat Exchange Effects. *The Journal of Physical Chemistry B* **2013,** *117* (30), 9083-9093.

118. Miyamura, K.; Mihara, A.; Fujii, T.; Gohshi, Y.; Ishii, Y., Unusually Strong Interactions Mediated by Both .pi.-.pi. Stacking and CH-.pi. Interactions Present in the Dimer of Nickel(II) Complex Coordinated with n-Butyl-Substituted Salen. *Journal of the American Chemical Society* **1995,** *117* (8), 2377-2378.

119. Hans, B., *Enzyme Kinetics Principles and Methods*. Wiley-VCH: Weinheim, 2008.

120. Medintz, I. L.; Clapp, A. R.; Mattoussi, H.; Goldman, E. R.; Fisher, B.; Mauro, J. M., Self-assembled nanoscale biosensors based on quantum dot FRET donors. *Nature Materials* **2003,** *2* (9), 630-638.

121. Snee, P. T.; Tyrakowski, C. M.; Page, L. E.; Isovic, A.; Jawaid, A. M., Quantifying Quantum Dots through Förster Resonant Energy Transfer. *The Journal of Physical Chemistry C* **2011,** *115* (40), 19578-19582.

122. Kowerko, D.; Schuster, J.; Amecke, N.; Abdel-Mottaleb, M.; Dobrawa, R.; Würthner, F.; von Borczyskowski, C., FRET and ligand related NON-FRET processes in single quantum dot-perylene bisimide assemblies. *Physical Chemistry Chemical Physics* **2010,** *12* (16), 4112-4123.

123. Conroy, E. M.; Li, J. J.; Kim, H.; Algar, W. R., Self-Quenching, Dimerization, and Homo-FRET in Hetero-FRET Assemblies with Quantum Dot Donors and Multiple Dye Acceptors. *The Journal of Physical Chemistry C* **2016,** *120* (31), 17817-17828.

124. van der Meer, B. W.; Coker, G.; Chen, S. Y. S., *Resonance energy transfer: theory and data*. VCH: 1994.

125. Lakowicz, J. R., *Principles of Fluorescence Spectroscopy*. Springer US: 2007.

126. Scott, R.; Heckmann, J.; Prudnikau, A. V.; Antanovich, A.; Mikhailov, A.; Owschimikow, N.; Artemyev, M.; Climente, J. I.; Woggon, U.; Grosse, N. B.; Achtstein, A. W., Directed emission of CdSe nanoplatelets originating from strongly anisotropic 2D electronic structure. *Nature Nanotechnology* **2017,** *12* (12), 1155-1160.

127. Hernández-Martínez, P. L.; Govorov, A. O.; Demir, H. V., Generalized Theory of Förster-Type Nonradiative Energy Transfer in Nanostructures with Mixed Dimensionality. *The Journal of Physical Chemistry C* **2013,** *117* (19), 10203-10212.

128. Achtstein, A. W.; Antanovich, A.; Prudnikau, A.; Scott, R.; Woggon, U.; Artemyev, M., Linear Absorption in CdSe Nanoplates: Thickness and Lateral Size Dependency of the Intrinsic Absorption. *The Journal of Physical Chemistry C* **2015,** *119* (34), 20156-20161.

129. Han, L.; Qin, D.; Jiang, X.; Liu, Y.; Wang, L.; Chen, J.; Cao, Y., Synthesis of high quality zinc-blende CdSe nanocrystals and their application in hybrid solar cells. *Nanotechnology* **2006,** *17* (18), 4736-4742.

130. Bertrand, G. H. V.; Polovitsyn, A.; Christodoulou, S.; Khan, A. H.; Moreels, I., Shape control of zincblende CdSe nanoplatelets. *Chemical Communications* **2016,** *52* (80), 11975-11978.

131.   Jiang, Y.; Ojo, W.-S.; Mahler, B.; Xu, X.; Abécassis, B.; Dubertret, B., Synthesis of CdSe Nanoplatelets without Short-Chain Ligands: Implication for Their Growth Mechanisms. *ACS Omega* **2018,** *3* (6), 6199-6205.

132.   Koketsu, M.; Nada, F.; Hiramatsu, S.; Ishihara, H., Reactions of acyl chlorides with LiAlHSeH. Preparation of diacyl selenides, diacyl diselenides, selenocarboxylates and cyclic selenoanhydrides. *Journal of the Chemical Society, Perkin Transactions 1* **2002,** (6), 737-740.

133.   Resch-Genger, U.; Rurack, K., Determination of the photoluminescence quantum yield of dilute dye solutions (IUPAC Technical Report). *Pure and Applied Chemistry* **2013,** *85* (10), 2005-2013.

134.   Müller, J.; Prozeller, D.; Ghazaryan, A.; Kokkinopoulou, M.; Mailänder, V.; Morsbach, S.; Landfester, K., Beyond the protein corona – lipids matter for biological response of nanocarriers. *Acta Biomaterialia* **2018,** *71*, 420-431.

135.   Lewis, E. A.; Murphy, K. P., Isothermal titration calorimetry. In *Protein-Ligand Interactions*, Springer: 2005; pp 1-15.

136.   Freire, E.; Mayorga, O. L.; Straume, M., Isothermal titration calorimetry. *Analytical chemistry* **1990,** *62* (18), 950A-959A.

137.   Bisswanger, H., *Enzyme kinetics: principles and methods*. John Wiley & Sons: 2017.

138.   Mahboub, M.; Huang, Z.; Tang, M. L., Efficient Infrared-to-Visible Upconversion with Subsolar Irradiance. *Nano Letters* **2016,** *16* (11), 7169-7175.

139.   Dilbeck, T.; Hill, S. P.; Hanson, K., Harnessing molecular photon upconversion at sub-solar irradiance using dual sensitized self-assembled trilayers. *Journal of Materials Chemistry A* **2017,** *5* (23), 11652-11660.

140.   Pedrini, J.; Monguzzi, A. In *Recent advances in the application triplet–triplet annihilation-based photon upconversion systems to solar technologies*, SPIE: 2017; p 16.

141.   Baluschev, S.; Yakutkin, V.; Miteva, T.; Avlasevich, Y.; Chernov, S.; Aleshchenkov, S.; Nelles, G.; Cheprakov, A.; Yasuda, A.; Müllen, K.; Wegner, G., Blue-Green Up-Conversion: Noncoherent Excitation by NIR Light. *Angewandte Chemie International Edition* **2007,** *46* (40), 7693-7696.

142.   Singh-Rachford, T. N.; Castellano, F. N., Triplet Sensitized Red-to-Blue Photon Upconversion. *The Journal of Physical Chemistry Letters* **2010,** *1* (1), 195-200.

143.   Monguzzi, A.; Tubino, R.; Hoseinkhani, S.; Campione, M.; Meinardi, F., Low power, non-coherent sensitized photon up-conversion: modelling and perspectives. *Physical Chemistry Chemical Physics* **2012,** *14* (13), 4322-4332.

144.   Schulze, T. F.; Schmidt, T. W., Photochemical upconversion: present status and prospects for its application to solar energy conversion. *Energy & Environmental Science* **2015,** *8* (1), 103-125.

145.   Ogawa, T.; Yanai, N.; Monguzzi, A.; Kimizuka, N., Highly Efficient Photon Upconversion in Self-Assembled Light-Harvesting Molecular Systems. *Scientific Reports* **2015,** *5*, 10882.

146.   Monguzzi, A.; Borisov, S. M.; Pedrini, J.; Klimant, I.; Salvalaggio, M.; Biagini, P.; Melchiorre, F.; Lelii, C.; Meinardi, F., Efficient Broadband Triplet–Triplet Annihilation-Assisted Photon Upconversion at Subsolar Irradiance in Fully Organic Systems. *Advanced Functional Materials* **2015,** *25* (35), 5617-5624.

147.   Pedrini, J.; Monguzzi, A.; Meinardi, F., Cascade sensitization of triplet–triplet annihilation based photon upconversion at sub-solar irradiance. *Physical Chemistry Chemical Physics* **2018,** *20* (15), 9745-9750.

148.   Zhou, Y.; Ruchlin, C.; Robb, A. J.; Hanson, K., Singlet Sensitization-Enhanced Upconversion Solar Cells via Self-Assembled Trilayers. *ACS Energy Letters* **2019,** *4* (6), 1458-1463.

149.   Hagstrom, A. L.; Weon, S.; Choi, W.; Kim, J.-H., Triplet–Triplet Annihilation Upconversion in Broadly Absorbing Layered Film Systems for Sub-Bandgap Photocatalysis. *ACS Applied Materials & Interfaces* **2019,** *11* (14), 13304-13318.

150.   Kovalenko, M. V.; Manna, L.; Cabot, A.; Hens, Z.; Talapin, D. V.; Kagan, C. R.; Klimov, V. I.; Rogach, A. L.; Reiss, P.; Milliron, D. J.; Guyot-Sionnnest, P.; Konstantatos, G.; Parak, W. J.; Hyeon, T.; Korgel, B. A.; Murray, C. B.; Heiss, W., Prospects of Nanoscience with Nanocrystals. *ACS Nano* **2015,** *9* (2), 1012-1057.

151.   Pietryga, J. M.; Park, Y.-S.; Lim, J.; Fidler, A. F.; Bae, W. K.; Brovelli, S.; Klimov, V. I., Spectroscopic and Device Aspects of Nanocrystal Quantum Dots. *Chemical Reviews* **2016,** *116* (18), 10513-10622.

152.   Mongin, C.; Garakyaraghi, S.; Razgoniaeva, N.; Zamkov, M.; Castellano, F. N., Direct observation of triplet energy transfer from semiconductor nanocrystals. *Science* **2016,** *351* (6271), 369.

153.   Mongin, C.; Moroz, P.; Zamkov, M.; Castellano, F. N., Thermally activated delayed photoluminescence from pyrenyl-functionalized CdSe quantum dots. *Nature Chemistry* **2017,** *10*, 225.

154.   Han, Y.; He, S.; Luo, X.; Li, Y.; Chen, Z.; Kang, W.; Wang, X.; Wu, K., Triplet Sensitization by "Self-Trapped" Excitons of Nontoxic CuInS2 Nanocrystals for Efficient Photon Upconversion. *Journal of the American Chemical Society* **2019,** *141* (33), 13033-13037.

155.   Wu, M.; Congreve, D. N.; Wilson, M. W. B.; Jean, J.; Geva, N.; Welborn, M.; Van Voorhis, T.; Bulović, V.; Bawendi, M. G.; Baldo, M. A., Solid-state infrared-to-visible upconversion sensitized by colloidal nanocrystals. *Nature Photonics* **2015,** *10*, 31.

156.   Boles, M. A.; Ling, D.; Hyeon, T.; Talapin, D. V., The surface science of nanocrystals. *Nature Materials* **2016,** *15* (2), 141-153.

157.   Christoph, G. J.; Stefan, F., Upconversion for Photovoltaics – a Review of Materials, Devices and Concepts for Performance Enhancement. *Advanced Optical Materials* **2015,** *3* (4), 510-535.

158.   Trupke, T.; Shalav, A.; Richards, B. S.; Würfel, P.; Green, M. A., Efficiency enhancement of solar cells by luminescent up-conversion of sunlight. *Solar Energy Materials and Solar Cells* **2006,** *90* (18), 3327-3338.

159.   Monguzzi, A.; Oertel, A.; Braga, D.; Riedinger, A.; Kim, D. K.; Knüsel, P. N.; Bianchi, A.; Mauri, M.; Simonutti, R.; Norris, D. J.; Meinardi, F., Photocatalytic Water-Splitting Enhancement by Sub-Bandgap Photon Harvesting. *ACS Applied Materials & Interfaces* **2017,** *9* (46), 40180-40186.

160.   Khnayzer, R. S.; Blumhoff, J.; Harrington, J. A.; Haefele, A.; Deng, F.; Castellano, F. N., Upconversion-powered photoelectrochemistry. *Chemical Communications* **2012,** *48* (2), 209-211.

161.   Ferreira, R. A. S.; Correia, S. F. H.; Monguzzi, A.; Liu, X.; Meinardi, F., Spectral converters for photovoltaics – What's ahead. *Materials Today* **2019**.

162.   Zou, W.; Visser, C.; Maduro, J. A.; Pshenichnikov, M. S.; Hummelen, J. C., Broadband dye-sensitized upconversion of near-infrared light. *Nature Photonics* **2012,** *6*, 560.

163.   Fischer, S.; Mehlenbacher, R. D.; Lay, A.; Siefe, C.; Alivisatos, A. P.; Dionne, J. A., Small Alkaline-Earth-based Core/Shell Nanoparticles for Efficient Upconversion. *Nano Letters* **2019,** *19* (6), 3878-3885.

164. Hagstrom, A. L.; Lee, H.-L.; Lee, M.-S.; Choe, H.-S.; Jung, J.; Park, B.-G.; Han, W.-S.; Ko, J.-S.; Kim, J.-H.; Kim, J.-H., Flexible and Micropatternable Triplet–Triplet Annihilation Upconversion Thin Films for Photonic Device Integration and Anticounterfeiting Applications. *ACS Applied Materials & Interfaces* **2018,** *10* (10), 8985-8992.

165. You, M.; Zhong, J.; Hong, Y.; Duan, Z.; Lin, M.; Xu, F., Inkjet printing of upconversion nanoparticles for anti-counterfeit applications. *Nanoscale* **2015,** *7* (10), 4423-31.

166. Mattiello, S.; Monguzzi, A.; Pedrini, J.; Sassi, M.; Villa, C.; Torrente, Y.; Marotta, R.; Meinardi, F.; Beverina, L., Bioimaging: Self-Assembled Dual Dye-Doped Nanosized Micelles for High-Contrast Up-Conversion Bioimaging (Adv. Funct. Mater. 46/2016). *Advanced Functional Materials* **2016,** *26* (46), 8446-8446.

167. Askes, S. H. C.; Leeuwenburgh, V. C.; Pomp, W.; Arjmandi-Tash, H.; Tanase, S.; Schmidt, T.; Bonnet, S., Water-Dispersible Silica-Coated Upconverting Liposomes: Can a Thin Silica Layer Protect TTA-UC against Oxygen Quenching? *ACS Biomaterials Science & Engineering* **2017,** *3* (3), 322-334.

168. Liu, Q.; Xu, M.; Yang, T.; Tian, B.; Zhang, X.; Li, F., Highly Photostable Near-IR-Excitation Upconversion Nanocapsules Based on Triplet-Triplet Annihilation for in Vivo Bioimaging Application. *ACS Appl Mater Interfaces* **2018,** *10* (12), 9883-9888.

169. Borisov, S. M.; Larndorfer, C.; Klimant, I., Triplet–Triplet Annihilation-Based Anti-Stokes Oxygen Sensing Materials with a Very Broad Dynamic Range. *Advanced Functional Materials* **2012,** *22* (20), 4360-4368.

170. Kwon, O. S.; Song, H. S.; Conde, J.; Kim, H.-i.; Artzi, N.; Kim, J.-H., Dual-Color Emissive Upconversion Nanocapsules for Differential Cancer Bioimaging In Vivo. *ACS Nano* **2016,** *10* (1), 1512-1521.

171. Ronchi, A.; Brazzo, P.; Sassi, M.; Beverina, L.; Pedrini, J.; Meinardi, F.; Monguzzi, A., Triplet–triplet annihilation based photon up-conversion in hybrid molecule–semiconductor nanocrystal systems. *Physical Chemistry Chemical Physics* **2019,** *21* (23), 12353-12359.

172. Zhou, Q.; Cho, Y.; Yang, S.; Weiss, E. A.; Berkelbach, T. C.; Darancet, P., Large Band Edge Tunability in Colloidal Nanoplatelets. *Nano Letters* **2019,** *19* (10), 7124-7129.

173. Huang, Z.; Xu, Z.; Mahboub, M.; Li, X.; Taylor, J. W.; Harman, W. H.; Lian, T.; Tang, M. L., PbS/CdS Core–Shell Quantum Dots Suppress Charge Transfer and Enhance Triplet Transfer. *Angew. Chem. Int. Ed.* **2017,** *56* (52), 16583-16587.

174. VanOrman, Z. A.; Bieber, A. S.; Wieghold, S.; Nienhaus, L., Green-to-Blue Triplet Fusion Upconversion Sensitized by Anisotropic CdSe Nanoplatelets. *Chemistry of Materials* **2020,** *32* (11), 4734-4742.

175. Rabouw, F. T.; van der Bok, J. C.; Spinicelli, P.; Mahler, B.; Nasilowski, M.; Pedetti, S.; Dubertret, B.; Vanmaekelbergh, D., Temporary Charge Carrier Separation Dominates the Photoluminescence Decay Dynamics of Colloidal CdSe Nanoplatelets. *Nano Lett.* **2016,** *16* (3), 2047-2053.

176. Xia, C.; Wang, W.; Du, L.; Rabouw, F. T.; J. van den Heuvel, D.; Gerritsen, H. C.; Mattoussi, H.; de Mello Donega, C., Förster Resonance Energy Transfer between Colloidal CuInS2/ZnS Quantum Dots and Dark Quenchers. *The Journal of Physical Chemistry C* **2020,** *124* (2), 1717-1731.

177. Ebenstein, Y.; Mokari, T.; Banin, U., Fluorescence quantum yield of CdSe/ZnS nanocrystals investigated by correlated atomic-force and single-particle fluorescence microscopy. *Applied Physics Letters* **2002,** *80* (21), 4033-4035.

178.   Pons, T.; Medintz, I. L.; Farrell, D.; Wang, X.; Grimes, A. F.; English, D. S.; Berti, L.; Mattoussi, H., Single-Molecule Colocalization Studies Shed Light on the Idea of Fully Emitting versus Dark Single Quantum Dots. *Small* **2011,** *7* (14), 2101-2108.

179.   Hirayama, S., Effect of substituent on the behaviour of the excited singlet and triplet states in carbonyl derivatives of anthracene of the type 9-X·CO·A. *Journal of the Chemical Society, Faraday Transactions 1: Physical Chemistry in Condensed Phases* **1982,** *78* (8), 2411-2421.

180.   Zhu, L.; Al-Kaysi, R. O.; Dillon, R. J.; Tham, F. S.; Bardeen, C. J., Crystal Structures and Photophysical Properties of 9-Anthracene Carboxylic Acid Derivatives for Photomechanical Applications. *Crystal Growth & Design* **2011,** *11* (11), 4975-4983.

181.   Pope, M.; Swenberg, C. E., *Electronic processes in organic crystals and polymers*. Oxford University Press on Demand: 1999.

182.   Hendricks, M. P.; Campos, M. P.; Cleveland, G. T.; Jen-La Plante, I.; Owen, J. S., A tunable library of substituted thiourea precursors to metal sulfide nanocrystals. *Science* **2015,** *348* (6240), 1226-1230.

183.   Li, Q.; Zhao, F.; Qu, C.; Shang, Q.; Xu, Z.; Yu, L.; McBride, J. R.; Lian, T., Two-Dimensional Morphology Enhances Light-Driven H2 Generation Efficiency in CdS Nanoplatelet-Pt Heterostructures. *Journal of the American Chemical Society* **2018,** *140* (37), 11726-11734.

184.   Inamdar, S. N.; Ingole, P. P.; Haram, S. K., Determination of Band Structure Parameters and the Quasi-Particle Gap of CdSe Quantum Dots by Cyclic Voltammetry. *ChemPhysChem* **2008,** *9* (17), 2574-2579.

185.   Kucur, E.; Riegler, J.; Urban, G. A.; Nann, T., Determination of quantum confinement in CdSe nanocrystals by cyclic voltammetry. *The Journal of Chemical Physics* **2003,** *119* (4), 2333-2337.

186.   Spittel, D.; Poppe, J.; Meerbach, C.; Ziegler, C.; Hickey, S. G.; Eychmüller, A., Absolute Energy Level Positions in CdSe Nanostructures from Potential-Modulated Absorption Spectroscopy (EMAS). *ACS Nano* **2017,** *11* (12), 12174-12184.

187.   Dai, Y.; Li, C.; Shen, Y.; Lim, T.; Xu, J.; Li, Y.; Niemantsverdriet, H.; Besenbacher, F.; Lock, N.; Su, R., Light-tuned selective photosynthesis of azo- and azoxy-aromatics using graphitic C3N4. *Nature Communications* **2018,** *9* (1), 60.

188.   Halliday, D.; Resnick, R.; Walker, J., *Fundamentals of physics*. John Wiley & Sons: 2013.

189.   Feynman, R. P.; Leighton, R. B.; Sands, M., The feynman lectures on physics; vol. i. *American Journal of Physics* **1965,** *33* (9), 750-752.

190.   Wang, B.; Deng, Z.; Li, Z., Efficient chemoselective hydrogenation of nitrobenzene to aniline, azoxybenzene and azobenzene over CQDs/ZnIn2S4 nanocomposites under visible light. *Journal of Catalysis* **2020,** *389*, 241-246.

191.   Zrazhevskiy, P.; Sena, M.; Gao, X., Designing multifunctional quantum dots for bioimaging, detection, and drug delivery. *Chemical Society Reviews* **2010,** *39* (11), 4326-4354.

192.   Gao, X.; Yang, L.; Petros, J. A.; Marshall, F. F.; Simons, J. W.; Nie, S., In vivo molecular and cellular imaging with quantum dots. *Current Opinion in Biotechnology* **2005,** *16* (1), 63-72.

193.   Zhang, F.; Ali, Z.; Amin, F.; Riedinger, A.; Parak, W. J., In vitro and intracellular sensing by using the photoluminescence of quantum dots. *Analytical and Bioanalytical Chemistry* **2010,** *397* (3), 935-942.

194.   Chen, O.; Zhao, J.; Chauhan, V. P.; Cui, J.; Wong, C.; Harris, D. K.; Wei, H.; Han, H.-S.; Fukumura, D.; Jain, R. K.; Bawendi, M. G., Compact high-quality CdSe–CdS core–shell nanocrystals with narrow emission linewidths and suppressed blinking. *Nature Materials* **2013,** *12*, 445-451.

195.   Jana, S.; Phan, T. N. T.; Bouet, C.; Tessier, M. D.; Davidson, P.; Dubertret, B.; Abecassis, B., On the stacking and colloidal stability of CdSe nanoplatelets. *Langmuir* **2015,** *31* (38), 10532-10539.

196.   Pelton, M.; Ithurria, S.; Schaller, R. D.; Dolzhnikov, D. S.; Talapin, D. V., Carrier Cooling in Colloidal Quantum Wells. *Nano Letters* **2012,** *12* (12), 6158-6163.

197.   Pellegrino, T.; Manna, L.; Kudera, S.; Liedl, T.; Koktysh, D.; Rogach, A. L.; Keller, S.; Rädler, J.; Natile, G.; Parak, W. J., Hydrophobic Nanocrystals Coated with an Amphiphilic Polymer Shell: A General Route to Water Soluble Nanocrystals. *Nano Letters* **2004,** *4* (4), 703-707.

198.   Kreyling, W. G.; Abdelmonem, A. M.; Ali, Z.; Alves, F.; Geiser, M.; Haberl, N.; Hartmann, R.; Hirn, S.; de Aberasturi, D. J.; Kantner, K.; Khadem-Saba, G.; Montenegro, J.-M.; Rejman, J.; Rojo, T.; de Larramendi, I. R.; Ufartes, R.; Wenk, A.; Parak, W. J., In vivo integrity of polymer-coated gold nanoparticles. *Nature nanotechnology* **2015,** *10*, 619-624.

199.   Carambia, A.; Freund, B.; Schwinge, D.; Bruns, O. T.; Salmen, S. C.; Ittrich, H.; Reimer, R.; Heine, M.; Huber, S.; Waurisch, C.; Eychmüller, A.; Wraith, D. C.; Korn, T.; Nielsen, P.; Weller, H.; Schramm, C.; Lüth, S.; Lohse, A. W.; Heeren, J.; Herkel, J., Nanoparticle-based autoantigen delivery to Treg-inducing liver sinusoidal endothelial cells enables control of autoimmunity in mice. *Journal of Hepatology* **2015,** *62* (6), 1349-1356.

200.   Yadav, S.; Singh, A.; Thulasidharan, L.; Sapra, S., Surface Decides the Photoluminescence of Colloidal CdSe Nanoplatelets Based Core/Shell Heterostructures. *The Journal of Physical Chemistry C* **2018,** *122* (1), 820-829.

201.   Lee, S. H.; Salunke, B. K.; Kim, B. S., Sucrose density gradient centrifugation separation of gold and silver nanoparticles synthesized using Magnolia kobus plant leaf extracts. *Biotechnology and Bioprocess Engineering* **2014,** *19* (1), 169-174.

202.   Koynov, K.; Butt, H.-J., Fluorescence correlation spectroscopy in colloid and interface science. *Current Opinion in Colloid & Interface Science* **2012,** *17* (6), 377-387.

203.   Negwer, I.; Best, A.; Schinnerer, M.; Schäfer, O.; Capeloa, L.; Wagner, M.; Schmidt, M.; Mailänder, V.; Helm, M.; Barz, M.; Butt, H.-J; Koynov, K., Monitoring drug nanocarriers in human blood by near-infrared fluorescence correlation spectroscopy. *Nature Communications* **2018,** *9* (1), 5306-5314.

204.   Morsbach, S.; Gonella, G.; Mailänder, V.; Wegner, S.; Wu, S.; Weidner, T.; Berger, R.; Koynov, K.; Vollmer, D.; Encinas, N.; Kuan, S. L.; Bereau, T.; Kremer, K.; Weil, T.; Bonn, M.; Butt, H.-J.; Landfester, K., Engineering Proteins at Interfaces: From Complementary Characterization to Material Surfaces with Designed Functions. *Angewandte Chemie International Edition* **2018,** *57* (39), 12626-12648.

205.   Shaner, N. C.; Steinbach, P. A.; Tsien, R. Y., A guide to choosing fluorescent proteins. *Nature Methods* **2005,** *2*, 905-909.

206.   Rossinelli, A. A.; Riedinger, A.; Marques-Gallego, P.; Knusel, P. N.; Antolinez, F. V.; Norris, D. J., High-temperature growth of thick-shell CdSe/CdS core/shell nanoplatelets. *Chem Commun* **2017,** *53* (71), 9938-9941.

207.   Foroozandeh, P.; Aziz, A. A., Insight into Cellular Uptake and Intracellular Trafficking of Nanoparticles. *Nanoscale Research Letters* **2018,** *13* (1), 339.

208.   Hu, Y.-B.; Dammer, E. B.; Ren, R.-J.; Wang, G., The endosomal-lysosomal system: from acidification and cargo sorting to neurodegeneration. *Translational neurodegeneration* **2015,** *4* (1), 18.

209.   Schöttler, S.; Klein, K.; Landfester, K.; Mailänder, V., Protein source and choice of anticoagulant decisively affect nanoparticle protein corona and cellular uptake. *Nanoscale* **2016,** *8* (10), 5526-5536.

210.   Schöttler, S.; Becker, G.; Winzen, S.; Steinbach, T.; Mohr, K.; Landfester, K.; Mailänder, V.; Wurm, F. R., Protein adsorption is required for stealth effect of poly(ethylene glycol)- and poly(phosphoester)-coated nanocarriers. *Nature nanotechnology* **2016,** *11*, 372.

211.   Zhao, J.; Stenzel, M. H., Entry of nanoparticles into cells: the importance of nanoparticle properties. *Polymer Chemistry* **2018,** *9* (3), 259-272.

212.   Aldana, J.; Wang, Y. A.; Peng, X., Photochemical Instability of CdSe Nanocrystals Coated by Hydrophilic Thiols. *Journal of the American Chemical Society* **2001,** *123* (36), 8844-8850.

213.   Kreyling, W. G.; Abdelmonem, A. M.; Ali, Z.; Alves, F.; Geiser, M.; Haberl, N.; Hartmann, R.; Hirn, S.; de Aberasturi, D. J.; Kantner, K.; Khadem-Saba, G.; Montenegro, J.-M.; Rejman, J.; Rojo, T.; de Larramendi, I. R.; Ufartes, R.; Wenk, A.; Parak, W. J., In vivo integrity of polymer-coated gold nanoparticles. *Nature Nanotechnology* **2015,** *10*, 619.

214.   Liu, J.; Guillemeney, L.; Abécassis, B.; Coolen, L., Long Range Energy Transfer in Self-Assembled Stacks of Semiconducting Nanoplatelets. *Nano Lett.* **2020,** *20* (5), 3465-3470.

215.   Rausch, K.; Reuter, A.; Fischer, K.; Schmidt, M., Evaluation of Nanoparticle Aggregation in Human Blood Serum. *Biomacromolecules* **2010,** *11* (11), 2836-2839.

216.   Simon, J.; Bauer, K. N.; Langhanki, J.; Opatz, T.; Mailänder, V.; Landfester, K.; Wurm, F. R., Noncovalent Targeting of Nanocarriers to Immune Cells with Polyphosphoester-Based Surfactants in Human Blood Plasma. *Advanced Science* **2019,** *6* (22), 1901199.

217.   Tonigold, M.; Simon, J.; Estupiñán, D.; Kokkinopoulou, M.; Reinholz, J.; Kintzel, U.; Kaltbeitzel, A.; Renz, P.; Domogalla, M. P.; Steinbrink, K.; Lieberwirth, I.; Crespy, D.; Landfester, K.; Mailänder, V., Pre-adsorption of antibodies enables targeting of nanocarriers despite a biomolecular corona. *Nature Nanotechnology* **2018,** *13* (9), 862-869.

218.   Brückner, M.; Simon, J.; Jiang, S.; Landfester, K.; Mailänder, V., Preparation of the Protein Corona: How Washing Shapes the Proteome and Influences Cellular Uptake. *SSRN Electronic Journal* **2020**.

219.   Silva, J. C.; Gorenstein, M. V.; Li, G.-Z.; Vissers, J. P.; Geromanos, S. J., Absolute quantification of proteins by LCMSE: a virtue of parallel MS acquisition. *Molecular & Cellular Proteomics* **2006,** *5* (1), 144-156.

220.   Bykov, Y. S.; Cortese, M.; Briggs, J. A. G.; Bartenschlager, R., Correlative light and electron microscopy methods for the study of virus–cell interactions. *FEBS Letters* **2016,** *590* (13), 1877-1895.

221.   Dukes, M. J.; Peckys, D. B.; de Jonge, N., Correlative Fluorescence Microscopy and Scanning Transmission Electron Microscopy of Quantum-Dot-Labeled Proteins in Whole Cells in Liquid. *ACS Nano* **2010,** *4* (7), 4110-4116.

222.   van Rijnsoever, C.; Oorschot, V.; Klumperman, J., Correlative light-electron microscopy (CLEM) combining live-cell imaging and immunolabeling of ultrathin cryosections. *Nature Methods* **2008,** *5* (11), 973-980.

223.   Yu Lee, J.; Heon Nam, D.; Hwa Oh, M.; Kim, Y.; Seok Choi, H.; Young Jeon, D.; Beum Park, C.; Sung Nam, Y., Serum-stable quantum dot--protein hybrid nanocapsules for optical bio-imaging. *Nanotechnology* **2014,** *25* (17), 175702.

224.   Dubertret, B.; Skourides, P.; Norris, D. J.; Noireaux, V.; Brivanlou, A. H.; Libchaber, A., In Vivo Imaging of Quantum Dots Encapsulated in Phospholipid Micelles. *Science* **2002,** *298* (5599), 1759-1762.

225.   Seleci, M.; Ag Seleci, D.; Scheper, T.; Stahl, F., Theranostic Liposome–Nanoparticle Hybrids for Drug Delivery and Bioimaging. *International Journal of Molecular Sciences* **2017,** *18* (7), 1415.

226.   Mi, C.; Wang, Y.; Zhang, J.; Huang, H.; Xu, L.; Wang, S.; Fang, X.; Fang, J.; Mao, C.; Xu, S., Biosynthesis and characterization of CdS quantum dots in genetically engineered Escherichia coli. *Journal of Biotechnology* **2011,** *153* (3), 125-132.

227.   Pavan Kumar, K. V.; Nirmal Ghosh, O. S.; Balakrishnan, G.; Thirugnanasambantham, P.; Raghavan, S. K.; Viswanath, A. K., Green synthesis of zinc oxysulfide quantum dots using aegle marmelos fruit extract and their cytotoxicity in HeLa cells. *RSC Advances* **2015,** *5* (22), 16815-16820.

228.   Clift, M. J. D.; Brandenberger, C.; Rothen-Rutishauser, B.; Brown, D. M.; Stone, V., The uptake and intracellular fate of a series of different surface coated quantum dots in vitro. *Toxicology* **2011,** *286* (1), 58-68.

229.   Landfester, K.; Mailänder, V., Nanocapsules with specific targeting and release properties using miniemulsion polymerization. *Expert opinion on drug delivery* **2013,** *10* (5), 593-609.

230.   Piradashvili, K.; Fichter, M.; Mohr, K.; Gehring, S.; Wurm, F. R.; Landfester, K., Biodegradable Protein Nanocontainers. *Biomacromolecules* **2015,** *16* (3), 815-821.

Curriculum Vitae

Henry Halim

Date of birth   22.07.1994

Place of birth   Jakarta, Indonesia

Nationality   Indonesian

Current Position

08/2017 – <u>Present</u>   Doctoral Candidate at the department of Physical Chemistry of Polymers,

Max Planck Institute for Polymer Research,

Mainz, Germany

Education

10/2015 – 07/2017   Master of Science at the department of Chemistry,

The University of Tokyo, Bunkyo-ku, Tokyo, Japan

09/2012 – 05/2015   Bachelor of Science with major in Chemistry,

The University of Hong Kong, Pok Fu Lam, Hong Kong

09/2005 – 05/2012   International secondary school Year 7 – Year 13,

Sha Tin College, Fo Tan, Sha Tin, Hong Kong

Work and Research Experience

08/2017 – Present   Research at Max Planck Institute for Polymer Research
<u>Topic</u>: "Semiconductor nanoplatelets for imaging and energy transfer"
<u>Tasks</u>: Colloidal synthesis of metal chalcogenide nanocrystals / nanoparticles and purification by centrifugation. Characterization and data analysis with spectroscopy (steady state and time resolved), transmission electron microscopy (TEM), dynamic light scattering (DLS) and NMR. Polymer coating of nanoparticles for phase transfer to aqueous dispersion.

10/2015 – 07/2017	Research at The University of Tokyo Topic: "Hybrid organic and inorganic perovskite solar cells" Tasks: Device engineering of thin film perovskite photovoltaics: spin coating in glove box, annealing, physical vapor deposition (PVD). Analysis of film morphology using x-ray diffraction (XRD), scanning electron microscopy (SEM) and atomic force microscopy (AFM). Device evaluation with solar simulator, external quantum efficiency and photoelectron yield spectroscopy (PYS / PES).
05/2014 – 07/2014	Summer Research Fellowship (SRF) at The University of Hong Kong Topic: "Catalytic conversion of acetylene to polycyclic aromatic hydrocarbons over particles of Silicon Carbide (SiC)" Tasks: Time of flight mass spectrometry (ToF-MS) of organic molecules generated by laser excitation and high temperature catalysis. Data collection from oscilloscope & analysis.

Scholarships

12/2018 – 01/2021	Max Planck Graduate Center (MPGC) Scholarship
2015 – 2017	University of Tokyo Graduate School of Science (GSS) fellowship

Software Skills & Languages

Working experience: MS Office, Paint Tool SAI, Adobe Photoshop

Basic knowledge: HTML, CSS, MATLAB, Gaussian

Indonesian: First language (mother tongue)

English: Primary language (native, fluent)

German: Professional proficiency (studied up to level C1)

10/2018 – 07/2019	Internationales Studien- und Sprachenkolleg (ISSK) Mainz (Level C1)
07/2010 – 08/2015	Goethe Institut Hong Kong, Berlin (A1 – B2) University of Hong Kong (B2)

Japanese: Basic

09/2018 – 01/2019	Self-taught Japanese
10/2015 – 07/2017	Learned Japanese at University of Tokyo Nihongo Center

Publications

1) Polymeric Nanocarriers with Hydrophilic Nanoplatelet Markers Unambiguously Localized by Correlative Light and Electron Microscopy. Marie-Luise Frey, Shen Han, <u>Henry Halim</u>, Maximilian Brückner, Yeliz Yangazoglu, Johanna Simon, Ingo Lieberwirth, Andreas Riedinger and Katharina Landfester. In preparation.

2) Intermolecular Interactions Between Anthracene Ligands on CdSe Nanoplatelet Surfaces Enable Delayed Fluorencene base onTriplet-Triplet Annihilation. <u>Henry Halim</u>, Alessandra Ronchi, Ricardo Báez, Nadzeya Nazarova, María Martínez-Negro, Svenja Morsbach, Stanislav Balouchev, Francesco Meinardi, Charusheela Ramanan, Katharina Landfester, Angelo Monguzzi and Andreas Riedinger. In preparation.

3) Semiconducting CdSe nanoplatelets with precisely controllable thickness for visible light-driven reduction of nitrobenzene towards azoxybenzene. Niklas Huber, <u>Henry Halim</u>, Katharina Landfester, Kai A. I. Zhang, and Andreas Riedinger. In preparation.

4) Surface Dynamics of Nominally Equivalent Nanoparticles Governs Cell Uptake Behavior. <u>Henry Halim</u>, Johanna Simon, Jennifer Oberländer, Kaloian Koynov, Katharina Landfester, Volker Mailänder and Andreas Riedinger. In preparation.

5) Plasmonic and semiconductor nanoparticles interfere with stereolithographic 3D printing. Rebecca Momper, Antonio Ibanez Landeta, Long Yang, <u>Henry Halim</u>, Héloïse Thérien-Aubin, Eberhard Bodenschatz, Katharina Landfester and Andreas Riedinger. *ACS Applied Materials & Interfaces.*, 2020, 12 (45), 50834-50843.

6) Lateral Size-Dependence in FRET between Semiconductor Nanoplatelets and Conjugated Fluorophores. <u>Henry Halim</u>, David Trieb, Niklas Huber, María Martínez-Negro, Lars-Arne Meyer, Thomas Basché, Svenja Morsbach, Kai Zhang and Andreas Riedinger. *Journal of Physical Chemistry C.*, 2020, 124 (45), 25028-25037.

7) Kinetic control over self-assembly of semiconductor nanoplatelets. Rebecca Momper, Heng Zhang, Shuai Chen, <u>Henry Halim</u>, Ewald Johannes, Stoyan Yordanov, Daniele Braga, Balthasar Blülle, David Doblas, Tobias Kraus, Mischa Bonn, Hai I. Wang, and Andreas Riedinger. *Nano Letters.*, 2020, 20 (6), 4102-4110

8) Water-dispersed semiconductor nanoplatelets with high fluorescence brightness, chemical and colloidal stability. <u>Henry Halim</u>, Johanna Simon, Ingo Lieberwirth, Volker Mailänder Kaloian Koynov and Andreas Riedinger. *Journal of Materials Chemistry B.*, 2020, 8, 146-154

9) Disodium Benzodipyrrole Sulfonate as Neutral Hole-Transporting Materials for Perovskite Solar Cells. Rui Shang, Zhongmin Zhou, Hiroki Nishioka, <u>Henry Halim</u>, Shunsuke Furukawa, Izuru Takei, Naoya Ninomiya, and Eiichi Nakamura. *Journal of the American Chemical Society.*, 2018, 140 (15), 5018–5022

10) Citric acid modulated growth of oriented lead perovskite crystals for efficient solar cells. Yunlong Guo, Wataru Sato, Kazutaka Shoyama, <u>Henry Halim</u>, Yuki Itabashi, Rui Shang, and Eiichi Nakamura. *Journal of the American Chemical Society.*, 2017, 139 (28), 9598-9604

11) Flexible organic-inorganic hybrid perovskite solar cells. <u>Henry Halim</u> and Yunlong Guo. *Science China Materials.*, 2016, 59 (6): 495–506